Self-Organized Pattern Formation in Geological Soft Matter

Julyan H. E. Cartwright[a,b], Charles S. Cockell[c], Lucas Goehring[d], Silvia Holler[e], Sean F. Jordan[f], Pamela Knoll[c], Electra Kotopoulou[g], Corentin C. Loron[c], Sean McMahon[c], Stephen W. Morris[h], Anna Neubeck[i], Carlos Pimentel[j], C. Ignacio Sainz-Díaz[a], Noushine Shahidzadeh[k], Piotr Szymczak[l]

[a] *Instituto Andaluz de Ciencias de la Tierra, CSIC, 18100 Armilla, Granada, Spain*
[b] *Instituto Carlos I de Física Teórica y Computacional, Universidad de Granada, 18071 Granada, Spain*
[c] *School of Physics and Astronomy, University of Edinburgh, Edinburgh, UK*
[d] *School of Science and Technology, Nottingham Trent University, Nottingham NG11 8NS, UK*
[e] *Cellular Computational and Biology Department, CIBIO, Laboratory for Artificial Biology, University of Trento, Via Sommarive 9, Povo, 38123, Italy*
[f] *Atlantic Technological University, Sligo, Ireland*
[g] *Laboratoire Écologie, Systématique et Évolution, Université Paris-Saclay, France*
[h] *Department of Physics, University of Toronto, 60 St. George St., Toronto, ON, Canada, M5S 1A7*
[i] *Department of Earth Sciences, Uppsala University, Uppsala, Sweden*
[j] *Departamento de Mineralogía y Petrología, Facultad de Ciencias Geológicas, Universidad Complutense de Madrid, 28040 Madrid, Spain*
[k] *University of Amsterdam, Institute of Physics-Van der Waals-Zeeman Institute, Science Park 904, 1098 XH Amsterdam, The Netherlands*
[l] *Institute of Theoretical Physics, Faculty of Physics, University of Warsaw, Poland*

Abstract

Geological materials are often seen as the antithesis of soft; rocks are hard. However, during the formation of minerals and rocks, all the systems we shall discuss, indeed geological materials in general, pass through a stage where they are soft. This occurs either because they form at a high temperature—igneous or metamorphic rock—or because they form at a lower temperature but in the presence of water—sedimentary rock. For this reason it is useful to introduce soft-matter concepts into the geological domain. There is a universality in the diverse instances of geological patterns that may be appreciated by looking at the common aspect in their formation of having passed through a stage as soft matter.

Contents

1 Introduction **3**

2 Soft matter **4**

3 Physical types of geological soft matter **4**
3.1 Gels 6
3.2 Polymers 6
3.3 Foams 6
3.4 Colloids 7
3.5 Liquid crystals 8
3.6 Membranes 8
3.7 Emulsions 9

Email addresses: julyan.cartwright@csic.es (Julyan H. E. Cartwright), cpimentelguerra@geo.ucm.es (Carlos Pimentel), piotrek@fuw.edu.pl (Piotr Szymczak)

3.8 Glasses . . . 9
3.9 Viscoelastic and viscoplastic materials . . . 10
3.10 Granular media . . . 11

4 Physical mechanisms underlying mesoscale geological self-organization 12
4.1 Reaction–diffusion systems . . . 12
4.1.1 Turing patterns . . . 12
4.1.2 Short-range activation and longer-range inhibition . . . 13
4.1.3 Excitable media . . . 13
4.1.4 Geological reaction–diffusion systems . . . 14
4.1.5 Liesegang patterns . . . 14
4.1.6 Oscillatory zoning . . . 15
4.2 Fluid-flow instabilities and convective processes . . . 16
4.2.1 Rayleigh–Bénard convection . . . 16
4.2.2 Rayleigh–Taylor instability . . . 17
4.2.3 Kelvin–Helmholtz instability . . . 18
4.2.4 Bénard–Marangoni convection . . . 19
4.2.5 Double-diffusive convection and mushy layers . . . 19
4.2.6 Capillary flow and coffee-ring instabilities . . . 22
4.2.7 Saffman–Taylor instability, viscous fingering, and reactive-infiltration instability . . . 23
4.2.8 Chaotic advection . . . 27
4.3 Osmotic processes . . . 28
4.4 Diffusion-limited aggregation . . . 29
4.5 Piezoelectricity . . . 31
4.6 Ostwald ripening . . . 31
4.7 Fracture processes . . . 32

5 Mesoscale self-organized pattern-forming systems in geology 33
5.1 Small and cold . . . 34
5.1.1 Agates . . . 34
5.1.2 Mineral dendrites . . . 43
5.1.3 Nuggets . . . 48
5.1.4 Opals . . . 48
5.1.5 Striped flint . . . 49
5.1.6 Zebra rock . . . 51
5.1.7 Zebra textures . . . 52
5.2 Large and cold . . . 54
5.2.1 Icicles, stalactites, and stalagmites . . . 54
5.2.2 Solution pipes, wormholes, and replacement fingers . . . 59
5.2.3 Dry salt lakes and convection . . . 66
5.2.4 Desert roses and other efflorescence structures . . . 69
5.2.5 Salt weathering, honeycomb weathering, and tafoni . . . 70
5.2.6 Sedimentary crack patterns . . . 72
5.2.7 Geodes . . . 73
5.2.8 Concretions and nodules . . . 74
5.2.9 Target patterns . . . 76
5.3 Small and hot . . . 77
5.3.1 Stylolites . . . 77
5.3.2 Porphyroblasts and spiral garnets . . . 80
5.3.3 Banded sphalerite . . . 82
5.3.4 Thunder eggs . . . 83
5.3.5 Orbicules . . . 84

5.3.6 Clathrites 84
5.3.7 Menilites 84
5.4 Large and hot 85
5.4.1 Basalt columns 86
5.4.2 Hydrothermal vents 90
5.4.3 Mud volcanoes, pockmarks and seeps 90
5.4.4 Fulgurites 92
5.4.5 Foliation in gneiss 94
5.4.6 Seismites 96

6 Summary and outlook **97**

1. Introduction

Pattern formation occurs at all scales in our universe, from the very largest of the large-scale structures of the cosmos, to the very smallest: how quarks organize themselves within atomic nuclei. In this review, we concentrate on an intermediate range spanning millimetres to metres. In this mesoscopic domain, the governing processes are no longer the chemistry of individual atoms, molecules, or crystals. Instead, patterns emerge from collective behaviour: interfaces, filaments, channels, and networks that organize under modest driving forces.

This is the realm of soft matter. Here, the stresses and energies that act are often comparable to k_BT, so thermal fluctuations, weak elasticities, and gentle flows can reorganize material configurations. A defining feature is the appearance of structures produced by self-organization and self-assembly; features large enough to be directly imaged and manipulated, yet still far below the overall extent of the material. These mesoscopic entities mediate transport, reactivity, and mechanics, and they often display universal motifs—branching, coarsening, fingering, rippling—that recur across disparate systems.

Our focus is on rocks; materials that hardly seem "soft". Yet at certain stages of their formation they behaved as soft matter, when thermal or mechanical stresses were sufficient to reshape their mesoscopic structure. Thus, understanding geological soft-matter systems is foundational for explaining how past processes produced the shapes and patterns we see in rocks and minerals today.

Although there is a large literature in physics on self-organization and pattern formation, it is rarely presented in relation to geology. There are a few notable exceptions. The first is Peter Ortoleva's *Geochemical Self-Organization* [1]; important in scope but mathematically intensive so that few geoscientists make it through. A second thread is *Growth, Dissolution and Pattern Formation in Geosystems* [2], followed by the review *Sculpting of Rocks by Reactive Fluids* [3]; These works focus largely on dissolution–precipitation processes mediated by fluid flow. While many geological patterns arise this way, a wide class of phenomena lies outside that framework. A closely related, soft-matter-oriented contribution is *Soft Matter Physics of the Ground Beneath Our Feet* by Voigtländer et al. [4], which centres on soils and sediments. By contrast, we turn to lithified systems: patterns preserved in hard rock that bear the imprint of earlier, transient soft regimes. Our aim is to show how signatures of that early softness govern the genesis and present architecture of these rock structures.

The recent advances in soft matter physics have revealed numerous new processes that provide critical insights into long-standing puzzles in geological pattern formation. These developments offer a fresh perspective, potentially unlocking key mechanisms behind the dynamics of mesoscale patterns in Earth's systems by linking them to the stage when they were soft. This focus on soft matter introduces novel insights that go beyond the scope of previous reviews, addressing complexities in geological phenomena that have long resisted explanation.

Our aim is that soft-matter physicists with an interest in geological applications will find this review of use. At the same time, we aspire to indicate to geologists the range of mechanisms in soft-matter physics that are involved in geological self organization.

It should be noted that some pattern-forming phenomena in rocks may involve biological contributions. This includes a broad grey zone of cases that may be biogenic or may instead reflect physical processes with microbial mediation when present. We discuss these in a separate review [5].

2. Soft matter

Soft matter is a relatively young field of condensed matter physics [6]. But what is soft matter? Common examples are complex fluids, gels, liquid crystals, polymers, foams, and colloids (Fig. 1). What these have in common is that the material properties are not based directly on the molecular-scale structure, but on mesoscopic structures that self organize in the system.

A number of definitions have been suggested to delimit the field: that soft matter is soft; that it's a complex liquid; that the building blocks are intermediate in size between atoms and the system size; that forces between the building blocks are of the magnitude of thermal fluctuations; and that soft matter shows a large response to weak forces. All of these definitions seek to characterize systems in which mesoscopic, intermediate-scale structures self organize and self assemble and can display a sensitive spatial dependence on the initial conditions that is similar to the sensitive temporal dependence that nonlinear chaotic systems experience. All of these definitions also work reasonably well to differentiate soft matter from traditional solid-state condensed matter like metals, semiconductors, superconductors, etc. That is to say, all give a cut-off at the small scale, but what about a cut-off at larger length-scales?

At large scales, things are less clear. Patterns form in condensed matter up to the large-scale structure of the universe. And the building blocks of those patterns—stars in a galaxy, galaxies in a cluster, etc—are effectively intermediate in scale. In this sense, it would suggest that there is no upper limit. Then, in the geological sciences, the whole of geomorphology, being deformable and sensitive to collective effects, might be viewed as soft matter. Indeed, this has been argued [7]. For example, during erosion, sediment transport and accumulation, relatively weak forces, acting over longish times, make dramatic changes to the landscape [8, 9]. It is clear, however, that this time-scale is different to that the pioneers of the field of soft matter had in mind. They were thinking of relatively short time-scales over which soft materials deform while geology deals with exceedingly long time-scales over which weak forces can make substantial changes. In this sense, the mesoscale in geology is especially broad and context dependent—and, more generally, reminds us that in physics any form of condensed matter can exhibit "soft" behaviour when viewed at sufficiently large length- and time-scales

We argue that it is reasonable to include these large-scale phenomena as *soft systems*, though not strictly as *soft materials*. Nevertheless, doing so opens up the field so much that it is in danger of becoming a catch-all. To remain grounded, we adopt an operational definition: soft matter is what is studied within soft-matter groups and discussed at soft-matter conferences (Fig. 1).

Admittedly, softness may seem a peculiar notion in the case of rocks, which are hard and not easily deformed by thermal fluctuations. Yet they were soft when they were formed, and they became hard after. In other words, many geological patterns originate through deformation, diffusion or flow in a liquid or gel medium that later solidifies.

In the following, we consider some common, and overlapping, classes of soft matter systems and examine how geological phenomena fit into these categories as forms of geological soft matter. As Evans et al. [10] put it, "predicting the structure and dynamics of such complex phases of matter from the constituent building blocks and their interactions defines soft-matter science".

3. Physical types of geological soft matter

Let us review some common types of soft matter and note instances in which they are found in geology. Note that these types overlap, so that many examples can fall into several of these categories.

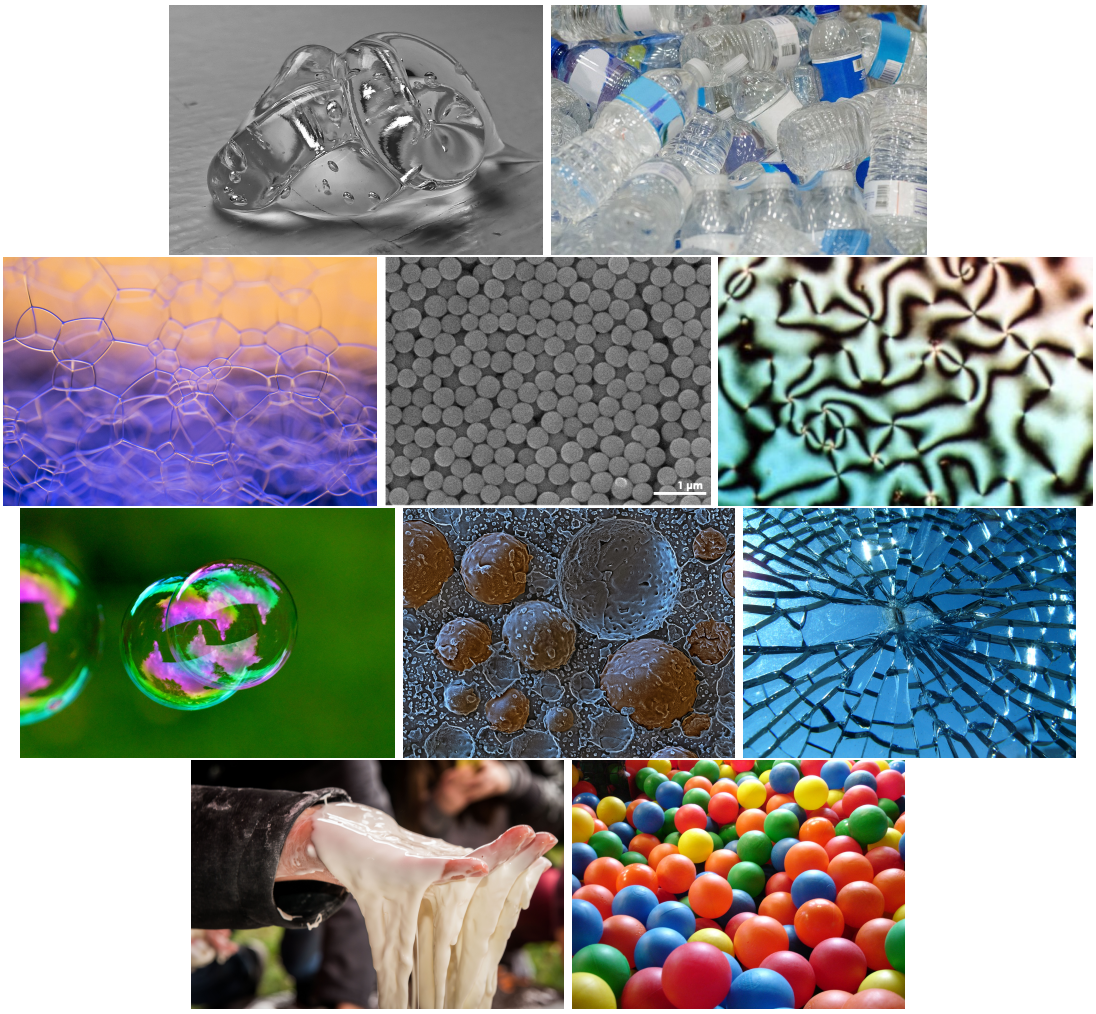


Figure 1: Examples of soft matter. From top left to bottom right: gel (image: Steve Johnson; CC-BY-2.0), polymer (public domain), foam (AdaptaLux; CC-BY-2.0), colloid (Yasrena, CC-BY-SA-4.0), liquid crystal (Minutemen, CC-BY-SA-2.5), membrane (public domain), emulsion (BASF, CC-BY-NC-ND-2.0), glass (Jef Poskanzer, CC-BY-2.0), viscoelestic material (image: Victor Wong, CC BY-SA 2.0) granular medium (image: Julie Kertesz, CC-BY-2.0).



Figure 2: Geological gels: these geological materials most probably passed through a gel stage in their formation. (left) Agate-filled geode, Brazil (image: James St. John; CC-BY-2.0). (centre) Flint, Poland (image: Ra'ike; CC BY-SA 3.0). (right) Gray chert, Knox County, Ohio, USA (image: James St. John; CC-BY-2.0).



Figure 3: Geological polymers: Crocidolite, blue asbestos, an amphibole mineral (image: Edgar Vonk; CC-BY-NC-SA-2.0).

3.1. Gels

A gel is a network of particles suspended in a fluid medium. Several geological materials passed through a gel stage during their formation, including agates (Sec. 5.1.1), flints and cherts (Sec. 5.1.5) [11, 12] (Fig. 2). Dendritic patterns originating from viscous fingering (Sec. 4.2.7) likewise reflect gel dynamics [13]. Basalt columns (Sec. 5.4.1) form when molten lava cools and cracks [14, 15] near the glass transition temperature [16, 17], making them both soft and fluidic during formation. Gold dendrites (Sec. 5.1.3) in rocks have also been shown to form within silica gel [18]. Silica gels may even play a role in earthquakes through weakening faults [19, 20].

3.2. Polymers

A polymer is a macromolecule composed of repeating structural subunits. In the Earth's crust, many alumino-silicate minerals, including clays, quartz, feldspar, and amphiboles, have polymeric atomic structures and thus can be regarded as geological polymers (Fig. 3). Agates (Sec. 5.1.1) and opals (Sec. 5.1.4) are examples. The term *geopolymer* is also used in materials research, though here it usually refers to synthetic substances, typically alumino-silicate in composition [21], with petroleum-based variants also described [22].

3.3. Foams

A foam consists of gas bubbles dispersed in a liquid or solid. Geological foams (Fig. 4) include bubbly volcanic rocks such as pumice and scoria [23, 24, 25]. Pumice is light and highly porous, formed when molten

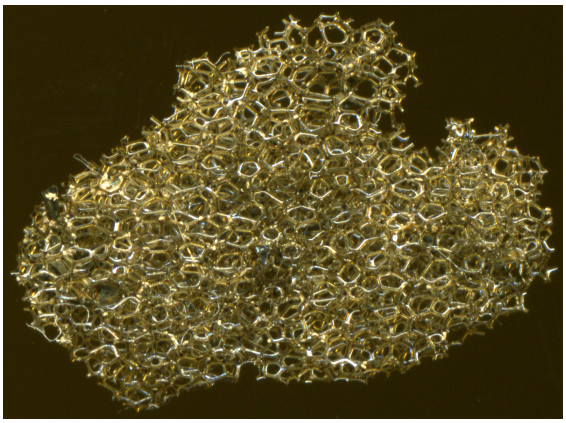


Figure 4: Geological foam: Reticulite from the Holocene of Hawaii, 1.8 centimetres across (image: James St. John; CC-BY-2.0).

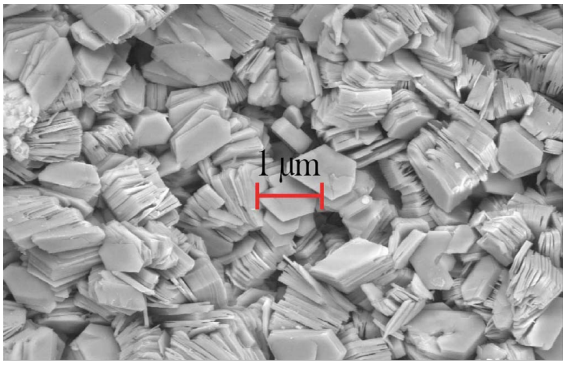


Figure 5: Geological colloids: phyllosilicates (image: Paedona; CC-BY-SA-4.0).

lava cools rapidly, trapping gas bubbles and producing a foam-like structure. Amygdaloidal basalts form when such bubbles later become infilled with secondary minerals precipitated from circulating fluids [26], as with agates (Sec. 5.1.1).

3.4. Colloids

A colloid is a two-phase system in which particles of one substance are dispersed within a continuous medium of another. Silica (amorphous SiO_2) and many clay minerals commonly occur as colloidal dispersions in water, with particle sizes on the order of ∼1—1000 nm [27] (Fig. 5).

Clays are aggregates of fine-grained minerals, typically less than 2 μm in size, so they often behave as colloids in water. Their small size and plate-like shapes give them very high specific surface area and, through structural and edge charges, substantial surface charge. These features govern their interactions with water and dissolved ions (e.g., hydration, double-layer forces, ion exchange), and can help keep particles suspended (alongside turbulence; Brownian motion dominates mainly for the finest fractions).

The colloidal nature of clays underlies several key properties. First, plasticity: with added water, clays deform readily and can be shaped, which is central to ceramics and pottery. Second, swelling: smectitic clays (e.g., montmorillonite) intercalate water and expand; behaviour important in drilling muds and landfill liners. Third, adsorption and ion exchange: charged surfaces and interlayers bind ions and organic molecules, enabling contaminant removal and catalytic uses.

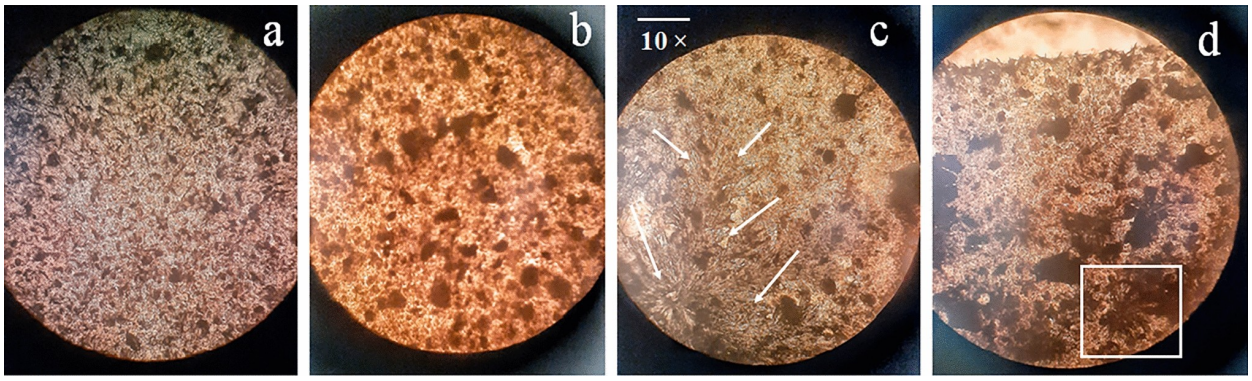


Figure 6: Geological liquid crystals. POM images observed for 0.055 g of clay in different Na_2SO_4 solvent concentrations. A: In 0.05 M Na_2SO_4 B: In 0.1 M Na_2SO_4 C: In 0.2 M Na_2SO_4, showing lyotropic aggregates with nematic phase; D: In 0.2 M Na_2SO_4, showing lyotropic nematic micelle formation in the lower right corner (image: Neelamma et al. [28]).

Clay minerals such as montmorillonite or kaolinite are important colloidal materials in soil and sedimentary rocks. They have a layered structure and can form colloidal suspensions due to their small particle size and surface charge. Colloidal silica, also known as silica gel, can be found in various geological settings, including hydrothermal systems, sedimentary environments, and volcanic ash deposits. Opals (Sec. 5.1.4) are colloidal crystals of silica nanospheres [29]. Colloidal iron and manganese oxides often occur in soils, sediments, and weathering profiles. They contribute to the colouration of rocks such as agates (Sec. 5.1.1) and play a role in the transport and sequestration of trace elements. Colloidal gold nanoparticles are thought to play a significant role in ore formation (Sec. 5.1.3) [30].

3.5. Liquid crystals

A liquid crystal is a phase of matter that exhibits fluidity together with long-range orientational, and sometimes positional, order. Suspensions of anisotropic mineral particles can form lyotropic liquid-crystal phases; this was noted a century ago [31] and is now an active area in chemistry and materials science [32]. Clays provide a key geological example (Fig. 6). When dispersed in water above certain concentrations, plate-like clay particles align due to their anisotropic shape and interparticle interactions, producing ordered phases. In nematic phases, particles share a common director without positional order; at higher concentrations they can form smectic phases, with parallel layers exhibiting both orientational and one-dimensional positional order. Such liquid-crystal textures have been observed in laboratory studies of aqueous clay gels [33, 34].

The liquid-crystalline behaviour of clays is significant in both natural and industrial contexts. In sedimentary basins, the alignment of clay particles can affect the porosity and permeability of the rock, influencing fluid flow and the extraction of resources. In industrial processes, understanding the liquid-crystal phases of clays can help in designing materials with specific mechanical or optical properties.

It has been proposed that zebra rock patterns (Sec. 5.1.6) may have originated as liquid crystals [35].

3.6. Membranes

A membrane is a two-dimensional interface that acts as a selective barrier, allowing some molecules, ions, etc to pass through while inhibiting others. Geological mineral membranes occur in clays [37, 38, 39], shales, siltstones, and zeolites, and in hydrothermal vents and vent fields (Sec. 5.4.2) [40, 41] (Fig. 7). These mineral membranes are often semipermeable, allowing only the solvent and not the solute species to pass, generating osmotic pressures in geological settings where fluids and semipermeable media interact. Such osmotic effects (Sec. 4.3) can influence fluid flow, chemical transport, and hence the formation of minerals and ore deposits [41]. Mechanisms involving osmotic membranes have been proposed for the formation of agates (Sec. 5.1.1) and menilites (Sec. 5.3.7).

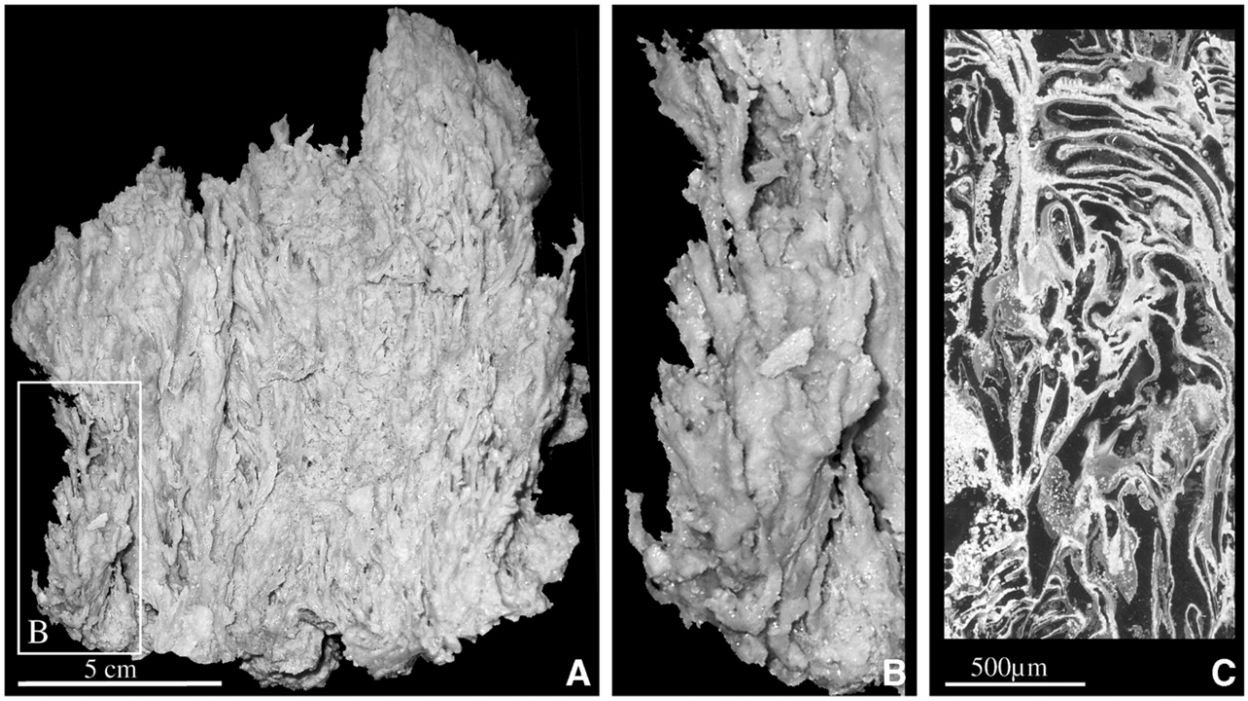


Figure 7: Geological membranes. A–C progressively zoom in from the centimetre to the micrometre scale on mineral membranes at Lost City hydrothermal field. From Kelley et al. [36].

3.7. Emulsions

An emulsion is a colloid of liquid droplets dispersed in an immiscible liquid. Like foams, emulsions occur in magmas, and may be preserved in events such as meteorite impacts. It has been proposed that the Sudbury Igneous Complex in Canada was formed through differentiation of a superheated impact melt sheet into a viscous emulsion [42]. Magma mingling has been proposed when two magmas of different compositions come into contact but do not fully mix into a single homogenous melt, leading to emulsion-like textures in igneous rocks; an example that has been proposed is amphibole-biotite veins [43].

In sedimentary settings, water–oil–clay emulsions are common (e.g., in heavy-oil reservoirs and oil sands), and early accounts describe organic–aqueous emulsions associated with oil shales [44]. Upon burial and diagenesis, however, the organic phase polymerizes into kerogen dispersed within a fine-grained mineral matrix—yielding oil shale—so the end product is not a preserved emulsion (Fig. 8).

3.8. Glasses

A glass is an amorphous (non-crystalline) solid. Natural glasses predate human manufacture [45], and geological glasses occur in igneous, metamorphic, and sedimentary contexts [46]. Obsidian is a volcanic glass that forms when silica-rich (felsic) lava cools rapidly, suppressing crystallization; it is typically dark, vitreous, and may contain vesicles or mineral inclusions, with occasional patterning [47] (Fig. 9). Tektites are impact glasses formed when meteorite strikes melt target rocks and soils; the ejecta cools in flight to glassy bodies (e.g., splashform, teardrop, or aerodynamically sculpted shapes). Fulgurites (Sec. 5.4.4) form when lightning melts sandy soil or sandy near-surface sediments, producing hollow glassy tubes and branching structures [48]. Agates (Sec. 5.1.1) and basalt columns (Sec. 5.4.1) may involve geological glasses in their formation.



Figure 8: Geological emulsion: oil shale from the Mahogany Zone of the Green River Formation, Colorado, USA (images: Georgialh; CC-BY-SA-3.0).

3.9. Viscoelastic and viscoplastic materials

The nonlinear rheology of geological materials has been studied for centuries [49] and underpins theories of tectonics and orogenesis [50]. Rocks commonly exhibit both viscoelastic and viscoplastic behaviour (Fig. 10). Viscoelasticity combines a viscous response (flow under sustained stress) with an elastic response (instantaneous, recoverable strain). This behaviour is time-dependent, meaning that the material response varies depending on the rate and duration of applied stress. Quicksands are a well-known example of complex viscoeleastic behaviour associated with shear thickening [51, 52, 53]. In rocks, viscoelastic behaviour is observed when the applied stress lies within a certain range and the loading period is relatively short. Under these conditions, deformation is partly elastic and partly viscous: the elastic component allows partial recovery of the original shape after unloading, whereas the viscous component leads to permanent deformation (creep).

Viscoplasticity refers to deformation that involves both viscous flow (fluid-like, lacking a fixed shape) and plasticity (inelastic, non-recoverable strain) once a yield stress is exceeded. Unlike viscoelasticity, viscoplasticity is governed primarily by the magnitude of the applied stress relative to the yield threshold (often with additional rate and temperature dependence), rather than by the loading duration itself. In rocks, viscoplastic behaviour is observed when the stress level exceeds a material-specific threshold: at high stresses, rocks deform permanently without elastic recovery. Such plastic deformation reflects the breaking, slip, and rearrangement of grains or crystal lattices, resulting in irreversible strain. Viscoplastic behaviour is prominent in geological processes such as folding, faulting, and the flow of rock masses under high-pressure conditions. Flowing lava frequently exhibits this type of behaviour and can be modelled as a yield-stress (viscoplastic) fluid [54].

Viscoelastic constitutive models have been applied to problems such as sinkhole formation [55] and the propagation and emplacement of dikes and diapirs within viscoelastic host rock [56]. Viscoplastic soils, such as clays, display striking pattern formation, for example shrinkage-crack networks (Sec. 5.2.6) that emerge as inelastic strains localize during drying or unloading [57]. More broadly, both viscoelastic

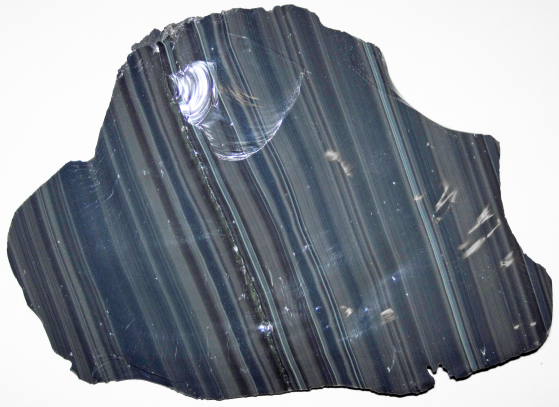


Figure 9: Geological glass: gray obsidian (image: James St. John; CC-BY-2.0).



Figure 10: Geological viscoelasticity and viscoplasticity. Left: Aphebian-aged marble showing plastic deformation (image: Mike Beauregard; CC-BY-2.0). Right: Soft sediment deformation in exposed Dead Sea sediment, Israel, gives rise to a Kelvin–Helmholtz shear instability (Sec. 4.2.3) (image: Mark A. Wilson; CC-BY-SA-3.0).

and viscoplastic responses are recognized as important for the development of compositional banding and foliation in rocks, where time-dependent relaxation, yield, and irreversible flow interact to reorganize fabric and mineral distributions [58]. Gneiss is one example (Sec. 5.4.5).

3.10. Granular media

A granular medium is composed of solid grains interacting primarily through contact forces and friction, so that assemblies can behave like solids or like fluids, depending on loading and confinement [59]. Many granular systems are treated within soft-matter physics [60]; geological examples (sand, soils, tephra) display solid-fluid duality and phenomena with no direct molecular analogue, such as jamming, shear banding, and avalanches [61].

Granular materials pervade Earth's surface environments (Fig. 11). All clastic sediments are granular: they form sedimentary rocks (sandstone, conglomerate, breccia) by accumulation and lithification; build river beds, bars, and deltas through erosion–deposition cycles; shape aeolian landforms (dunes, sand sheets, desert pavements); create glacial deposits (moraines, eskers, kames, drumlins); constitute volcanic fall and flow products (ash, lapilli, pyroclasts); and dominate coastal features (beaches, barrier islands, sandbars, shoreface deposits). In the marine realm they blanket continental shelves and abyssal plains and are funnelled through canyons as turbidites.



Figure 11: Geological granular media. Left: sand dunes near Dakhla Oasis, Western Desert, Egypt (image: Vyacheslav Argenberg, CC-BY-2.0); Right: travertine-cemented conglomerate (image: James St. John; CC-BY-2.0).

Many of the examples of geological patterns we describe involve granular media at some stage in their formation, including concretions and nodules (Sec. 5.2.8), efflorescence patterns (Sec. 5.2.4), fulgurites (Sec. 5.4.4), opals (Sec. 5.1.4), porphyroblasts (Sec. 5.3.2), sedimentary crack patterns (Sec. 5.2.6), and stylolites (Sec. 5.3.1).

4. Physical mechanisms underlying mesoscale geological self-organization

We hope that the geological examples presented above have convinced the reader that soft matter provides a helpful physical classification applicable to a wide variety of geological systems. What, then, are the common underlying physical mechanisms responsible for the emergence of patterns in these systems? In what follows we "round up the usual suspects" to indicate the breadth of mechanisms involved in geological self-organization; for fuller treatments, we refer the reader to the physics literature.

4.1. Reaction–diffusion systems

Reaction–diffusion systems describe processes where substances spread out in space (diffuse) and interact with each other through chemical reactions. These have the general mathematical form

$$\partial_t u = D\nabla^2 u + R(u), \tag{1}$$

where D is the diffusion matrix and R represents the reaction component. Often, we associate diffusion with the smoothing of concentration gradients over time, leading to a uniform homogenized soup, as substances move from regions of high concentration to low concentration. However, introducing chemical reactions into these systems may disrupt uniformity and drive the spontaneous formation of complex spatial structures. Such systems occur in various physical, chemical, and biological settings.

4.1.1. Turing patterns

At the core of pattern formation is the concept of Turing instability. In 1952, Alan Turing [62] demonstrated that diffusion, when combined with nonlinear chemical reactions involving two interacting species, can spontaneously break the symmetry of an initially uniform mixture of chemical compounds. In the simplest case of a Turing model, one species acts as an activator, promoting its own production, while the other functions as an inhibitor, suppressing the activator's growth. Both diffuse, but the inhibitor has a larger diffusion coefficient than the activator: $D_A > D_I$. Through the coupling of diffusion and reactions, small perturbations from uniformity can grow, leading to the spontaneous appearance of spatial patterns.



Figure 12: Reaction–diffusion systems. (left and centre) Turing patterns. (images: Courtesy of Jacques Boissonade and Patrick De Kepper, University of Bordeaux). (right) Belousov-Zhabotinsky target and spiral patterns. (image: Stephen Morris).

Depending on the parameters, a Turing system can generate spots, stripes, or even labyrinthine patterns, reflecting the self-organizing capacity of reaction-diffusion dynamics (Fig. 12A,B).

The mechanism behind pattern formation in such systems was creatively illustrated by James Murray in his book *Mathematical Biology* [63] with an analogy of "sweating grasshoppers": Imagine a dry grassy field with grasshoppers scattered throughout. If a fire starts in one part of the field, it will naturally spread, burning everything in its path. However, grasshoppers, sensing the approaching flames, react by moving ahead of the fire and sweating profusely, which dampens the grass and prevents it from burning. In this analogy, the fire is the "activator", spreading destruction, while the grasshoppers are the "inhibitors", stopping the fire from spreading by moistening the grass. The key to the pattern's emergence is that the grasshoppers react faster than the fire spreads, creating a non-uniform, repeating pattern of charred and unburnt areas, similar to the spotted patterns on animal coats. Two mechanisms are key to the creation of a pattern: self-activation (a short-range positive feedback loop), where small perturbations in the uniform state tend to grow over time, similar to fire spreading, and screening (long-range inhibition), where the formation of a structure at one point reduces the likelihood of similar structures appearing nearby. In the grasshopper example, this corresponds to grasshoppers surrounding the fire and stopping its spread.

4.1.2. Short-range activation and longer-range inhibition

What we have just described is akin to how many natural patterns emerge from generic mechanisms of self-organization: the interplay between local positive feedback and long-range suppression. Geological examples include patterns in sand (Fig. 11): "As a ridge gets bigger, it enhances its own growth by capturing more sand from the moving air. But in doing so it acts as a sink, removing sand from the wind and suppressing the formation of other ripples nearby. The balance between these two processes establishes a roughly constant mean distance between ripples" [64]. Honeycomb weathering (Fig. 61) [65] and travertine patterning [66] are further geological examples of patterns emerging from the combination of short-range activation and longer-range inhibition.

4.1.3. Excitable media

Another related type of reaction–diffusion system is termed an excitable medium [67]. In excitable systems a small perturbation leads only to a small transient effect; however a perturbation above a certain threshold excites the system, which then remains in its excited state for some time before returning to quiescence, and upon this return has a refractory period during which it cannot be excited a second time. A classic example is the Belousov–Zhabotinsky (BZ) reaction [68]. Geologically relevant instances of excitable media include the example of crystal growth [69]. Earthquake dynamics, as modelled by the Burridge–Knopoff model [70] describing a chain of blocks connected by springs and pulled across a surface, may be viewed as a type of excitable medium with elastic rather than the usual diffusive coupling [71]. Also in the temporal domain, it has been suggested that the oceanic carbon cycle may be excitable, and that mass

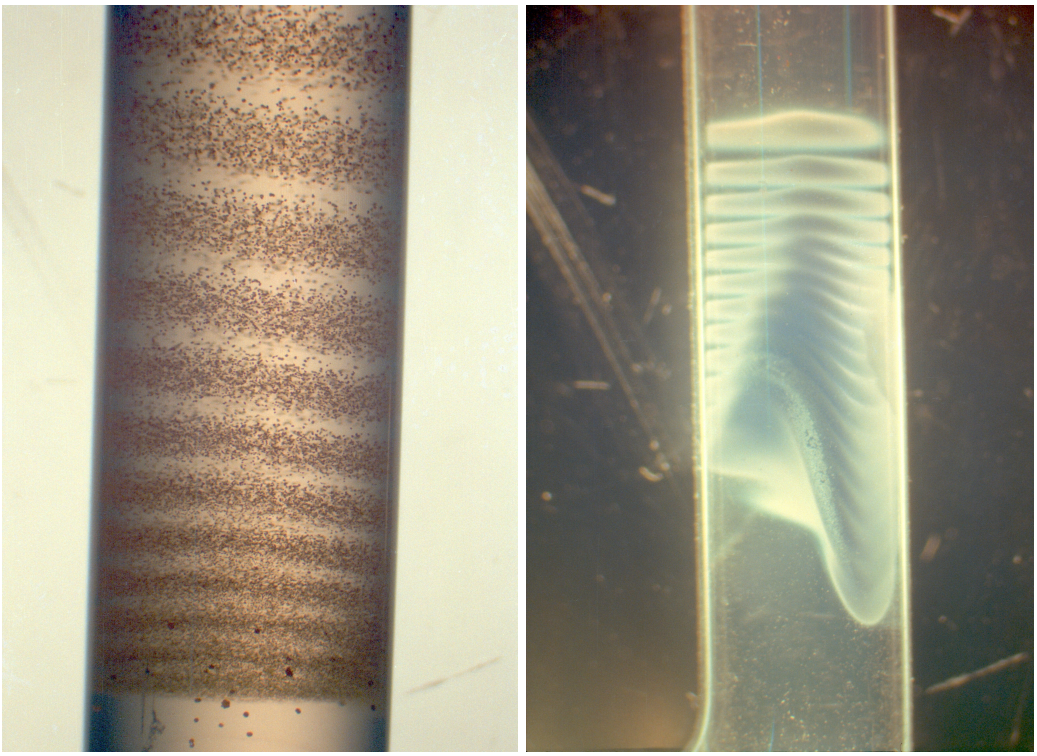


Figure 13: Liesegang bands in laboratory experiments (images: Julyan Cartwright).

extinction events may correspond to large perturbations that excite the system [72]. As for spatio-temporal geological patterns, an excitable model for the coupled evolution of ice-surface temperature and elevation produces spiral waves similar to those observed in the Martian north polar ice cap [73].

4.1.4. Geological reaction–diffusion systems

Reaction–diffusion systems remain an active area of research in both biological and geological pattern formation. While the complexity of biological systems often makes it difficult to identify the specific morphogens responsible for a given pattern, geological systems are usually simpler, involving just a handful of chemicals. Examples such as zebra rock (Fig. 45) or target patterns in sandstone rocks (Fig. 65) strongly suggest a reaction–diffusion origin, although other banded patterns, like striped flints (Fig. 44) or sphalerites (Fig. 68) elude such a simple description. However, there are two important factors to consider when thinking about geological systems. First, in order for a reaction–diffusion pattern to survive the millennia, it needs to be literally turned to stone, sculpted into the rock [3]. This means that not only bulk reactions need to be involved but also surface reactions, such as precipitation. The second key factor is the importance of fluid flow. For large enough system size L, the advective time-scale, $\tau_a = L/v$, is always shorter than the diffusive time-scale, $\tau_d = L^2/D$. Thus, it is invariably advection—usually through fractures, joints, and bedding planes—that brings reactants to rock strata, leading to its chemical transformation. Diffusion can be a controlling factor, particularly on smaller spatial scales, such as in the cracks observed in Fig. 65A. We discuss fluid-flow-mediated instabilities in Sec. 4.2.

4.1.5. Liesegang patterns

One particular reaction–diffusion system is Liesegang banding (Fig. 13). Liesegang band formation is a rhythmic precipitation phenomenon that occurs when a solute diffuses through a gel and reacts with another solute, resulting in distinct bands or rings. The spacing of these bands increases geometrically outward from

the point of diffusion [74, 75],

$$x_n \approx x_0(1+p)^n, \tag{2}$$

where x_n is the position of the nth band and p a spacing coefficient. Although the phenomenon was initially reported by Runge [76] and Ord [77], it became more widely known after the systematic experiments conducted by Liesegang [78]. In his experiments, Liesegang observed the diffusion of silver nitrate in a gelatin layer containing potassium dichromate, leading to visually striking rhythmic precipitates oriented parallel to the diffusion front. Rings are formed in a radial geometry, while bands are found in linear geometries. Often, these structures are referred to as periodic precipitation structures [79], which is somewhat misleading; as we have noted, the primary defining characteristic of Liesegang structures is that they are generally not simple periodic patterns but instead have aperiodic spacings that follow a geometric series. To complicate matters further, the term *Liesegang* is frequently found in geological publications to describe any banding observed in rocks, without regard to its provenance.

Despite the phenomenon being known for well over a century, the mechanism of Liesegang band formation is still a matter of discussion. Two main groups of theories have been proposed, termed pre- and post-nucleation models, differentiated by the timing of precipitate nucleation in the system [80, 81].

In the pre-nucleation models, following Ostwald [82] and Prager [83], bands are proposed to result from a feedback loop between nucleation and diffusion. Precipitation starts at a specific value of supersaturation, the nucleation threshold, and subsequently depletes the solute around it, preventing it from reaching the nucleation threshold in adjacent regions. This process is followed by renewed nucleation farther from the initial band, resulting in a rhythmic pattern that regularly obeys quantitative spacing laws.

In contrast, post-nucleation models consider the interaction between growth, diffusion, and surface tension effects. The pattern is generated through Lifshitz–Slyozov instability [84], in which homogeneous systems with uniformly distributed precipitate particles may become unstable due to Ostwald ripening (Sec. 4.6). Smaller particles tend to dissolve because their surface energy is higher due to their greater curvature. The dissolved material then diffuses through the surrounding matrix and redeposits onto larger particles, which have a lower surface energy. This process results in the growth of larger particles over time at the expense of smaller ones. In an initially non-uniform system, this can generate bands that evolve through coarsening after the nucleation phase is over [85]. In contrast to the pre-nucleation models, post-nucleation models can generate patterns even in the absence of an initial concentration gradient.

It is possible that both these mechanisms may be found in nature. Experiments and simulations show examples of various different morphologies beyond the classical bands and rings, including spirals, rods and spots [86, 87, 88] as well as bands of two crystalline phases [89].

One of our aspirations with this review is to discourage the indiscriminate use of the word *Liesegang* in geology for any spatial oscillation; as we show here, the Liesegang pattern formation mechanism is just one of a variety of physical mechanisms that can produce banding, both periodic and aperiodic.

4.1.6. Oscillatory zoning

Classical crystallization is itself a form of self-organization in condensed matter. Growth from a melt or a solution may also be regarded as a soft-matter process, as it gives rise to mesoscopic structures such as growth steps, target patterns, and spirals. The more complex growth modes that produce mesoscale compositional patterns, such as oscillatory zoning, are even more clearly manifestations of soft-matter behaviour.

Oscillatory zoning is another reaction–diffusion pattern-formation mechanism observed in geological systems. Depending on the formation conditions, three different zoning patterns have been described in crystals: normal, reverse and oscillatory zoning [93]. Normal and reverse zoning involve monotonic changes: in normal zoning, the crystal core is compositionally less evolved than the rim (e.g., reflecting cooling of a magma chamber), whereas in reverse zoning the trend is opposite (e.g., indicating heating). Oscillatory zoning, by contrast, consists of repetitive, concentric compositional bands.

For natural crystals showing oscillatory zoning, both extrinsic and intrinsic mechanisms have been proposed [94]. Extrinsic mechanisms reflect system-wide physical and chemical changes (e.g., fluid mixing, pressure or temperature shifts), whereas intrinsic mechanisms arise from crystal growth dynamics and local phenomena [94]. Although oscillatory zoning is common, identifying the dominant controls is difficult.

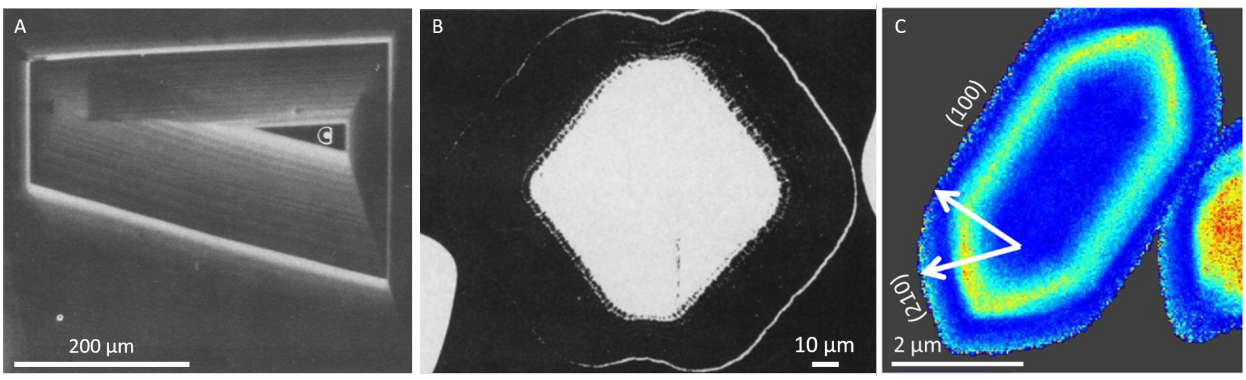


Figure 14: Oscillatory zoning. Examples of synthetic crystals showing oscillatory zoning. A: Calcite crystal with white areas enriched in Mn [90]. B: $(Ca,Cd)CO_3$ crystal, white areas are enriched in Cd [91]. C: $Ba(SO_4,HAsO_4)$ crystal, blueish areas are depleted in As, while yellowish-greenish areas are enriched [92].

Laboratory syntheses, where all parameters can be controlled, are particularly valuable for studying cases in which oscillatory zoning develops through intrinsic mechanisms, in consequence, offering clear insight into self-organization during crystal growth.

Among the internal mechanisms proposed to explain oscillatory zoning, two are particularly well established. One invokes a feedback between growth rate and the partition coefficient of the substituting ion [90]. For example, in manganese-rich calcite, incorporation of Mn slows the calcite growth rate; the slower growth increases the Mn partition coefficient, enhancing Mn incorporation into the lattice. This depletes Mn in solution, which in turn accelerates calcite growth and lowers the Mn partition coefficient. The cycle then repeats, producing oscillatory zoning (Fig. 14A).

Another mechanism relies on the difference in solubilities of the solid-solution end-members [91]. If this difference is large, the less soluble phase precipitates first until it becomes undersaturated owing to depletion of one ion; growth then switches to the other phase until depletion of its controlling ion allows the first phase to reappear. This behaviour has been documented for $(Cd,Ca)CO_3$, where otavite forms first; as [Cd] falls, calcite grows, and when [Ca] later drops, a new otavite layer nucleates (Fig. 14B). An analogous mechanism operates in anionic solid solutions, e.g., $Ba(SO_4,HAsO_4)$ (Fig. 14C).

4.2. Fluid-flow instabilities and convective processes

Because many geological processes operate on long time-scales and at low velocities, they can often be modelled as viscous fluid flows (e.g., [95, 96]). A common pathway to geological self-organization in such cases is a physical instability arising from fluid interactions. Such instabilities may be categorized by the nature of the driving mechanism.

4.2.1. Rayleigh–Bénard convection

Rayleigh–Bénard instability, or buoyancy- (density)-driven convection, occurs when a fluid layer is heated from below and cooled from above, leading to the formation of convection cells as the fluid moves (convects) under this forcing [97, 98]. This occurs above a critical Rayleigh number, the ratio of the time-scale for diffusive heat transport to the time-scale for convective heat transport in the fluid,

$$Ra = \frac{g\beta\Delta T L^3}{\nu\alpha}. \tag{3}$$

Here g is the acceleration due to gravity, β is thermal expansivity, ΔT is temperature difference, L is a characteristic length-scale, ν is the kinematic viscosity, and α is the thermal diffusivity.

On a planetary scale, Rayleigh–Bénard instability is a key process in the Earth's thermal evolution and in the dynamics of fluid movement within geological settings [99]. It provides a framework for understanding

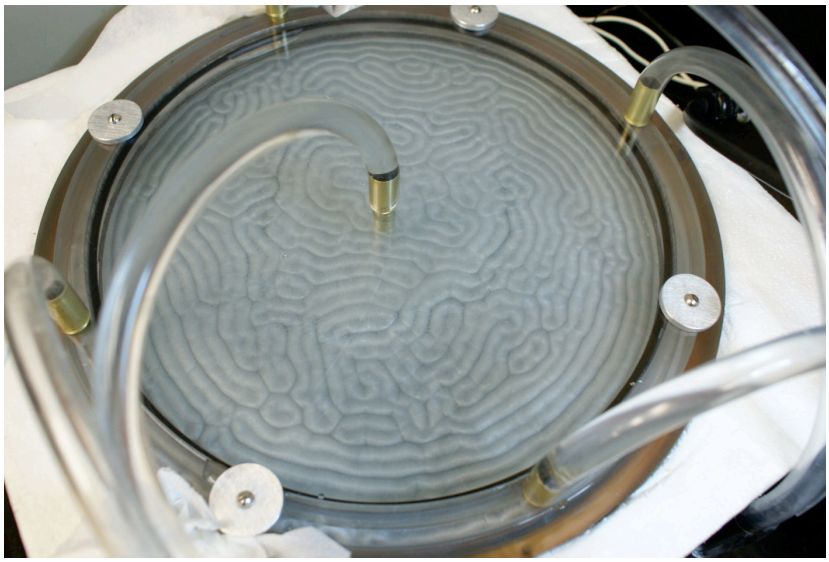


Figure 15: Rayleigh–Bénard convection seen in an experimental set up with a rigid boundary condition at the transparent top wall ($Ra = 2490$) (image: Sarah Chang TREND REU Media Project).

how heat is transported in the Earth's interior, influencing everything from plate tectonics [100] to the cooling of magmatic bodies and the circulation of fluids in hydrothermal systems.

The RB instability plays a central role in the formation of layered geological structures, particularly within igneous bodies such as plutons and layered intrusions. These sheet-like bodies of igneous rock display distinct mineralogical layering produced by convection-driven differentiation during magma cooling. In a magma chamber, buoyant, hot magma at the base rises while cooler, denser magma near the top sinks, establishing convective currents. As the melt cools, minerals crystallize at characteristic temperatures: early-forming, high-temperature minerals like olivine and pyroxene settle toward the base, while lower-temperature phases such as plagioclase accumulate above. The resulting convective motion produces stratified structures that reflect successive stages of crystallization. The resulting layers may be sharply bounded or more diffuse, depending on the vigour of convection and the cooling rate, and they often exhibit variations in mineral proportion, texture, and chemical composition

In some intrusions, cyclic layering occurs, with sequences of mineral bands repeated at different levels due to periodic fluctuations in temperature or episodic magma recharge. The Bushveld Complex, containing extensive layers of chromite, magnetite, and other minerals, is a classic example in which convection driven by RB instability contributed to magmatic differentiation [101, 102]. Similarly, the Skaergaard Intrusion in Greenland exhibits well-defined layers of gabbro formed through this process [103].

RB instability also operates at smaller scales and lower temperatures. During early diagenesis, the process by which sediments are lithified into rock, RB instability can drive pore-fluid motion in fine-grained sediments heated from below, e.g. from underlying geothermal gradients. Upward migration of warm, less dense fluids and sinking of cooler, denser ones may lead to the formation of soft-sediment deformation features, such as load casts or convolute bedding. In permafrost regions, RB instability in the seasonally thawed active layer can promote soil mixing, leading to patterned ground forms such as stone circles and stripes [104, 105] (Fig. 16). More generally, fluid-venting structures such as hydrothermal vents (Sec. 5.4.2), mud volcanoes and cold seeps (Sec. 5.4.3), are also ultimately sustained by buoyancy-driven convection of this type.

4.2.2. Rayleigh–Taylor instability

The Rayleigh–Taylor (RT) instability occurs when a denser fluid is accelerated into a lighter one, producing characteristic interpenetrating structures as the fluids mix [107]; Fig. 17. In the absence of surface tension

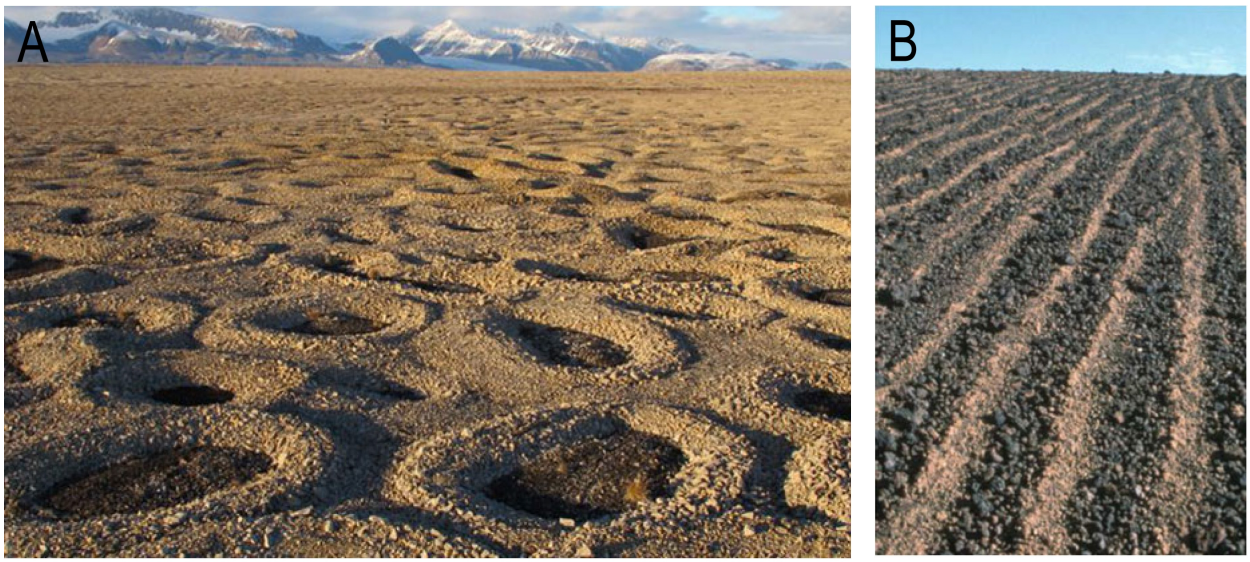


Figure 16: Patterned ground: A) Circular domains of fine-grained soil approximately 2 m in diameter ringed by gravel approximately 0.25 m high, Broggerhalvoya, NW Spitsbergen. (B) Narrow sorted stripes approximately 0.15 m wide, near summit of Mauna Kea, HI, USA.

at the interface, all wave-lengths are unstable; surface tension suppresses short wave-lengths, introducing a cut-off to the instability.

In geology, RT-like overturning arises whenever density contrasts act under gravity. In seismites (Sec. 5.4.6), seismic shaking transiently accelerates denser slurries into lighter layers, triggering RT deformation. The RT instability is also relevant to mantle dynamics: buoyant, hot mantle material rises through cooler, denser mantle rock can form mushroom-shaped plumes, a hallmark of RT behaviour [108]. In evaporite basins, less dense salt buried beneath denser sedimentary rocks can pierce the overburden to form salt diapirs (domes) [109], that can trap oil and gas, making them important in petroleum geology [110, 111].

4.2.3. Kelvin–Helmholtz instability

Kelvin–Helmholtz (KH) instability, Fig. 18, a lateral shear instability often seen in the atmosphere and ocean [112], is not uncommon in large-scale geological settings, where earthquake-induced, layer-parallel displacement of soft sediments creates strong interfacial shear (e.g., [113]). In seismites (Fig. 81) KH deformation commonly occurs hand in hand with Rayleigh–Taylor overturning: RT generates load casts, flames, and pillows under normal acceleration, while synchronous shear along bedding planes superimposes KH-type wavy or rolled interfaces.

On smaller scales, a related shear-driven mechanism has been proposed as driver for mesoscale rock folding (Fig. 10B). Wollkind and Alexander [95] incorporated surface tension into earlier laboratory folding models, deriving instability onset conditions consistent with capillary-modified KH instability and successfully accounting for the characteristic undulatory patterns in gypsum-limestone couplets of the Castile Formation in New Mexico (Fig. 19). KH dynamics also appear in volcanic contexts. Lava coils—helical surface textures formed where relatively low-viscosity lava solidifies within slow, shear-dominated flow—are well documented on Earth and Mars [114] (Fig. 19). At the interface of geological and biological soft matter, KH instability has been invoked to explain the formation of the (pseudo)fossil Kinneyia [115, 116]: passive deformation of a viscoelastic microbial mat under shallow, flowing water produces ripple-like corrugations that can later be preserved diagenetically [117].



Figure 17: Rayleigh–Taylor instability, seen here between two different viscous soap solutions of slightly different densities, the denser overlying the lighter (image: Thermoskanne).

4.2.4. Bénard–Marangoni convection

Bénard–Marangoni convection, or Marangoni flow, occurs when surface tension gradients drive fluid motion [118, 119]; Fig. 20. Temperature or concentration gradients along a free surface create variations in surface tension, inducing flow from regions of lower surface tension towards regions of higher surface tension.

Bénard–Marangoni instability also appears in geological contexts. It has been proposed to influence segregation of basaltic lithologies in the lower mantle [120]. At Earth's surface, clay rafts floating on shallow lake water can experience Marangoni-driven circulation near shorelines, producing complex, Suminagashi-like depositional patterns upon precipitation [121].

4.2.5. Double-diffusive convection and mushy layers

Double-diffusive convection is driven by buoyancy forces arising from two components with different diffusivities [124, 125, 126]. Unlike convection where density is determined only by temperature, double-diffusive convection occurs when, for example in the ocean, thermal gradients and compositional gradients (like salt or dissolved minerals) meet each other. Because heat diffuses much faster than molecular components, this process can trigger instability even in otherwise stably stratified fluids, often resulting in layered, staircase structures. Double-diffusive convection thus arises from a difference in diffusion rates, and there are two possibilities. The finger regime (salt fingers; Fig. 21) occurs when hotter, salty water overlies colder, fresh water. This provides an unstable salinity gradient alongside a stable thermal gradient; in other words the instability is driven by the slower diffuser. The other, diffusive regime, occurs when cold, fresh water overlies hot, salty water. This situation couples a stable salinity gradient to an unstable thermal gradient; the instability here is drive by the faster diffuser. The instability looks very different in the two instances.

Double-diffusive convection appears in geological settings where multiple components affect fluid density, such as in magma chambers [127], lavas [128], the planetary core–mantle boundary [129], and hydrothermal systems [130]. However, while double diffusive processes may certainly play a role in the dynamics of molten

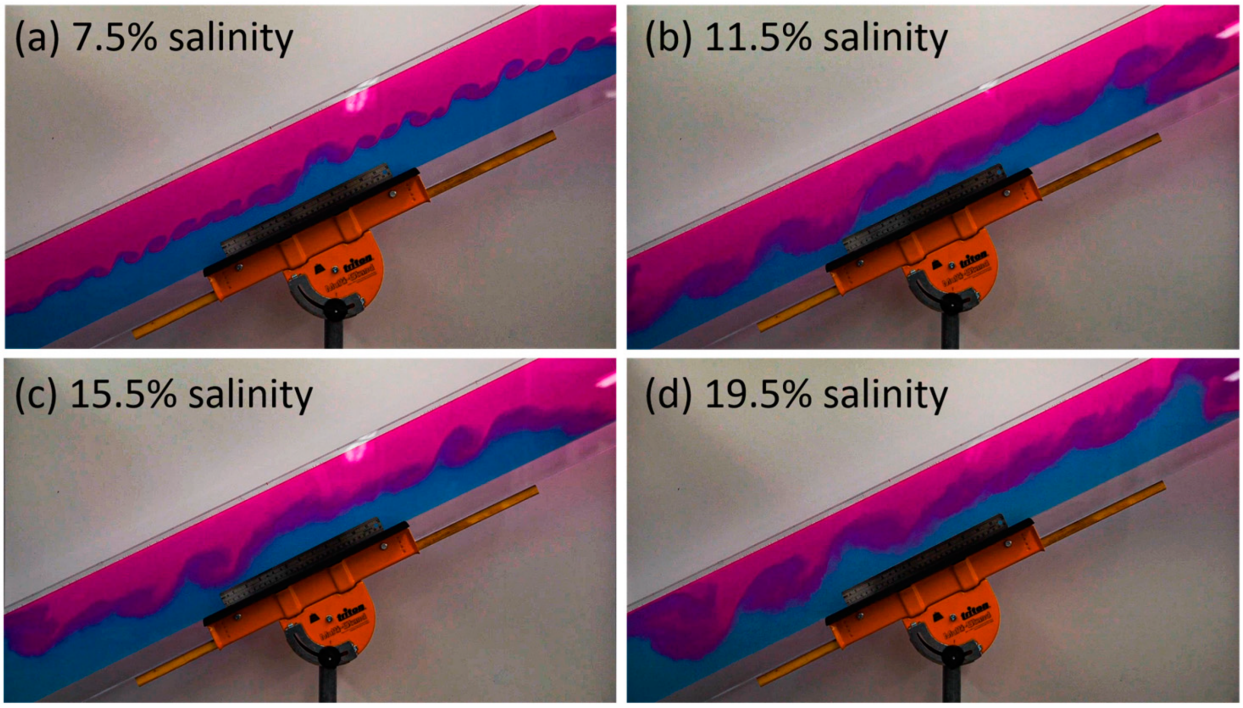


Figure 18: Kelvin–Helmholtz instabilities in a laboratory experiment in which the interface between the two fluids is sheared by tilting the container. (Image: CC-BY, Gibbons et a. [106]).

and otherwise fluidized rock, there is less evidence of rock *patterning* linked to double diffusive convection.

There have been suggestions that large-scale layering in igneous rocks [131] (Fig. 22 [123]) might arise, like thermohaline staircases in the ocean, from double diffusive convection [132]. This is now viewed as being an oversimplification [133], and mechanisms involving coupled solidification and desorption processes producing a geometric pattern of layer spacing have been derived [134]. When considering patterning in rocks one should keep in mind the differences between bulk fluids and porous media [135]. However, it is clear that spatio-temporal concentration variations in the liquid phase should affect a forming solid phase, and this links double diffusive convection to oscillatory zoning, Sec. 4.1.6. Some soil patterns of the finger type may have an origin in double diffusive convection in porous media [136], but it should be noted that there are other reactive-infiltration instabilities, as we discuss below in Sec. 4.2.7 and Sec. 5.2.2.

During the solidification of multicomponent solutions, such as in magma chambers, lava lakes, or sea ice, a solidifying matrix of crystals—a *mushy layer*—forms alongside interstitial liquid. Convection can cause local melting or increased solidification, depending on whether the rising fluid is hotter or colder than the surrounding, affecting the permeability and structure of the layer. Convection in mushy layers often leads to the formation of tubular *chimneys*, vertical channels within the mushy layer, in which rise fluid plumes that enhance transport and modify solidification rates. In magma chambers, convection in mushy zones can drive the formation of *freckles*, chains of mafic minerals and other localized chemical heterogeneities, impacting the differentiation of igneous rocks. And during sea ice formation, when seawater freezes, it forms a mushy layer of ice crystals and saline brine. The brine, being denser, can convect, affecting the rate of ice growth and the transport of salt. As mushy layers are characterized by the interaction between compositional (solutal) buoyancy—due to the rejection of lighter or denser elements during freezing—and thermal buoyancy, creating a density difference, one can consider the possibility of double diffusive convection because heat and solute diffuse at different rates. However, the question is complicated by the consideration of whether temperature and concentration fields are linked through local thermodynamic equilibrium. It turns out that double diffusive effects may appear in a ternary case [137]. Although geological systems

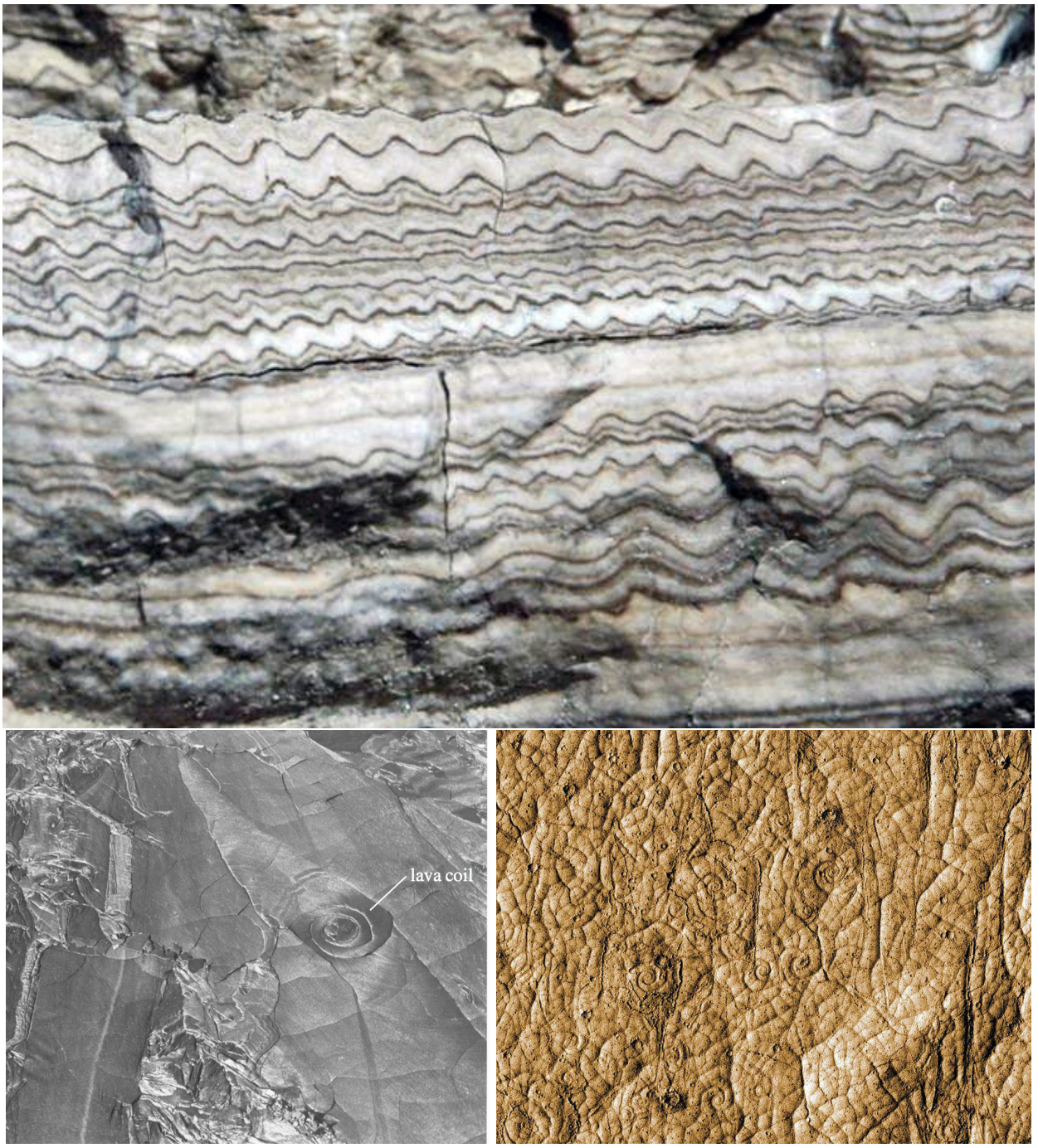


Figure 19: Geological Kelvin–Helmholtz instabilities. (Above) Castile Formation gypsum–calcite laminites (white gypsum; dark calcite, Upper Permian), from New Mexico–Texas border, USA. Finely laminated gypsum–calcite couplets with pronounced crinkling and small-scale folding, interpreted as a Kelvin—Helmholtz shear instability in soft sediments (image: James St. John, CC-BY 2.0). (Below left) Lava coil approximately 10 m in diameter in pahoehoe lava north east of Pu'u Koa'e, Hawaii. (image: USGS photo by Elliot Endo, public domain). (Below right) lava coils in Cerberus Palus, a volcanic region on Mars. Image taken from HiRISE camera on the Mars Reconnaissance Orbiter; field of view approximately 500 m (image: NASA, public domain).



Figure 20: Bénard-Marangoni convection seen in the same experimental set-up as seen in Fig. 15, but with a free liquid surface (image: Sarah Chang TREND REU Media Project).

might well be good places to look for three coupled elements, this idea has as yet been little investigated in a geological context.

4.2.6. Capillary flow and coffee-ring instabilities

Salt dissolution in water enables long-distance transport of ions, with subsequent crystal precipitation occurring upon evaporation or cooling. This process manifests itself in various scenarios, such as the capillary rise of groundwater to soil or rock surfaces and evaporation near salt lakes (Sec. 5.2.3). Crystal precipitation generally occurs in regions where evaporation is strongest and ions are advected by the liquid flow. The increase in ion concentration in these areas raises the probability of crystal nucleation.

This is similar to the coffee ring effect, the pattern left behind when a particle-laden liquid droplet dries, characterized by a ring-like deposit along its perimeter [119, 138]. It arises because evaporation is faster at the droplet's edges, and liquid from the centre flows outward to replenish the edge. This outward flow carries suspended particles to the droplet's perimeter and, as evaporation finishes, particles accumulate at the edge, forming a ring.

In the case of salt solutions, the accumulation of ions induces multiple nucleation at the evaporation front. This generates salt creeping, a self-amplifying process that forms three-dimensional porous crystalline networks at considerable distances from the original solution source [139]. While salt creeping occurs on flat surfaces, a similar process known as salt efflorescence develops on porous surfaces such as soils or stones, driven primarily by capillary flow of the salt solution towards the evaporative region at the top of the porous medium. Studies show that the ion concentration near a receding meniscus in pores is controlled by evaporation and can be quantified by the Péclet number. This dimensionless number, the ratio of advective to diffusive transport of ions, is central in continuum transport [140]. When $Pe > 1$, advection dominates diffusion and promotes crystal precipitation. Early large crystals precipitating at the evaporation front create macropores that enable subsequent nucleation of smaller crystals, which in turn generate progressively smaller pores. In addition, crystal-mediated spreading of the salt solution increases the invaded area by capillarity. Marangoni flows are negligible in salt creeping dynamics because the concentration gradient between the bulk salt solution and the liquid film in contact with precipitated crystals at the evaporative points is small, preventing high supersaturation and leading to immediate secondary nucleation of crystals.

Figure 23 illustrates the dynamic nature of salt creeping and efflorescence formation and its ability to propagate well beyond the initial boundaries. Scanning electron microscopy (SEM) images of sodium chloride

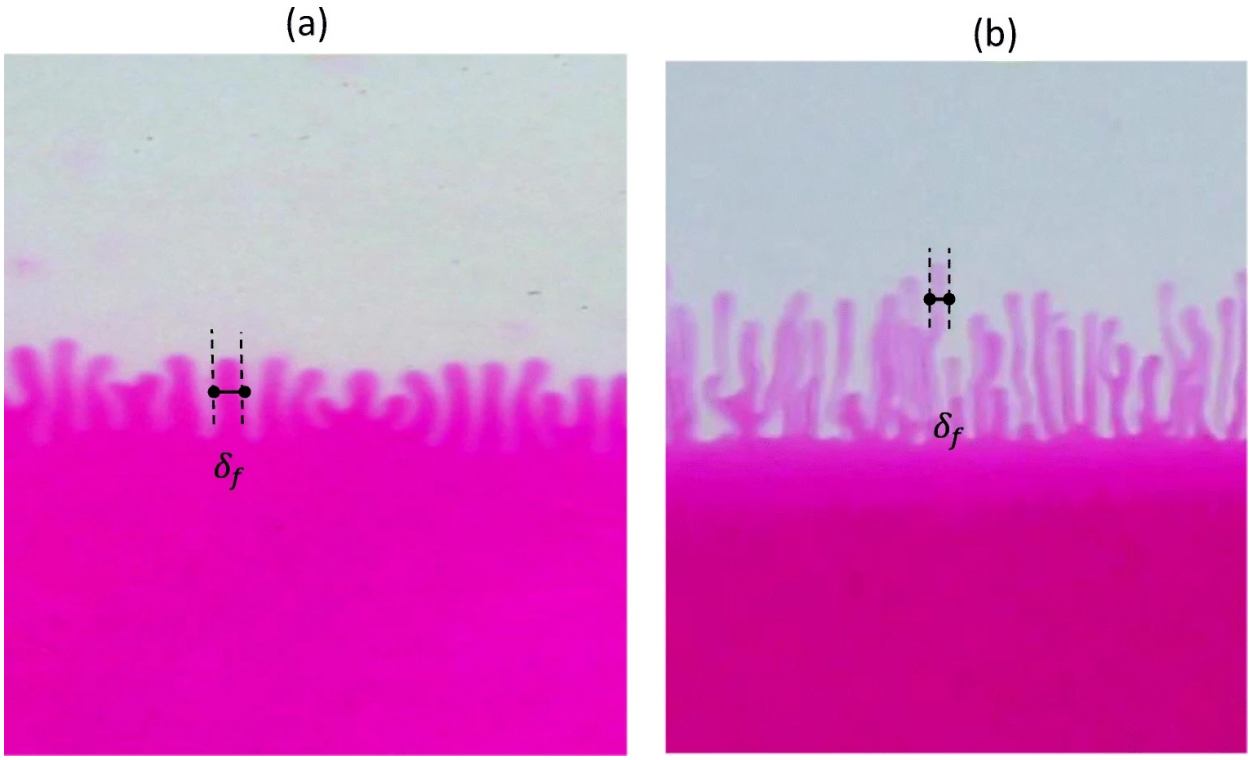


Figure 21: Double-diffusive convection; salt fingers in an experimental study illustrating how finger structures and time-scales vary with Rayleigh number. A: low Rayleigh number $Ra = 4.3 \times 10^3$, evolution time 1 h 4 min, wavelength $\delta_f = 2$ mm; B: High Rayleigh number $Ra = 4.3 \times 10^5$, evolution time 2 min 33 s, wavelength $\delta_f = 1.25$ mm [122].

(NaCl) creeping efflorescence reveal porous polycrystalline structures and show that this phenomenon spans many orders of magnitude in length-scale, so that it appears fractal [140]. The crystalline porous structure, with a pore-size distribution set by the range of crystal sizes, allows saline water to be drawn in by capillary pumping (wicking). Consequently, crystallization continues further upward at the top of the efflorescence. The rate of evaporation plays a critical role in the development of salt creeping, efflorescence, and salt pillar formation [141]. For creeping to occur, the evaporation rate should be high enough to induce multiple nucleation processes at the evaporation front ($Pe > 1$). This can be achieved with air flow (wind), low relative humidity, or elevated temperature during evaporation. By contrast, a slow evaporation rate induces the precipitation of fewer nuclei which grow larger and evolve towards their equilibrium shape; this can suppress creeping. Very low relative humidity may also suppress the salt creeping process, as precipitation kinetics can change at very high evaporation rates, promoting crust formation [141]. Another important parameter is the properties of the porous medium or surface on which salt precipitation occurs, which can strongly affect the final deposition morphology [139].

These mechanisms can result in spectacular structures such as desert roses and other efflorescence structures in natural environments in arid regions (Sec. 5.2.4).

4.2.7. Saffman–Taylor instability, viscous fingering, and reactive-infiltration instability

Whenever a more mobile fluid is rapidly injected into a less mobile one, the interface between them becomes unstable. This occurs because the fluid tends to flow along the path of least resistance. Therefore, if there is a protrusion on the advancing interface, it will focus the flow, leading to a faster growth of the protrusion and transforming it into a finger of the more mobile phase propagating within the less mobile one.

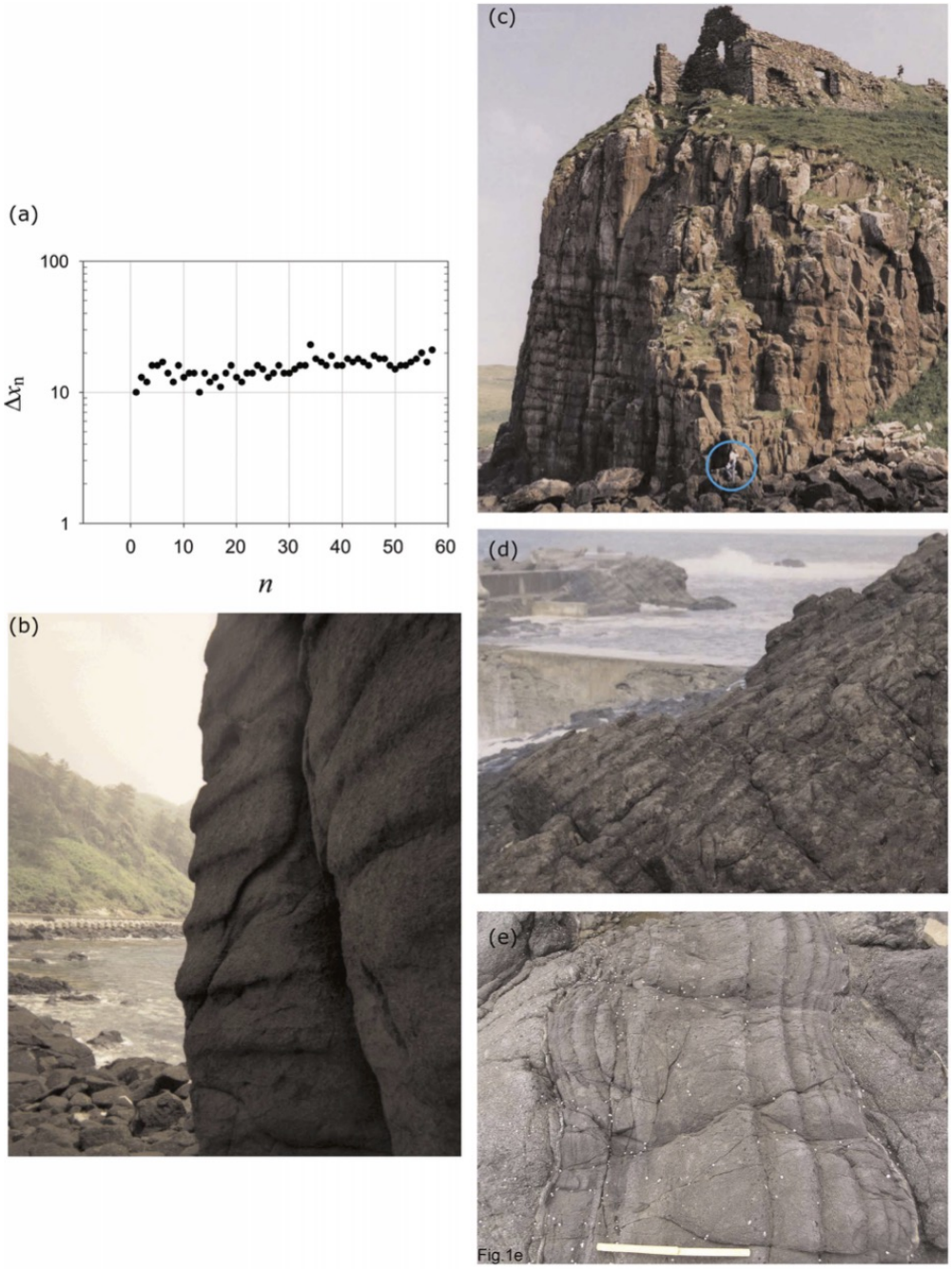


Figure 22: Igneous layering. A Layer width Δx_n (cm) versus numbers indicating the order from the reference layer n at Ogi picrite sill, Sado Island, Japan. The trend approximately follows $\log \Delta x_n = \log \Delta x_0 + 0.003n$. Photographs showing cyclic layering: B Picrite sill at Ogi, Sado Island, Japan. Layer spacing is approximately 30 cm. C Dolerite sill at Duntulm Castle, Isle of Skye, Scotland. A geologist in a blue circle provides scale. D Dolerite sill at Konpiraiwa, Atsumi, Japan. Layer spacing is approximately 20 cm. E Tertiary basaltic andesitic dyke at Shibushi, Hirado Island, Japan. The country rocks are dolerite. The scale bar is 37 cm long. From [123].

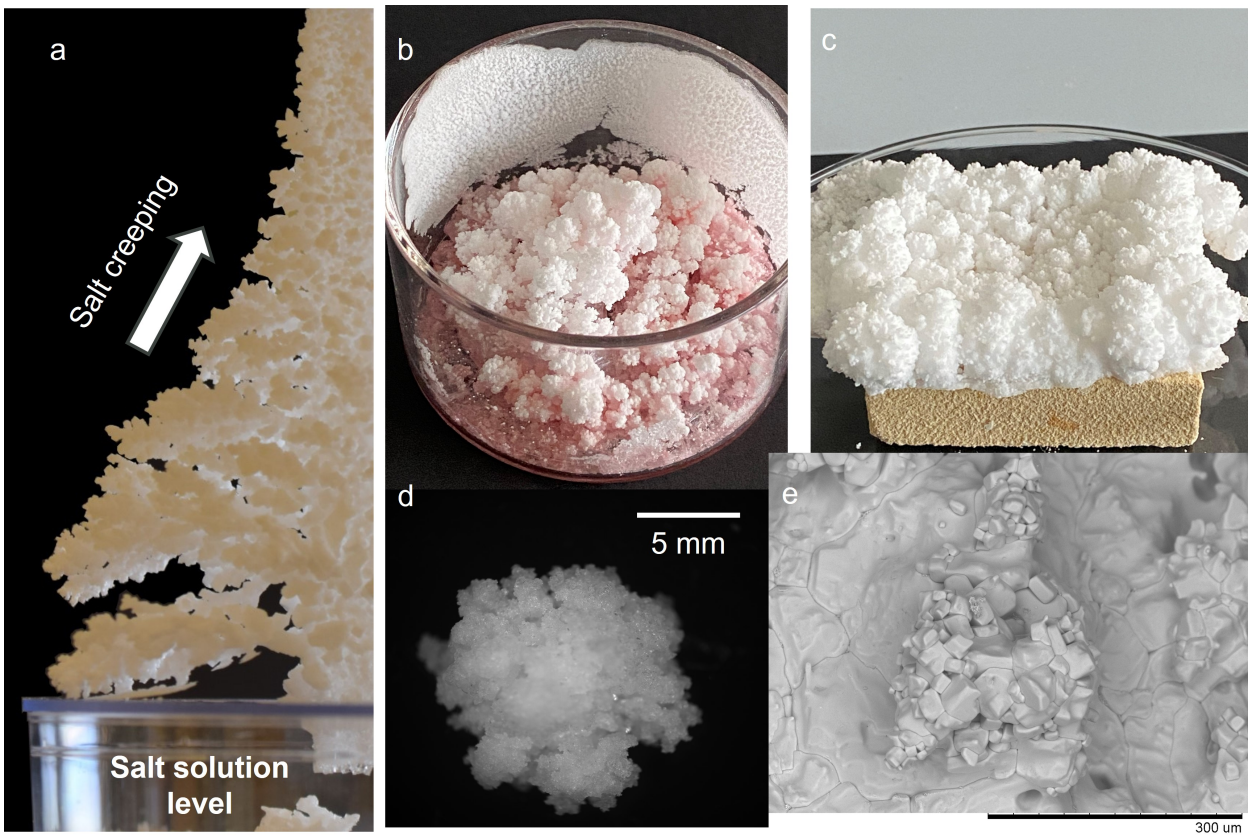


Figure 23: Salt crystallization patterns at different scales. A: laboratory experiment of salt creeping on a cylindrical glass rod (flat surface) far from the evaporative salt solution in the petri dish. B: salt crystallization as efflorescence on large NaCl crystals and creeping on glass wall of the NaCl solution evaporating in a beaker (laboratory scale experiment of the drying of a salty lake). C: Salt efflorescence on the top of piece of limestone D,E: zoom on the morphology of salt efflorescence; SEM images of the porous structure of the efflorescence at the microscale showing an assembly of microcrystals. (images: N.Shahidzadeh, UvA).

Examining Darcy's law, which relates the flow rate $\mathbf{u}$ to the pressure gradient ∇p in a porous medium

$$\mathbf{u} = -M\nabla p = -\frac{K(\phi)}{\eta}\nabla p, \tag{4}$$

we see that mobility M can be controlled in two ways: by altering the viscosity of the fluid η or by changing the permeability of the medium K, which depends on the porosity ϕ. The first approach leads to the viscous fingering phenomenon [146, 142, 147], where less viscous fluid penetrates the medium in narrow, finger-like channels, displacing the more viscous fluid.

The second method can be achieved by dissolving the porous medium using a chemically active fluid that reacts with the pore surfaces. This is so-called reactive-infiltration instability [148, 149, 150, 151]. A classic example here are karst processes, initiated by the dissolution of limestone by CO_2 saturated water. Flow focusing due to the reactive-infiltration instability impacts cave system formation [152, 153, 154] and surface karst features such as solution pipes (Sec. 5.2.2) [155]. In industrial applications, much stronger acids, such as HCl or HF, are used for stimulation of petroleum reservoirs [156, 157, 158] or sustaining fluid circulation in geothermal systems [159, 160]. A similar instability of an initially flat propagating dissolution front is seen in stylolites (Sec. 5.3.1) [161].

It is interesting to note what happens to the initial protrusions on the unstable front during the course

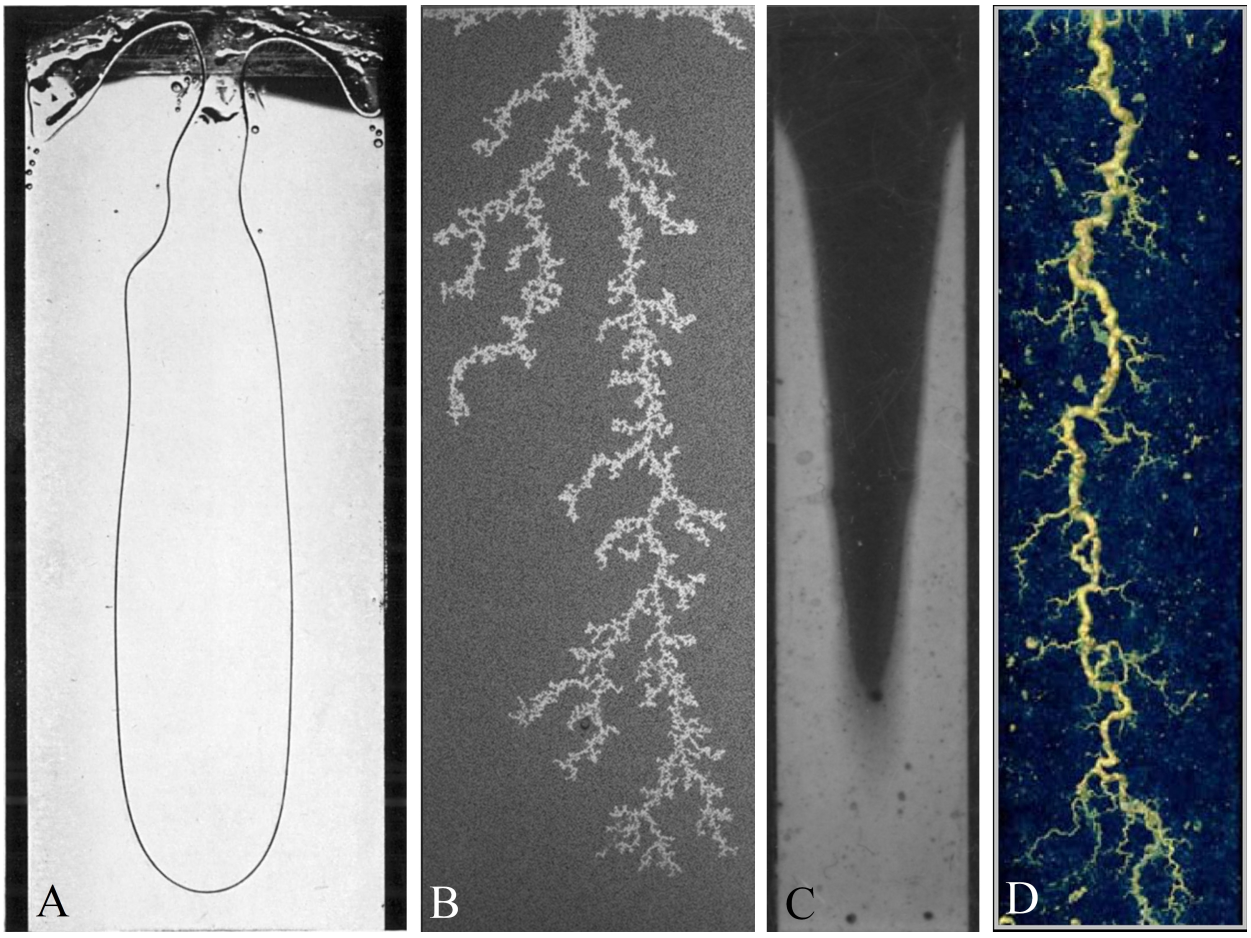


Figure 24: Fingering. A: Saffman–Taylor finger that appears in the long-time limit in the viscous fingering experiment [142]. B: The irregular, fractal finger formed in viscous fingering experiment in porous medium, where air was displacing glycerine in a Hele-Shaw cell filled with glass beads [143]. C: A smooth dissolution finger arising in a Hele-Shaw cell with a soluble bottom [144]. D: A fractal dissolution finger (wormhole) formed during acidization of limestone [145].

of the evolution of the instability. As they grow larger, they transform into fingers that begin to interact with each other. Two processes take place here: one is the competition of the fingers for the flow, causing the longer ones to advance ahead of the shorter ones. The other is the merging of fingers, reducing their total number. As a result, the pattern coarsens, and eventually, a single finger emerges. In the theory of viscous fingering such a final, stable finger-like structure is known as a Saffman–Taylor finger (Fig. 24A). If the Saffman–Taylor experiment is conducted in a Hele-Shaw cell filled with glass beads, mimicking a porous medium, the finger appearing in the system has a highly ramified, fractal structure, not unlike diffusion-limited aggregates [162] (Fig. 24B). This is due to the fact that the local interface curvature controlling the capillary pressure drop depends on the local pore geometry and is thus sensitive to the frozen disorder associated with the structure of this system [143].

A similar situation occurs in the case of reactive-infiltration instability. If we conduct experiments in a homogeneous system, such as a Hele-Shaw cell with a soluble bottom, we end up with relatively regular fingers, which merge and transform into a single dissolution finger in the long-time limit [144] (Fig. 24C); compare the geological solution pipes of Fig. 52. On the other hand, in the dissolution of porous rocks, twisted and ramified wormholes form (Fig. 24D; Sec. 5.2.2).

A further application of such reactive-infiltration instability is to carbon dioxide, both natural geological accumulations and its engineered storage in saline aquifers. Natural chemical reaction between the dissolved

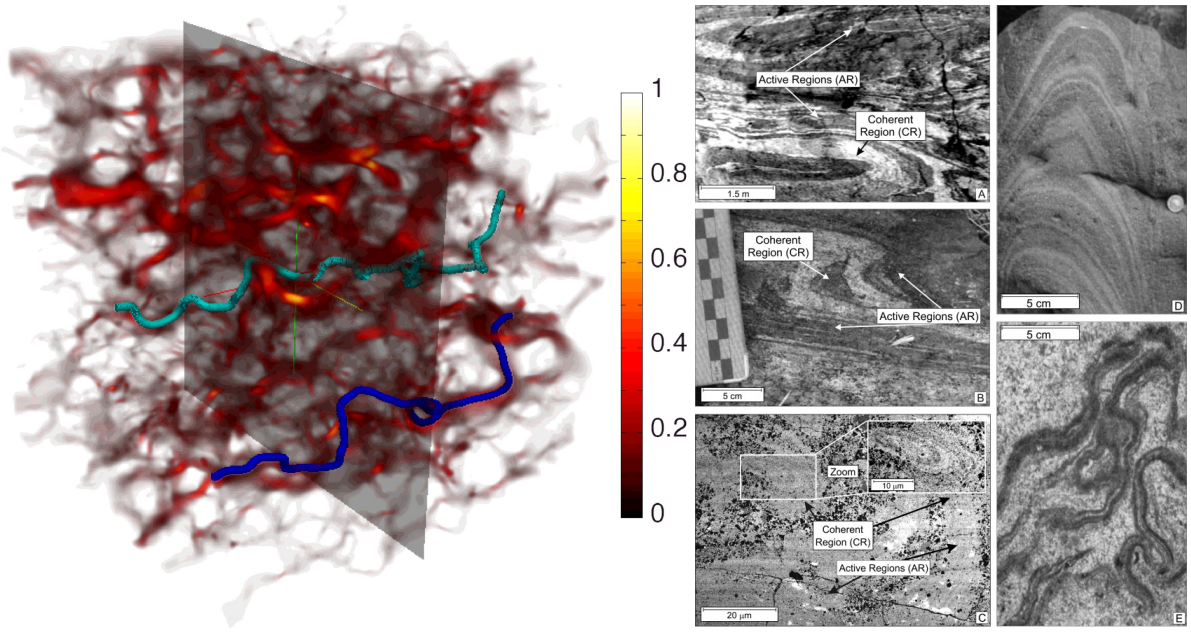


Figure 25: Chaotic advection. Left: Digital reconstruction of the 3D flow field through a Berea sandstone block (1.6 mm cube). The normalized velocity magnitude is rendered according to the colour bar; yellow zones indicate high velocity bursts. Two flow paths (blue and cyan) show evidence of branch and merge behaviour. Adapted from Kang et al. [164]. Right: Examples of magma mixing structures in lava flows from the islands of Lesbos (A–C), Vulcano (D) and Salina (E). The dark flow structures consist of B magmas dispersed through light-coloured A magmas. In all lava flows mixing structures have the same patterns at many scales of magnification. Adapted from Perugini et al. [165].

CO_2 and the rock formation may alter the hydrodynamic behaviour of a diffusive layer of carbon dioxide in a porous medium and either permit, or inhibit fingering. The control parameter, the Cardoso number, is the ratio of the Damköhler number to the square of the solutal Rayleigh–Darcy number,

$$Ca = Da/Ra^2 = k_r a D\varphi/(k\Delta\rho_0 g/\mu)^2, \tag{5}$$

where $\Delta\rho_0$ is the maximum density contrast between pure and solute-saturated fluid, D is the diffusivity of the solute in the aqueous layer, φ is the porosity of the rock matrix and g is the acceleration due to gravity. The permeability of the porous medium k and the fluid viscosity μ are constant. The Cardoso number is a measure of the relative magnitude between the timescale for onset of convection and the timescale for reaction; a small Cardoso number reflects a slow reaction with little effect on the development of convection, while a large Cardoso number implies a fast reaction with consequent impact on the intensity of the instability [163].

4.2.8. Chaotic advection

Chaotic advection, a phenomenon recognized in fluid mechanics since the 1980s [166], shows that deterministic nonlinear dynamics can render fluid trajectories chaotic [167]. Stretching and folding generate intricate, often fractal structures that greatly enhance mixing, with consequent enhancements in heat transfer and reaction rates. Chaotic advection is distinct from turbulence: it arises in slow (low-Reynolds-number) flows, whereas turbulence characterizes fast, inertially dominated flows [168].

Since a considerable portion of geophysical flows are slow, chaotic advection has important consequences in geological systems. One key application is pore-scale fluid flow in rocks (Fig. 25). A series of studies has addressed this question and shown its importance for macroscopic heat and solute transport [169, 164, 170, 171]. Lester et al. [172] show how fluid mixing and chemical reactions significantly affect the mechanics of hydrothermal systems. Trefry et al. [173] discuss how temporal fluctuations, together with

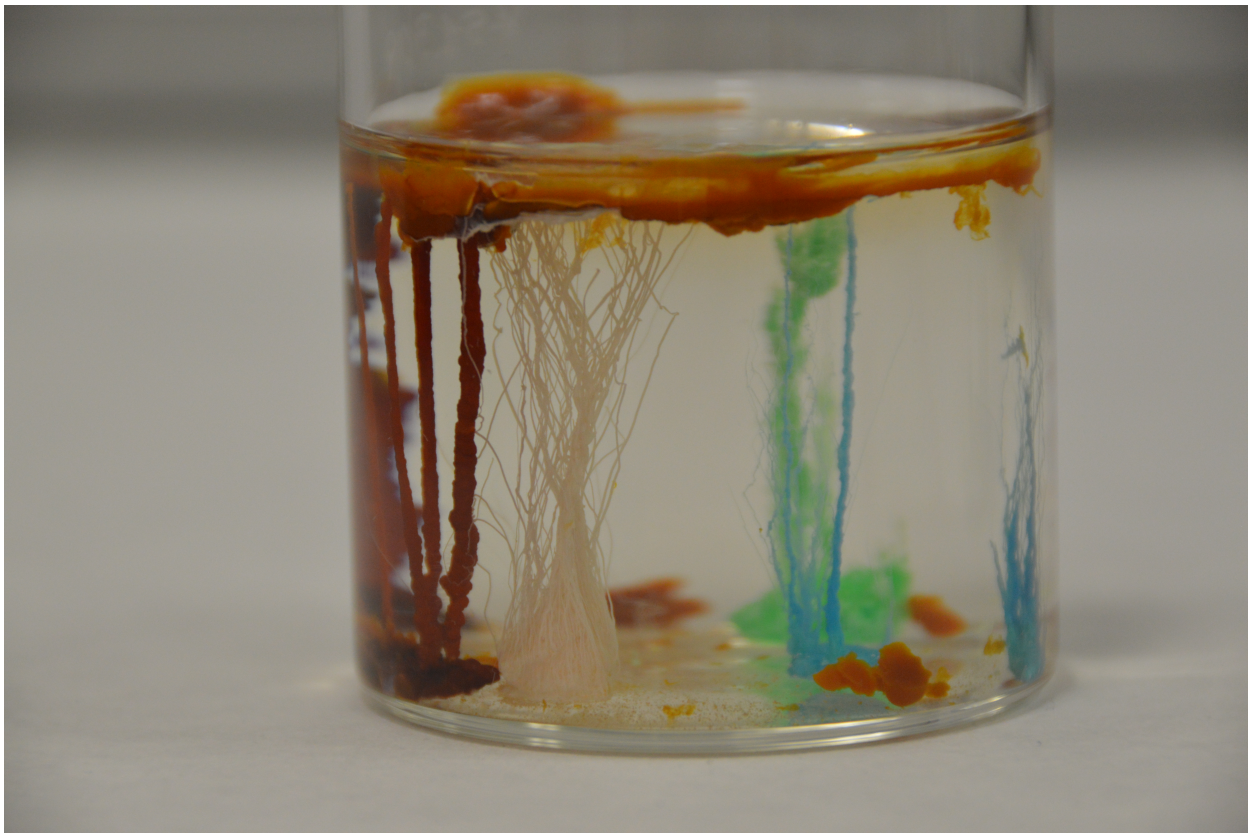


Figure 26: Osmotic processes. The chemical laboratory demonstration known as a chemical garden depends on osmotic forces for its growth (image: Julyan Cartwright).

poroelasticity, generate chaotic advection in natural groundwater systems. Schoofs et al. [174] show that, for typical geological parameters, thermohaline circulation in the Earth's crust is intrinsically chaotic. This dynamics impacts heat transport at mid-ocean ridges, ore genesis, metasomatism and metamorphism, and the diagenetic history of sediments in subsiding basins. Oberst et al. [175] propose that feedbacks between thermochemical and deformation processes are important for the deposition of vein-filling minerals such as pyrite and gold. Further work has examined chaotic advection in magma flow (Fig. 25), its role in mixing, and its effects on the time-scales of cooling and crystallization of magma [176, 165, 177, 178, 179].

4.3. Osmotic processes

Osmosis is a phenomenon that arises from the differential mobility of molecular species in a fluid. In the simplest case, if the solvent (water) can pass through a membrane, whereas a solute (e.g., metal ion) cannot, then exclusion of the solute generates an osmotic pressure across the membrane. In this case the membrane is termed semipermeable. Such a barrier to movement can result from pore size (sieving), but also chemical affinities and electrical potentials.

Osmosis and osmotic pressure are ubiquitous in biology, since cells possess membranes, and are both influenced by and exploit these forces. However, osmosis also occurs in geological systems. Clays and shales are typical instances of geological semipermeable porous media [39]. Wherever water interacts with a porous medium that acts as a semipermeable substrate, osmotic pressure can develop [180]. Osmosis, alongside buoyancy forces, may drive the convective processes of submarine mud volcanoes and seeps [181, 182]. Modelling studies indicate that osmosis may be at the root of permafrost explosions producing large craters in the high arctic of Siberia [183].

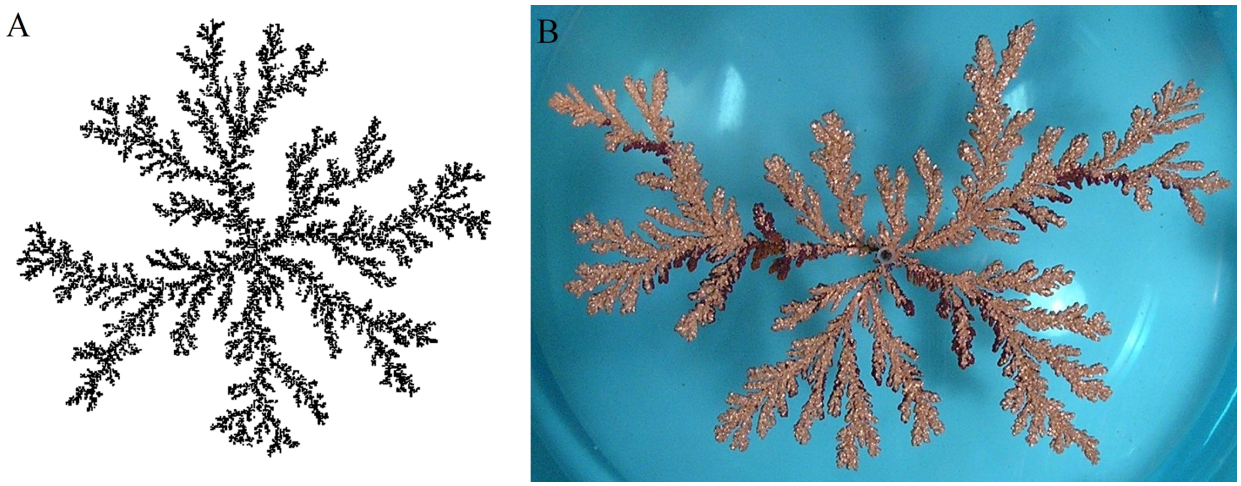


Figure 27: Left: A cluster created by the diffusion-limited aggregate (DLA) model. Right: A dendritic copper aggregate, produced through electrodeposition from a copper sulfate solution, which can be described by the DLA model. (image: Kevin R Johnson CC-BY-2.5).

Osmotic processes can also drive striking self-organized precipitation phenomena, most notably in so-called chemical gardens. Chemical gardens are biomimetic structures that form tubular solids which twist into multiple forms resembling plants. This phenomenon has fascinated researchers for centuries, from Glauber in 1646 [184] to the present [185]. Their formation begins by adding a solid seed crystal of a metal salt to a solution, often silicate, but also carbonate, phosphate, and others. The surrounding liquid partially dissolves the seed surface, forming a semipermeable membrane. External solvent enters the interior of the membrane by osmosis. This influx increases the internal volume, stressing the membrane until it ruptures. Then, the internal solution is expelled under osmotic and buoyancy forces. When the internal solution contacts the external solution, a precipitation reaction occurs, forming the tube walls. These osmotic and buoyancy forces, together with precipitation, produce structures with continuously evolving direction and morphology that resemble biological gardens. This phenomenon is a self-organizing, non-equilibrium, reaction-advection process [41].

Many studies on this phenomenon have been performed at the laboratory scale (Fig. 26). However, chemical gardens can also be found in nature as geological structures. Although the length- and time-scales are clearly different, the same physical drivers recur in natural settings: semipermeable membranes, osmotic pressure, concentration and pH gradients, buoyancy, fluid dynamics, and precipitation. Some examples of geological chemical gardens are hydrothermal vents on the seafloor (Sec. 5.4.2) [186, 187, 188]. In the cryosphere are found brinicles in seawater [189, 190] and on other celestial bodies [191]. Furthermore, these structures, in particular in the form of alkaline submarine hydrothermal vents, are now regarded among the prime candidates for the environments where life may have originated on Earth [40, 192, 188, 193], within inorganic pores and vesicles [194, 195], via processes that embed patterns and information at interfaces between mineral phases [196, 197, 198].

4.4. Diffusion-limited aggregation

Diffusion-limited aggregation, DLA [162, 199], Fig. 27, is a numerical model that describes how complex, disordered structures, often fractal-like in nature, form through the random movement and attachment of particles to a growing cluster. The simulation starts with a seed or nucleation site, and particles are added one at a time via random-walk paths starting outside the region occupied by the cluster. If a particle comes close to the cluster, it attaches to the perimeter, contributing to cluster growth. This process is repeated, and over time, the cluster develops a complex, ramified structure.

DLA can be a good model for aggregation from solution, provided that certain conditions are met. First, it assumes that diffusion of the particles is the slowest process shaping the cluster, while the attachment

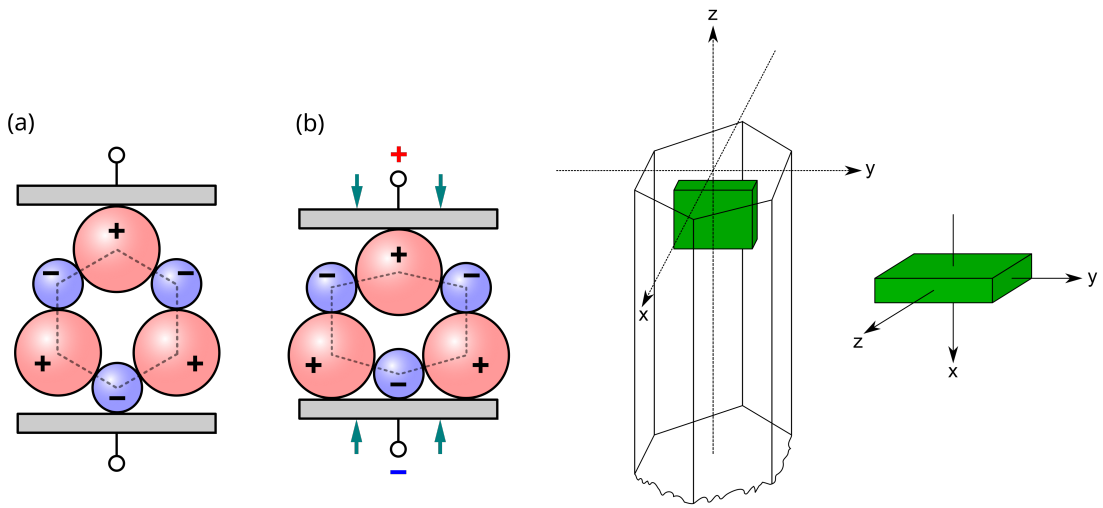


Figure 28: Piezoelectricity: Left: (a) simplified model of a quartz (SiO_2) crystal between two electrodes. Mechanical pressure (b) shifts the positive and negative centres of charge. This creates an electrical dipole, inducing an voltage at the electrodes (image: MikeRun, CC-BY-SA-4.0). Right: Part of a quartz crystal with marked crystallographic axes and a piezoelectric plate (Curie cut) cut from it (image: CLI, CC-Zero).

process is faster. Second, since only one random walker is released at a time, the model corresponds to the infinite dilution limit of the particles. In such a limit, the cluster growth time-scale is much longer than the relaxation time of the particle concentration to the stationary profile. Finally, aggregation is considered to be irreversible, and the cluster does not interact with the incoming particles. Many generalizations of the DLA model exist, which relax one or more of these assumptions [200, 201, 202, 203], thereby extending the applicability of these models to a broader range of phenomena.

The origin of the complexity of DLA aggregates lies in the competition between different regions of the growing cluster. A branch extending from the centre is able to capture more particles since random walkers tend to stick to the first part of the cluster they encounter. Between the growing branches, there are regions, known as fjords, that remain shielded from incoming particles, which become more pronounced as the branches extend.

The limited penetration of the fjords results from a strong screening effect [203]. Particles following random-walk paths tend to become trapped along the edges of the fjords, making it highly unlikely for them to reach the interior of the cluster. This phenomenon is analogous to the screening of a Laplacian field, with absorbing boundary conditions applied to the surface of the DLA fractal, resulting in an exponentially small probability of penetration as a function of the penetration depth.

Similar screening mechanisms apply to other fields, such as pressure fields or electric potentials, leading to a resemblance between diffusion-limited aggregates and other fractal growth patterns, such as viscous fingers or electrodeposition structures.

Although DLA is widely used to model far-from-equilibrium growth in physical and biological systems, it remains a theoretical challenge to fully describe its structure using scaling models. Most approaches assume a self-similar fractal pattern, but this does not fully capture the complexity of DLA [203, 204]. The mathematical structure underlying DLA, as well as more general Laplacian growth models, is quite involved, with the link to the theory of integrable systems and even quantum gravity models [205, 206], providing further evidence that a simple model can indeed generate complex structures. In geological systems, mineral dendrites (Sec. 5.1.2) can be described using DLA.

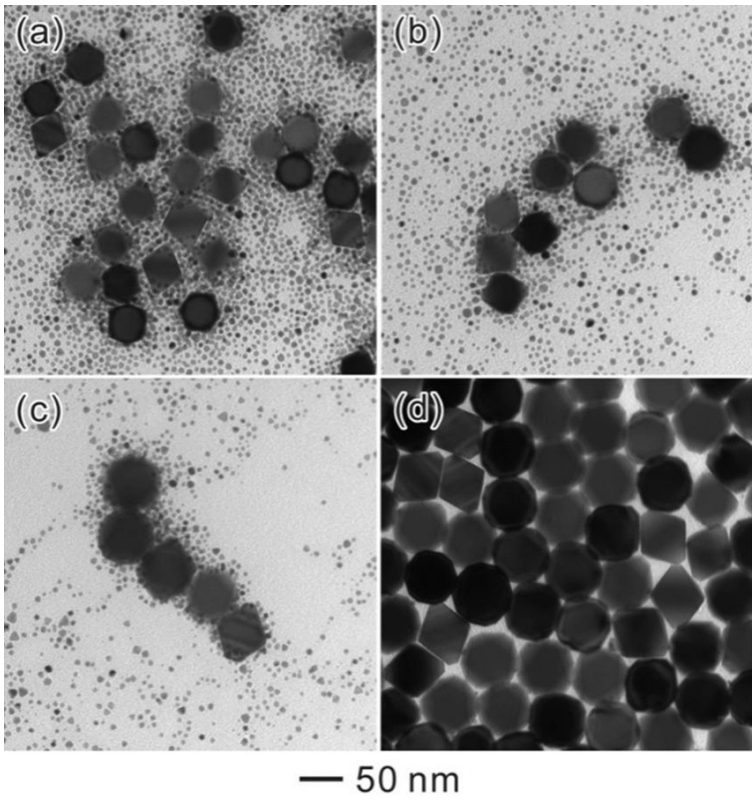


Figure 29: Ostwald ripening process in palladium nanoparticles in formaldehyde. In (A) it can be seen that there are two populations of particles with different sizes. During the reaction, (B) and (C), it can be seen that the smaller particles are dissolving in favour of the growth of the larger ones. Until the end, (D), when only the population of larger crystals remains, which have increased in size. (Image: CC-BY, Zhang et al. [210]).

4.5. Piezoelectricity

Piezoelectricity, the generation of electric charge in response to mechanical stress, is a less commonly discussed mechanism of pattern formation. The piezoelectric effect arises from broken inversion symmetry and is observed in non-centrosymmetric crystals (lacking a centre of symmetry). Under stress, such crystals polarize, producing measurable charge. Quartz is a particularly common geological example (Fig. 28).

Piezoelectricity is used in engineering applications, for example to form patterned thin films via piezoelectric printing [207] and in functional soft-matter systems [208]. As described in Sec. 5.1.3, it may be involved in concentrating gold nanoparticles into nuggets [209].

4.6. Ostwald ripening

The Ostwald ripening process was first described in the late 19th century by Wilhelm Ostwald [82], from whom it takes its name. Under identical conditions, differences in particle size alone drive mass transfer: subcritical (smaller) crystals dissolve while larger ones grow at their expense (Fig. 29). Ostwald ripening constitutes the late stage of a first-order phase transition, during which domains coarsen by material redistribution. Its governing physics is classically captured by Lifshitz–Slyozov–Wagner (LSW) theory, which predicts self-similar coarsening with growth rates set by either diffusion or interfacial kinetics [84, 211]. In LSW theory, the particle-size distribution approaches a self-similar form when rescaled by a characteristic length (e.g., the mean radius). That characteristic size grows as $t^{1/3}$ for diffusion-controlled ripening [212] and as $t^{1/2}$ for interface-kinetics–controlled ripening [211]. These predictions have been observed qualita-

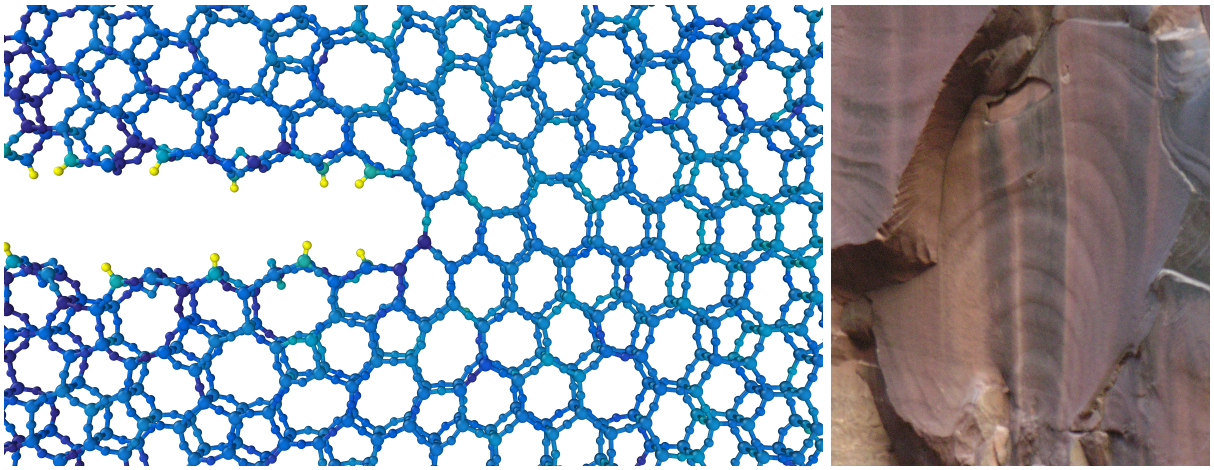


Figure 30: Fracture processes. Left: SiO_2 fracture. Crack propagation in a two-dimensional bilayer of amorphous silicon dioxide modelled with a polarizable interatomic potential [214]. Atoms are coloured by their local potential energy on a scale normalized from dark blue, lowest energy, to yellow, highest energy. (Image: Marco Caccin and Alessandro De Vita, King's College London; James Kermode, University of Warwick. CC-BY-NC-SA-2.0). Right: Plumose fracture patterns in sandstone, North Canyon, Arizona, USA (image: Awickert, CC-BY-SA-3.0).

tively in experiments, but quantitative discrepancies remain, so Ostwald ripening continues to be an active subject of research today [213]

Geologically-relevant instances of Ostwald ripening include processes occurring in clays minerals and metamorphic rocks [215], mineral paragenesis in sediments [216], olivine and plagioclase in magmas [217], coarsening of gold nanoparticles [218] and advection-mediated chiral autocatalysis in which complete chiral symmetry breaking is attained from an initially unbiased mixture of seed crystals [219]. Banded sphalerite, Sec. 5.3.3, may be another geological example.

4.7. Fracture processes

When a material is subjected to stress, the internal forces may exceed its cohesive strength, causing fracture [220], Fig. 30. The way a material fractures is governed by the material's properties and the applied loading conditions, leading to a variety of patterns.

Fracture typically begins with the nucleation of a crack [221], which then propagates through the material. The path of this crack is controlled by the stress field within the material. As a crack advances, it relieves stress in its immediate vicinity yet can concentrate stress at its tip, which can cause the crack to branch or change direction, depending on the material heterogeneity and the external loading conditions. For example, in brittle materials like glass, cracks tend to propagate approximately straight under uniform stress, whereas in more ductile materials, they may follow more tortuous paths, creating complex patterns.

Several mechanisms contribute to fracture-pattern formation in materials. One such mechanism is the interaction between multiple cracks [222]. When multiple cracks propagate simultaneously, their paths can intersect or mutually influence each other, leading to branching [223] and the formation of intricate networks of cracks. Another important factor is material anisotropy [224], which can cause cracks to preferentially propagate along certain directions, resulting in directional patterns.

Fracture patterns often exhibit self-similarity [225, 226], meaning they appear similar at different scales. This self-similarity is governed by scaling laws that describe how the fracture process operates similarly across length-scales [227]. For example, the branching patterns in a shattered car windscreen or the cracks in dried mud both exhibit fractal characteristics, where smaller branches or cracks resemble the larger overall pattern. These scaling laws highlight the universal nature of fracture processes, showing how similar patterns can emerge in different materials under varying conditions.

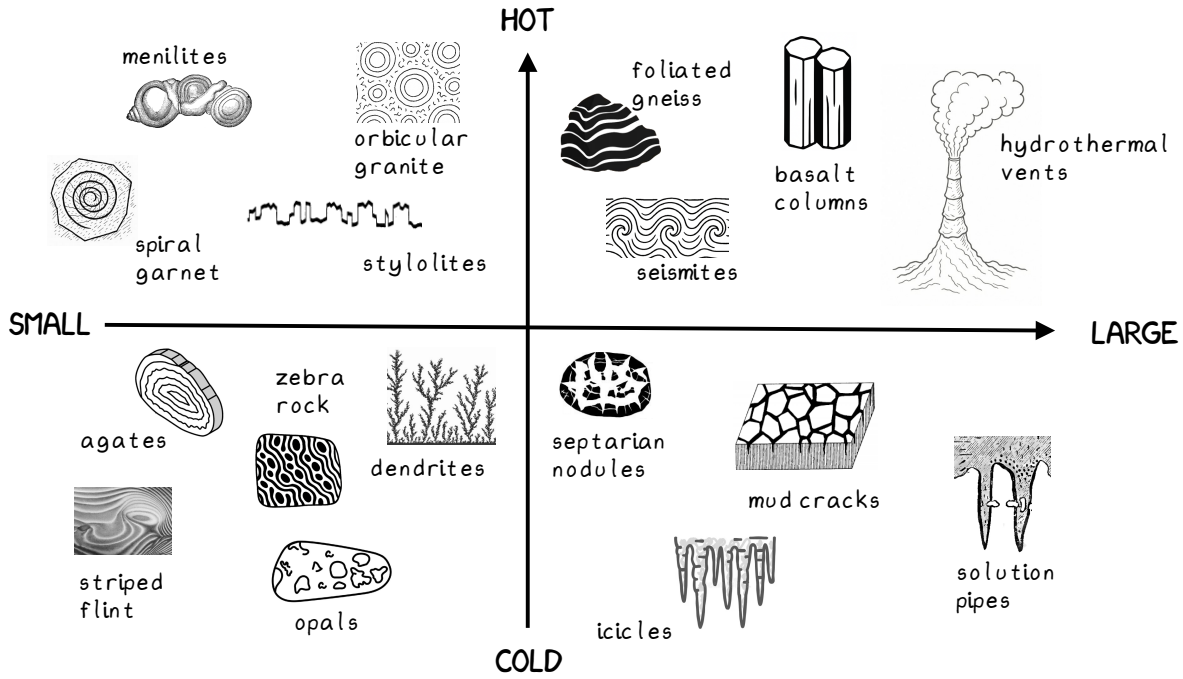


Figure 31: Energy–size morphospace for self-organized geological patterns. The horizontal axis records the characteristic spacing or wave-length of each structure and is broken at ∼10 cm to distinguish small- from large-scale patterns; the vertical axis records the dominant energy density that drives formation, rising from low-temperature, diffusion-controlled systems at the base to high-temperature or high-stress regimes at the top.

Chemical processes significantly influence the development of fracture patterns in geological materials, a factor that has often been underestimated. There exists an intricate relationship between mechanical and geochemical processes, and progress in understanding geological fracture patterns requires integration of these two domains [228]. One illustrative setting where reactions reorganize fracture patterns is mineral replacement. Mineral replacement processes are common in various geological settings and involve the transformation of one mineral into another, often under conditions that change solid volume. Such reaction-driven volume changes generate internal stresses within the mineral framework. These stresses can fracture the parent mineral, thereby influencing the development of replacement minerals [229].

Some geological instances that we discuss here are sedimentary crack patterns, Sec. 5.2.6; and basalt columns, Sec. 5.4.1.

5. Mesoscale self-organized pattern-forming systems in geology

Geological pattern formation refuses to confine itself to a single yardstick: rhythmic structures appear at wave-lengths that range from microns to metres, and they are powered by energy sources that vary just as widely, from the modest chemical free energy of supersaturated groundwater to the latent heat released when magma solidifies or the mechanical work done under tens of megapascals of burial stress. To keep that broad vista in focus we introduce a two-axis framework in which the abscissa records the characteristic length-scale of a pattern—which might be its band spacing, crack pitch or convection-cell diameter—while the ordinate records the governing energy-scale, defined as the dominant energy density required to create or sustain the structure. Plotting the examples on this length- and energy-scale map, Fig. 31, makes it immediately clear which physical ingredients a successful model must capture and how apparently disparate phenomena relate to one another.

In the lower-left quadrant, low-energy and small-scale coincide. Here we find the sub-millimetre banding of agates (Sec. 5.1.1); branching dendrites on bedding planes (Sec. 5.1.2); and the rhythmic micro-bands of striped flint (Sec. 5.1.5) and zebra rock (Sec. 5.1.6). Although none of these structures requires elevated temperatures, each is controlled by reaction–diffusion or dissolution–precipitation feedbacks that act over millimetres to centimetres.

Sliding rightwards along the low-energy tier brings us to patterns that remain cool but express themselves on larger spatial scales. Icicles (Sec. 5.2.1) that grow centimetre-wide flutings while releasing latent heat to sub-zero air; vertical solution pipes that punch metre-wide shafts through limestone (Sec. 5.2.2); the familiar polygonal mud-cracks of drying lake beds (Sec. 5.2.6); and concentric shrinkage cracks that fill septarian nodules (Sec. 5.2.8), all share this quadrant: the energy budget is modest, yet the geometric wave-length is measured in tens of centimetres or more.

Ascending into the higher-energy half of the figure we meet structures whose formation budgets are dominated by latent heat or by high mechanical work. At small length-scales this quadrant hosts the serrated teeth of stylolites (Sec. 5.3.1), which record tens of megapascals of differential stress even though their amplitude is only a few millimetres; spiral garnets (Sec. 5.3.2), the formation of which taps both metamorphic heat and considerable differential stress; the concentric shells of orbiculate granitoids (Sec. 5.3.5); and the glassy menilite nodules thought to be silica bodies sculpted by earthquake-triggered fluidization (Sec. 5.3.7).

Finally, the high-energy, large-scale quadrant hosts patterns whose spacing climbs to decimetres or metres while their formation taps substantial heat or stress reservoirs. Among these are the columnar joints that fracture cooling basalt into metre-wide prisms (Sec. 5.4.1); hydrothermal-vent chimneys that build porous spires centimetres across yet tower metres above the seafloor (Sec. 5.4.2); the broad compositional layering of foliated gneiss (Sec. 5.4.5), generated under the combined heat and stress of deep crustal metamorphism; as well as seismites: soft-sediment convolutions shaken into metre-scale relief by strong earthquakes (Sec. 5.4.6).

Placing the examples on this length- and energy-scale map immediately signals which physical ingredients a successful model must capture: diffusion lengths and reaction kinetics govern the lower band, whereas latent heat, fracture mechanics, and differential stress dominate the upper; meanwhile, the horizontal position reminds us of the geometric scale that any theory must reproduce.

In the pages that follow we tour the four quadrants of the energy–size morphospace. For each quadrant we highlight one or two patterns in depth to expose the underlying physics in measurable detail, then move more briskly through a suite of additional examples; sometimes because their mechanics are now well established, but just as often because they remain open puzzles awaiting decisive experiments or field evidence. We accompany our text with the best illustrations we have been able to find of each pattern. That, unfortunately, means that many of the images are without a scale, as more often than not they were taken without a scientific purpose in mind. However, despite this inconvenience we think the images will be of interest, and in the text we give typical size ranges for each case. We hope that this tour will let the reader see both the secure foundations and the outstanding questions that make pattern formation in geology such a lively research frontier.

5.1. Small and cold

Chemical supersaturation and diffusion feedbacks dominate at sub-centimetre wave-lengths. Agate and opal bands, mineral dendrites, striped flint and the rhythmic micro-laminae of zebra rock and zebra textures all form in cool diagenetic environments. The same low-energy regime fosters microporous gold-nugget overgrowths and cavity-filling geodes controlled by millimetre-scale reaction fronts.

5.1.1. Agates

Agates, Fig. 32, are a banded type of chalcedony, a cryptocrystalline form of silica. They are renowned for their stunning appearance, characterized by unique, translucent layers of multiple colours. The term ‘agate’ originates from the Greek word *akhátes*, referring to a river in Sicily where agates were commonly found. Agates form in cavities created by gaseous bubbles trapped in erupted lavas, which eventually become filled with silica. While the characteristic layered structures lining the walls are perhaps the most well-known features of agates, other interesting patterns also require explanation, such as the horizontal,

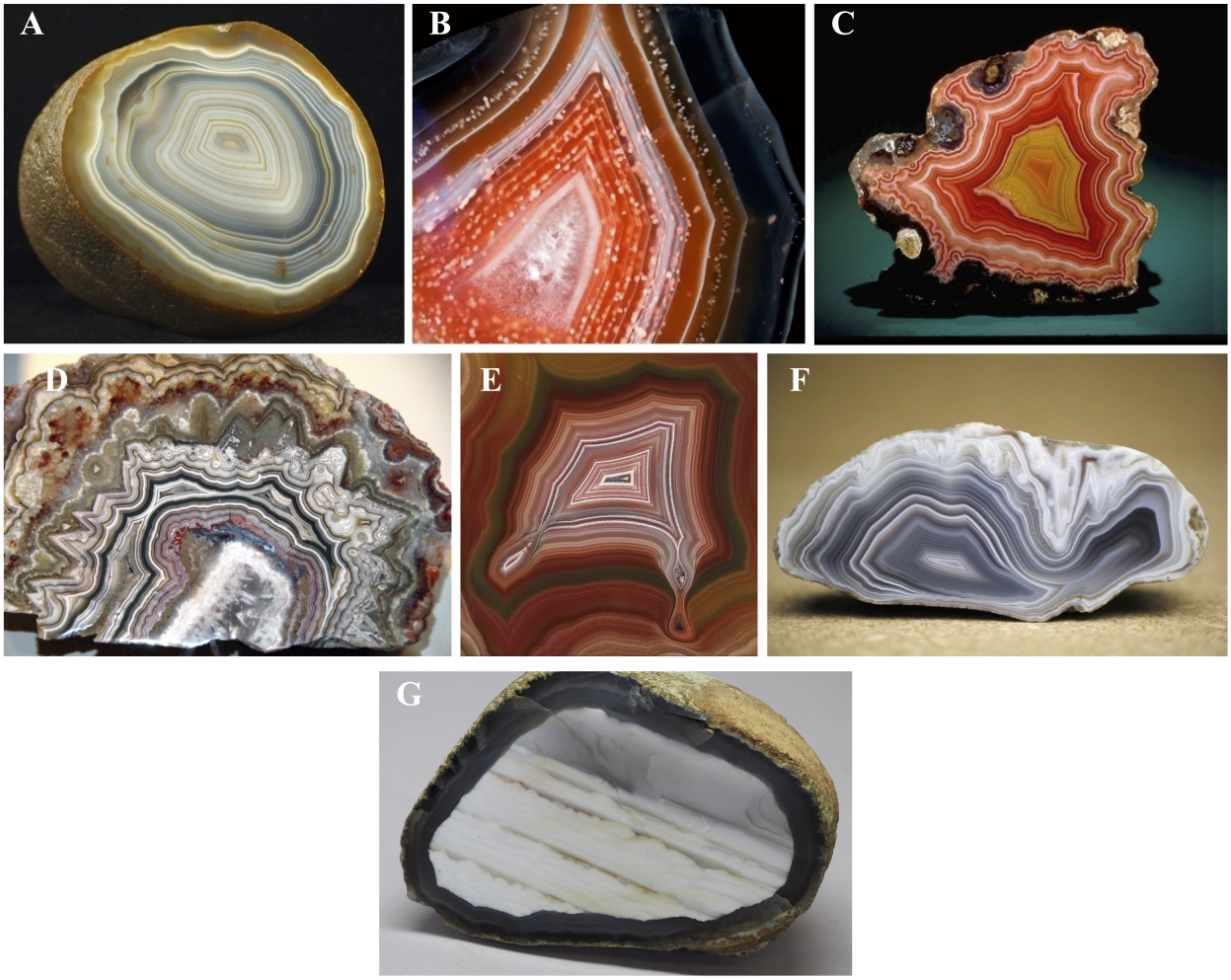


Figure 32: Agates and their banded patterns. A: Black River Agate (photo by Matthew Wood, reproduced with permission); B: Lake Superior agate with a smoky quartz exterior and carnelian centre with mineral spherulites (photo by Karen Brzys, Gitche Gumee Museum/Agatelady Rock Shop, Grand Marais, MI, USA, www.agateladyrockshop.com, reproduced with permission); C: Laguna Agate, Mexico (Smithsonian Museum, distributed under CC license); D: Crazy Lace Agate, Mexico (photo by James St. John, distributed under CC license); E: Laguna Agate (Conejeros Claim), from Chihuahua, Mexico (specimen from Hannes Holzmann collection, photographed by Albert Russ, reproduced with permission); F: Botswana agate from near Bobanong, Botswana (photo by Takehiro Toge, distributed under CC license). G: Agate with Uruguay-type banding from Brazil (photo by HolDu, distributed under CC license).

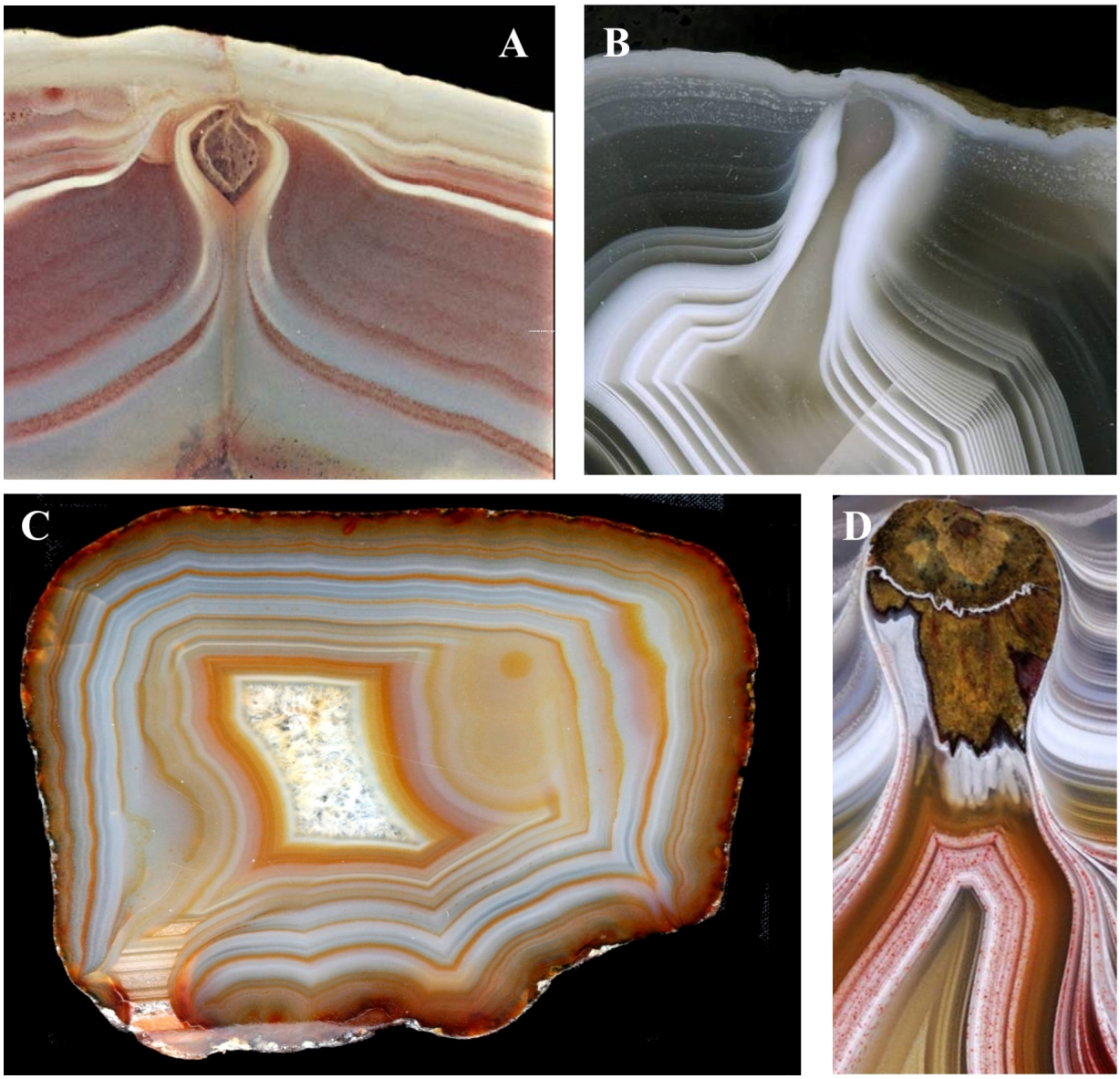


Figure 33: Close-up views of infiltration channels in agates. A: Infiltration channel in an agate from Neuwald near Flonheim, Germany [230]; B: Infiltration channel in an agate from Scotland, UK [231]; C: Infiltration channel in Brazilian agate (Rio Grande do Sul) (Image: CC-BY Moxon and Palyanova [232]); D: Close-up of an infiltration channel in Laguna Agate (Mexico) (Image: Karen Brzys, Gitche Gumee Museum/Agatelady Rock Shop, Grand Marais, MI, USA, www.agateladyrockshop.com, reproduced with permission).

parallel layers known as Uruguay or gravitational banding (Fig. 32G) and infiltration channels (Fig. 33): bulbous structures that develop near the boundary of the agate-containing amygdale (a vesicle in an igneous rock containing secondary minerals). The origin of colours in agate is linked to the presence of pigments on one hand and variations in crystallite size and microstructure, including water content, on the other, as noted by Götze et al. [233]. The most common colours in agate are white, grey, and blue. White agate bands are associated with the presence of thick, plate-like crystallites, which can totally reflect incident light, while the surrounding clear areas contain globular crystallites that allow a portion of white light to be transmitted. The blue colour is caused by the dispersion of light by the microparticles; the Tyndall effect. On the other hand, the colour pigments are mostly iron and manganese oxides and hydroxides, responsible for red and yellow colourations. This results in a wide range of colours and patterns, making each agate distinct and visually appealing.

However, there is more to an agate pattern than what is visible to the naked eye; microscopic studies reveal a much finer banded structure with alternating layers of defect-rich chalcedony and macrocrystalline quartz [234, 235, 236, 237], as illustrated in Fig. 34. The banding in Fig. 34 has a wave-length in the range of approximately 100 μm, but similar oscillatory zonation in defect concentration has been reported at the length-scale of a 0.5–5 μm [238, 239, 234], clearly visible in cross-polarized light (Fig. 35A). The change of refractive index along these bands produces a rainbow-like display of colours in iris agates (Fig. 35B). Zones with iris banding exist in nearly every agate, although they are often concealed by pigmentation.

Microscopic images suggest that microcrystalline chalcedony fibres nucleate on the cavity walls and grow inward towards the centre of the cavity. Initially, there is spherulitic growth, with the fibres radiating outward from separate nucleation points at the edges of the system. Soon, a common banding is formed, running equidistant to the cavity walls [240, 233]. The underlying spherulitic structure is particularly striking when observed in cross-polarized light (Fig. 34B and 36C), which shows the chains of quartz crystals of similar orientation growing from different nucleation points.

The debate surrounding the genesis of agate is both challenging and contentious, primarily due to the lack of a genuine laboratory synthesis that replicates natural agate formations. As a result, numerous theories and approaches have emerged, many of which contradict each other. Consequently, debates about the origin of agate remain as heated today as they were in the 19th century, when most of the agate-genesis models were first formulated. An unsurpassed review of these debates can be found in the paper by Landmesser [240]; more recent reviews can be found in Götze et al. [233], Moxon and Palyanova [232].

In general, theories about the genesis of agate patterns can be divided into two broad classes based on what they consider to be the cause of the banding [241]. External rhythm models hypothesize that agate is an accumulation structure, its pattern reflecting alternating or periodic changes in environmental conditions. Agate, in this view, could be seen as a geological counterpart to the pseudo-mineral fordite (Fig. 37), an accumulation of enamel paint deposited in hundreds of layers in automobile factories during lacquering [242, 243]. However, questions remain about how this geological 'lacquering process' is carried out, including the temperature and form in which silica enters the cavity—here, numerous theories and ideas abound. Internal rhythm theories, on the other hand, link the formation of the agate structure to self-organization processes within the developing agate itself, treating it as a closed system. They usually assume that the agate was filled first by gelatinous silica, and then a reaction–diffusion process of some kind took place that resulted in the formation of the banded pattern.

The first external rhythm theories were formulated in the 19th century. Haidinger [246] hypothesized that agate patterns form where aqueous silica solutions seep into rock pores, precipitating on the cavity walls. This led to a debate about how the silica solution could enter the cavity after the layers had solidified. Noeggerath [247] proposed infiltration channels as possible pathways for the solution, facilitating the continuous development of precipitate layers. On the other hand, Kenngott [248] argued that the silica deposits in a gel state and only gradually hardens due to contraction, suggesting that the deposition, while not yet solidified, remains permeable to seeping solutions.

The above models involve ambient temperatures and pressures, but there are also several theories involving elevated temperatures. Reusch [249] proposed that the cavities were repeatedly filled and then emptied due to intermittent hydrothermal activity in the rock. Solutions fill the cavities when driven upward by advancing steam; once the steam reaches the cavity, it empties again. Each infiltration produces a single layer

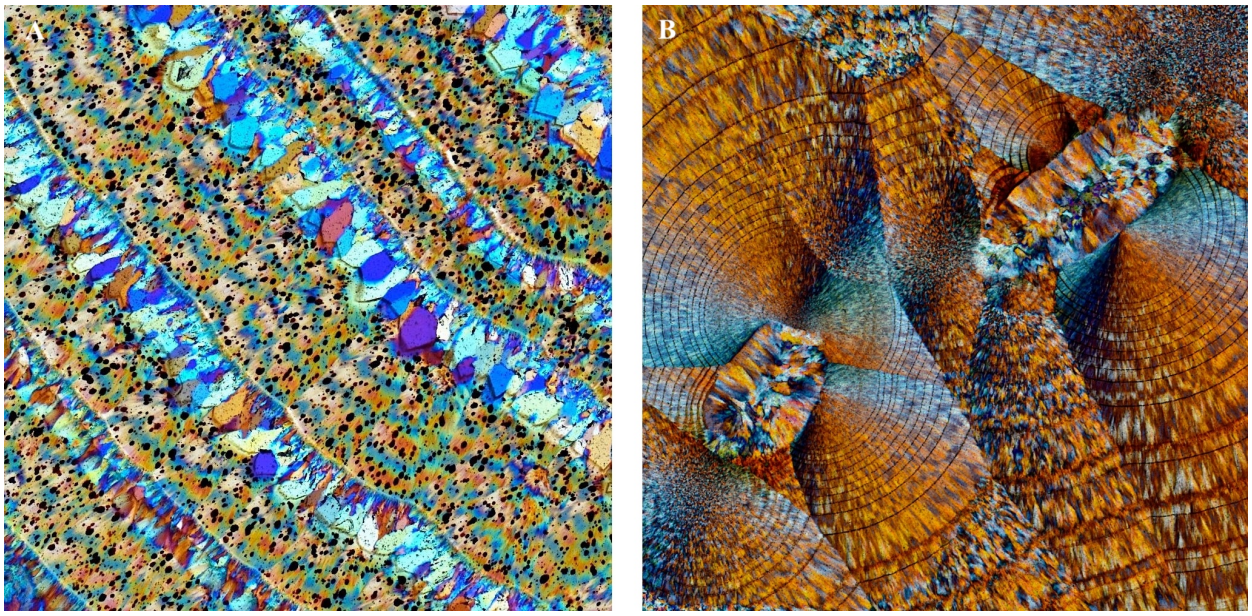


Figure 34: A: Agate micro-banding with fibrous chalcedony interspersed with macrocrystalline quartz. B: Spherulitic pattern in an agate with chalcedony fibres radiating from the nucleation points on the rim of an agate. Photos courtesy of Prof. Bernardo Cesare, University of Padova, Italy.

of silica, again in close resemblance to the fordite lacquering process. More recently, Harris [250] concluded, based on an oxygen isotope study of Jurassic agates, that the agate formation process involved periodic boiling of the hydrothermal solutions, with quartzine layers in agates forming from water vapour and the chalcedony layers crystallizing from liquid water. With each filling process, a fine layer of agate forms from the solution adhering to the cavity edge.

In external rhythm theories, agate, as an accumulation structure, should reflect the changing hydrogeological conditions. Returning to the comparison with fordite, one can reconstruct the colours of cars lacquered at a particular workstation by analysing the successive layers. It is also expected that two fordites, created nearby, will have the same succession of stripes. However, this is not the case for agates; the banded structures of nearby agates are not correlated (Fig. 38), an argument frequently put forward against the external rhythm concepts.

Among the internal rhythm theories, arguably the most famous is that proposed by Liesegang [251], which links agate patterns to the banded structures (Sec. 4.1.5) that form when two components diffuse in a gel and react to form an insoluble precipitate (Fig. 37B). The similarity of patterns that can be created in this way to the agate banding is at first glance striking. However, a closer inspection reveals a number of important differences between these two systems, some of which were noted by Liesegang himself [251]. Firstly, Liesegang patterns lack the sharp corners that are characteristic of agate structures. Next, many structural defects are present in Liesegang rings, such as one ring splitting into two or being displaced in a direction perpendicular to the banding; these defects are absent in agates. Additionally, the distances between successive Liesegang rings obey a well-defined functional relationship, Jabłczynski's Law [74]; Eq. (2), due to the diffusive nature of the underlying process, which is not seen in agates [240]. Moreover, for the rings to form, reacting species must diffuse in the gel, and it is difficult to definitively identify them in the case of agates, and even more challenging to associate their potential presence with the crystallite microstructure. Finally, as with other internal rhythm models, these models encounter a volume problem: the density of the gel is lower than that of the final chalcedony. As the gel dries, it would then shrink, always leaving an empty space in the centre of the cavity. In real agates, this is sometimes the case, but we equally often find fully filled specimens. Additionally, in all actual experiments with Liesegang rings,

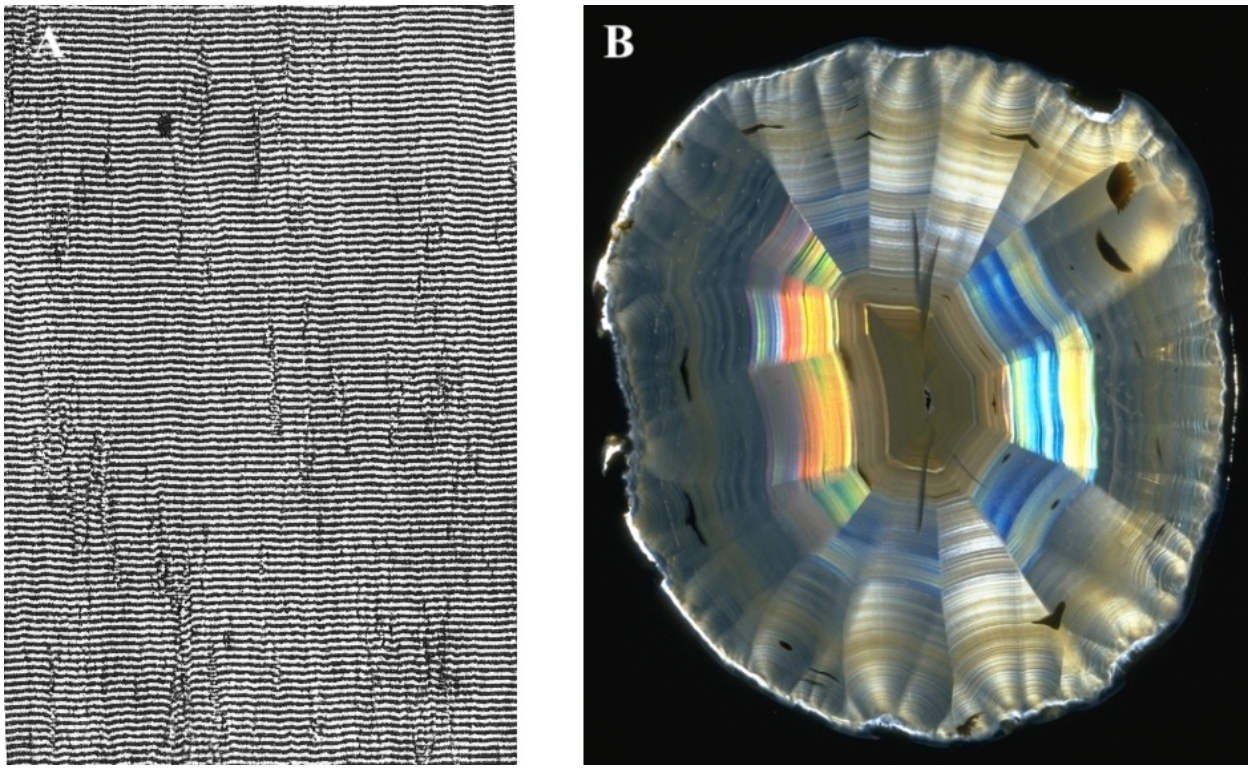


Figure 35: Left: Micron-scale banding in iris agate. The distance between the bands is $\sim 2\mu$m [238]. Right: Iris agate produces a rainbow of colours in transmitted light. The photo in (B) is by Chip Clark, Smithsonian Institution, public domain.

the integrity of the banding is lost during the desiccation process as the gel dehydrates and becomes cracked. Similar criticisms can be levelled against the model of Pabian and Zarins [252] linking agate patterns with the Belousov–Zhabotinsky reaction (Sec. 4.1) (although the reader will notice that this time the corners between the bands in Fig. 37D are sharp, resembling the agate pattern).

A more compelling internal rhythm theory was proposed by Wang and Merino [253]. The advantage of this model is that this time the self-organization process is directly linked to crystallization. According to Wang and Merino [253], silica gel has the potential to crystallize in a patterned, repetitive manner. This is due to the acceleration of quartz crystallization by Al^{3+} cations, which accumulate at the growth front. The model suggests that fluctuations in the concentrations of trace elements could account for the alternating formation of chalcedony and quartz bands, resulting in patterns similar to those depicted in Figs. 34 and 35.

The preceding models assumed that the precursor of an agate is a silica-gel-filled cavity. However, there are also models that assume agates to be transformed glass droplets. The first model of this kind was proposed by Nacken [254], inspired by his experimental observation that silica glass crystallizes into chalcedony and quartz while preserving its outer form when exposed to weak alkaline solutions at a temperature of approximately 400°C. In this process, both the formation of spherulites at the edges of the system and the spontaneous development of a banded structure are observed [254, 255]. Based on this, Nacken proposed that already during the magmatic stage, isolated molten silica droplets separated from the magma and rose upwards, acquiring a shape resembling ascending gas bubbles. With the influence of superheated water vapour, agates then develop from these glass droplets. In fact, the transformation process itself does not need to involve high temperatures, since a banding structure is known to appear in leached archaeological glass [245]; Fig. 37D.

However attractive the high-temperature models with a glassy precursor may sound, as pointed out by

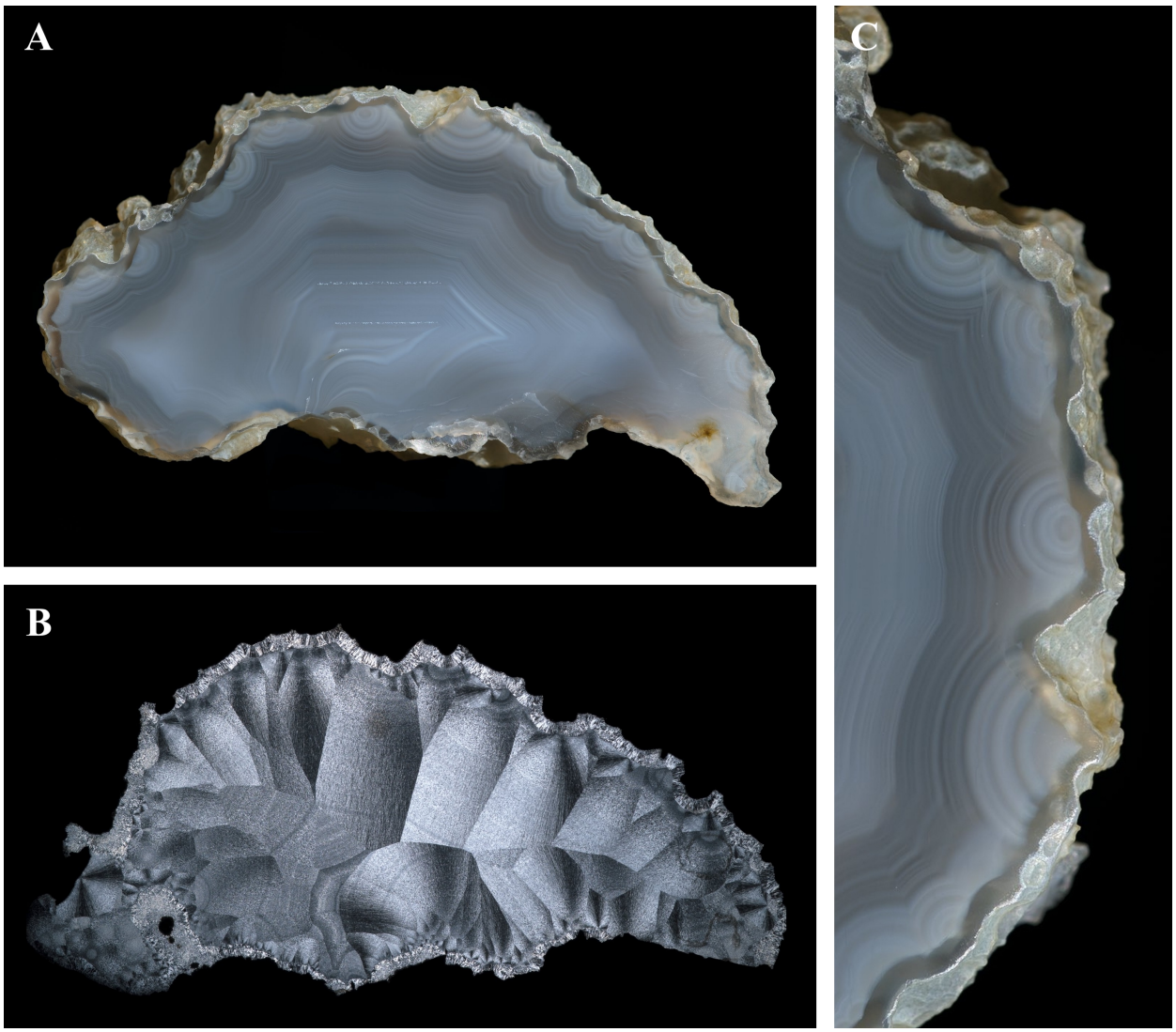


Figure 36: Agate from Ashland, Oregon in plane light (A) and cross-polarized light (B). The enlargement on the right, C, shows the growth of spherulitic nuclei on the boundary of the agate. The photos are courtesy of A. C. Akhavan (quartzpage.de).

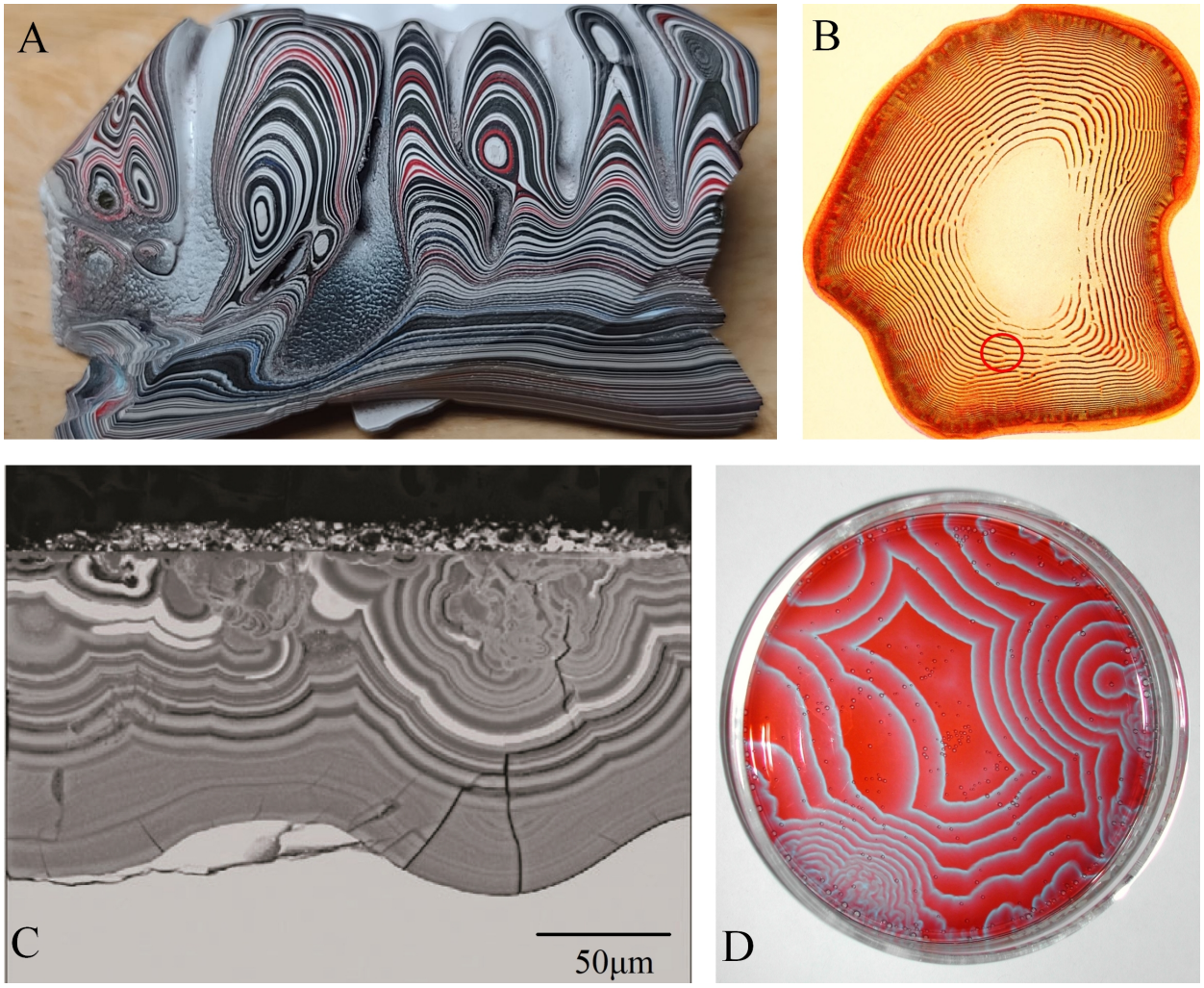


Figure 37: Four banded patterns resembling agates. A: Fordite, hardened enamel paint that has accumulated in hundreds of layers in vehicle factories during the lacquering process. Image by Jeremy Cook (Willett Creek Agate Co.) distributed under CC BY-NC-SA 4.0 license. B: Liesegang rings; rhythmic precipitation zones from supersaturated solutions in colloidal systems. The circle marks a defect in the structure. Adapted from [244]. C: A banded structure in a leached layer of an archaeological glass fragment from a 15th-century stained glass window [245]. D: Patterns arising in the Belousov–Zhabotinsky reaction (image S. W. Morris).

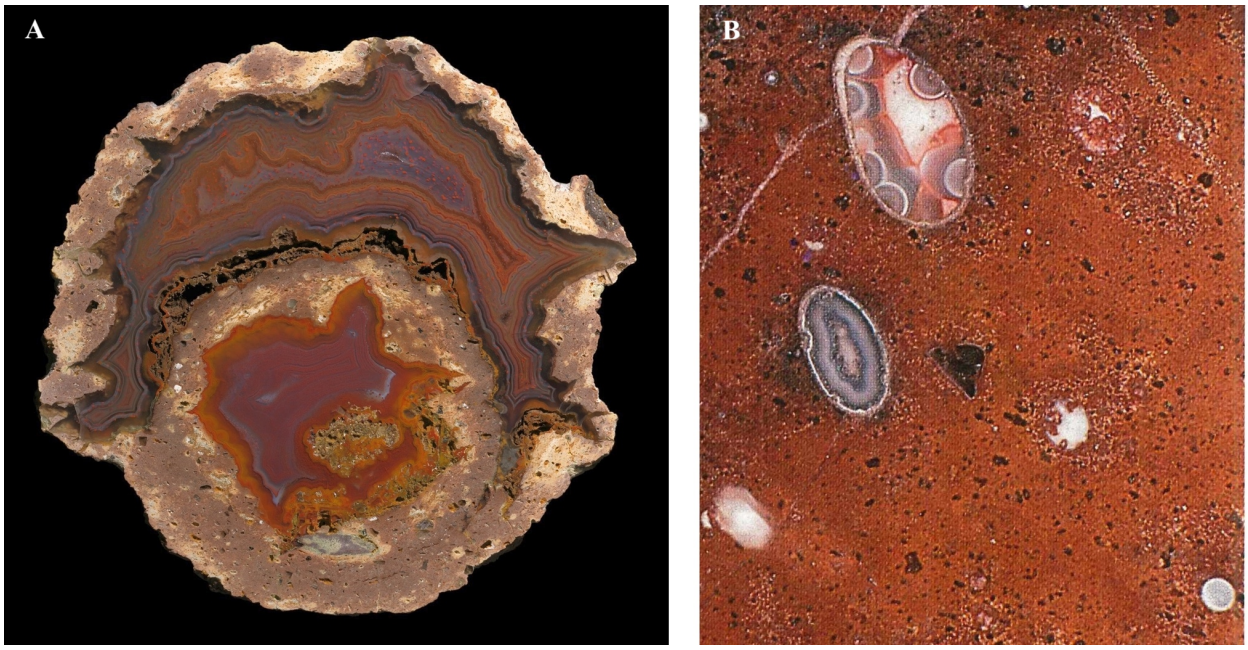


Figure 38: Two nearby agates do not exhibit the same banding structure. A: a photograph by A. C. Akhavan, B: a photograph by Landmesser [240].

Landmesser [240], such separation into pure glass does not occur in multicomponent magma, even with small amounts of alkalis. Additionally, there have been cases identified where agates formed in carbonate cements, thus being separated from the magmatic rock. Furthermore, oxygen and hydrogen isotope analysis on Scottish agates by Fallick et al. [256] demonstrated that their formation temperature was in the range of 50°C. In general, there is a growing consensus in the literature that agates form at temperatures below 100°C [240, 232].

One of the most significant issues with the internal rhythm models is that of volume preservation. Regardless of the assumptions made about the original filling of the cavity, whether it be a solution, gel, or glass, its density is not sufficiently high to generate enough silica to completely fill the entire cavity [240]. In the case of a glass precursor, assuming the density of silica glass is 2.2 g/cm^3 and the density of chalcedony is 2.6 g/cm^3, approximately 15% of the mass is missing. On the other extreme, if we suppose that silica precipitates from the solution under normal conditions with a solubility of about 100 mg/L, then we would require about 1700 L of solution to fill a cavity with a 5 cm diameter.

It would thus seem that a successful agate formation theory should combine the self-organization characteristic of internal rhythm theories with a continuous supply of silica, typical for external rhythm theories. One such model was proposed by Heaney and Davis [234], who hypothesized that the observed alternating crystallization of quartz and chalcedony in agate micro-banding is linked to varying degrees of silica saturation in the solution. Cavity fluids that are partially polymerized rapidly precipitate spherulitic chalcedony. If the depletion of silica near the fibre tips outpaces diffusion toward these tips, then the reduced activity of silica in the solution facilitates the progressively slower growth of larger crystals with fewer defects. Heaney and Davis [234] assume that the crystallization proceeds directly from solution; other researchers suggest that the sol–gel transition takes place first [240, 230, 233].

As for the mechanism that sustains a continual flow of silica into the cavity, one obvious factor is the difference in solubility between the small pores and the large cavity space. Owing to interfacial energy effects, the saturation concentration in small pores is considerably higher [257]. This not only can explain why silica precipitates in the cavities while keeping the small pores free, but also provides a chemical potential

difference driving silica diffusion towards the cavity. However, this diffusion becomes hindered as the first chalcedony layers are formed. An interesting mechanism, which can significantly speed up the process, is the 'reverse osmotic pump' concept proposed by Walger et al. [230]. Walger identifies the infiltration channels (Fig. 33) as potential entrance points for the silica solution, noting that they often correlate with fractures in the first chalcedony layer. The solution would then enter the cavity and precipitate on the walls, either as a gel or as a direct crystal layer. In any case, the pores in the wall-lining layers are too small for the partially polymerized silica to pass through, while still allowing water transport. This water then exits the system through the walls. In this way, solvent circulation in the system is sustained, with the solution entering through the infiltration channels and the solvent leaving through the walls. This is similar to the flow pattern in osmotic pumps [258], but in a reversed direction. In osmotic pumps, the solvent is drawn through the porous walls and leaves the system, along with drugs, through a small orifice. As Walger points out, the presence of the flow in the infiltration channels hinders the precipitation there, leading to thinning out of the wall-lining layers and the formation of a characteristic onion-like shapes of the channels as observed in Fig. 33. It is important to note that there is not agreement in the literature about the role of these channels: some claim that they are the solution entry points [247, 248, 249, 230], pressure release valves [259, 260] or gel deformation structures [240, 233].

This necessarily brief overview of concepts regarding the genesis of agate shows the astonishing diversity of these concepts. Many of them explain certain aspects of agates, but usually not all, and unfortunately, none have resulted in the replication of agate-like pattern generation in the laboratory. However, it is evident that despite its appearance as a hard rock, soft-matter phenomena are underlying the agate formation process. Initially, silica enters the amygdales either as a suspension or a gel. Following this, its deposition on the walls involves crystallization competing with diffusion, potentially influenced by fluid flow. Some theories argue that the deformation and stretching of the gel shape the infiltration channels, while others point to osmosis as central to agate formation. Although the formation of agates still contains many unknowns, it is clear that the answer must ultimately be grounded in the physics of soft matter.

5.1.2. Mineral dendrites

Two-dimensional mineral dendrites—the name is from the Greek *dendritēs* 'treelike'—in the form of black or red-brown deposits on the surfaces of limestones, sandstones, opals or agates, have intrigued people for centuries. We can find mention of them as early as Pliny the Elder's *Natural History* of 77 CE [262], but more detailed descriptions and classifications appeared with the rise of naturalism and mineral collecting in the early 18th century [263, 264]; Fig. 39 shows a reproduction of a plate illustrating dendrites in Mylius' *Memorabilium Saxoniæ Subterraneæ* of 1709. The organic-like form of dendrites led some naturalists to the conviction that they are fossilized plants. However, by mid-18th century, they were pinpointed as patterns emerging as a result of physical processes. Some early authors even attempted to recreate this process; for example, Emanuel Mendes da Costa in his 1757 *Natural History of Fossils* [265] notes that similar patterns can be created by inserting oil in between two sandstone plates and then pulling apart the plates, making this perhaps the first known experiment in viscous fingering (Sec. 4.2.7). For a modern, detailed review of the various geochemical types and shapes of mineral dendrites the reader is referred to the excellent paper by Van Straaten [266].

Dendrites can be composed of different minerals, including manganese and iron oxides, copper, silver, and other metallic minerals. The most common are planar manganese and iron oxide dendrites formed along the bedding planes in limestones and sandstones, such as the ones shown in Fig. 40B-D. The bases of the dendrites are usually associated with the intersections of the bedding planes with joints or other fractures, from where they grow in a direction perpendicular to that of the fracture at the starting point (Fig. 40B-C). However, other forms also occur, which consist of a multitude of small, radial clusters, not connected to the base (Fig. 40D).

Mineral dendrites are low-crystallinity solids, with the absence of even short range three-dimensional periodic structure [267], which suggests that they were formed by the precipitation of colloidal particles. This distinguishes them from the crystalline dendrites often encountered in metallurgy [268]. Dendritic growth occurs at high supersaturation (i.e., highly concentrated solutions). The latter can be achieved in some environmental conditions via supercooling or evaporation in confinement. Crystalline dendrites are

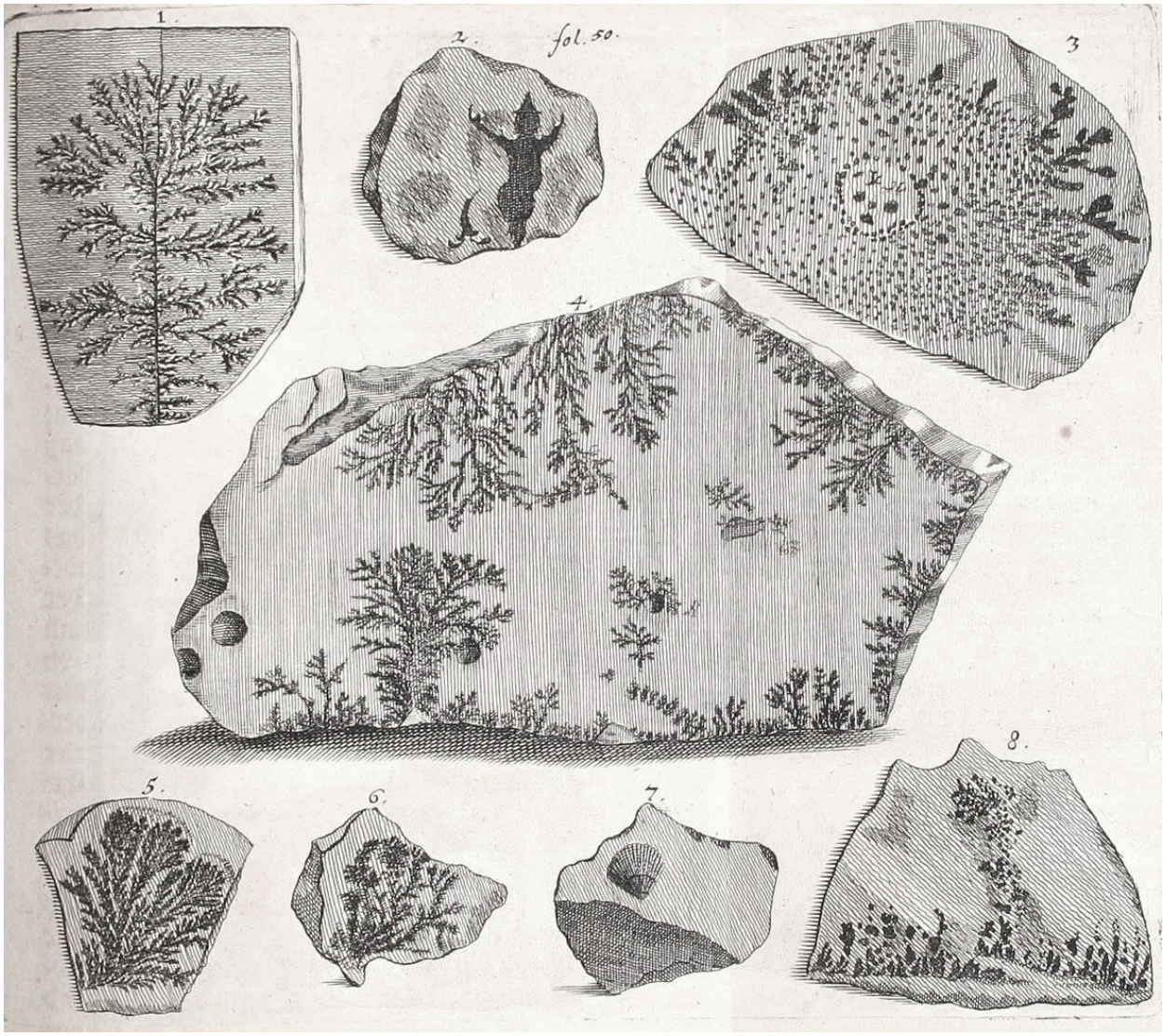


Figure 39: Dendrite drawings in *Memorabilium Saxoniæ Subterraneæ* by Gotfried Friedrich Mylius (1709).

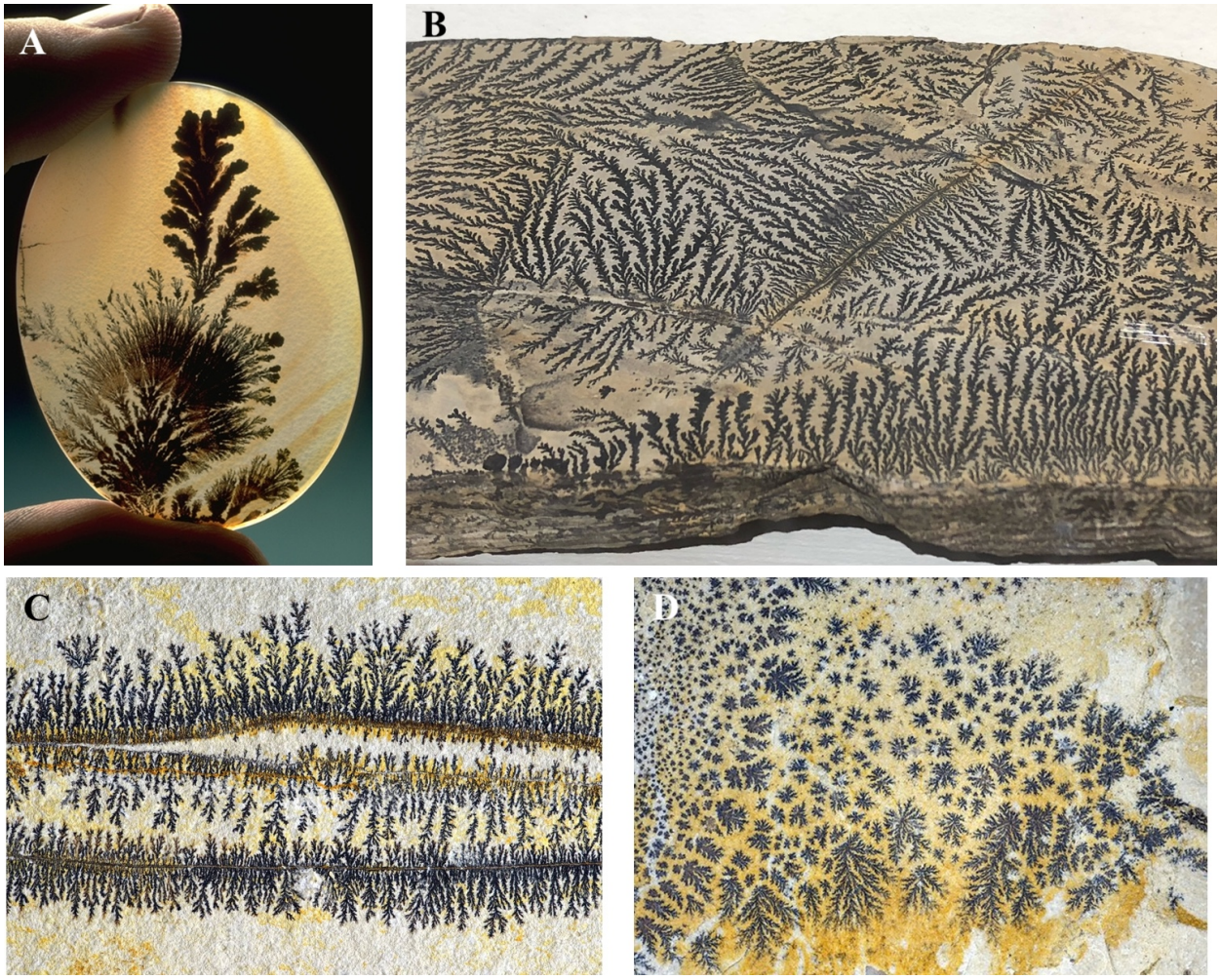


Figure 40: Quasi-2d dendrites in agate (A), and limestone (B–D). In B and C they originate from fractures, whereas in D there are multiple nucleation point. (Images: A, Chip Clark, Smithsonian Institution, public domain; B, Jessica Rosenkrantz, published with permission; C, Adobe stock photography; D, Dr. Jürg Alean, published with permission.)

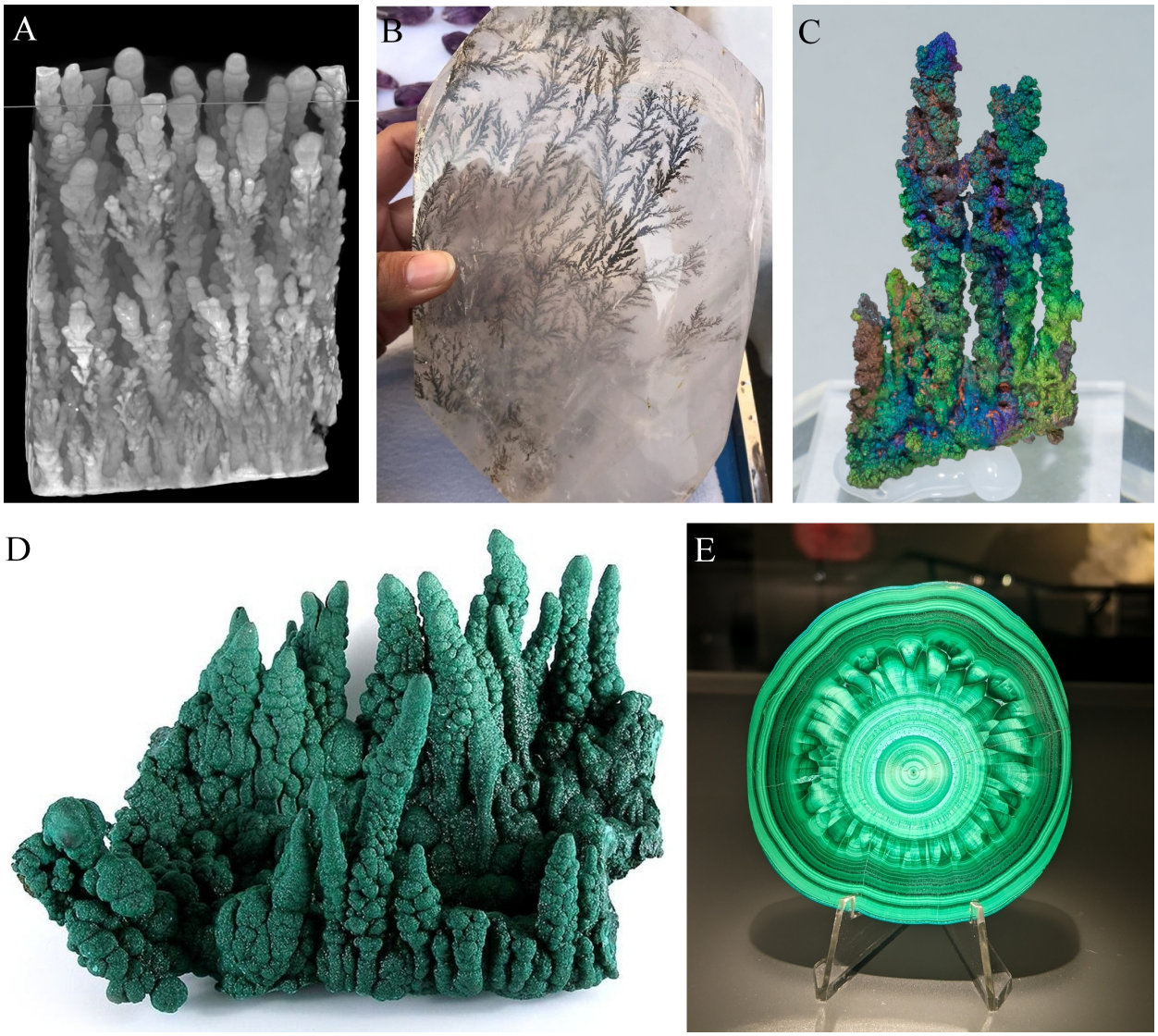


Figure 41: Upper row: Three dimensional manganese oxide dendrites in A: zeolites [261], B: quartz, and C: columnar goethite. Lower row: D: malachite, and E: a cross section of a malachite column. The image in (B) is taken from Yuping Crystal Wholesale, reproduced with permission. The specimen and photo in (C) is from MVM (Minerals Virtual Museum), reproduced with permission. The photo in (D) is by Robert M. Lavinsky, distributed under cc license. The photo in (E) is the property of Alfie Norville Gem & Mineral Museum of the University of Arizona, reproduced with permission.

usually needle-like, with a significant control of the crystalline anisotropy and with thermal effects playing a key role during their formation. In the petrological context, such dendritic crystals often form as a result of magma crystallization in rapidly cooled rocks [269, 270, 271]. Mineral dendrites, on the other hand, have a branched, fractal structure strikingly similar to diffusion-limited aggregation, DLA [162]; Sec. 4.4. This observation led Chopard et al. [272] to propose a model in which two species, A and B, diffuse, forming species C that then aggregates, although the geochemical details of this process and the nature of the particles remain unspecified. This model has been extended by Hou et al. [261]. In their model, fluid pushes an oxygenated matrix pore fluid away from the joints and mixes with it, generating an oversaturated manganese oxide solution. The resulting fern-like dendrites are made up a trunk, which grows very rapidly at the start of crystallization, followed by primary and secondary branches which grow in a more advanced state with slower growth rates. Laboratory studies on Mn oxide formation [273, 274] have confirmed that such conditions promote the initial growth of Mn-oxide nanoparticles. Such particles, once formed, diffuse through the rock matrix, and become attached to the Mn-oxide-coated joint, initiating dendrite growth. Dendrite formation would then be a non-classical crystallization pathway, via particle attachment, which is increasingly recognized as an important and widespread type of crystal growth [275, 276]. Hou et al. [261] emphasize that the shape of the dendrite will also be a function of its interfacial energy as well as the concentration of the manganese oxide particles around it.

García-Ruiz et al. [267] alternatively proposed that dendrites are a viscous fingering pattern (Sec. 4.2.7) created when manganese-rich fluid infiltrated a fracture space filled with presumably much more viscous, oxygenated fluid, possibly a colloidal suspension. In essence, this mechanism aligns with da Costa's 1757 conjecture [265]. However—and frustratingly—as they are in the same universality class [277], both models, DLA and viscous fingering, give rise to patterns of the same fractal dimension, around 1.70; thus geometric attributes of these patterns are insufficient for discerning the correct physical growth process. Other arguments invoked in this discussion are the lack of manganese outside the dendrites, which is easier to explain in terms of a viscous fingering model, unless one assumes that the DLA mechanism is highly effective in clearing the entire bedding plane of MnO particles formed in the space outside the dendrites [267]. On the other hand, viscous fingering cannot easily explain the formation of isolated dendrites, not connected to the main joint, as in Fig. 40D, or banding structures, like the ones in Fig. 40A. Additionally, one can raise a mass conservation issue. Manganese concentrations in dendrites are much higher than those in Mn-bearing groundwater solutions, thus a large volume of solution, significantly larger than the volume of the visible pattern, is needed to create a dendrite.

In contrast to the quasi-2D planar dendrites growing along bedding planes, internal dendrites are fully three-dimensional structures (Fig. 41), which start from fissures and penetrate into the porous rock [266, 278, 261]. Some of these dendrites are composed of manganese and iron oxides, just like their 2D counterparts, but there is also an interesting class of precious metal dendrites—of gold, silver and their alloy electrum—, which occur, in particular, in ultra-high-grade gold "bonanza" veins [279, 280, 30, 18] and are thus economically important. Two models of their formation have been proposed. The first is the particle attachment model, in which dendrites form by accretion of colloidal gold or silver particles [281, 282]. This is similar in spirit to the particle attachment growth model of the manganese oxide dendrites described above, with the only difference being that gold/silver particles are not produced locally, but are formed deep in the hydrothermal system and then carried up by the fluid to the epithermal setting. An alternative mechanism for the growth of gold dendrites, following a classical crystallization pathway based on ion addition, was proposed by Monecke et al. [18]. See also Sec. 5.1.3.

As is often the case in earth sciences, a similar appearance of the structure does not necessarily imply a similar genesis. The three-dimensional dendrites growing in a zeolite matrix, as shown in Fig. 41A, are similar in appearance to some of the free-standing stalagmite-like forms of minerals, such as goethite (Fig. 41C) or malachite (Fig. 41D), which form in rock cavities from slowly dripping solutions. This might suggest a growth mechanism similar to that of stalactites, as discussed in Section 5.2.1, although in the latter, CO_2 degassing is important, which does not have a clear parallel in malachite, goethite, and other columnar forms. Instead, they are most probably formed by an evaporative growth mechanism (Sec. 4.2.6) [283], although other mechanisms, involving reaction-diffusion self-organization (Sec. 4.1), have also been invoked [284]. It is worth noting that, in contrast to agates (Sec. 5.1.1), malachite can be formed in the



Figure 42: Nuggets. Left: Gold-quartz hydrothermal vein from Colorado, USA; Right: dendritic gold nugget, California, USA (images: James St. John; CC-BY-2.0).

laboratory by evaporative growth, with patterns virtually indistinguishable from natural ones [285, 286].

5.1.3. Nuggets

A nugget is a lump of precious metal, most commonly gold, found in geological settings; nuggets may also be composed of other metals such as copper, silver, and platinum. Gold is a rare element, so how does it become concentrated into gold nuggets that occur within quartz veins (Fig. 42, left) [287, 288]? During earthquakes, seismic pumping, driven by pressure variations in fault zones, drives the circulation of hydrothermal fluids, in which gold can be present under high-temperature, high-pressure conditions.

As faults experience repeated cycles of opening and closing during seismic and interseismic periods, cracks open and are gradually sealed via a fault-valve mechanism. During these processes, gold from the circulating fluids can precipitate and accumulate within faults. This mechanism leads to the episodic growth of gold veins or nuggets over time. Quartz-rich rocks within fault zones can generate electric charges due to piezoelectric effects, particularly during seismic deformation. These charges may influence the redox conditions in the fluid, potentially facilitating the reduction of dissolved gold to its elemental state, leading to the precipitation of gold particles [209].

Gold nanoparticles can aggregate to form larger structures in colloidal gold suspensions. This process can be enhanced by the presence of carbon-rich fluids, which can stabilize the colloidal particles and promote the formation of high-grade gold deposits. Diffusion-limited aggregation (Sec. 4.4) is one mechanism by which gold particles grow in size, resulting in the dendritic, branched structures observed in natural gold nuggets (Fig. 42, right).

5.1.4. Opals

Opal, Fig. 43, although considered a mineral for historical reasons by the Internation Mineralogical Association (IMA), is in fact a mineraloid due to its amorphous (or amorphous with paracrystalline components) nature. Even though opal is often referred to in general terms, there are four different types of opal [289, 290]: opal-A (amorphous), which is subdivided into opal-AN (amorphous network) and opal-AG (amorphous gel); opal-CT (cristobalite–tridymite); and opal-C (cristobalite).



Figure 43: Opal. Left: Cut and polished black opal from Lightning Ridge, Australia (image: Daniel Mekis; CC-BY-SA-3.0). Centre: Harlequin opal (image: Aisha Brown; CC-BY-SA-2.0). Right: Zoned opal from the Pliocene of Idaho, USA (image: James St. John; CC-BY-2.0).

Opal-C is a rare phase in nature [289], and thus it has been little studied. Opal-AN does not exhibit micro- or nano-structural order [290, 291]. Opal-CT, which, in addition to spherulitic morphologies, presents different forms of aggregation, can form as disoriented nanograins, fibrous nanograins, platy nanograins, and lepispheres (i.e., spheres composed of silica plates, with a morphology similar to desert roses) [290, 291]. In the following, we focus on opal-AG, because it is characteristically formed by the self-organized aggregation of silica nanospheres [290, 291]. Opal-A is often used as a synonym for opal-AG [290].

The formation of opals from colloidal silica involves the self-assembly of tiny silica spheres, formed by polymerization or condensation of silica monomers, into a highly ordered, three-dimensional structure; a form of colloidal (liquid) crystal. The process begins with the formation of colloidal silica particles in a supersaturated silica solution. These particles are typically in the nanometre size range and remain suspended in solution owing to their small size and the repulsive forces between them. Over time, these silica spheres begin to organize themselves into a regular, close-packed lattice structure driven by the minimization of free energy in the system. The formation of a densely packed colloidal crystal has not yet been fully elucidated; two main mechanisms have been proposed: the older and classical model is sedimentation due to gravity [292, 293, 290], while a more recent view holds that changes in solution conditions drive aggregation via electrostatic forces [294]. The spaces between the packed silica spheres are gradually filled with silica gel which helps stabilize the structure and cements the spheres together, leading to the formation of a rigid solid material [290].

Opal formation can take place over long geological time-scales or be accelerated under laboratory conditions. The specific conditions, such as temperature, pH, and solution composition, control the final size of the silica spheres and the quality of the opal produced [295, 296, 297, 298]. The periodic arrangement of the silica spheres within the opal causes diffraction of light, which is responsible for the characteristic play-of-colour observed in precious opals [290]; opals are natural photonic crystals.

5.1.5. Striped flint

Layered, banded, striped, or wave-like patterns are common in rocks and are related to the processes that form them. These patterns are common in sedimentary rocks, where layers form due to the gradual deposition of sediments over time. Each layer represents a different period of deposition, possibly reflecting changes in the environment, such as water flow, climate, or sediment sources.

Nevertheless, the genesis of many patterns remains elusive. One of the most intriguing examples is the highly anisotropic, interference-like pattern of striped flint (Fig. 44), which resembles neither sedimentary banding, nor target patterns (Sec. 5.2.9) or agate banded patterns (Sec. 5.1.1). Surprisingly, petrographic, crystallographic and chemical analyses show little difference between the bands except for differences in pore distribution, with fewer and smaller pores in the darker bands [299].



Figure 44: Striped flint. A,C,D: specimens from Świętokrzyskie Mountains, Poland. B: Striped flint nodule at the limestone wall at the prehistoric flint mine in Krzmeionki Opatowskie, Poland. Images (A) and (B) are by Piotr Szymczak. Images (C) and (D) are by Ewa Siemońska (Museum of Minerals and Fossils in Święta Katarzyna, Poland)



Figure 45: Zebra rock, from Kimberly, Western Australia (image: CC-BY Coward et al. Coward et al. [306]).

Striped or banded flint (Fig. 44) was first described in the 19th century [300, 301]. It is found in localities around the world, but the most well known is from Poland [302], where it occurs in Middle Oxfordian to Lower Kimmeridgian carbonate sediments at the north-eastern edge of the Świętokrzyskie Mountains. It belongs to a class of nodular cherts, occurring in nodules between few centimetres and 2 metres in diameter (Fig. 44B), commonly more or less flattened parallel to their horizontal axes and to the bedding of the host rock. The origin of silica forming nodular cherts (not only striped) is still under debate with some authors pointing to a hydrothermal origin [299], while others invoke a diagenetic alteration product of biogenic oozes [303]. The origin of nodular structures in cherts is also unknown, with "self-organization processes of enigmatic character" [304] invoked, and no theoretical framework predicts the sizes of the nodules and characteristic distances between them. As to the formation of the nodule body itself, most often coupled dissolution–precipitation processes are considered [303] with replacement of original limestone with silica on a volume-for-volume basis, analogous to petrified wood. Other theories assume that silica crystallized from a gel [305] or precipitated from solution [299].

5.1.6. Zebra rock

Before addressing zebra rocks and zebra textures (Sec. 5.1.7), it is necessary to mention that the term *zebra rocks* is often found used colloquially for any banded rocks. However, in this review we use the term *zebra* to refer to two specific structures: the zebra rocks of Australia, the subject of this section, and the zebra textures characteristic of carbonate rocks, Sec. 5.1.7.

Zebra rocks, characterized by their alternating bands of light and dark hues, Fig. 45, are found only in the Kimberly region of Western Australia [307, 308, 306]. Although these bands give the rock its name, other patterns, such as spots, pillars, or rods, can also be observed. Zebra rocks are composed of a fine-grained, clay-rich siltstone; the lighter bands are mainly quartz and clay minerals, whereas the darker bands are enriched in iron oxides (hematite) [309, 308]. What makes these rocks remarkable, apart from the fact that they appear in only one very specific place, is the degree of symmetry, regularity, and morphological pattern observed, which is unparalleled elsewhere [306].

Furthermore, the geological processes that led to the formation of these rocks remain uncertain, although several have been proposed since their first description in 1925 [310]. In this review, we will mention those that seem to have become obsolete and briefly describe the formation processes that have been worked on in recent years. However, all these hypotheses remain controversial.

The first hypothesis of the origin of these rocks was proposed by Larcombe [310, 307], who described how zebra rocks would have to have formed in deep, calm waters, far from land. Soon after, Trainer [311] suggested four possible origins for these zebra rocks: (1) original sedimentary banding followed by deformation, (2) crystallization of a fine grained flow rock, (3) infiltration of iron-bearing solutions into a white rock, and (4) leaching of hematite from a red rock. Currently, three main hypotheses are considered to explain the origin of these rocks: (1) hydrothermal alteration [308], (2) acid sulfate soil weathering [309], and (3) liquid crystals [35].

The first proposed process, i.e., formation by hydrothermal alteration, can be summarized in the following steps [308, 312]: first, Fe^{2+}-rich acidic hydrothermal fluids infiltrated into micaceous siltstones and shales. This fluid interacted with carbonate minerals, raising the pH and causing iron precipitation as Fe-oxyhydroxide at the reaction front. Continued diffusion of the Fe^{2+}-bearing fluid led to successive neutralization reactions, creating a rhythmic banding pattern. This hydrothermal fluid also altered other primary silicates in the bedrock, leading to the formation of secondary clay minerals. Over time, Fe-oxyhydroxides were converted to hematite as oxidation progressed.

The second proposed mechanism relates the origin of zebra rocks to the presence of Ediacaran palaeosols with iron oxides [309, 312]. These palaeosols were subsequently weathered by sulphate-bearing acid solutions, which leached iron from some of the soil horizons, changing their colour from red to white.

The third proposed process invokes liquid-crystal phases in the rock's mineral structure [35]. This theory stems from the observation that the banding patterns in zebra rocks resemble those seen in certain liquid-crystal materials, which exhibit regular, repeating structures when undergoing phase changes. In the case of zebra rocks, it is hypothesized that liquid-crystal behaviour could have occurred in the minerals present during the rock's diagenesis or early lithification stages. During these stages, mineral-rich fluids could have flowed through sedimentary siltstone, and under certain physical and chemical conditions, these minerals might have organized themselves into liquid-crystal phases. The theory posits that as the minerals cooled and solidified, they could have preserved these liquid-crystal patterns as alternating bands of dark (iron oxide-rich) and light (silica-rich) layers.

Most studies agree that the origin of these rocks is related to the presence of acidic solutions that altered the original host rock. The alternation of the bands, as well as the other patterns observed in these rocks, have been described as Liesegang patterns [313, 312, 306, 314]; however, they do not display the variable spacing characteristic of Liesegang bands (Sec. 4.1.5). The possibility that zebra rocks might be Turing patterns was explored by Coward in his doctoral thesis [312]. However, in his conclusions he indicates that he did not find Turing instabilities in the reactions studied. The mechanism thus remains an open question.

5.1.7. Zebra textures

Zebra textures (Fig. 46) are very common in carbonate rocks occurring in a variety of geological settings, such as Mississippi valley-type deposits and hydrothermal dolomite deposits [317, 318, 315]. In all these settings, the host rock is carbonate, while the mineralization producing the zebra texture may consist of carbonates (e.g., dolomite and magnesite) or non-carbonate minerals (e.g., sphalerite and fluorite). These textures are characterized by a rhythmic alternation of light and dark bands of similar thickness. Generally, the bands are millimetric and, although they can be parallel to stratification, they more commonly dip at a small angle [315]. These structures have been classified as examples of self-organized patterns [319, 320].

The origin of these textures has historically been attributed to three main mechanisms: dissolution [317, 318], fracturing [321, 322], and metasomatism-replacement-recrystallization [316, 323]. Other mechanisms have also been proposed on an ad hoc basis [324, 325, 320]. Recently, however, a unifying theory for their origin has been proposed that combines the three main mechanisms. This theory, proposed by Wallace and Hood [315], posits co-located processes: mineral replacement, and dissolution/void generation. These two processes together imply that in the hollows where new crystals are growing, crystallization can generate sufficient pressure to fracture the host. These fractures may then be dissolved and filled by new cement. The net result is the formation of the zebra banding.

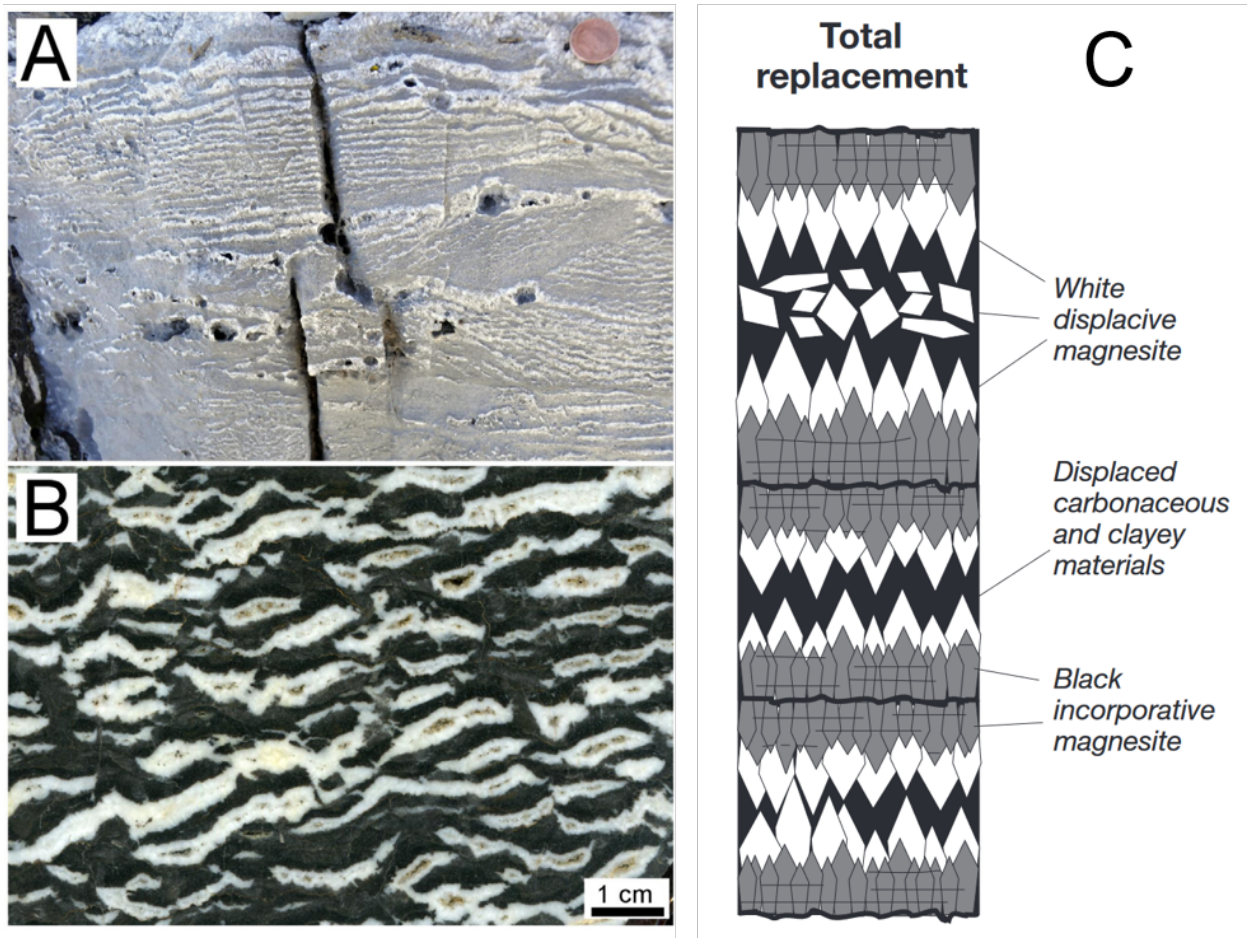


Figure 46: Zebra textures. A: Zebra dolomite outcrop and B: zebra dolomite hand-polished specimen (images: Wallace and Hood [315]). C: Schematic representation of the zebra texture in Eugui magnesites, Spain (image: Lugli et al. [316]).

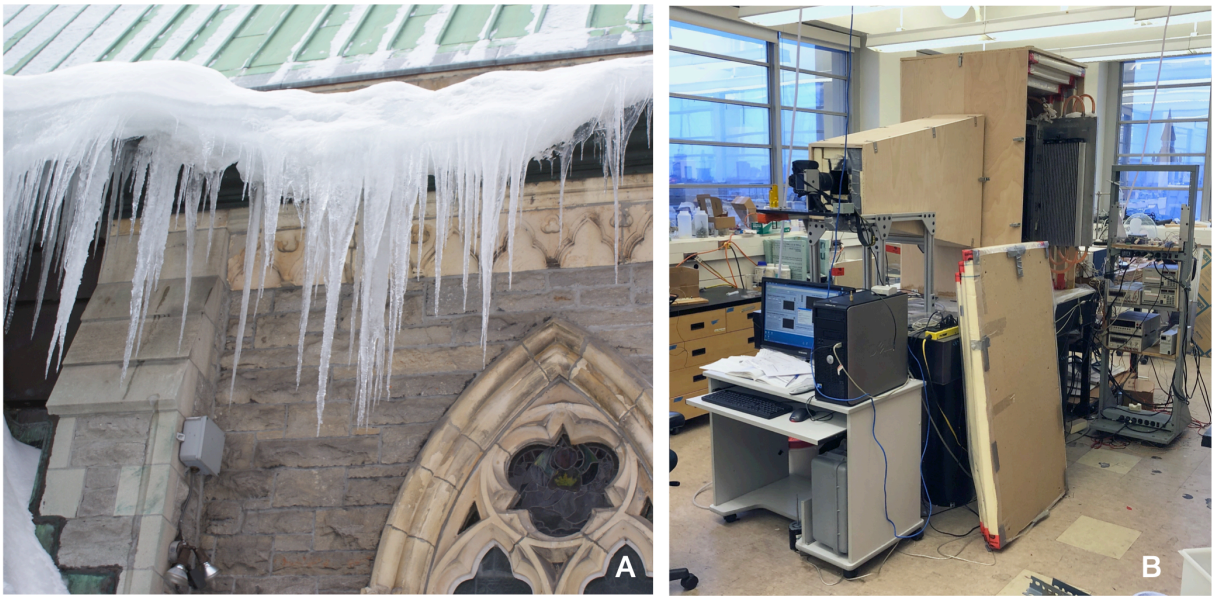


Figure 47: Natural and laboratory icicles. (A) Natural icicles hanging from a church roof in Montréal. Both conical and drapery-like formations can be seen. (B) The laboratory icicle growing machine, showing the insulated, temperature controlled, refrigerated box with one side opened, and its computer controlled digital camera and associated electronics. Temperature controlled feed water of known composition is introduced from the top of the box onto a slowly rotating support, while drip off water is collected below. The humidity of the air inside the box is measured and may be turbulently stirred. Using edge detection of images taken with slow rotation, the entire 3D shape of the icicle can be measured as a function of growth time [326, 327, 328, 329, 330, 331]. Data from these experiments are published in the *Icicle Atlas* [332].

5.2. Large and cold

Near-surface processes with modest energy inputs nonetheless organize matter on centimetre to metre scales. Latent-heat release and fluid flow sculpts icicles and stalactites, salt-crust convection draws hexagons across dry lakes, and impact-like target patterns punctuate evaporitic flats. Shrinkage and weathering generate polygonal mud cracks, honeycomb tafoni, desert-rose efflorescences and vertical solution pipes or wormholes, all spaced tens of centimetres or more despite their low-temperature setting.

5.2.1. Icicles, stalactites, and stalagmites

An *icicle* is the familiar elongated structure of ordinary ice that forms when water drips into freezing air from a point of support. Since ice formation requires the removal of latent heat, we can infer that heat transfer is most efficient at the fast growing tip and slower on the sides [336]. The shape forms a substrate for the subsequent flow of water, some of which freezes while some drips off; the dripping water assists the heat transfer, causing faster growth at the tip. Examples of natural icicles are shown in Fig. 47A. Very similar fluid-mechanical transport is presumably involved in the formation of *stalactites*, which are calcium carbonate deposits that hang from roofs of caves. Here, the solid $CaCO_3$ is deposited when CO_2 comes out of solution [337, 338, 339], but the water is not consumed. Both icicles and stalactites usually have a single dripping tip, but may sometimes develop multiple branches [326]. Other common morphologies are also observed, such as sheet-like *drapery* formations in which the water flows only along a leading edge, or *flow stone*, in which water flows over a broad surface [340].

The suffix *-icle* has also been applied to other elongated structures, such as *snoticles* (also known as *snottites*), *brinicles* and *rusticles*. Snoticles [341] are drips of mucus-like microbial mats that hang from cave roofs, resembling small stalactites. Brinicles [190] are ice structures that form on the underside of sea ice

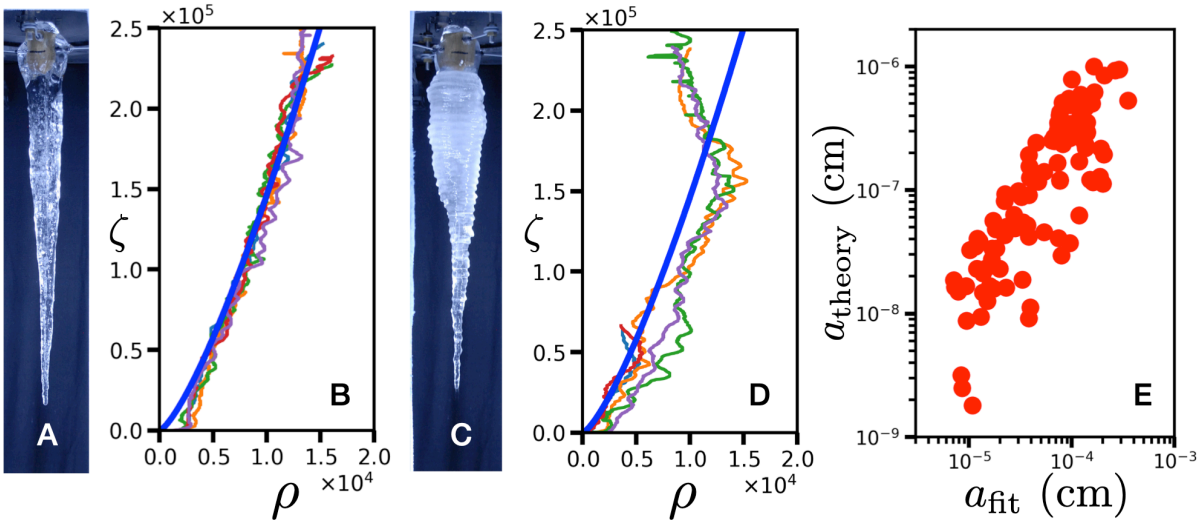


Figure 48: Universal icicle shape. (A) and (C) show the final states of two icicles grown from different water sources under otherwise identical conditions, using the apparatus shown in Fig. 47(B): (A) was made with distilled water [333]; (C) was made with Toronto tap water [334]. The temperature of the stirred air was −6.8 °C, the input mass flux of water was 2.6 g/min, and the input water temperature was 3.2 °C. These results show clearly that even very small concentrations of impurities have a profound effect on icicle shapes [326]. Using 76 icicles grown under a variety of conditions and water sources, edge detected shapes were fit to Eq. 7, using the dimensionless variables given in Eqn. 6, with $a = a_{\rm fit}$ as a fitting parameter. (B) Shows the best five fits, while (D) shows the worst five fits, as measured by reduced χ^2. (E) shows a comparison of $a_{\rm theory}$ to $a_{\rm fit}$ for a series of 106 icicles, grown using controlled concentrations of NaCl as an impurity [328].

when plumes of dense, supercooled brine descends from channels in the ice, causing the surrounding sea water to freeze into an elongated pipe. Rusticles [342] are long, iron-oxide rich structures that form on shipwrecks. In all cases, gravity- or buoyancy-driven fluid flows interact with the evolving shape, producing long, downward-pointing structures. Submerged, elongated pipe-like structures are also formed by chemical gardens [189]; these are generally upward pointing, with positive rather than negative buoyancy.

Unlike stalactites and most other geological formations, icicles are unusually amenable to laboratory growth studies. Fig. 47B shows an apparatus for growing icicles under controlled conditions in the laboratory. Detailed experiments on icicles [326, 327, 330, 329, 343] have revealed a wealth of subtle phenomena. Analogous laboratory experiments on stalactites are somewhat impractical owing to the longer time-scale.

Both icicles [344] and stalactites [337, 338] have been theoretically predicted to have universal shapes, independent of growing conditions. According to the "platonic" icicle theory, assuming axis-symmetry, the radius R and distance from the tip z may be scaled by a common length a, so that if the shape is expressed in dimensionless coordinates,

$$\rho = R/a \ , \quad \zeta = z/a, \tag{6}$$

then the predicted universal icicle shape is given by

$$\rho(\zeta) = \frac{4}{3}\left(\zeta^{\frac{1}{2}} + 2\right)\sqrt{\zeta^{\frac{1}{2}} - 1} \quad \sim \zeta^{3/4} \ \text{ for small } \ a. \tag{7}$$

The shape is universal because all the physical parameters are absorbed into a, which is given by

$$a = a_{\rm theory} = \frac{g\beta_A(\Delta T_A)^5}{\nu_A^2}\left(\frac{\Lambda_A}{L_f\rho_I C v_t}\right)^4, \tag{8}$$

where g is the acceleration due to gravity, β_A is the volumetric thermal expansion coefficient of air, ν_A is the kinematic viscosity of air, ΔT_A is the difference between the surface temperature and the ambient

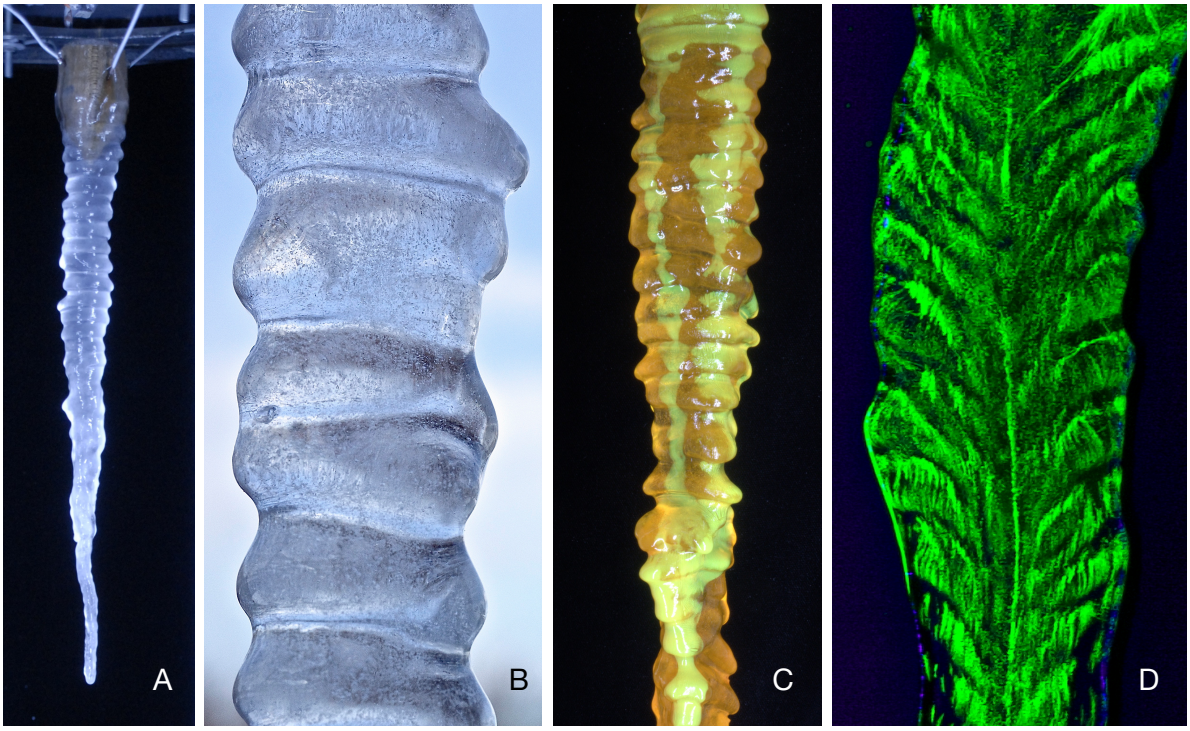


Figure 49: Rippled icicles: (A) laboratory grown icicle [335], made from distilled water with 320 ppm NaCl as an impurity. (B) close up of the ripples on a natural icicle. In all cases, the ripple wave-length is close to 1 cm (image: S. W. Morris). (C) a lab-grown icicle with 519 ppm sodium fluorescein dye as the impurity. The dye glows green in the liquid phase, but appears orange when trapped in inclusions in the ice. The partial wetting of the surface is evident (Image: CC-BY Ladan and Morris [330]). (D) a vertical section of a lab-grown icicle near 0°C with 171 ppm sodium fluorescein. Here, the dye in the inclusions glows green. The chevron pattern of the inclusions tracks the slow upward motion of the ripples during growth. The chevrons have a substructure of crescents [329].

temperature, Λ_A is the thermal conductivity of air, L_f is the latent heat of fusion of water and ρ_I is the density of ice. C is a dimensionless constant of order unity and v_t is the speed of the growing tip. The theory relies on a number of simplifying assumptions, in addition to axis-symmetry. The growth rate of ice is assumed to be limited by the heat transfer across the rising thermal boundary layer that surrounds the icicle. The boundary layer is assumed to be laminar. The advection of heat by the film of flowing water on the sides of the icicle is neglected. Pure water is assumed.

The universal theory of icicle shapes has been thoroughly tested experimentally [326, 328, 343]. Results of one such study [326, 328] are summarized in Fig. 48. It is found that the most important parameter affecting icicle morphology is the purity of the feed water. Even the very low level of impurity in ordinary tap water is enough to produce drastically non-universal shapes, as in Fig. 48C,D; on the other hand, icicles grown from nominally distilled water can be close to the universal shape, as in Fig. 48A,B. The agreement with the universal shape seen in Fig. 48B is impressive considering that only one fit parameter, $a_{\rm fit}$ was used, and the slope of the fit line is independent of the parameter. However, icicles grown from ultra-pure Milli-Q water [343] have a "dripping candle" shape which is poorly described by the universal shape. Thus, universal "platonic" icicles are only observed for nearly pure, but not ultra-pure, water. These very low levels of impurity are ignored by the theory, but will of course be present in any natural icicle. Several other assumptions of the universal shape theory are also violated; the air motion was turbulent, rather than laminar, for example. Furthermore, the physical interpretation of $a_{\rm theory}$ is obscure, given its very small typical value of $\sim 10^{-7}$ cm, taking $C = 1$ in Eq. 8. But the values of the fit parameter $a_{\rm fit}$ are also very

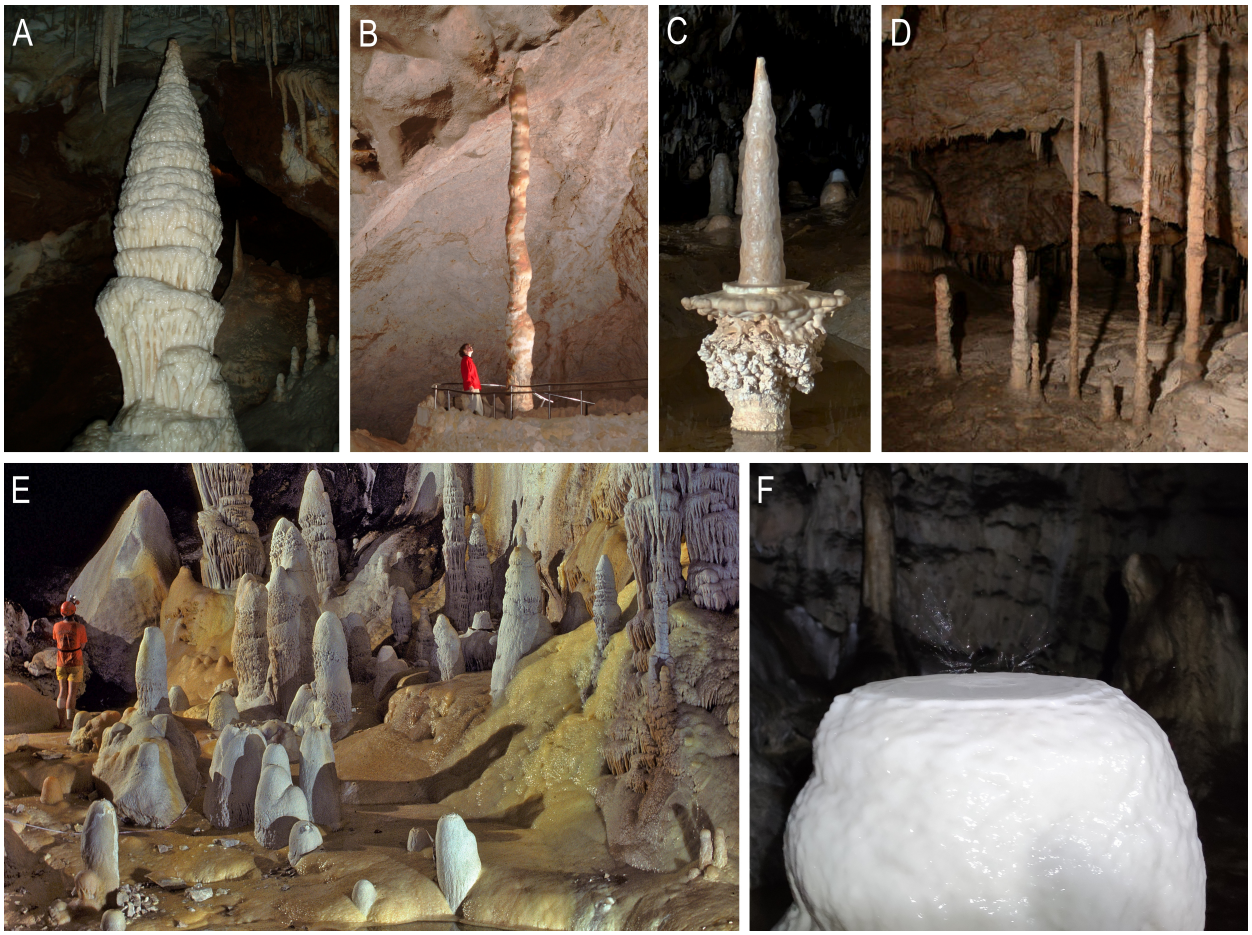


Figure 50: (A) "Minaret" stalagmite in the Jenolan Caves, NSW, Australia; (B) "Witch's Finger" columnar stalagmite in Carlsbad Caverns, USA; (C) "Candlestick", conical stalagmite in Sloupsko-šošůvské caves, Czechia; (D) long columnar stalagmites in Katarynske caves, Czechia; (E) columnar stalagmites in Lechuguilla Cave, New Mexico, USA (F) flat-top stalagmites in Postojna Cave, Slovenia; Photo credits: A: Bellman (public domain), B: Peter Jones, National Park Service, USA (public domain) C: Piotr Szymczak, D: Jochen Duckeck (public domain), E: Dave Bunnell/Under Earth Images (CC BY-SA 2.5), F: Matej Lipar (reproduced with permission)

small, and do appear to be positively correlated with the expected values of a_{theory}, as shown in Fig. 48E. The magnitude discrepancy between a_{fit} and a_{theory} can be removed by taking $C = 0.2$ in Eq. 8. Thus, we may say that the universal shape theory is, at best, a qualified success.

In addition to their overall pointy shape, icicles and stalactites may also exhibit ripple patterns about their circumference. These ripples have a near-universal wave-length of about 1 cm, independent of the growing conditions [345, 346, 339, 327]. Examples of rippled icicles are shown in Fig. 49. Ripples are another manifestation of impurities present in the feed water [327, 328]. The effect of impurities on the wetting properties of the ice turns out to be crucial [330, 331]. It is counterintuitive, but ultra-pure water does not wet ultra-pure ice very well [347]. On an ultra-pure icicle [343], water does not coat the whole icicle but rather descends in discrete sliding drops that hardly wet the ice at all. Even extremely low levels of impurity suffice to increase the wetting of the ice surface and change the overall morphology of the resulting icicle [326, 327, 330]. At moderate, but still very low, levels of impurity, ripples emerge on the surface during growth [327], which are presumed to be due to a morphological instability. Even natural icicles which form from atmospheric precipitation are often impure enough to be in this regime, as in Fig. 49B. Ripples are observed to travel upward slowly during growth. As the impurity concentration is increased, ripples grow



Figure 51: Icicles, hanging from the ceiling, and their rare cousins, the ice version of stalagmites, on the floor, in a lava tube cave in Iceland. The columnar jointing of the lava (Sec. 5.4.1) may also be appreciated (image: Julyan Cartwright).

faster and to larger amplitude and eventually become disordered, but their wave-length always remains very close to 1 cm.

When a fluorescent dye is used as the impurity, it becomes possible to visualize the surface flow over the icicle [330] and the fate of impurities trapped in the ice [329]. The most well-formed ripples are found in an impurity concentration regime in which the ice is only partially wetted by the liquid phase, which descends in branching rivulets; see Fig. 49C. At high concentrations [330, 343], liquid coverage becomes complete and the ripples are very disordered. A substantial fraction of the impurity concentration ends up trapped in small liquid inclusions inside the ice; these inclusions are roughly spherical and 100 μm in size. They form clusters that make a distinct pattern of chevrons following the peaks of the ripples [329]. Each chevron has a substructure of crescents, which are discrete layers rich in inclusions. These crescents are just visible in Fig. 49D. At high concentrations, the ice becomes completely spongy with liquid inclusions.

At present, none of these phenomena are quantitatively described by linear stability theories for the onset of icicle ripples [345, 346, 348]. These theories assume complete wetting and do not treat the role of impurities at all. When generalized to include impurities [330, 331], they fail to predict the wave-length of the ripples. The rippling instability thus depends on the impurity dependence of the non-equilibrium partial wetting of the ice, a process that is very poorly understood [349, 347]. The process by which impurities are trapped to become inclusions is also not understood. A linear stability theory of ripples on stalactites has been proposed [339], which uses an analogous assumption of complete wetting, but much less is known about stalactite growth dynamics. Sectioned stalactites do not exhibit anything analogous to the pattern of inclusions in icicles. It would be interesting to examine the path of water descending an actively growing stalactite using a dye tracer to probe the role of wetting in that case. While icicles and stalactites are superficially similar, they differ in many important details.

A somewhat more complex but analogous argument for the universal shape of stalactites leads to the same universal scaling as for icicles $\rho(\zeta) \sim \zeta^{3/4}$ for large a. For stalactites, the ideal outer shape turns out to share the same scaling as icicles, $\rho(\zeta) \sim \zeta^{3/4}$ for $\zeta \gg a$, but it follows from different physics [337, 338]. In icicles, growth is constrained by removal of latent heat through an air-side thermal boundary layer; in stalactites, growth is controlled within the gravity-driven water film, where the carbonate deposition rate is limited by the net conversion of carbonic acid to aqueous CO_2. Consequently, the prefactor differs: icicles depend on ventilation and air properties (via heat transfer), whereas stalactites depend on drip rate, water pCO_2, temperature, and film rheology. In both cases the invariant (shape-preserving) outer solution erases tip details, while the amplitude retains sensitivity to the ambient environment.

Stalagmites, their floor-growing counterparts, do not mirror stalactites. Stalactites are typically slender and elongated (i.e., like icicles), whereas stalagmites are generally bulkier (Fig. 50). This morphological asymmetry indicates different controlling mechanisms. Stalagmite growth is well described by surface-reaction–limited precipitation in a thin film that has largely equilibrated by the time droplets strike the tip [350, 351, 352]. Under form-preserving upward translation, the analytic "ideal stalagmite" solutions form a one-parameter family indexed by the Damköhler number $\mathrm{Da} = k\pi R^2/Q$, where k is a precipitation rate constant, R is the radius of the stalagmite, and Q the volumetric drip flux. Three end-member morphologies arise and are observed in caves: flat-top ($\mathrm{Da} > 1$), columnar ($\mathrm{Da} = 1$), and conical ($\mathrm{Da} < 1$). Selection reflects droplet delivery near the apex: when the fall height is large, impact and splash spread wetting over a finite radius R_c, producing a flat cap that joins smoothly to the outer profile (flat-tops). When the wetted radius is negligible ($R_c \ll R$), the columnar limit is selected. Conical stalagmites have pointed tips; their innermost region is well fit by an inverted-stalactite profile, but farther out the shape steepens as surface-reaction control dominates. Field photographs and CT sections show that these analytic profiles fit natural examples using radii alone as free parameters. Ice stalagmites, Fig. 51, do not seem to have been studied.

5.2.2. Solution pipes, wormholes, and replacement fingers

Solution pipes, Fig. 52, are vertical, finger-like structures found in the epikarst zone of porous calcareous rocks. They vary in size from a few centimetres to a few metres in diameter, but are generally less than 1 m in diameter with variable length, the deepest reaching 100 m. They also vary in shape; some are more conical, tapering slowly towards the tip, whereas others have almost constant cross-section and a cigar-shaped termination. Their cross-sections are almost perfectly circular and very smooth (Fig. 52E-H), such

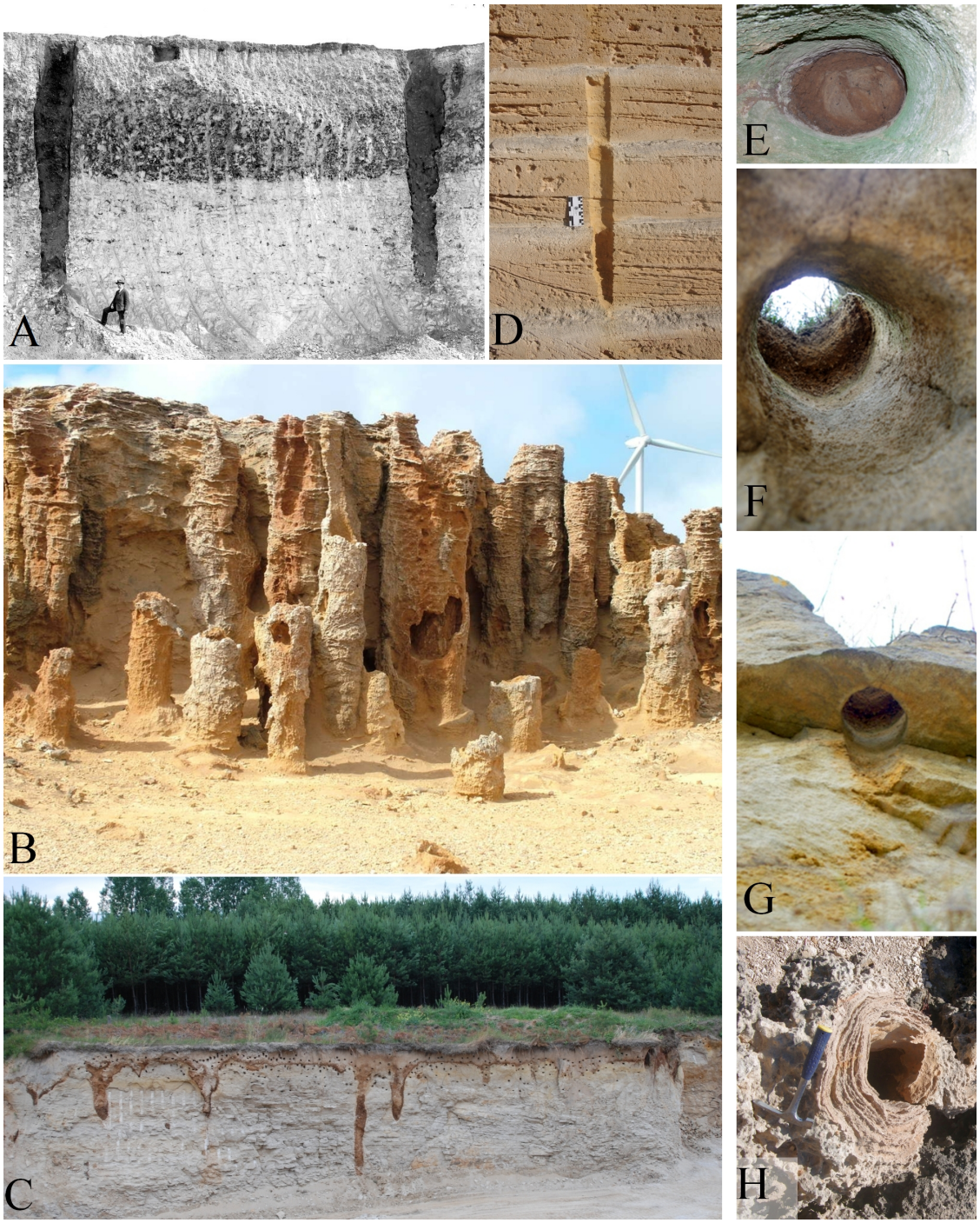


Figure 52: Solution pipes. A: pipes in Cretaceous chalk (Swanscombe, UK) photo by J. Rhodes (courtesy of British Geological Survey), B: pipes in Quaternary calcarenite (Cape Bridgewater, Australia), C,E–G: pipes in Miocene calcarenite, (Smerdyna quarry, Poland); D: pipes in Neogene calcarenite (Guilderton quarry, Australia); H: pipe in Pleistocene calcarenite at Cape Perron, Perth, Australia. Photos B and D–H, Piotr Szymczak. Photo C is courtesy of Dr. Łukasz U˙zarowicz, Warsaw University of Life Sciences - SGGW, Poland.

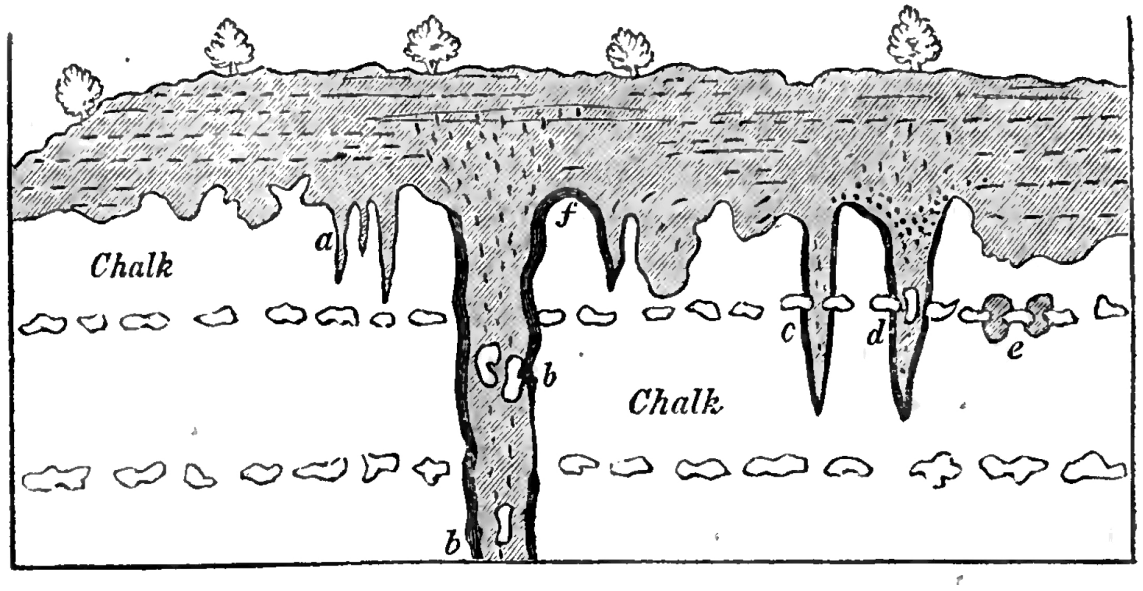


Figure 53: Solution pipes in chalk at Eaton near Norwich, UK, as sketched by Lyell [353].

that one may have the impression that they were artificially drilled rather than formed by natural processes.

One of the first to describe in detail the morphology of solution pipes was Charles Lyell, the father of modern geology. His 1839 paper *On the tubular cavities filled with gravel and sand called sand-pipes in the chalk near Norwich* [353] remains to this day a great example of deductive reasoning based on observations from nature. Lyell describes a group of solution pipes in chalk strata (Fig. 53), and observes that they are elongated with lengths up to 20 m and round in cross-section. He also comments that they do not merge, tend to stay separated from one another, and that they are not guided by the fractures. When the smaller pipes cross the horizontal layers of flint nodules (c & d in Fig. 53), the nodules tend to stay in place, sticking out of the pipe, whereas in larger pipes (b in Fig. 53) the nodules are found somewhat lower than their original position. All of that leads him to the hypothesis that the pipes are solutional in origin, that the chalk has been removed by the corroding action of water charged with acid, in which the flint nodules, being insoluble, were left in situ in the smaller pipes after the calcareous matrix had been dissolved. He also concludes from the manner in which the large detached flints were dispersed through the contents of the widest pipes that the excavation and filling of the pipe were gradual and contemporaneous processes. He further comments that the fact that piping always proceeds under the cover of sand or gravel and never on the exposed rock may be related to the fact that these upper layers provide space for the water to focus.

Not all researchers agreed with Lyell. In particular, Trimmer [355] expressed the opinion that pipes originate from the mechanical action of water, similar to potholes near waterfalls. However, as argued by Prestwich [356], this would imply that they were empty during their formation, and thus all the insoluble material, like the flint nodules in Fig. 53, should be found at their base, which is not the case. Additionally, the pipes do not seem to contain grinding materials required for pothole erosion (e.g., resistant pebbles), Furthermore, some of the pipes have a huge aspect ratio (even 100:1), much larger than any known potholes, making it hard to imagine the vertices of such an elongation actively carving pipes.

The pipes in tropical and Mediterranean climates differ from those in temperate regions, as they feature hard rims cemented with calcite (Fig. 52B). In some areas, the eroded matrix around the pipes reveals a reversed landscape, resembling a forest of vertical pipes standing closely together. The resemblance of these pipes to tree trunks has historically led to their misidentification as petrified trees [357, 358]. This model suggested that decaying tree trunks, rapidly buried by aeolian sand, could form conduits for groundwater, leading to the precipitation of calcrete and forming a solid cast around the original trunk.

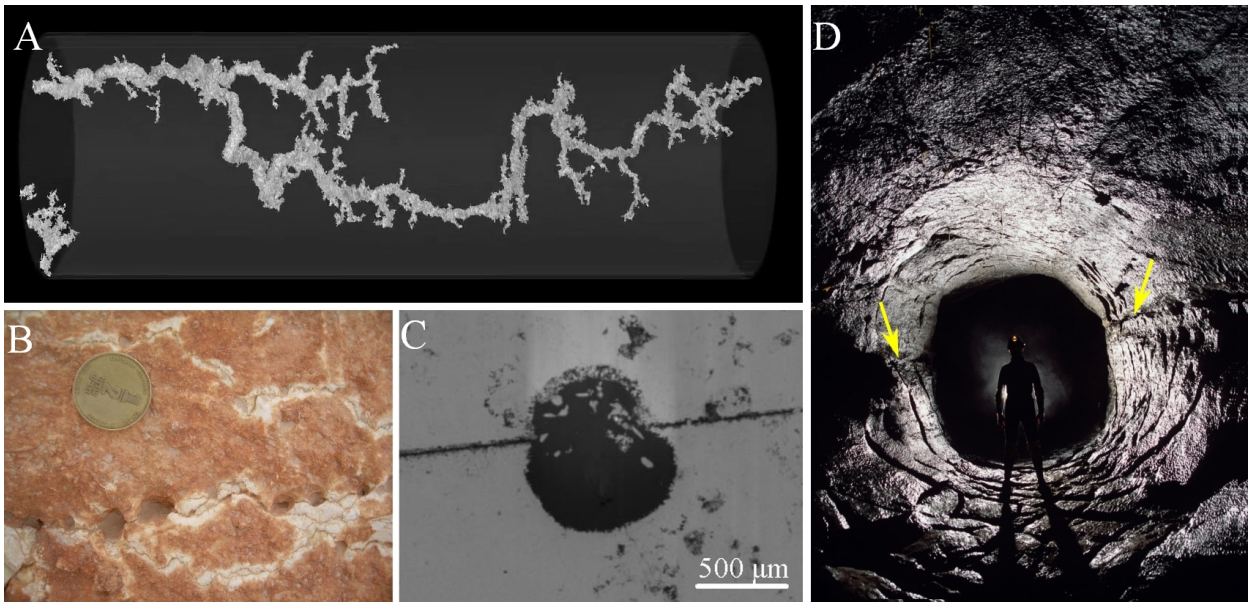


Figure 54: Wormhole formation in porous rocks and fractures. A: tomographic image of a wormhole etched by carbonic acid in limestone core [354]. B: A dissolutionally enlarged stylolite with several wormholes in a limestone wall of Mitzpe Ramon quarry, Israel. C: Wormhole at the outlet of a fractured limestone core. D: A conduit in a phreatic cave in Dan yr Ogof, Swansea Valley, South Wales. The white arrows mark the initial fissure. Panel B courtesy of Pawel Kondratiuk, University of Warsaw. Panel C courtesy of Maria Garcia Rios and Linda Luquot, Technical University of Catalonia. Panel D courtesy of Brendan Marris, Dudley Caving Club.

However, this hypothesis was challenged by several researchers [359, 360], who noted that the close spacing of the pipes, less than 0.5 m in some places, is too dense for a forest, the bases of the pipes are rounded hemispheres without paleosol horizons or branching root structures [360], and some pipes reach depths up to 20 m and are unbranched vertical cylinders, which would imply rather peculiar, column-like trees. Despite these objections, interpretive signs erected at Cape Bridgewater (Fig. 52B) in the early 2000s still described this as a petrified forest [360].

Nevertheless, it seems that the only hypothesis that has withstood scrutiny posits that the rimmed pipes in tropical climates are solutional in origin [361, 362, 363, 155], i.e., their genesis is similar to that postulated by Lyell for the chalk pipes in England, with the only difference being the rim cementation triggered by high evaporation rates in tropical climates. Formation of the pipes would then linked with the reactive–infiltration instability (Sec. 4.2.7): small inhomogeneities in the porous matrix tend to focus the flow, which is followed by enhanced dissolution, which eventually transforms initial inhomogeneities into a mature pipe.

A question remains regarding the sources of the large quantities of water that carved the pipes. While most researchers suggest that it is CO_2-charged rainwater acting over millennia, an alternative hypothesis exists for pipes formed in colder areas, which links their formation with deglaciation. Morawiecka and Walsh [364], Walsh and Morawiecka-Zacharz [365] and Dobrowolski and Mroczek [366] studied pipes in Miocene calcarenite in Poland that could have formed subglacially under the cover of a continental glacier till. Piping there is restricted to areas beneath a till cover, and pipes did not develop where till is absent. This links the formation of the pipes to the deglaciation at the end of the Elsterian period, when large volumes of cold water were suddenly released into the fully saturated subglacial aquifer. In such conditions karstification becomes very intense [367]. See also the tubular concretions of authigenic carbonates that can preserve the subsurface plumbing network of methane seep systems; Sec. 5.4.3.

An interesting issue related to the formation of solution pipes, and more broadly, to the formation of self-organized structures in geological systems, is whether every structure necessarily needs a precursor. A geologist would naturally lean towards an affirmative answer to this question: since something is here

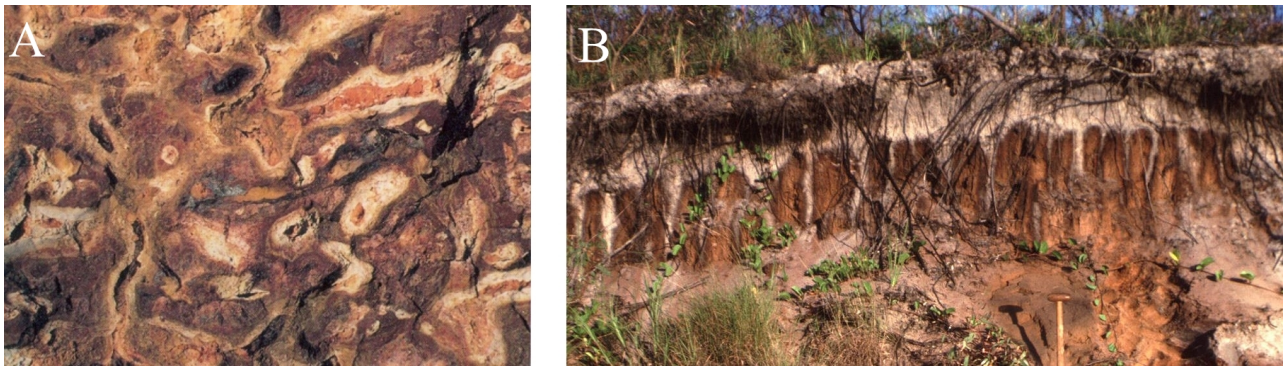


Figure 55: A: close-up view, which spans about 1 dm vertically, of typical laterite showing tubular structures surrounded by various iron oxides. Image from Werner Schellmann [41]. B: Podzol tongues, K'gari Island, Australia. Photograph by Ken G. Grimes, reproduced with permission.

now, there must have been a cause for it to form here, rather than elsewhere. Physics, on the other hand, points to positive feedback mechanisms underlying the onset of instabilities, which can produce ordered structures from any small disturbance. In the case of solution pipes, this discussion has been ongoing for several decades. Many studies suggested that pre-existing heterogeneities in rock or soil have caused the flow to focus in a particular spot. The factors invoked included animal burrows [368, 369], surface hollows, potholes or cracks [370, 361, 360, 371, 362, 363], stemflow and rootflow [359, 372, 373, 363]. On the other hand, numerical models [374, 375, 155] suggest that dissolution patterns are largely insensitive to the initial conditions in the rock matrix. Inhomogeneities do impact the time-scale and length-scale over which the channels are first observed [153, 376, 377, 378, 379], however in a large enough system naturally growing instability eventually overwhelms any local perturbation [374].

Recent experiments and theory show that solution fingers and pipes can evolve into form-preserving bodies that simply translate without changing shape: after a brief transient near the tip, the entire body profile becomes time-invariant and advances at nearly constant speed [144]. In competitions, the winner maintains invariance while the loser fattens and stalls, which helps to understand why a dominant pipe maintains a uniform circular bore and why mergers are uncommon. Invariance thus acts as a shape attractor in reactive infiltration: once the invariant regime is reached, geometry is fixed by a small set of controls (flow and transport properties), and the tip merely translates. A practical corollary is that the far-field side slope of the invariant body is set by those controls, so measuring it, together with radius, provides a direct route to infer discharge [144]. In this way, pipe outlines serve as paleo-flow gauges without requiring system-specific chemistry.

Another manifestation of reactive-infiltration instability are wormholes, which dissolution fingers create when a pressurized reactive solution is pushed through porous or fractured rock. The distinction between solution pipes and wormholes is somewhat arbitrary, but in general the term solution pipes is used for gravity-driven dissolution fingers formed in the vadose zone near the surface and extending downwards whereas wormholes appear in fully saturated flow driven by external pressure gradients.

Wormholes are relatively easy to obtain in experiments (Fig. 54A), and they have been used for at least 100 years by petroleum engineers to enhance oil and gas production by increasing the permeability of the rock. The shapes of the wormholes formed during acidization depend strongly on the flow rate, with more conical, smoother wormholes forming at lower flow rates, and highly ramified, tortuous wormholes appearing at high flow rates. Long, thin (dominant) wormholes, formed at intermediate flow rates, are the most effective for petroleum engineering, since they minimize the acid required for a given increase in permeability. Estimates of wormhole growth rates and, in particular, the so-called breakthrough time, the moment when the longest wormhole reaches the outlet of the system, are crucial for a number of geotechnical problems. These include risk assessment of potential leakage of sequestered carbon dioxide, safety of dam

sites in soluble rocks, risk of catastrophic ground subsidence due to solutional widening of fractures, and the danger of water seepage into toxic waste repositories.

Instabilities in fracture dissolution were first discovered by numerical simulations [153] and later confirmed by experiments [380, 381]. Linear stability analysis shows that fractures are even more unstable to dissolution than porous media [154], where a minimum wave-length is needed for unstable growth [148]. However, fracture dissolution is almost always unstable [150, 382], and intense wormholing is to be expected (Sec. 4.2). The onset of a reactive-infiltration instability has been observed in a microfluidic fracture system, with good agreement with theoretical predictions of the wave-length of the initial instability [383].

Wormholing is the driving force behind cave formation in karst systems [154, 153, 384], and cave conduits are beautiful manifestations of nonuniform dissolution. Caves are initiated along fractures and bedding planes, which have a quasi two-dimensional structure, while the mature cave is almost always a system of pipe-like conduits (Fig. 54D). Wormholes are formed across a range of length-scales. Fig. 54B shows cm-size wormholes growing along a stylolite in a limestone block, while Fig. 54C shows a mm-scale wormhole emerging in fracture dissolution experiments.

Wormholes provide a way in which aggressive solutions can penetrate deeply into limestone formations. A simple estimate of the penetration length in uniform fractures gives $l_p < 1$ m, meaning limestone caves should not exist at all [255]. One possible resolution of this paradox is the sharp drop in the dissolution rate of $CaCO_3$ near saturation [386]. However, wormhole formation offers a simpler explanation [154]; flow in the spontaneously formed conduits (Fig. 54) is several orders of magnitude larger than the initially uniform flow across the fracture width, and the penetration length increases accordingly. Numerical simulations [382] show that highly unsaturated solutions can penetrate deeply into wormholes etched in fracture surfaces.

We should mention here that similar processes acting at the surface produce further patterns. Karren, or lapies, are small- to medium-scale, intricate surface features in karst landscapes, formed by the dissolution of soluble bedrock like limestone, dolomite, or gypsum by acidic water. These miniature, sculpted landforms—including grooves, ridges, pits, and channels—often appear on exposed rock surfaces forming landscapes known as karrenfields or limestone pavements [387]. There is physical modelling work on Rillenkarren, parallel grooves typically formed on steep slopes [388, 389].

Another instance of tubular void formation is in laterites [390]. Laterites are soils that are geological soft matter, like a clay in their physical properties of being soft but cohesive. They are often used as building material in the subtropical regions in which they abound. As Fig. 55A shows, they are often seen to contain tubular voids, attributed to "interstitial, chemically active pore liquids or gases contained within the rock body, or introduced from external sources" [391]. The iron chemistry involved may be related to that of laboratory chemical gardens and the physics to osmotic processes (Sec. 4.3) [41].

While solution pipes and wormholes are associated with the dissolution of rock, replacement fingers are connected with dissolution–precipitation processes, where the primary mineral is replaced by a secondary one [392, 393, 394]. Examples include dolomitization (Fig. 56A), which involves the replacement of limestone (calcium carbonate) with dolomite (calcium magnesium carbonate). Since the molar volume of dolomite is less than that of calcite, the primary mineral in limestone, dolomitization can create additional pore space if the process is not accompanied by significant compaction or cementation. The higher permeability of the dolomite then triggers instability, which can lead to the formation of dolomite fingers [395, 396, 397]. Another example is the formation of uranium rolls (Fig. 56B), in which uraninite precipitates at the redox front that separates oxidized rock from reduced rock. The oxidized rock is more porous than the reduced one because the redox reactions produce sulfuric acid that dissolves potassium feldspars. Increased porosity again results in instability leading to the formation of characteristic fingers with a thin band [398]. Finally, Figs. 56C & D show the terra-rossa fingers above limestone. An intriguing hypothesis on their genesis has been put forward by [399]. They proposed that terra-rossa is formed by authigenic replacement of the underlying limestone at a reaction front. The hydrogen ions produced in such a reaction further dissolve the rock matrix, triggering a reactive-infiltration instability which should result in intense piping [394].

Another manifestation of reactive-infiltration instability are *podzol tongues* in sandy soils (Fig. 55B) - downward-extending fingers of bleached eluvial horizon material that penetrate into the underlying illuvial horizon, giving an irregular, wavy boundary that may reach deep into the subsoil [400, 401].

Podzol tongues are a product of the podzolization process, which involves intense leaching of upper



Figure 56: Replacement fingers. From top left to bottom right: A dolomite finger (marked with white dashed line) in limestone outcrop [385]; Uranium roll with uraninite precipitation around its tip. Photograph by C. L. Van Alstine (U. S. Atomic Energy Commission), courtesy of Dr. Robert Gregory (Wyoming State Geological Survey); Terra Rossa fingers over limestone at Greatstone Winery near Coonawarra, South Australia. The photo is courtesy of Les Sampson (Claremont Wines, South Australia); Closeup of one of the pipes, showing the terra rossa layer (dark red) and more recent siliceous sands overlying it. Photograph by Piotr Szymczak.

horizons by organic acids, leading to translocation of dissolved organic matter, iron, and aluminum downward in the soil [400]. In a typical Podzol, the surface organic layer and topsoil produce acidic compounds that percolate into the mineral soil. These acids chelate Fe and Al from the sand and silt particles, removing pigments and clay from the upper layer [402]. The result is a bleached, ash-gray albic horizon from which metals and clays have been eluviated. As the leachate moves downward, it encounters conditions (higher pH, reactive minerals, or saturation zones) where the organic complexes break down and deposit their load. This forms a darker spodic horizon enriched with illuvial humus, Fe, and Al, often appearing as a reddish-brown or black layer [400].

Tongue formation occurs when this leaching-illuviation process is spatially non-uniform. Instead of a level, horizontal E/B boundary, certain vertical zones experience more intensive leaching, causing the eluvial horizon to protrude downward in finger- or tongue-shaped extensions [403]. Essentially, podzol tongues mark preferred flow pathways where water and acids penetrate deeper [401, 404]. Chemically, the material within a tongue is highly leached: it is mostly quartz sand with coatings removed. The edges and bottoms of a tongue tell the story of where mobilized solutes redeposit: the center is filled with bleached sand, the periphery is fringed by orange-brown iron (hydr)oxide coatings, and the base of the tongue often accumulates iron-organic compounds, forming a ferruginous or humus-rich halo at the tongue's terminus [401]. This indicates that as acidic leachate travels down a tongue, some iron diffuses laterally and precipitates along the margins, while further down the remaining iron and organic matter precipitate at the tongue's end where flow diminishes or soil chemistry changes. Thus, a podzol tongue can be viewed as a vertical conduit of eluviation surrounded by a zone of illuviation (iron/humus staining) at its margins [405, 403, 406].

In essence, a tongue is self-reinforcing: as eluviation strips coatings and fines, the column becomes more porous and permeable, capillary retention drops, and Darcy flow focuses into the same low-resistance path. The higher advective flux delivers more ligands and oxidants, accelerating Fe–Al stripping and deepening the bleached conduit—i.e., a classic reactive-infiltration instability driven by hydraulic focusing. At the same time, illuviation at the tongue rim lowers permeability in the surroundings, which further confines flow to the conduit. Structural features (roots, burrows) are not required to trigger the growth - when present, they merely bias spacing and orientation. Growth saturates only when rim cementation chokes the path, reactants are depleted, or a textural/capillary break diverts flux laterally.

5.2.3. Dry salt lakes and convection

Dry salt lakes, also called evaporite pans, saline flats or playas, are found in arid environments where evaporation of groundwater exceeds precipitation [407, 408, 409]. A common situation is a terminal or endorheic valley with no outflow route for water, such as the case of Death Valley, California, shown in Fig. 57A. Evaporites can develop from the decline and disappearance of a natural lake, like Owens Lake, Fig. 57B, which dried up after the Owens River was diverted into aqueducts near Los Angeles [410, 411, 412]. Large natural evaporite pans are also found in arid basins including the Danakil salt plain, Ethiopia, Fig. 57C. In coastal settings, similar features called sabkha can result from seawater evaporation, as in Fig. 57D.

Striking patterns of closed polygonal shapes, bounded by narrow ridges, often appear and decorate the surface of dry lakebeds. Here, as groundwater evaporates over time, it leaves behind any dissolved salt that it had been carrying. These salts accumulate at the surface of the soil, forming into a solid salt crust, in which the patterns develop. The polygons typically have a diameter of a few (1–10) metres, separated by 1–10 cm high ridges or raised features [413, 414, 415]. The surface patterns show dynamics on time-scales of only a few months [413, 415].

Although beautiful, dry salt lakes produce mineral-rich dust through erosion [416, 417], which is detrimental to air quality and human health and a major source of uncertainty in modelling climate sensitivity [418]. Changes in water use policy and climate are exacerbating these problems worldwide, as saline lakes like the Aral Sea, Dead Sea and Great Salt Lake are receding, leaving salt flats behind [419]. In this context, Owens Lake is seen as a case study for developing remediation strategies and dust control at dry lakes, given its situation as a man-made dry lake that was at one time the largest source of hazardous aerosols (PM-10) in the United States [412].

Early interpretations of the polygonal patterns in the salt crusts of dry lakes focused on a range of mechanical instabilities of the surface crust itself, such as fracture [420] or buckling [421]. However, more



Figure 57: Polygonal patterns of salt frequently appear in dry salt lakes and evaporite pans. Examples include at A: Badwater Basin, Death Valley, California, B: Owens Lake, California, C: Danakil salt pan, Ethiopia and D: the Skeleton Coast, Namibia. In all cases, a salt crust develops on the surface of the pan, with narrow raised ridges defining the edges of the polygons. (images: A,B,D: Lucas Goehring; C: Electra Kotopoulou.)

recently an appreciation of the hidden fluid dynamics of dry salt lakes has developed into an explanation of the remarkably well-ordered surface shapes of this pattern [422, 415]. Evaporite pans are maintained by evaporation of groundwater, and the groundwater table at active pans is usually very shallow, close enough to the surface to ensure good connection through capillary action [407, 410, 408]. Dissolved salt concentrates in the groundwater near the surface, forming a boundary layer of salt-rich, denser fluid. Measurements of the density and salinity of groundwater have demonstrated this layer, for example, in the upper $\sim$1 m of Owens Lake [410, 415]. This scenario of denser fluid resting atop a deep reservoir of less saline, and thus more buoyant, groundwater, is inherently unstable.

Since dry salt lakes occur in desert areas, thermal fluctuations might also be expected to contribute to their dynamics. In contrast to the more well-known double-diffusive fingering structures (Sec. 4.2.5) that produce stratification and 'salt-fingers' in the ocean [124, 125], however, thermal buoyancy does not appear to be relevant to dry lake convection: based on temperature logs and groundwater sampling at Owens Lake, the density contrast due to salinity is estimated to be two orders of magnitude larger than that caused by thermal expansion [422]. A significant contribution, instead, might arise from the effects of temperature on the hydration states of some salts. For example, sodium sulfate can swell in volume by up to 300% when it changes from an anhydrous mineral (thenardite) to a hydrated one (mirabilite) [423]. This phase transition occurs at temperatures and relative humidities routinely experienced in dry lake environments, but its effects on the salt crusts have not yet been explored.

The soil of a dry salt lake can be considered as a porous medium, saturated in water. Density-driven convection in porous media is a well-studied topic, and the subject of several recent, detailed reviews [424,

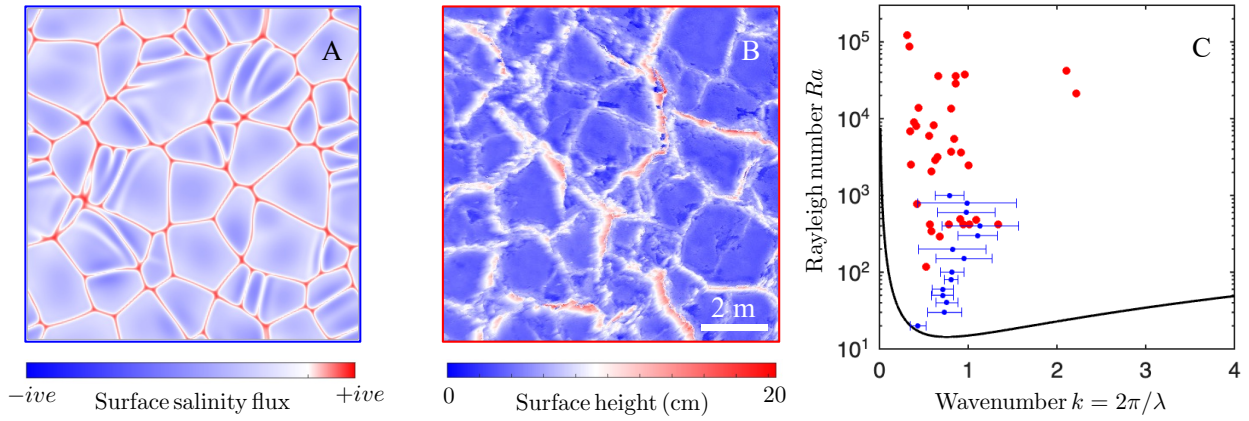


Figure 58: Characteristic patterns and length-scale selection in dry salt lakes. A: Results of a simulation of the dry salt lake problem given by Eqs. 9–11, and a constant through-flow driven by surface evaporation. Colours give the pattern of surface salinity flux, with red indicating areas of enhanced salt crust growth, and blue indicating where crust growth is inhibited. The surface shown has size 12π. In dimensional terms, for a natural length of 0.15 m [415], this corresponds to a square of approximately 6 m in size. (Image: Matthew Threadgold and Cédric Beaume.) B: Surface height profile map of the natural salt crust at Badwater Basin [422]. C: The dominant wave-number $k = 2\pi/\lambda$ of the patterns arising from dry salt lake models (blue) and field data (red). Linear stability analysis predicts the neutral stability curve (solid black line), above which the model is unstable. Data reproduced from [415].

425]. In the context of a dry lake, a simplified model considers evaporation at a rate E occurring at the upper surface of the ground, while water is recharged from below, or from some distant reservoir, at a rate just sufficient to balance the evaporative losses [426, 422]. These boundary conditions lead to the problem of one-sided convection with a through-flow of fluid. Dissolved salt accompanies the flow, but is left behind by evaporation, accumulating above the soil surface in a salt crust, and near the surface in salt-rich fluid. In dimensionless terms, the system of equations taken to model this system is

$$\nabla \cdot \mathbf{u} = 0, \tag{9}$$

$$\frac{\partial S}{\partial t} + \mathbf{u} \cdot \nabla S = \nabla^2 S, \tag{10}$$

$$\mathbf{u} = -\nabla p + Ra\, S \hat{z}, \tag{11}$$

which describes the flow of an incompressible fluid in a porous medium, with some velocity $\mathbf{u}$, accompanied by the transport of dissolved salt that moves along with the fluid flow, and by diffusion. The salt concentration of the groundwater is represented by the salinity S. This is bounded by the background salt concentration present in the reservoir source ($S = 0$), and the saturation limit ($S = 1$) at which dissolved salt will precipitate out as a solid. Salinity increases the density of the water, and these buoyancy forces are represented on the right hand side of Eq. 11 in the Boussinesq approximation, along with any other contributions to the fluid pressure p.

The system of equations given above was first studied for the analogous but thermally-driven case of a geyser [427], and later adapted to the setting of a dry salt lake [426, 428]. In this model, the stability of the salt-rich, near-surface boundary layer is controlled by a dimensionless Rayleigh number, $Ra = \kappa \Delta \rho g / \mu E$, Here, κ is the permeability of the soil, $\Delta\rho$ is the density contrast between reservoir fluid and salt-saturated water, g is the magnitude of acceleration due to gravity, μ is the viscosity of water, and E is the evaporation rate in terms of a volume flux of water. The Rayleigh number describes the balance between diffusive and advective effects. It is also the ratio of the speed at which a large denser plume of fluid will fall under its own weight, to the speed of the flow moving upward through the soil to replace water lost to evaporation. The steady-state boundary layer of the dry salt lake model is unstable to convection when Ra exceeds about 7 when the upper surface is modelled with a uniform pressure boundary condition [427], or 14.3 for the

case of a uniform vertical flow [429]. Analogue laboratory experiments in Hele-Shaw cells have confirmed the critical value for convection [426], and explored the longer-term convective dynamics [415]. Similarly, linear stability analyses have been made for an initially uniform lake, to investigate the time needed to build up a sufficiently thick boundary layer that will be unstable to convection [422, 430, 431]. At several dry lakes and sabkhas around the world, Rayleigh numbers have been estimated to be between about 10^2–10^5 [432, 415], showing that groundwater should be actively convecting at these sites. Indeed, large, denser plumes of salt-rich water have been directly observed near the surface of sabkhas using electrical conductivity measurements [432, 433].

Simulations of the groundwater flows in dry salt lakes have shown that the pattern of the convective cells that develops near the surface of a modelled lakebed strongly resembles the patterns seen in natural salt crust [422, 415], as demonstrated in Fig. 58A,B. These models also predict that the typical size of convective features is governed by a characteristic scale given by the ratio of the diffusion constant of salts in the groundwater, to the volumetric evaporation rate. These predictions, along with data extracted from surface profilometry of dry salt lakes, are shown in Fig. 58C. Since the typical diffusivity of salts in water is around 10^{-9} m/s^2, while the groundwater evaporation rates measured in active dry salt lakes are of order 0.1 mm/day or 10^{-9} m/s, the characteristic scale that emerges in the model system is of order 1 m in most cases, close to what is observed at places like Badwater Basin, Owens Lake, and Sua Pan [415]. Furthermore, the models can predict rates of salt crust growth by estimating the salt flux into the surface from a balance between advection and diffusion. In this context, the polygonal salt ridges should appear over downwelling sheets of salt-rich water, as has been confirmed by mapping out the groundwater salinity through direct sampling [415]. Under the field conditions typical of Owens Lake, convective transport of salt has been estimated to contribute to growth rates about 1 mm/month, which is comparable to the growth rates observed at similar dry lakes in Botswana [413]. Since more salt should enter the crust above the salt-rich downwelling flows, these models also predict that salt ridges should grow about twice as fast as the rest of the crust [415].

As explored further in Sec. 5.2.4, the growth and internal structure of salt crusts can be quite complex. A better understanding of how water and salt move through the crust, and of the feedback between crust growth and local evaporation, are likely to be the next steps in further developing predictive models of dry salt lakes. The effects of an unsaturated capillary fringe have also recently begun to be investigated [434, 431], as have the effects of more efficient convective flows within any cracks in the ground, as might be caused for example by desiccation or a cycling of water availability [435].

5.2.4. Desert roses and other efflorescence structures

The presence of salts in natural environments can create spectacular landscapes but can also poses significant threats to ecosystems and historical artifacts [437, 438, 439]. With environmental fluctuations such as rainfall or temperature and relative humidity changes, salt present in granular materials—consolidated or unconsolidated—such as stones or soil can dissolve and form salt solutions that can flow. Consequently, the salts can be transported and precipitate when the water evaporates at the surface [141]. This is the origin of salt creeping, a phenomenon in which salt crystals continue to precipitate far from an evaporating salt solution boundary [440, 441, 442, 139]. Salt creeping can initiate and grow on flat surfaces but also on top of porous materials such as soil, sand and stones; this is called efflorescence; Fig. 59 [141, 443, 444]. The latter can, for example, occur with ground water in soils or at salt lakes. Salt creeping can result in spectacular structures in natural environments, such as the formation of desert roses in arid regions, Fig. 60A,B, and salt crystallization motifs near the Black and Dead Sea coasts. In addition, salt creep can lead to soil salinization, vegetation decline, and water quality issues, impacting biodiversity [437].

Salt creeping is a general phenomenon that happens for different salts under conditions of low relative humidity and is affected by the presence of impurities and other microcrystallites that provide secondary nucleation sites near the evaporation front [139]. As salt crystals are wettable by their own salt solutions, such multiple nucleation sites provide a platform for a film of salt solution to spread even further over the newly formed microcrystallites, well beyond the initial evaporation front [442, 139]. This in turn enlarges the evaporative area, which leads to a faster precipitation, causing an exponential increase in the precipitating crystal mass in time. This self-amplifying process results in spectacular three-dimensional crystal networks

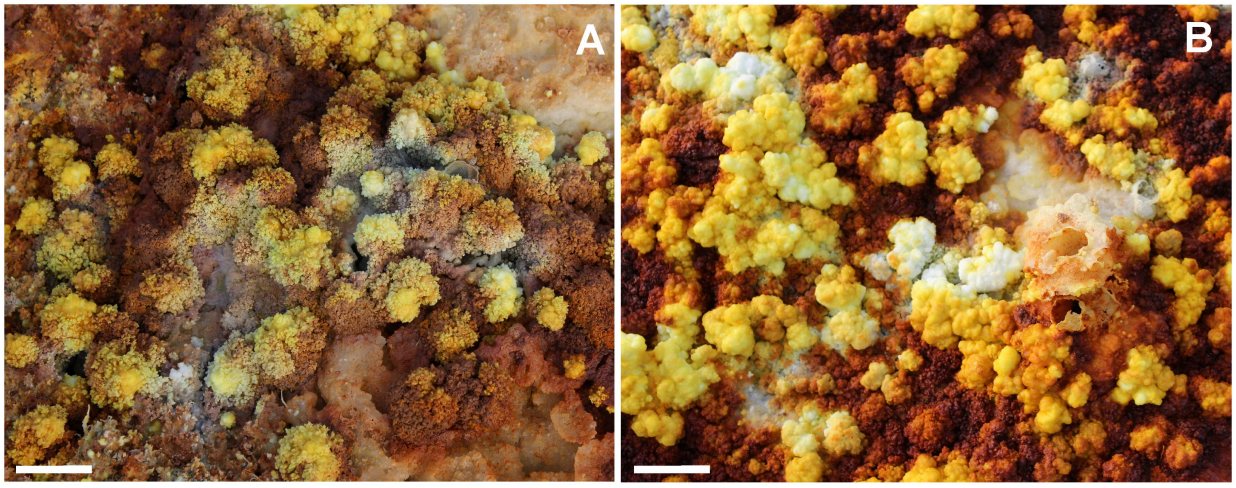


Figure 59: Salt efflorescence at the acidic hydrothermal field of Dallol, Ethiopia [436]. Dendritic (A) and cauliflower (B) efflorescence of gypsum ($CaSO_4{\cdot}2H_2O$), sylvite (KCl), carnallite ($KCl.MgCl_2{\cdot}6H_2O$), jarosite ($KFe_3(SO_4)_2(OH)_6$) and iron-oxide minerals. Scale bars are 3 cm. (Images: CC-BY Kotopoulou et al. [436]).

at macroscopic distances from the salt solution source. Microscopic analysis of the 3D network of such efflorescence reveals an internal porous structure of the crystalline salt network with a fractal structure characterized by a self-organized, self-similar arrangement of salt crystals, as we discuss in Sec. 4.2.6.

Laboratory and field observations on different salts suggest that as different minerals have different crystalline structures reflecting the seven possible lattice structures, the macroscopic patterning differs between different salts. Desert roses typically consist of calcium sulfate (gypsum) or barium sulfate (barite) with sand grains (SiO_2) interspersed between the crystalline structures. When investigated in detail, desert roses reveal a spectacular self-organized structure: large petals, smaller petals in between these and even smaller ones between those, in a fractal organization. A close-up of the structure by SEM imaging, Fig. 60C,D, reveals that each petal itself is composed of parallel smaller leaflets crystals, emphasizing the universality of this pattern and the internal porous structure of the 3D salt network [445]. This crystal structure in nature can grow to 1 to 3 m in height.

Salt creeping is therefore both universal and self-amplifying, typically initiated by the presence of salt crystals or impurities. It hinges on the formation of numerous crystallites under low humidity conditions, with impurities often serving as nucleation centres or salt mixtures catalysing this spectacular self-organized process. Addressing salt creep is vital for preserving our geo- and cultural heritage [446], calling for further research and interdisciplinary collaboration to develop sustainable solutions for their conservation. On the other hand, when salt crystallization occurs at the pore scale within the porous materials it can induce weathering and damage outdoor historic and archaeological sites such as Petra in Jordan [447], or Pharaonic sandstones monuments in Luxor, Egypt [448], and more generically our outdoor built cultural heritage.

5.2.5. Salt weathering, honeycomb weathering, and tafoni

Salt weathering, haloclasty, honeycomb weathering, and tafoni, Fig. 61, are terms that describe a set of related geological processes and features. Salt weathering [449, 450], also known as haloclasty, is a suite of physical weathering processes in which dissolved salts infiltrate pore and fracture networks and then crystallize and/or hydrate, generating stresses within rock pores or fractures. This phenomenon is particularly common in arid and semi-arid regions where evaporation rates are high, and salt solutions can become concentrated, as well as in coastal environments where salt spray is present. In both settings, saline solutions enter the rock; concentration by drying or cooling leads to nucleation and growth of salt crystals, and crystal growth or hydration cycles exert crystallization pressures on pore walls. Over time, this

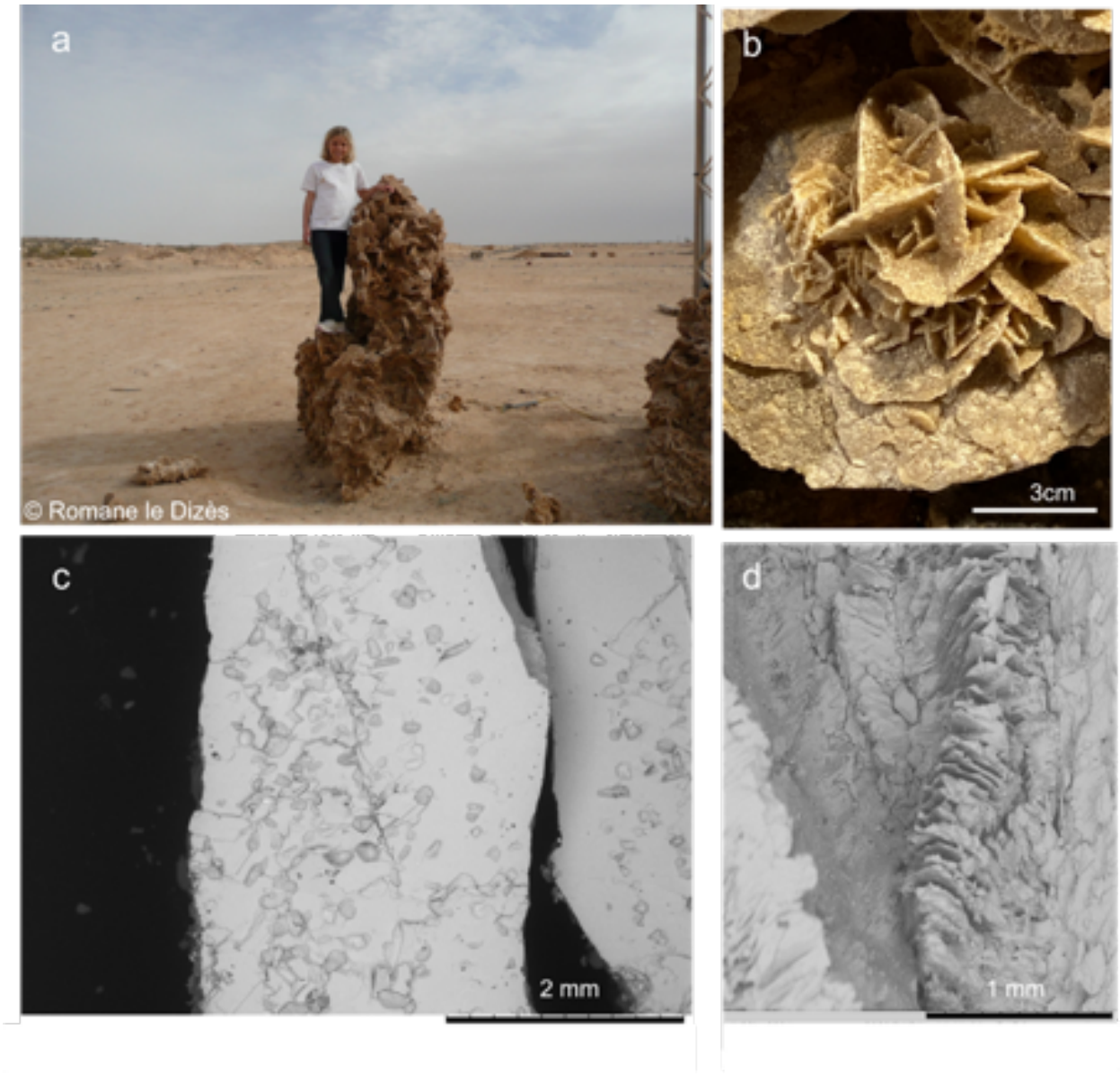


Figure 60: Desert roses formed by crystallization viewed at different scales. A: typical structure of sand rose structure in the Moroccan desert arid region (image: courtesy of Romane le Dizès Castell). B: a close up view of one desert rose with its polycrystalline structure made of large and small petals. C: SEM image of sand grains entrapped between two broken crystalline petals. D: SEM image of the internal structure of one petal showing a self-organized crystallization at an even smaller scale. images B-D : N. Shahidzadeh, UvA.



Figure 61: Salt weathering: honeycomb / tafoni patterns. Left: Le Grotte di Soprasasso, Bolognese Apennines, Italy (image: Elena Tartaglione; CC-BY-SA-4.0); Right: Elgol, Isle of Skye, UK (image: Kalense; CC-BY-SA-3.0).

stress field causes the rock to break apart, leading to granular disintegration, flaking, and the emergence of characteristic surface relief.

Honeycomb (alveolar, cavernous) weathering is characterized by small, closely spaced cavities resembling a honeycomb pattern on rock surfaces [451, 452]. It is often found in coastal and desert environments where salt spray or other saline moisture sources are present and is typically associated with sedimentary rocks, such as sandstones, which have high porosity. Salt weathering is widely regarded as a dominant driver of honeycomb formation, acting together with microclimatic gradients and case-hardening of surface crusts, though additional processes may contribute. Related iron-oxide banding and staining on many outcrops reflect similar transport–reaction feedbacks; depending on boundary conditions these can range from irregular bands to well-ordered concentric banding [453].

Tafoni are rounded, cave-like features found on the surfaces of granular rocks such as sandstone, granite, and basalt. Tafoni structures can range from small pits to large hollowed-out spaces. There is no clear consensus on the threshold between honeycomb weathering and tafoni [454]. Usage in the literature is primarily morphological: *honeycomb* is typically used for centimetre-scale cellular pits and *tafoni* for decimetre- to metre-scale alcoves, with overlap between categories. There are a number of modelling studies of honeycombs and tafoni [455]. In addition to salt-weathering feedbacks, a Turing-type mechanism has been proposed for the formation of these honeycomb / tafoni features [65], although its applicability likely depends on lithology, transport regimes, and environmental forcing.

5.2.6. Sedimentary crack patterns

Fractures in soft sedimentary layers arise when the material accumulates tensile strain from drying, cooling, or differential shear. Once nucleated, cracks propagate and link to relieve the stress, assembling plan-view networks; Fig. 62 [456]. The resulting morphologies range from polygonal meshes—often near-hexagonal or orthogonal—to branched, hierarchical patterns. Outcomes depend on composition, moisture content, layer thickness, substrate adhesion, and the drying/cooling history [457]. Their geometry is amenable to scaling descriptions: stress build-up and release set characteristic spacings and size distributions, and many fracture systems display scale-invariant statistics [458]. Two canonical examples illustrate the range. In desiccating mud (Fig. 62, left), evaporation drives surface shrinkage; tensile stresses concentrate near the surface, cracks nucleate, and the network expands as drying proceeds [459]. In permafrost (Fig. 62, right), repeated winter cooling produces thermal-contraction cracking that, over years to millennia, organizes into ice-wedge polygons [460].

Beyond these, several sedimentary settings develop crack networks through internally driven volumetric



Figure 62: Sedimentary cracking patterns: Left: cm-scale desiccation cracks in dried sludge (image: Hannes Grobe, CC-BY-SA-2.5); Right: hm-scale ice-wedge polygons in permafrost (image: Brocken Inaglory, CC-BY-SA-3.0).

strain under burial, dewatering, or early cementation. Polygonal fault systems in fine-grained marine tiers form during early burial and dewatering, producing layer-bound, near-planar meshes that are largely independent of far-field tectonic stress. Spacing scales with tier thickness and mechanical layering; modelling and seismic mapping document a robust wave-length—thickness relation and arrest at mechanical boundaries [461, 462]. Subaqueous, syneresis cracks record shrinkage and dewatering in cohesive muds below water. Unlike classic mudcracks, they may be discontinuous, cut lamination at high angles, and show meniscate voids; proposed drivers include salinity shocks (deflocculation), slow compaction, and earthquake-induced dewatering with sand/silt injection that later fills the fissures [463, 464]. In peritidal carbonates, early cementation and displacive crystal growth generate in-plane expansion of thin crusts; the result is buckling, ridge-and-polygon or *teepee* topography, and associated breccias. The dominant wave-length reflects crust thickness, stiffness, and substrate coupling, and in some successions rapid, earthquake-triggered failure has been inferred [465, 466]. Lastly, organic-rich shales develop bedding-parallel and cross-cutting microfracture networks during thermal maturation. Imaging and experiments show cracks nucleating near kerogen domains as internal pressure rises during conversion and then coalescing into percolating pathways; spacing and connectivity reflect kerogen distribution, mechanical heterogeneity, and maturation kinetics [467, 468].

These examples fit naturally into a scaling viewpoint: in burial-compaction tiers and cemented crusts the dominant wave-length scales with an active-layer thickness H (tier or crust thickness), whereas in maturation-driven shales it additionally reflects kerogen patch size and pressure-generation rates; in all cases, boundary conditions and mechanical layering set arrest lines and pattern coarsening pathways.

5.2.7. Geodes

Geodes, Fig. 63, are hollow, spherical or oval rock cavities lined with inward-facing crystals or mineral deposits [469, 470]. They can range in size from a few centimetres to over a metre in diameter. The largest known geode, located in Pulpí, Almería, Spain, measures approximately 8 m long, 2 m wide, and 2 m high [471]. Geodes occur in a variety of geological environments; they are commonly found in areas with volcanic activity and in sedimentary rock regions where water has caused dissolution of rocks, such as limestone and shale. Their hollow interiors are often lined with minerals such as quartz, amethyst, calcite, agate, and other silicate or carbonate minerals.

The formation of geodes occurs in two major stages: cavity creation and mineral deposition. Geodes begin as hollow cavities within rocks, which can form through several processes: In volcanic environments, molten lava can trap gas bubbles as it cools. These bubbles, or vesicles, form empty spaces within the solidifying rock. Over time, these cavities serve as the initial space for mineral deposition. In sedimentary environments, cavities can form due to the dissolution of minerals (e.g., limestone or gypsum) by ground-



Figure 63: Geodes. Left: Ameythyst geode (image: Madeleinemcc, CC-BY-SA-3.0). Right: Geode with aragonite, Bloomington, Indiana, USA (image: James St. John, CC-BY-2.0).

water. Acidic groundwater can dissolve portions of the rock, leaving behind voids that become the basis for geode formation.

Once a cavity exists, the second stage involves mineral deposition on the inner walls. Groundwater or hydrothermal fluids, often rich in dissolved ions, infiltrate the cavity. Over time, the minerals precipitate and crystallize along the inner walls of the cavity. As mineral-laden water continues to flow through the cavity, crystals slowly grow inward. Depending on the local geochemistry, different minerals precipitate, creating colourful and varied geodes. Quartz is the most common mineral, but other varieties, such as amethyst (a purple form of quartz), calcite, and agate, are also frequent.

Geodes often display banding of layers of different minerals, as changes in water chemistry or temperature over time cause sequential deposition of different minerals. This can result in intricate patterns of colours and textures. Quartz geodes are the most common and feature clear or white quartz crystals lining the cavity. Some may also contain amethyst (purple quartz) or smoky quartz (grey-brown quartz). Calcite is another common mineral found in geodes, often forming larger, blockier crystals compared to quartz. Some geodes have a lining of banded agate, which forms concentric layers of microcrystalline quartz around the inner walls.

5.2.8. Concretions and nodules

Concretions and nodules (Fig. 64) are secondary mineral features found in sedimentary rocks, but they differ in origin and internal structure. Terminology varies in the literature; in this review, *concretion* refers to early-diagenetic mineral precipitation around a nucleus—often with radial or concentric fabrics—whereas *nodule* denotes a diagenetic replacement body lacking concentric growth. Both are rounded or irregularly shaped mineral masses, typically harder than the surrounding rock, and occur in a range of geological settings.

Concretions [472, 473, 474] are hard, compact masses of mineral material that form by the precipitation of minerals around a nucleus or core, typically in sedimentary rocks like sandstone, shale, or limestone. Concretions form when minerals precipitate from groundwater that percolates through sediment. These minerals accrete around a nucleus, which can be an organic object, like a fossil, shell, or plant fragment, or an inorganic particle, such as a grain of sand. As minerals continue to precipitate, the concretion grows outward, often developing concentric layering. The growth occurs syndepositionally (during deposition) or early diagenetically (soon after burial), before the surrounding sediment fully lithifies. Common minerals that precipitate to form concretions include calcite, silica (quartz or chalcedony), iron oxides (such as hematite), and siderite (iron carbonate). Concretions are often spherical or elliptical in shape, but they

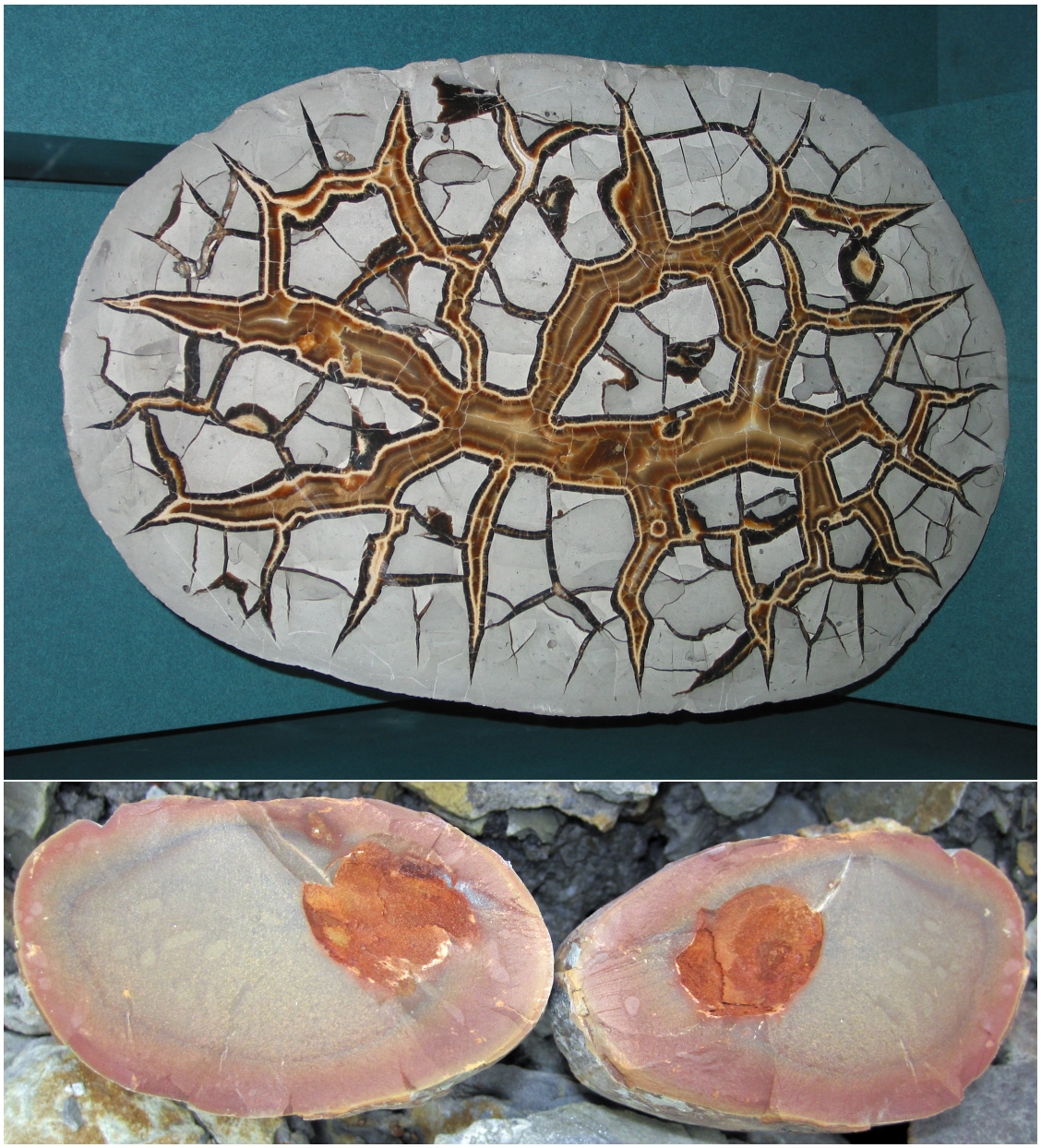


Figure 64: Concretions and nodules. Above: Septarian concretion (image: Keith Pomakis, CC-BY-SA-2.5). Below: Siderite (ironstone) nodule, Ohio, USA (image: James St. John, CC-BY-2.0).

can also be irregular. They vary in size from a few centimetres to several metres across. Concretions often exhibit a radial internal structure, with mineral layers emanating out from the nucleus. This distinguishes them from nodules, which lack this concentric growth pattern. Concretions are typically harder than the surrounding sedimentary rock, so they tend to be preferentially exposed as the host rock weathers.

Septarian concretions couple early carbonate growth with later shrinkage fracturing and crack-seal infill. A millimetre-scale precipitation front builds a stiffening carbonate body around a nucleus while the host mud remains weak and permeable [474, 475, 476]. As the concretion densifies, internal volumetric strain and pore-fluid evolution trigger tensile failure of the still-weak interior. Proposed drivers include dewatering/shrinkage of clay-rich gels (syneresis-style strain), localized pore-pressure transients, differential compaction, and even shaking by earthquakes, all of which naturally produce polygonal or radial crack meshes [477, 478, 479, 480]. The resulting septaria act as short-lived high-permeability conduits; later fluids precipitate sparry calcite (often ferroan), ankerite or barite in crack-seal fashion, commonly in multiple generations that post-date the micritic matrix [481, 482, 483, 484, 485, 486]. Stable-isotope, cathodoluminescence and clumped-isotope studies document distinct fluid histories for matrix versus septarian cements and repeated opening–sealing cycles [483, 487].

Nodules [488] are mineral masses that form by post-depositional (diagenetic) replacement of the surrounding sediment or rock, rather than by mineral precipitation around a core. Unlike concretions, nodules do not have a clear concentric structure. Nodules form through diagenetic replacement, where the original sedimentary material is replaced by minerals as groundwater circulates through the rock. This process often occurs after lithification. Common minerals found in nodules include flint (a variety of microcrystalline quartz), chert, pyrite, phosphate, and gypsum. The replacement process can result in nodules that are chemically different from the surrounding rock. Nodules tend to be irregular in shape and are often found scattered within the host rock. They can vary significantly in size, similar to concretions, from small pebbles to large boulders. Nodules typically lack the concentric layering that concretions possess. Their internal structure is more uniform, often reflecting the mineral that replaced the original material. Nodules are often found in sedimentary rocks like limestone, chalk, and shale. For example, flint nodules are commonly found in chalk formations.

Quantitative descriptions of concretion growth treat the body as a moving precipitation front (concretions) or a coupled dissolution–precipitation front (replacement nodules), embedded in a porous medium governed by transport and reaction. Classical field syntheses constrain the geometry and timing windows [472, 473, 474], while forward models for iron–oxide systems couple transport with pH/redox buffering to reproduce rinds and banding [453] and link to observed rhythmic features [489, 490].

5.2.9. Target patterns

Geological target patterns—nested, approximately concentric bands around a nucleus—occur in many rock types (Fig. 65) and are conspicuous in agates (Sec. 5.1.1). In much of the geological literature these rings are casually labelled *Liesegang* by analogy with laboratory precipitation experiments (Sec. 4.1.5). We reserve Liesegang rings for the reaction–diffusion mechanism *sensu stricto*: a diffusing reactant drives repeated exceedance of a precipitation threshold, producing quasi-periodic bands with characteristic spacing laws and front-controlled chemistry [491, 492]. Where such diagnostics are absent, *target* or *concentric banding* are neutral morphological terms. Recent reviews emphasize this mechanistic definition and its tests (spacing progression, front kinematics, band chemistry) [81].

Geological examples of target morphology include rhythmically banded iron-oxide concretions (Sec. 5.2.8), e.g., the layered end-members in the Navajo Sandstone *moqui marbles* (Fig. 65D), which show millimetre-scale, concentric Fe-oxide bands throughout the body [489, 490]. In metamorphic settings, reaction coronas can likewise present repeated, compositionally alternating shells around relict grains (Fig. 65E); when this rhythmic alternation is present, the resulting concentric banding constitutes a target-like analogue, with layer successions and growth captured by diffusion–thermodynamic rim-growth models [493, 494]. A broader family of iron-oxide banding on outcrops—ranging from irregular stains to well-ordered concentric banding—highlights how transport–reaction feedbacks in similar materials can yield both highly ordered targets and less ordered banding, depending on boundary conditions and supply [453].

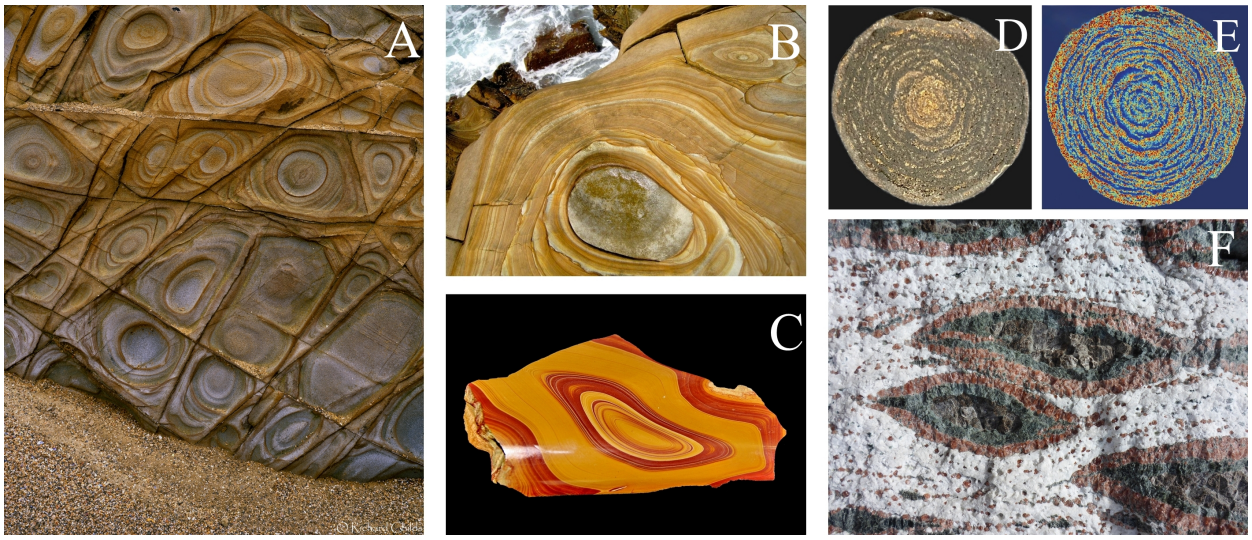


Figure 65: Geological target patterns. A: in sandstones at Widemouth Bay, Bude, England. B: at Bouddi National Park, New South Wales, Australia. C: in volcano-sedimentary rock, Gobi desert. D: Layered moqui marble, an iron oxide concretion from the Navajo Sandstone in the southwestern United States, with a radius of approximately 1.2 cm [490]. E: Iron distribution within the concretion shown in panel D [490]. F: Reaction corona in metamorphosed anorthosite: the original igneous rock was dominated by plagioclase with orthopyroxene; the green clinopyroxene and garnet grew during subsequent metamorphism. (A) Richard Childs, reproduced with permission. (B) Evelyn Ward, reproduced with permission. (C) Dmitry Demezhko (distributed via imaggeo.egu.eu on the Creative Commons license), (F) Chris Clark, reproduced with permission.

5.3. Small and hot

High heat or high stress acts on micro-scales, forging patterns measured in millimetres to a few centimetres. Banded sphalerite layers, the agate-lined cavities of thunder eggs, and orbicular granitoid shells record episodic crystallization in magmatic settings, while stylolite teeth and spiral "snowball" garnets capture differential stress during metamorphism. Menilite nodules, clathrite cages and other earthquake-fluidized or hydrothermal growths complete this hot-yet-small collection.

5.3.1. Stylolites

Stylolites [495], Fig. 66, are serrated, interlocking dissolution surfaces commonly found in sedimentary rocks, especially carbonates and sandstones [496, 497]. They form under compressive stress in the Earth's upper crust by a process of pressure solution: minerals dissolve at stressed grain contacts and re-precipitate in pore spaces, causing a net volume loss [161]. The resulting structure is a rough, tooth-like interface enriched in insoluble residues (clays, organics) that were left behind as the host mineral dissolved [496]. Stylolites play a significant role in rock deformation and diagenesis: they accommodate strain, influence fluid flow, and record stress history. Their characteristic "tooth" geometry (pointing in the direction of maximum compressive stress) reflects the underlying physics of their growth. Stylolites can act as conduits for fluid migration, influencing fluid flow and replacement reactions [498], helping transport fluids and precipitating minerals in the fractures [499, 500].

At the heart of stylolite formation is a thermodynamic driving force for dissolution under stress. A mineral under a normal stress σ_n at a contact has a higher chemical potential or solubility than the same mineral under less stress. To first order, the change in chemical potential due to stress is

$$\delta\mu = \Omega\sigma_n, \tag{12}$$

where Ω is the molar volume of the solid. This means that material at highly stressed contact points can dissolve into the pore fluid, increasing the local ion concentration, and then diffuse away, precipitating in

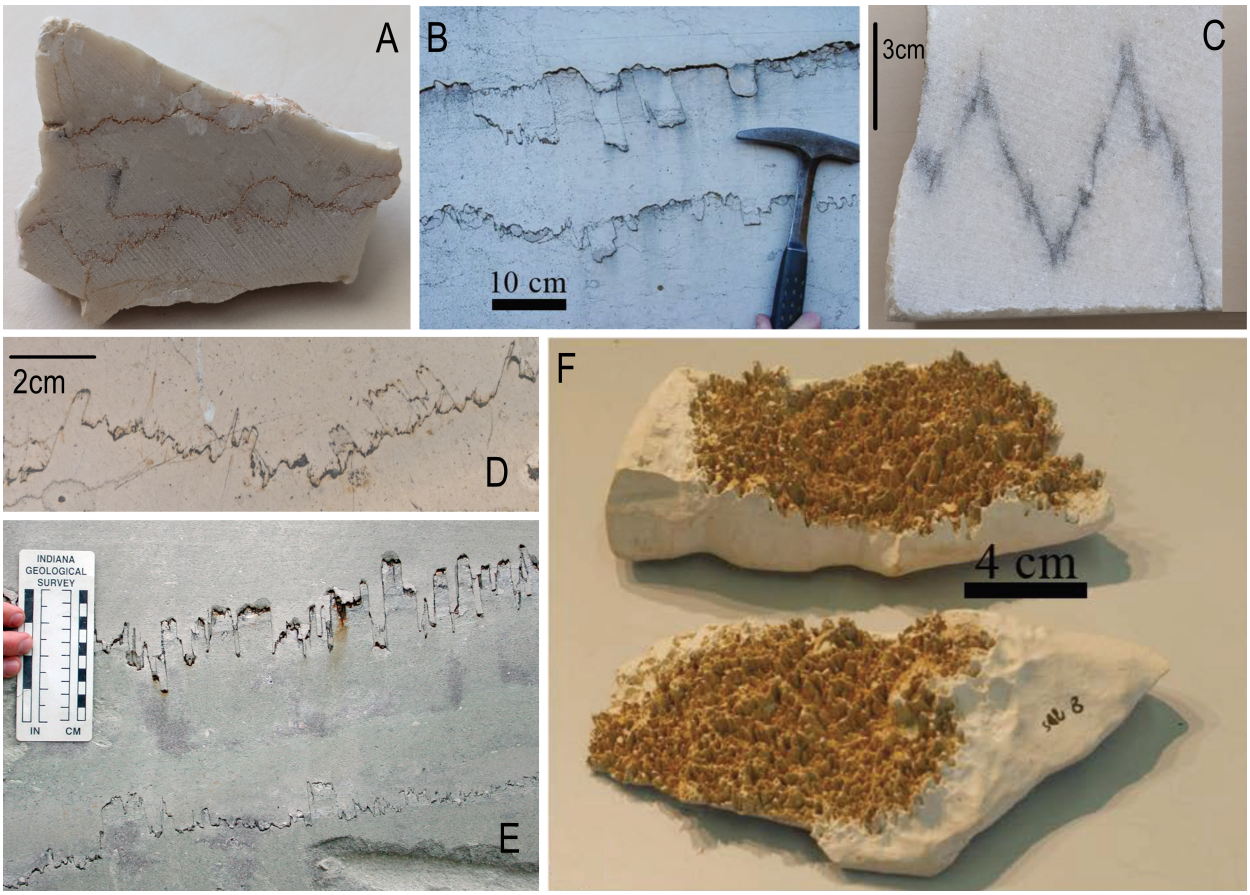


Figure 66: Stylolites. A: Stylolite in limestone from Mitzpe Ramon, Israel; the red colour comes from clay residue. B: Stylolites in limestone from Burgundy, France [161] C: Stylolites in marble from Dolni Morava quarry, Czechia. D: Stylolites in limestone from Morawica, Poland. E: Stylolites in the Salem Limestone from Bloomington, Indiana (Michael C. Rygel; CC-BY-SA-3.0). F: Surface of a stylolite in limestone from Vercors, France [161].

regions of lower stress; e.g., open pore space. In essence, the system tends toward lower free energy by removing material from stressed locations. This thermodynamic principle—sometimes called the pressure solution or stress-induced dissolution mechanism—was recognized early on as the origin of stylolites [501, 502]. However, a flat dissolution surface cannot persist under non-uniform stress: even minute undulations raise the normal stress on the peaks and lower it in the valleys, so the peaks dissolve faster while the valleys are protected. This positive feedback, an Asaro-Tiller–Grinfeld–type instability [503, 504, 505], continually amplifies the roughness until the strain-energy gain from removing stressed material is balanced by the surface-energy cost of creating new interface.

A stylolite can be viewed mechanically as a sort of anticrack; the opposite of a tensile crack. Instead of opening and creating void space, material is removed by dissolution and the opposing faces move together. Fletcher and Pollard [506] formalized this idea, noting that stylolite teeth focus compressive stress at their tips, much as crack tips focus tensile stress. In an elastic host, a corrugated interface under compression bears higher normal stress on protrusions; if those protrusions dissolve, the interface advances locally and bulk shortening accrues as compaction strain. In some models the stylolite seam is treated as a thin, soft (residuum-filled) layer embedded in an elastic medium; the associated stress redistribution can even produce small tensile zones just beyond tips, occasionally nucleating microcracks or veins.

The anticrack picture is a useful qualitative guide, but by itself does not guarantee indefinite propagation

under compression. In simulations by Aharonov and Katsman [507], purely stress-driven pressure-solution defects do not self-propagate laterally: calculated stresses are low along the flanks, suppressing dissolution there, and continued tip dissolution progressively smears out the tip stress concentration, which limits further advance. Sustained lateral growth therefore requires an additional mechanism that maintains high tip stresses and/or enhances flank dissolution; e.g., clay-assisted pressure solution together with material heterogeneity that pins parts of the interface and promotes tooth formation. Clays can enhance pressure solution by maintaining a thin water film and providing ionic pathways. Spring-network and related heterogeneous models show that a homogeneous medium tends to dissolve uniformly, whereas weak zones ("clay patches") trigger localization into stylolite planes. In nature, one often sees stylolites initiating where a shale parting or a marl layer is present within limestone; exactly what the clay-enhanced dissolution theory would suggest.

The development of a stylolite's characteristic jagged morphology can be viewed through the lens of interface dynamics and roughening. Initially, a roughly planar dissolution seam localizes, perhaps along a bedding plane or a thin clay layer. As pressure solution proceeds, any slight geometric irregularity on that interface will tend to amplify because of the stress-driven instability described earlier. The corresponding evolution equation for the stylolite height on a 2D interface (x, y) reads [508, 509, 510]

$$\partial_t h(x,t) = v_0 + \nu\,\mathrm{PV}\int_{\mathbb{R}} \frac{h(x,t)-h(y,t)}{(x-y)^2}\,\mathrm{d}y - \kappa\,\partial_x^2 h(x,t) + \eta(x,h), \tag{13}$$

where the Cauchy principal-value integral $\mathrm{PV}\int$ is the nonlocal elastic term, $\kappa > 0$ captures stabilizing surface energy, v_0 sets the mean advance from kinetics, ν collects together a combination of physical constants, and η is quenched heterogeneity, arising from the spatial variability of the material properties composing the grain [510]. In Fourier space,

$$\partial_t \hat{h}(k,t) = \left[\nu\,|k| - \kappa k^2\right]\hat{h}(k,t) + \hat{\eta}(k), \tag{14}$$

so long wave-lengths are elastically unstable ($\propto |k|$) while short wave-lengths are stabilized by capillarity ($\propto k^2$), implying a fastest-growing wave-number $k_{\max} = \nu/(2\kappa)$ and the corresponding length-scale $L^\star = 4\pi\kappa/\nu$.

Stylolite surfaces exhibit fractal characteristics, indicating scale-invariant roughness over certain ranges. Geometrical analyses of natural stylolites in limestone have found that the height profiles are self-affine with different Hurst exponents at different scales [510, 508]. Specifically, a three-regime scaling is often observed in sedimentary stylolites: At small scales of tens to hundreds of microns, comparable to grain size, the interface is relatively smooth with a high Hurst exponent $H \approx 1.1 \pm 0.1$. This implies strong correlation and gentle variations at the grain-scale; the stylolite does not look very jagged under the microscope, partly because grain heterogeneity pins the interface. At intermediate scales of 0.1—10 mm up to centimetres, a roughening regime appears with $H \approx 0.5$–0.6. This regime is interpreted as the result of the stress-driven instability: the interface wanders in a statistically rough manner governed by elastic interactions and dissolution kinetics, largely independent of individual grain structure. At large scales of several cm and above, sedimentary stylolites often show a saturation of roughness with Hurst exponent effectively 0, and a flat power spectrum [511]. Thus there is an upper cut-off to the self-affine behaviour; beyond a certain length, the amplitude of stylolite teeth no longer grows with scale. Tectonic stylolites formed by tectonic stress, not just burial, can show more anisotropic scaling: the roughness exponent differs in the direction parallel to bedding versus perpendicular, reflecting stress anisotropy in the plane of the stylolite [512]. For example, a stylolite in folded limestone might have longer, more spine-like teeth in the vertical direction, due to vertical stress, but more irregular smaller serrations along the horizontal direction, due to lateral confining stress being lower.

The existence of scaling laws for stylolites has practical implications. One major result from recent studies is that the crossover length between the small-scale and intermediate-scale regimes encodes the stress that was present during stylolite formation [513, 510, 161]. This crossover length is essentially the critical wave-length of the instability, $L^\star$, determined by the balance of surface energy and elastic strain energy. In effect, stylolites can serve as a gauge of past stress. This has been demonstrated by comparing stylolite-derived stress values with independent estimates; e.g., calcite twinning paleostress. Additionally, the height of the largest teeth, related with the plateau of the roughness spectrum, correlates with the total amount

of dissolution/compaction that occurred. These insights show how a deep understanding of interface roughening dynamics and scaling laws not only explains stylolite shapes but also unlocks quantitative geological information from them.

Because stylolites typically form over millions of years under geological conditions, reproducing them in the laboratory is challenging. Nonetheless, experimental efforts have been made to simulate stylolite formation in accelerated time, usually by using more reactive minerals or higher temperatures. Gratier et al. [514] conducted a landmark experiment in which they compacted a layer of quartz sand in a pressure vessel at 350°C and ∼50 MPa differential stress. Over the course of a few weeks to months, they successfully grew miniature stylolites at the contacts between the quartz grains. High-resolution imaging revealed tiny tooth-like dissolution features on the order of μm in height that qualitatively resemble natural stylolite shapes. This experiment confirmed that stylolites can form via pressure solution under controlled conditions, and provided direct observation of the process: small dissolution pits initiated at random defect points and gradually coalesced into a rough dissolution seam, with grains becoming truncated and material re-precipitated in pore space. The geometry of the experimental stylolites showed an interplay between heterogeneity and mechanical constraints, consistent with theory. For instance, peaks tended to form where there were harder grains or impurities that dissolved slower, and the overall amplitude of the teeth was limited by the need to accommodate within the thin sample layer. Despite these successes, lab-grown stylolites are inherently limited in scale. The experimental stylolite teeth were at most on the scale of one or two grain diameters in height—tens of microns—whereas natural stylolites can have teeth from mm up to cm high penetrating many grain diameters. The time scale is the limiting factor: to grow large stylolites requires dissolving a significant volume, which is extremely slow at laboratory time-scales unless one uses unfeasibly high temperatures or very soluble minerals.

Ongoing work continues to refine both the experiments and the models. Stylolites, once merely a curious serration in rocks, are now appreciated as natural laboratories of far-from-equilibrium thermodynamics and fractal growth, where the interplay of stress, chemistry, and time produces complexity from simplicity.

5.3.2. Porphyroblasts and spiral garnets

Porphyroblasts (Fig. 67) are large mineral crystals that grow within a finer-grained matrix in metamorphic rocks. These crystals form during metamorphism, the process whereby rocks recrystallize under elevated temperature and pressure. Common minerals that grow as porphyroblasts include garnet, staurolite, and andalusite. Porphyroblasts begin to form when specific minerals nucleate during metamorphism. As metamorphic conditions (temperature and pressure) increase, these minerals grow larger than the surrounding matrix owing to differences in mineral stability and growth kinetics. Porphyroblasts commonly develop in reaction zones, where minerals become unstable and new, more stable minerals grow. The growth of porphyroblasts reflects the rock's chemical and physical evolution during metamorphism.

As they grow, porphyroblasts can trap small fragments of the surrounding rock, known as inclusions, preserving a record of the rock's history prior to their formation. During metamorphism, rocks are often subjected to deformation, such as folding or shearing. This can cause porphyroblasts to rotate within the matrix. Under simple shear, relatively rigid porphyroblasts may undergo rotation within a flowing matrix. Alternatively, under some conditions porphyroblasts may grow essentially without rotation. Some garnet porphyroblasts exhibit spiral-shaped inclusion trails, known as spiral garnets or snowball garnets, which were once thought to indicate rotation. However, this spiral pattern can also arise from progressive overgrowth while the external foliation reorients, so that successive inclusions are entrained at slightly different azimuths.

There has been a long-standing argument in geology about porphyroblast rotation [516, 517]. The question about whether porphyroblasts rotate or not is clearly one that lies within the ambit of physics, in particular of fluid dynamics. A classical result in fluid dynamics due to Einstein gives that, for a Newtonian fluid undergoing creeping flow, a sphere within the fluid that undergoes shear at a rate $\dot{\gamma}$ will rotate by precisely half that amount: i.e., at a rate $\dot{\gamma}/2$. This has been used to argue that porphyroblasts must rotate as the rocks shear about them. However, that result applies only to Newtonian fluids, whereas rocks deform as complex non-Newtonian media. For non-Newtonian fluids, Brunn [518] and Gauthier et al. [519] showed theoretically and experimentally that the rotation rate is the same as in a Newtonian fluid in the case of an isolated sphere in a second order fluid (i.e., at low shear rates). On the other hand, simulations of D'Avino



Figure 67: Porphyroblasts. A: Garnet porphyroblast (3 cm width) in a gneiss matrix (image: Eurico Zimbres (FGEL/UERJ) and Tom Epaminondas (mineral collector), CC-BY-SA). B,C: Crossed polars optical microscope images of spiral garnets showing (B) clockwise and (C) anticlockwise asymmetry. (image: Shah et al. [515]).



Figure 68: Banded sphalerite. Banded precipitation in hydrothermal ore deposition, Schalenblende and Zincblende Pomorzany, Poland. (Images: Left, Przemysław Budzyński, reproduced with permission; right, Piotr Szymczak.)

et al. [520] and experiments of Snijkers et al. [521] found reduced rotation at higher shear rates relative to the Newtonian case. Michele et al. [522] showed that for sufficiently high rates of shear, spherical particles of size 60–70 μm suspended within a non-Newtonian fluid self-organize into string-like structures oriented in the direction of flow. They observed, moreover, that the particle rotation rate was strongly reduced relative to the Newtonian case; it decreased further as interparticle spacing diminished and practically vanished when the spheres lined up, as if the string of particles were a long rigid thread. Won and Kim [523] and Scirocco et al. [524] showed that the formation of these chains increases with the degree of shear thinning of the fluid and with the shear rate. Hwang and Hulsen [525] performed numerical simulations with several different non-Newtonian fluids and showed a transition in particle structures in a sequence: random, clustering, clustered string, and string formation, as the solvent viscosity decreases and the Weissenberg number increases. Thus the physics of non-Newtonian fluids predicts a rotation of a single particle much lower than in the Newtonian case, and the formation of strings of particles that behave as quasi-rigid structures. Note the similarity of these string-like structures to the millipede structures of porphyroblasts [526].

5.3.3. Banded sphalerite

An example of a layered structure with an elusive origin is banded sphalerite, a prominent zinc ore, Fig. 68, which often has light coloured ZnS rich cores surrounded by sub-mm nested, sequentially coloured, bands of ZnS crystals that are arranged in cm-sized clusters [527].

In a similar fashion to the agate problem (Sec. 5.1.1), both intrinsic and extrinsic mechanisms have been proposed to explain the formation of these patterns. In particular, the origin of banding has been sought in pressure–temperature fluctuations, where shifts in these conditions during sphalerite formation alter the solubility of various elements. For instance, Zhu et al. [528] demonstrate that sphalerite deposits show variations in zinc and sulphur isotopes, which correlate with changes in fluid temperatures over time. This results in the rhythmic deposition of sphalerite layers with slightly different compositions, contributing to band formation. Other models [529, 530] suggest episodic fluid flow during hydrothermal mineralization, with long hiatuses separating periods of rapid crystallization. Variations in the concentration of chemical elements in successive hydrothermal infiltrations can lead to alternating layers of different compositions, creating banding. A common criticism of these models is that attributing each of the tens or hundreds of thousands of layers to an episodic event, such as a crack-seal cycle, seems to violate the principle of Ockham's razor [94].

Intrinsic models, on the other hand, suggest that the origin of the sphalerite banding is a process of self-organization and that it was formed in a single event of oscillatory zoning [531, 532, 527, 533] (Sec. 4.1.6). A pioneering model of this kind [531] attributes oscillatory zoning in sphalerite to cyclic supersaturation and

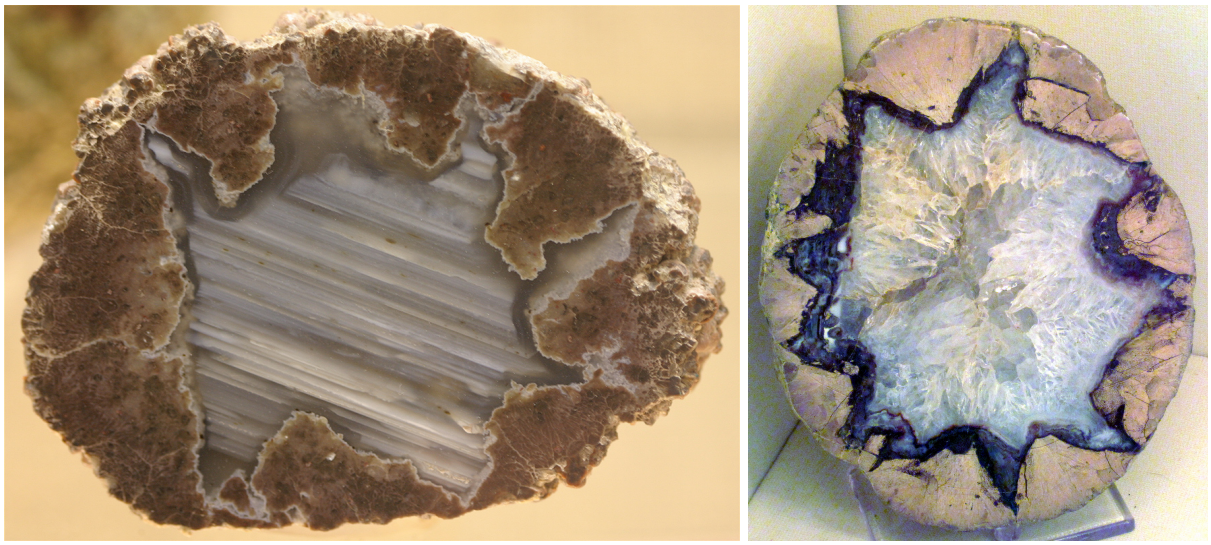


Figure 69: Thunder eggs. Left: Agate thunder egg (image: Cacophony, CC-BY-SA-3.0,2.5,2.0,1.0); Right: Quartz thunder egg, Oregon, USA (image: James St. John, CC-BY-2.0).

diffusion-controlled concentration gradients during crystallization. There is a feedback loop here occurring during crystallization when two or more different cations compete for incorporation into a mineral structure. Initially, one cation is preferentially incorporated into the growing crystal while the other accumulates in the surrounding fluid. Once the concentration of the excluded cation reaches a threshold, it begins to be incorporated into the crystal, which results in a banding pattern [534].

A somewhat more complex mechanism has been proposed by L'Heureux [532], Katsev et al. [527], Katsev and L'Heureux [533]. Their model combines the effects of geochemical reactions, crystal growth, dissolution, and ripening under far-from-equilibrium conditions. An important role in the final formation of the banded structure is played by a self-propagating sequence of growth and dissolution events, known as coarsening waves [535, 85]. The mechanism here is a form of Ostwald ripening (Sec. 4.6): as larger particles grow, they deplete the solute in their vicinity, causing smaller particles to dissolve and the solute to diffuse toward the larger particles. As shown by Feeney et al. [535] and Boudreau [85], this feedback mechanism leads to the formation of periodic structures or bands, which propagate as waves through the medium. These waves represent regions of alternating high and low particle concentration, coarsening over time as the system evolves toward a more stable state. In the case of sphalerite patterns, this process can occur over geologically short time-scales: although the formation of the entire cm-scale sphalerite cluster may take thousands of years, the band pattern itself is predicted to form on a time scale of months [527]. This opens the possibility that intrinsic and extrinsic models may work in conjunction, with intrinsic mechanisms responsible for sub-mm scale features and external conditions controlling cm-scale variability.

Lastly, it is worth noting that sphalerite banding has also been linked to microbial activity [536], with microglobular sphalerite textures interpreted as fossil microbial mats of sulfate-reducing bacteria, as evidenced by sulphur isotope data.

5.3.4. Thunder eggs

Thunder eggs or lithophysae [537] are spherical to ovoid cavities (Fig. 69) typically found within rhyolitic and other silicic volcanic rocks [538]. They may look externally similar to geodes (Sec. 5.2.7), but thunder eggs have a distinct origin and internal structures. They are often filled with minerals such as agate [539], quartz, chalcedony, or opal [540]. Thunder eggs form in silicic volcanic rocks, particularly rhyolites and tuffs, during or shortly after emplacement [541]. Their formation is commonly described as two main stages: cavity formation and mineral infill. Initial cavities within solidified volcanic rock generally form from trapped gas



Figure 70: Orbicules in granitoid rocks (images: kristallin.de; CC-BY-SA 3.0).

bubbles in the viscous magma or through shrinkage cracks as the lava cools and contracts. An alternative or complementary mechanism involves spherulitic growth, in which silicate minerals like quartz or feldspar crystallize radially from a central nucleus, creating a ball-like structure. These structures may then develop voids or fractures that later become filled with minerals. After the cavities form, mineral-rich solutions, often silica-laden, permeate the volcanic rock. Over time, chalcedony, agate, quartz, or opal precipitate from these solutions and fill the hollow centres of the thunder eggs.

5.3.5. Orbicules

Orbicular granitoid rocks containing orbicules, Fig. 70, are uncommon rocks with localized occurrence that have attracted the attention of geologists for at least a century [542]. They are characterized by orbicules, spheroidal bodies with concentric shells, comprising layers of mafic minerals, primarily phyllosilicate, and felsic minerals, predominantly quartz and feldspar [1]. These layers comprise elongated crystals growing radial or tangential to the shells [543, 544]. The orbicules seems to form around a grain in a cooling magma chamber, although alternative theories about a metasomatic origin have been proposed in the past; see references in Vernon [544]. The diameter of these orbicular structures can range from less than 5 cm (ultrabasic rocks), 5–10 cm (basic rocks) and up to 40 cm for granites [545]. Finland has the highest number of reported occurences, although this kind of rocks can be found elsewhere.

5.3.6. Clathrites

Clathrites, Fig. 71, are methane-derived precipitates formed by the transformation of clathrates into carbonates. Clathrates, clathrate hydrates, or gas hydrates are partially solid structures composed of water molecules arranged in crystalline cages. Within these structures, small molecules, usually non-polar gases, are confined within the ice-like polyhedral water cages. Clathrates can evolve into clathrites over time. This replacement is directly linked to the transformation of clathrates into carbonates, while partially preserving and mirroring their patterns and mesoscale structures. Kennett and Fackler-Adams [547] coined the term chlathrite in 2000 to describe mesoscale structures showing soft-sediment deformation associated with gas hydrate formation or dissociation. These structures are found within massive gas-hydrate layers and sometimes exhibit surface morphologies created by a direct mirroring of clathrates bubble structures. Examples of sites where clathrites have been observed include the Gulf of Mexico [548, 549], north Italian Apennines [546], Mediterranean Sea mud volcanoes [550], and Cascadia, (north west America [551].

5.3.7. Menilites

Menilites are rocks of botryoidal appearance composed mainly of opal (Sec. 5.1.4) and dolomite [553, 552]. They occur mainly in simple centimetric forms such as spheres, dumbbells or rods (Fig. 72A). However, the

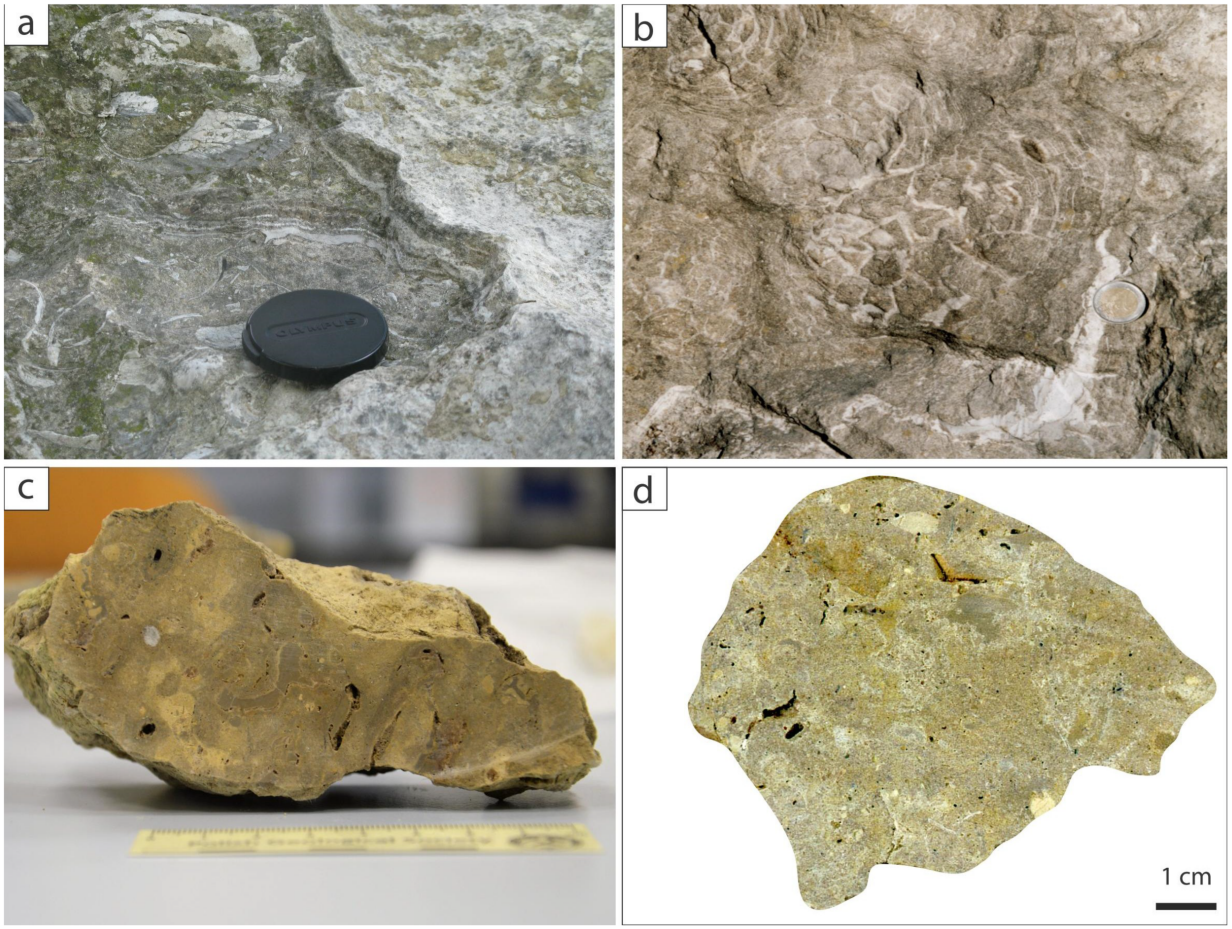


Figure 71: Clathrite structures. A: Thin layered structures surrounding a carbonate breccia with shell fragments. B: Irregular network (mainly radial to concentric) of carbonate-filled veins. C,D: Vacuolar, spongy and vuggy-like fabrics: cavities have various shapes, empty or filled with carbonate cements and/or coarser sediments and coquina debris. (Images: CC-BY Argentino et al. [546]).

most interesting are the larger specimes ($>$ 5 cm) with more complex shapes (Fig. 72B). Recently, it has been proposed that the formation of these rocks may be related to paleoseismic events [552]. A fluid phase is involved in their formation, developing within porous strata above the water table and becoming fluidized by earthquake shaking that drives upward water flow. The density contrast between these nodules (opaline, less dense) and the bedrock (marls and limestones, denser) implies that, under wet conditions, an osmotic-pressure difference (Sec. 4.3) can develop if the opal-carbonate interface is considered a membrane (i.e., an elastic interface). If inflowing water ruptures this membrane, the pressurized internal fluid is extruded, forming the characteristic shapes of these rocks.

5.4. Large and hot

Here we meet metre-scale structures powered by intense thermal or mechanical budgets. Cooling magmas fracture into columnar joints, lightning fuses sand into hollow fulgurites, buoyant hydrothermal fluids build towering chimneys, and deep-crustal stress forges gneissic foliation. Mud volcanoes, pockmarks, seeps and earthquake-driven seismites round out the set, all tapping high heat flow or transient tectonic energy to pattern rock and sediment over decimetres to metres.



Figure 72: Menilites with simple (A) and complex (B) shapes (image: Pimentel et al. [552]).

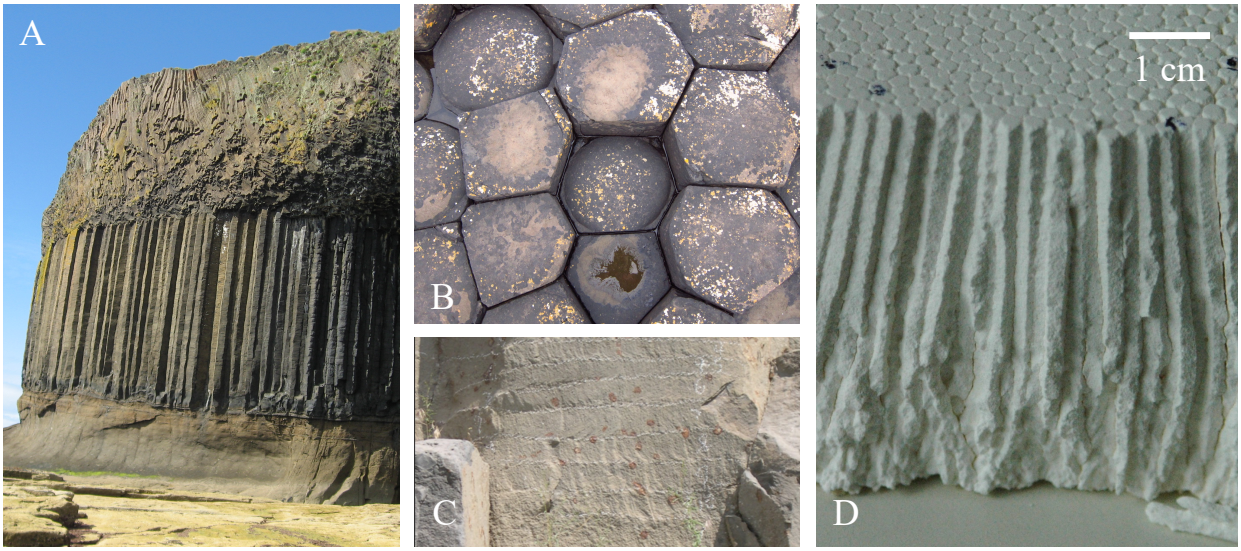


Figure 73: Columnar jointing in lava and starch. A: At Staffa, Scotland, a well-formed colonnade sits atop an ash layer, and is surmounted by an entablature of thinner, more disordered columns. The colonnade cooled from the ash-contact upwards, while the entablature cooled from above. B: A cross-section of columns at the Giant's Causeway, N. Ireland, highlights their polygonal shape. C: Striae, appearing as short bands on the face of any column, record the stick-slip motion of the column's formation. Plumose (left/right-leaning feathery lines, marked by arrows) also indicate the direction in which each crack advance occurred. D: When a slurry of corn starch is dried, it also cracks into columnar joints. The sample here is shown inverted, with the base of the colonnade exposed, to better display the hexagonal pattern that developed. (images: Lucas Goehring).

5.4.1. Basalt columns

Appearing as a striking pattern of roughly hexagonal pillars of rock, columnar joints are famous from landscapes like those of the Giant's Causeway in Northern Ireland, and the Devil's Postpile in California. At these places, basalt has broken into a colonnade consisting of regular, prismatic columns of rock, each a few tens of centimetres across. The cracks that delimit the edges of these columns were formed as the basalt cooled from molten lava, millions of years ago. Subsequently exposed by erosion, the evocative scenery of columnar jointing, as shown in Fig. 73, has attracted scientific attention for centuries [554]. The origins of

columnar joints in the thermal contraction of a cooling lava flow have been recognized since at least the 19th century [14], and recent research has focused on explaining the origins of the regular pattern of cracks that form the joints, as well as the physics that determines the size of the columns.

Although best known in the form of columnar basalt [555, 556, 557, 17, 558], columnar joints occur in a wide variety of materials. They are common in other lava types, including rhyolite and andesite [15, 559], and have been reported in igneous rocks on Mars [560, 561] and the moon [562, 563]. Columns can also be found in sandstone [564] and chalk [565] where they are thought to result from the cooling and contraction after some intense thermal treatment, for example by the invasion of a nearby dyke or sill; for similar reasons, columns are sometimes found in smelter slag, coal, and rapidly quenched glass [559, 566].

Columnar joints in lava typically form when a lava flow cools slowly over time. The lava could be emplaced as a massive flood basalt, covering thousands of square kilometres [556, 559, 17] or as a pond or stream that formed after a smaller volcanic eruption, as is common in Hawaii [567, 555]. As the initially fluid lava cools, it solidifies. The details of this process will depend on the specific chemistry of a lava, with a series of distinct minerals crystallizing from the melt over a range of temperatures. However, to a good approximation, there will be a change from a fluid-like to a solid-like rheology, corresponding to a glass transition or liquidus-solidus transition around 800–900°C [567, 568, 569, 570]. Below this temperature the lava will behave as an elastic solid, and accumulate tensile stress due to thermal contraction. This situation sets up a stress gradient in the lava, mirroring the thermal gradient, which drives fracture.

Since a molten lava flow will cool inwards from its boundaries, the initial cracks will appear at the surfaces of the flow. This process has been observed, for example, in the cooling of fresh lava lakes from the Kilauea volcano [567]. As time and cooling proceed, the cracks from the surface will grow deeper. They will develop into a network of crack tips following just behind the solidification front, where the cooling lava supports an elastic stress. This crack network effectively carves out the columnar features as it advances [14, 15]. The motions of the crack tips are not smooth, however, but rather the cracks that will form the column faces advance intermittently. When any crack grows, its active tip will move into warmer conditions. As a result, the tensile forces driving the fracture become weaker, and it will soon slow down and halt. After sufficient thermal stress has then had time to build up again, the crack can be reactivated, grow forward, and halt once more. As shown in Fig. 73C, this stick–slip motion is recorded by a roughly periodic banding along the faces of the columns; features called striae that look similar to chisel marks [555]. Within each band, the crack surface is smoothest under the more brittle conditions of the crack initiation, and becomes rougher as the crack advances into warmer rock and slows down [555, 559]. Combined with slight mismatches in the orientation of subsequent striae, and with plumose markings—faint feathery lines that develop perpendicular to the direction of crack propagation—these periodic variations in texture can be used to determine the direction in which a colonnade developed [555, 559, 571, 17]. For further details, see Pollard and Aydin [572] who review the geology and petrology of columnar joints, and explain how to interpret the surface features (striae, plumose, hackle) on column faces.

The directional growth of columnar joints also provides the route for columns to take on well-ordered polygonal shapes. Near the flow margin, the fracture network that defines the columns looks similar to the contraction cracks that can be seen in dried mud or clay (Sec. 5.2.6) [567, 557, 571]. This pattern is dominated by cracks intersecting at T-shaped junctions, which is the result of the sequential fragmentation of the surface: later cracks will curve to intersect earlier ones at right angles, to maximize their energy release rate [573]. As the columns grow, the incremental advances that leave the striae features allow the crack network to change: each crack advance can be slightly misaligned with the previous step. Over time, the crack intersections that form the corners of the columns will then shift towards Y-shaped junctions. In lava flows, this can be seen within the first 1–2 m of a flow margin [557]. The Y-junctions are energetically favoured in situations where the advancing cracks are guided or triggered by the locations of previous features, but where the sequence in which the cracks form is randomized in each cycle of fracture growth [574]. Goehring and Morris [575] review in more detail this process of the ordering of hexagonal fracture patterns.

The manner in which a colonnade grows means that it records how a lava flow cools. In particular, the columns extend along the direction of cooling, and perpendicular to isotherms at the cracking front, near to the solidus or glass-transition temperature [14, 15, 571, 576]. Some common structures formed in this way

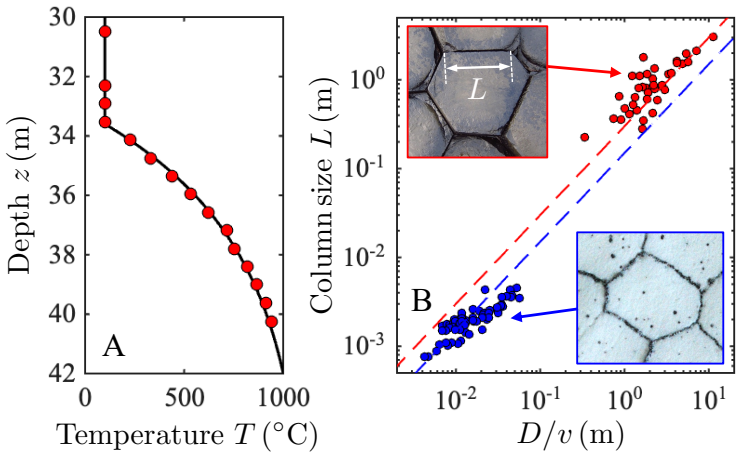


Figure 74: Scaling of columnar joints. A: Temperature measurements (red points) from boreholes at Kilauea Iki, Hawaii, are well-fit by stationary solutions to the advection-diffusion problem (black line); data reproduced from Hardee [577], Helz [584], borehole KI75-1. B: Testing of the thermoelastic/poroelastic model of columnar joint scaling. The size of the columnar features, L, can be taken as the distance between adjacent vertices of a column. The corresponding advection-diffusion length, D/v can be estimated for the cases of cooling lava columns (red points) and drying starch columns (blue points). Both cases show a simple scaling of $Pe = vL/D \sim 1$. Data reproduced from Goehring et al. [582].

include fans of columns, rosettes and chevrons, in addition to the more typical horizontal colonnade [15]. A fan can form as columns radiate away from a strong cooling site, for example. The fracture network of a developing colonnade is highly permeable, allowing water and gas to circulate within the cracks, enhancing cooling [577, 556, 571, 17, 570]. Clear evidence for this comes from borehole measurements in the cooling Kilauea Iki lava lake [577], which for many years maintained a near-constant 100°C temperature from the surface to within about ten metres of the still-molten regions of the lake, see Fig. 74Aa. It is thought that water percolating through the cracks boils near the molten lava, then flows away as steam to condense near the flow margins [577, 16, 571, 17]. The efficiency of this two-phase convective mechanism means that a relatively constant cooling rate can be maintained over the periods of time—years or decades—that a regular colonnade takes to develop.

A large lava flow will tend to spread out into a thin but wide layer, which cools simultaneously from above and below. This leads to the common arrangement of an upper colonnade, which cooled from the top down, and a lower colonnade, which cooled from the bottom up. In many landscapes multiple flow units, each from a different volcanic event, can be layered on top of each other; there are at least four such layers visible in the cliffs above the Giant's Causeway, for example [578]. More complex, multi-tiered structures have also been reported within a single flow unit, such as at the Columbia Plateau [556, 559]. Finally, the upper colonnade is frequently replaced by a layer of narrow and much more randomly oriented columns, a structure called entablature, as in the top layer of Fig. 73A. It is still not clear why or how entablature forms, although it has been implicated with enhanced and localized cooling [556, 579]. Hamada and Toramaru [580] give a recent, detailed discussion of this curious open problem.

The rate at which the lava cools also affects the size of the columns, with faster cooling generally leading to smaller columns [555, 581, 571, 17, 582]. The striae provide the best evidence of this connection, which is also supported by analysis of the crystal texture [556]. In particular, the thickness or height of the striae provide insight into the cooling rate of the lava, and there is a strong correlation between the size of the striae, and the size of the columns on which they appear [581, 583, 17, 570]. This would be the case if the column size is inversely proportional to the cooling rate of the lava when the columns formed.

A simple physical model of the elastic stresses generated as a lava lake cools can summarize much of our current understanding of the formation of columnar joints [582]. Above the boiling point of water, heat will only be transported by diffusion, with some effective thermal diffusivity D. Attention can thus focus

on the temperature T of a slab or layer of rock, lying between this isotherm, and that of the glass-transition temperature. This region represents a cooling front that is advancing at some speed v into the lava lake. By transforming to a coordinate system that moves with the cooling front, heat transport is modelled by a one-dimensional advection–diffusion equation,

$$\partial_t T = v\partial_z T + D\partial_{zz} T, \tag{15}$$

for depth z and time t. Away from the surface, the temperature profiles across the cooling front will evolve towards a steady-state solution in the co-moving reference frame. This problem can then be made dimensionless by scaling the system by a characteristic length-scale L, such that

$$Pe\partial_z T + \partial_{zz} T = 0, \tag{16}$$

where $Pe = vL/D$ is the Péclet number, which represents the relative strengths of advection and diffusion. In support of this model, borehole measurements of the cooling of the Kilauea Iki lava lake in Hawaii show good agreement with the solutions of Eq. 16, as first reported by [577] and shown in Fig. 74A.

As lava cools, thermal contraction leads to the development of tensile stress, which is relieved by fracture, as has been described above. The key point here is that the crack tips, and their driving force for fracture, are confined to a thin layer near the solidification front. This elastic layer is the direct result of thermal contraction and its thickness will be inherited from thermal profile of the lava, obeying the same scaling as Eq. 16: faster cooling, or weaker diffusion, will result in a thinner, more compact front. When a thin, brittle layer cracks, each crack will release the stress in its immediate vicinity and the crack spacing will tend to saturate when the average distance between cracks is a small multiple of the layer thickness [585, 586]. This is also the case when a layer of mud, paint, or slurry dries: the final crack spacing is a few times the layer thickness [587, 588, 589]. By identifying the column size as the representative length-scale, L, of the thermoelastic problem, this model of columnar joint formation predicts that all colonnades should grow under conditions of some fixed Pe, of order one. In other words, that the column size L is proportional to, and of the same order as, the advection-diffusion length D/v. This prediction is shown in Fig. 74B, along with field data from Goehring et al. [582] that is best fit by $Pe = 0.3$. The observed scaling also explains the earlier finding that a column's size, on average, is inversely proportional to the cooling rate, and hence v, of a colonnade.

The development and validation of this model of columnar joints has been greatly aided by analogue laboratory experiments involving colonnades produced in drying starch; see Fig. 73D. The interpretation of such studies relies on the mathematical analogy between the theories of poroelasticity and thermoelasticity, i.e., the equivalence between the elastic stresses generated by drying and by cooling, respectively [582]. This correspondence is demonstrated in Fig.74B, where data from dried starch colonnades are plotted against a best-fit line of $Pe = 0.15$. The first detailed experiments of Müller [590] highlighted the value of drying starch as an analogue system, although there are occasional mentions of it in earlier literature [591, 566]. Müller's work was followed by a series of quantitative studies that showed how to control column size by adjusting the drying rate of the starch [592]; tracked how the pattern ordered with depth [593]; linked column growth to the passage of a sharp drying front [594]; and provided numerical simulations of crack arrays advancing along with the drying front [595]. Plumose structures on the larger joints of dried starch [596] and other pastes [597] confirmed the interpretation of their appearance in lava joints. Three-dimensional images of dried starch colonnades, obtained by X-ray tomography [590, 594, 593, 598, 599, 580], also confirmed how columns grow normal to the direction of drying, analogous to cooling, and led to the current appreciation of how the column size depends inversely on the drying / cooling rate. These analogue experiments, and the mathematical analogy between cooling and drying that enables a strong interpretation of their results, are reviewed in detail in chapter 7 of Bacchin et al. [600], and chapter 9 of Goehring et al. [601].

More recently, research on columnar jointing has progressed into a number of promising additional areas. Detailed mapping of the topology and geometry of columnar joints has led to the development of simple, low-dimensional metrics that can distinguish between a wide variety of crack patterns with distinct origins [602, 603, 604]. The origins of entablature remain enigmatic, but innovative lines of experiment [580] have begun to unravel their nature. The related concept of *master cracks*, joints that enable faster local cooling,

is also being explored [579, 605, 580, 606]. With more practical aims, research has been made into how the strongly anisotropic texture of columnar joints affects their hydrological and mechanical properties, such as their relative permeability to fluid flow along different directions [607, 608, 609], and their strength and resistance to deformation [610]. These applications address questions such how to best utilize basalt formations for carbon geosequestration [611, 612].

5.4.2. Hydrothermal vents

Submarine hydrothermal vents on the ocean floor form by the precipitation of minerals from hydrothermal fluids as they mix with the surrounding seawater. As hotter, mineral-rich water exits the vent and encounters colder seawater of a different pH, minerals precipitate, forming characteristic structures (Fig. 75).

There are several varieties of vents [613]. Hotter *black smokers* emit dark, particle-rich, acidic plumes primarily composed of iron and sulphide minerals. Cooler *white smokers* emit lighter-coloured plumes, often rich in barium, calcium, and silica. A third category, discovered more recently, comprises cool alkaline vents first documented at the Lost City hydrothermal field in the mid-Atlantic [36]. The chemical and thermal differences between the vent types are reflected in differing physical growth mechanisms [186].

A black smoker attains a thickness of 7 cm in 5 days [614], while a white smoker needs 2 years to achieve a thickness of 10 cm [615]. Thus transport across the wall for hot black-smoker vents should be slower than for cold white-smoker vents, all other conditions being equal, and so hot vents are more isolated from the surroundings. Radial tube growth can be driven by (1) thermal diffusion or (2) chemical diffusion; the former is faster and produces a solid wall more rapidly than the latter. Consequently, hot vents experience less contact between vent fluids and and seawater (the chimney becomes solid quickly), whereas cold vents permit longer exchanges across the wall. These differences are seen in Fig. 76, which shows the growth rates of different vent types [616].

Hydrothermal vents display certain characteristic patterns, particularly chimneys and flanges (Fig. 75). The primary structures at vents are chimneys: tall, tubular structures formed by mineral precipitation that builds a sheath around the fluid plume as it emerges from the seabed. Thus chimneys grow over time and can reach many tens of metres in height. Their internal structure may consist of a single conduit through which the mineral-laden water flows, or it may be much more complex, comprising a multitude of micro- to nano-scale channels permitting slower, more diffuse flow through a porous matrix (Fig. 7). Such flows are likely to display chaotic advection (Sec. 4.2.8). Flanges are horizontal structures that project from the sides of chimneys, creating ledge-like features from which secondary chimneys may also grow upward. Flanges form from by mineral deposition as the hydrothermal fluids cool and precipitate minerals. They often trap pockets of superheated water beneath them [617].

Hydrothermal vents are natural analogues of chemical laboratory experiments called chemical gardens [41]. In a chemical-garden experiment, a soluble metal salt introduced into a solution containing a counter-anion, often silicate or carbonate, precipitates an insoluble salt [618]. The precipitate forms a cohesive membrane that envelopes the jet while still permitting ion transport and continued reaction [619].

Hydrothermal vents, specifically those of the Lost City type emitting cool alkaline fluids associated with serpentinization [36, 187], have been suggested as candidate sites for the origin of life on Earth [192, 620, 188]. The hypothesis is that micro-compartments in submarine alkaline hydrothermal vents separated by mineral membranes may have been where the first proto-bio-chemistry emerged [621, 622]. As well as the deep ocean site of Lost City, similar vents have been found in shallow waters at Strytan, Iceland [623, 616] and at Prony Bay, New Caledonia [624].

5.4.3. Mud volcanoes, pockmarks and seeps

Submarine seeps and mud volcanoes are structures that form part of the Earth's fluid venting systems. These structures expel fluids, including liquids, principally water but also hydrocarbons, and gases (e.g., carbon dioxide and methane), from the subsurface to the seafloor [626] or land surface [627]. Cold seeps are associated with the slow seepage of hydrocarbons, methane, and other fluids at or near ambient seafloor temperatures. Hot seeps involve the expulsion of warmer fluids, often associated with hydrothermal systems. Pockmarks are shallow depressions formed by the escape of fluids and gases from the seabed, resulting in crater-like morphologies. Submarine mud volcanoes occur on the seafloor and are often linked to deep-seated

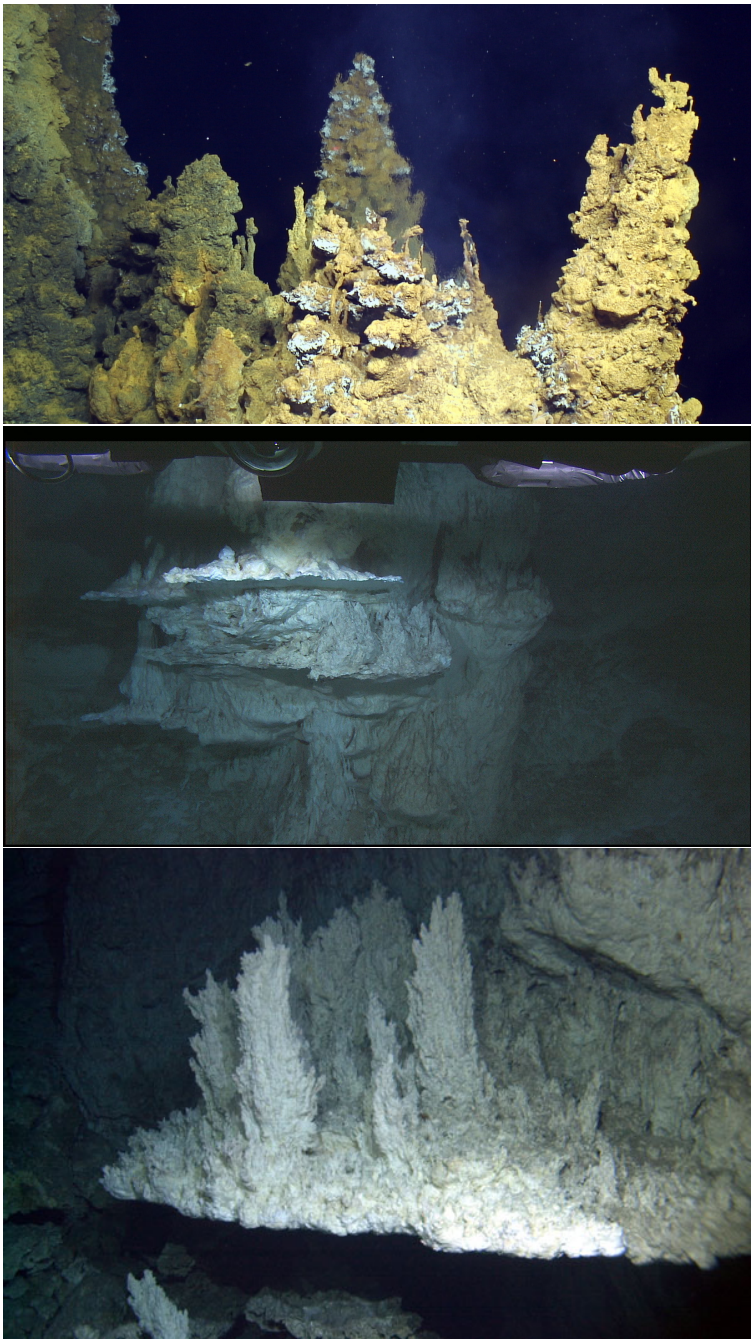


Figure 75: Hydrothermal vent structures: chimneys and flanges (images: Submarine Ring of Fire 2014 - Ironman, NSF/NOAA, CC-BY-SA-2.0; NOAA, public domain; NSF, public domain).

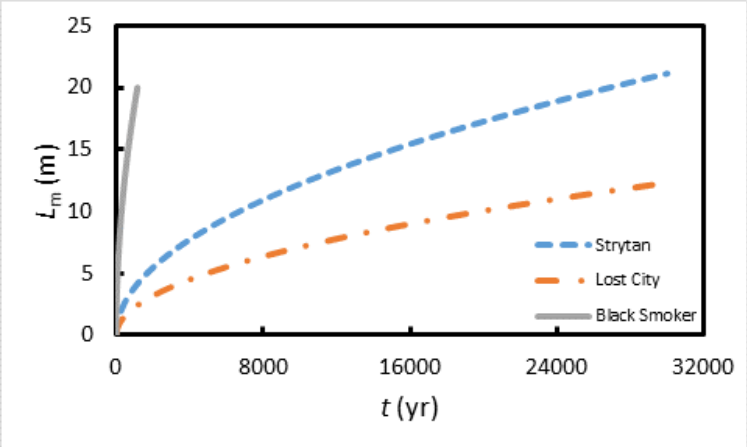


Figure 76: Fluid-mechanical model prediction of the growth of a hydrothermal vent over time t in terms of wall thickness L_m compares black smokers (grey) Strytan (blue) and Lost City Hydrothermal Field (orange) vents [186].

overpressure zones, faulting, or hydrocarbon reservoirs. Terrestrial mud volcanoes are found on land and are often associated with tectonic plate boundaries or sedimentary basins with high fluid pressure.

Submarine seeps typically involve the upward migration of fluids through vertical conduits, such as fractures, faults, or permeable sedimentary layers. Mud volcanoes, both submarine and terrestrial, are characterized by the upward movement of fluidized sediments, mud, and gases through a central vertical conduit. These conduits allow fluids to move from deep subsurface reservoirs to the seafloor or land surface. The vertical conduits of mud volcanoes are typically associated with high-pressure environments, where fluid overpressure exceeds the strength of overlying sediments, leading to the formation of fractures and the eruption of materials. The process is driven by buoyancy forces, where lighter fluids like hydrocarbons and gases rise through denser surrounding sediments, and by osmotic pressure [181] (Fig. 77). In some cases, fluids may migrate laterally along permeable layers before reaching the seafloor [182]. Horizontal migration is influenced by geological structures like unconformities or bedding planes, as well as by self-sealing/self-capping processes [628].

Submarine seeps and mud volcanoes often lead to the precipitation of carbonate minerals, forming distinctive authigenic carbonate structures, such as mounds, tubes, or chimneys (Fig. 78). As in most geological instances in this review, we do not have experimental confirmation of the formation mechanisms. But there are at least three aspects to the formation of these structures. 1) there can in some instances be dissolution; this would depend, like in the case of solution pipes (Sec. 5.2.2), on the rock type and the solution pH. 2) Probably more common than dissolution is unconsolidated sediment being washed out by the fluid fluid in a self-concentrating flow process. 3) There is frequently precipitation around the walls of the flow as CO_2 turns to carbonate rock. This is frequently bacterially mediated. Expelled materials from mud volcanoes, such as mud and brecciated rock fragments, can lithify over time, forming mudstone or breccia deposits. These rocks serve as evidence of past mud volcanic activity. Mud volcanoes may leave behind diatreme-like structures or intrusive bodies of mudstone that cut through surrounding sediments, providing clues to the ancient venting processes [629]. In some cases, large carbonate structures known as chemoherms can form around seeps due to the activity of chemosynthetic organisms [630]. These features are preserved in the rock record and indicate past fluid seepage events [631].

5.4.4. Fulgurites

Fulgurites are hollow glass tubes formed in sand, soil or rock by high-intensity electrical discharges, with lengths ranging from centimetres to metres [634, 635]. The first formal description of fulgurites may have been by Hermann [632] in the early 18th century (Fig. 79A) [636, 637, 638], but in the 13th century [639, 640], in the lapidary of Alfonso X *El Sabio*, King of Spain, they may appear under the name mazintarincan (Fig.

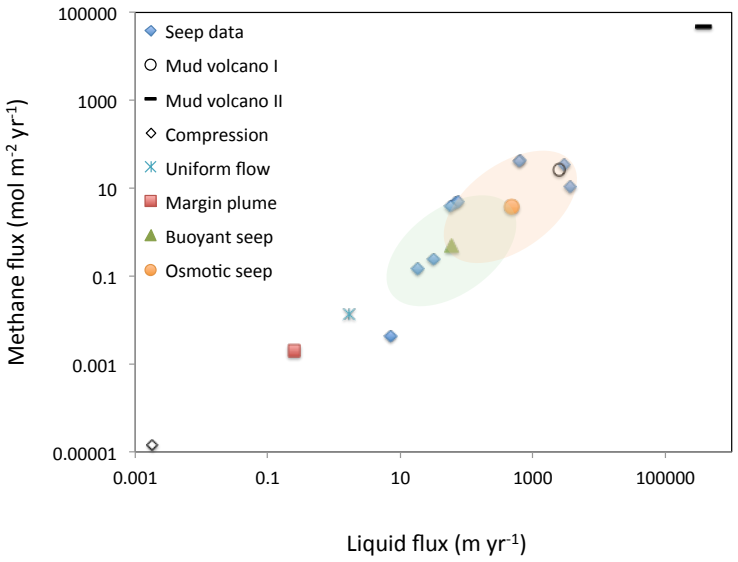


Figure 77: Dissolved methane flux plotted against liquid flux; comparison of field measurements at seeps and mud volcanoes with theoretical predictions for a uniform source of solute and a margin heat plume, and a buoyant or osmotic plume in a developed seep. The predictions are for a sediment permeability of 10^{-12} m^2 and an exit methane concentration of 8 mM; the green and orange shaded ellipses represent the range of permeabilities 10^{-13}–10^{-11} m^2 (along the major axis) and methane concentrations 0.6–126 mM (along the minor axis) for a buoyant and osmotic seep flow, respectively. An estimate of efflux from sediment compression alone is shown as a baseline. (Image: CC-BY Cardoso and Cartwright [181]).

79B) [633]. They form when lightning rapidly heats the substrate via the high-current discharge, producing glass. The substrate may be sand, clay soil, caliche, rock, or anthropogenic material. The substrate may be sand, clay soil, caliche, rock, or anthropogenic material [634, 48]. For a comprehensive survey of artificial fulgurites, see Pasek and Pasek [634].

When lightning strikes, rapid heating generates voids and vesicles along the discharge path, allowing volatile escape. These processes produce a glassy silica wall of cylindrical or elongated conical, usually hollow, morphology. This vitreous inner wall is surrounded by a rough outer rind containing partially melted and unmelted grains (Fig. 79) [48]. The origin of the central cavity has been attributed classically to gas expansion that presses and fuses the sand as the lightning travels through the ground [636], and, more recently, to sand vaporization along the discharge path [634]. The central hole, which may be single or composed of multiple closely spaced voids, is aligned with the lightning propagation direction (z-direction in Fig. 79). Secondary branches commonly emanate from the primary tube. The primary branch is typically the widest, though seldom more than a few centimetres in diameter [48].

Fulgurites have been divided into four categories, based on the ground composition [48]. Type I, sand fulgurites, are mainly composed of silica glass, and develop a thin inner wall (interior wall in Fig. 79C). If present, the outer wall is also composed mainly of silica glass with traces of Al and Fe oxides. Type II, clay fulgurites, form in soils composed of clays, sand and/or small rock fragments. Both inner and outer walls are clearly visible in these fulgurites. This type is wider and has larger glassy regions than type I. Type III, caliche fulgurites, form in desert hardpan or caliche. Silica glass constitutes less than 10% of the material and and is embedded within calcite. Type IV, rock fulgurites, form in bedrock; the glass walls are surrounded by unmelted host rock. They often occur as narrow tubes on the rock surface. In addition, a subcategory has been proposed: exogenic/droplet fulgurites (type V) [48]. This type forms when, after a very powerful lightning strike, (> 100 GW), melted substrate is ejected into the atmosphere, solidifying in the air. Rapid air cooling yields amorphous, droplet- or bubble-shaped morphologies that are generally greenish in colour [48, 640]. These fulgurites are mainly composed of glass and are often associated with Types II and IV fulgurites [48]. It has been proposed that the phosphide mineral schreibersite, $(Fe,Ni)_3P$,



Figure 78: Tubular concretions of authigenic carbonates, Pobiti Kamani, Varna, Bulgaria, preserve the subsurface plumbing network of an Early Eocene methane seep system in the Balkanides foreland [625] (image: Diego Delso, CC-BY-SA-4.0).

which can form as spherulites in fulgurites, may have provided an important source of prebiotic phosphorus on the early Earth, potentially facilitating the synthesis of phosphorus-bearing organic compounds [641].

Similar discharge morphologies are also observed in insulating materials, providing a useful counterpart to fulgurites. In this context, one speaks of Lichtenberg figures: intricate, branching patterns formed by dielectric breakdown in insulators [642]. They develop on the surface or within materials such as wood, acrylic, or glass when subjected to high voltage, and resemble fern-like or lightning-bolt shapes. These patterns trace the path of least resistance that the electrical current takes through the insulating material, leaving permanent marks or indentations. Breakdown can occur either on the surface or within the bulk, depending on material properties and field strength. Both Lichtenberg figures and fulgurites preserve the geometry of electrical discharge paths, but in different media: Lichtenberg figures record breakdown channels within solid dielectrics, while fulgurites capture the same process in geological materials, vitrified by extreme heating.

5.4.5. Foliation in gneiss

Foliation or banding in gneiss refers to the distinctive layering observed in this metamorphic rock, Fig. 80 [643]. Gneiss is formed through the process of metamorphism, which involves the alteration of pre-existing rocks under high pressure and temperature conditions. During this process, the minerals within the rock recrystallize and reorganize, leading to the development of a foliation. The foliation in gneiss is a result of the alignment of minerals or mineral layers parallel to the direction of pressure during metamorphism. This alignment gives gneiss its characteristic layered appearance, with alternating bands of different mineral compositions and colours. The banding is typically visible to the naked eye and can be straight or wavy. Foliation in gneiss can be classified into two main types: compositional and structural. Compositional foliation refers to the variation in mineral composition across the rock, creating bands of different minerals such as quartz, feldspar, and mica. Structural foliation, on the other hand, is related to the deformation of the rock during metamorphism, resulting in the alignment of mineral crystals or the development of preferred orientations. The presence of foliation in gneiss provides important information about its geological history and the conditions under which it formed. It indicates the intense pressure and temperature that the rock experienced during metamorphism. Additionally, the distinct layering in gneiss can be used to determine the direction and intensity of tectonic forces that acted on the rock.

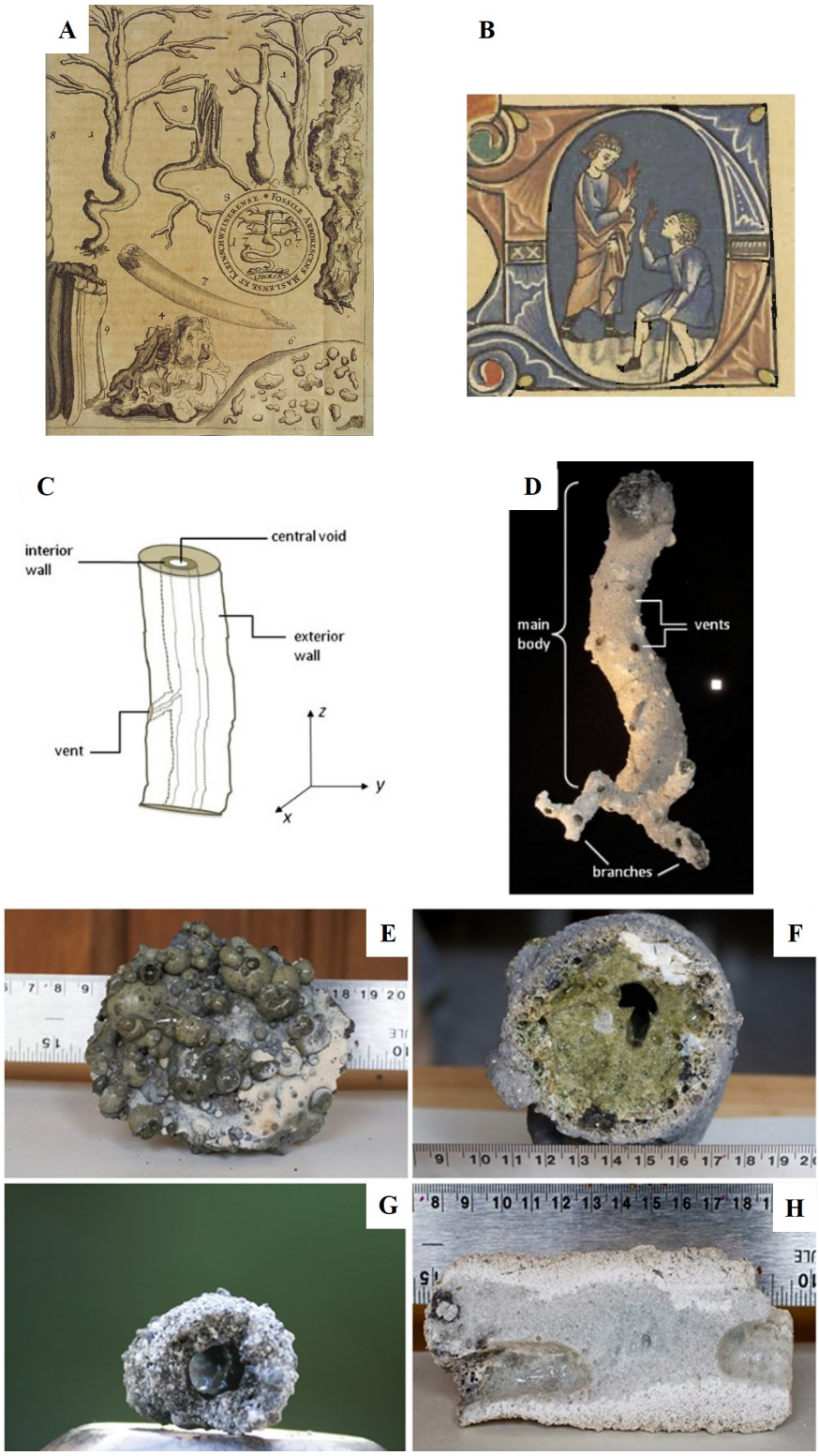


Figure 79: A: Fulgurite illustrations from the book written by Hermann [632]. B: Illustration of the lapidary of Alfonso X El Sabio [633], where there can be seen rocks with an arborescent aspect that resemble fulgurites. C) Scheme of fulgurite structure [48]. D) Lateral view of a natural fulgurite [48]. E–H) Fulgurites of ambiguous (natural or artificial/anthropogenic) origin [634]. An exogenic fulgurite can be seen in E, while in F–H fulgurites with a hollow tube in the inner part are shown.



Figure 80: Foliation in gneiss. Left: Gneiss foliation, Archean; Ennis Lake North roadcut, Madison County, Montana, USA; Right: Chevron folds in gneiss, Precambrian; Medicine Bow Mountains, Wyoming, USA (image: James St. John; CC-BY-2.0).

5.4.6. Seismites

The term *seismite* was coined in 1969 by Seilacher to describe structures in the Miocene Monterey Formation at Santa Barbara, California, USA [644]. He described a regular sequence comprising, from top to bottom, a liquefied zone, a debris zone, and a step zone, with gradational internal contacts and a sharp upper boundary, and interpreted this succession as earthquake generated [644]. Since then, numerous authors have used the term *seismite* to denote an earthquake-induced sedimentary structure [645, 646, 647, 648]. However, the term is debated, because many purported seismites reflect sediment liquefaction [649], and liquefaction can be triggered by multiple mechanisms; up to 21 have been described, including earthquakes, sediment loading, salt tectonics, and volcanic activity. Accordingly, some authors advocate the broader term soft-sediment deformation structures (SSDS) [649]. Settling this terminological debate is beyond the scope of this review (see, e.g., Shanmugam [649], which lists 27 SSDS types). Here we describe structures that have been reported as earthquake-related and we refer to them to as seismites.

Seismites (Fig. 81) occur all over the world, e.g., in the USA [644, 650], Germany [651], and Israel [652], to name just a few. In the work of Rodriguez-Pascua et al. [653], focused on the Miocene basins of the Prebetic Zone, Spain, the different SSDS found in the region are described and related to earthquake magnitude. According to Rodriguez-Pascua et al. [653], seismites in this region fall into two groups: features formed without liquefaction—typically linked to earthquakes of $M < 5$—and those formed after sediment liquefaction, generally requiring larger magnitudes. Non-liquefaction structures include loop bedding, disturbed varved lamination, and mixed layers without fluidization. Liquefaction-related structures include mushroom-like silts protruding into laminites, mixed layers with fluidization, pseudonodules, sand dykes, pillow structures, and intruded and fractured gravels; metre-scale features observed in shallow-lake, detrital settings. Among these soft-sediment deformation structures, the most striking are pillow structures, of which exceptional examples are found in the Baza Basin, Spain (Fig. 81). These pillow structures occur in deformed beds with thickness varying from a few cm to 2.5 m, the best examples being 1.5–2 m thick and 2–4 m in width [645]. These structures were generated when a lower-density unit (clays and silt) was overlain by a higher density unit (fine- and coarse-grained sands). When an earthquake occurred, the liquefaction of the clays caused them to rise upwards, breaking the overlying layer, generating escape structures and imparting the sand unit with a pillow-like morphology [645] in a geological manifestation of the Rayleigh–Taylor instability (Sec. 4.2.2). In some cases, lateral shear between mobilized and overlying layers may also produce secondary Kelvin–Helmholtz billows (Sec. 4.2.3), adding a wavy or rolled appearance to the interface.



Figure 81: Seismites. Above: giant seismites of Galera, Granada, Spain; on the left an overview of the pillow-like structures, on the right a detail of one of the pillows, about two metres across (images: Julyan Cartwright). Below: seismites in Lake Lisan (Pleistocene Dead Sea) sediments, Israel (images: Piotr Szymczak).

6. Summary and outlook

The physical mechanisms outlined in Section 4 generate the mesoscale geological patterns compiled in Section 5. They act on the material classes of Section 3, which align with soft-matter systems (Section 2). In this sense, mesoscale geological pattern formation is mediated by soft-matter physics, with mesoscopic building blocks (grains, pores, films) assemble into structures that remain mechanically compliant and reconfigurable while they form. Understanding their formation mechanisms is essential for explaining geological self-organization and constraining the physicochemical and mechanical conditions in the environments where these patterns originate. This, in turn, is critical for reconstructing Earth's past environmental conditions and geodynamic processes, and for distinguishing complex abiotic patterns from potential biosignatures—especially when evidence is sought for ancient life on Earth and, potentially, on other planets.

One key aspect is *self*-organization, i.e., structure generated by internal feedbacks within a minimally defined system. Because "the system" can always be expanded to make any pattern appear self-organized, we adopt the smallest system that closes the feedback loop and treat Earth's boundary conditions and large-scale drivings as external.

Although Earth scientists have long studied paradigmatic geological pattern-forming systems, they have not always labeled them *self-organized*. An oscillatory mesoscale mechanism was first proposed by Harloff [656], Phemister [657], and Hills [658] to explain plagioclase zoning. In the 1970s–80s, studies by Fisher [659], Fraser [660], Ortoleva [661] and Ortoleva et al. [662] explicitly attributed some rock and mineral patterns to geochemical self-organization. Since then, nonlinear dynamics ideas have spread from crystals and rocks to diverse geological systems. Interest has recently grown for two reasons: (i) mounting evidence



Figure 82: Equifinality of pipe-like forms produced by different processes. (Left) Karst solution pipes in dune limestone, Canunda National Park, South Australia. (Centre) Pipe-like conduits in a lateritized duricrust (lateritic pseudokarst), southern Queensland, Australia. (Right) Soil pipes formed along decaying tree roots, near Troy, Idaho, USA [654]. Similar morphologies arise from distinct mechanisms: dissolution in carbonate rock (left), mechanical erosion in soil (right) and a mixed chemical–mechanical regime in laterite (centre), which is harder to classify [655]. (Images at left and centre by Ken G. Grimes, reproduced with permission.)

that geochemical self-organization may have catalyzed steps in the transition from geochemistry to biology [40, 663, 664, 193, 665, 666, 667]; and (ii) the realization that abiotic self-organized structures such as silicate–carbonate biomorphs, though of limited geological relevance, can mimic cellular morphologies and risk misinterpretation [668].

Many geological patterns are *equifinal*: distinct mechanisms and environments can converge to nearly indistinguishable morphologies. Shape alone is therefore an ambiguous indicator of origin. Solution pipes in karst, for example, can resemble soil pipes in regolith even though one arises from dissolution along focused flow paths while the other reflects seepage-induced piping and mechanical removal (Fig. 82). Polygonal networks in columnar joints share pitch, node geometry, and arrested fronts with permafrost polygons, yet the active layer and energy source differ. Dendritic motifs in Mn-oxide films echo the branching statistics of drainage basins or electrochemical deposition, but the governing transport laws and kinetic thresholds are not the same. Banded textures — Liesegang rhythms, oscillatory zoning in crystals, varve-like laminations, or travertine and silica-sinter layering — likewise repeat at different scales under different couplings between transport, nucleation, and surface renewal. Even spherical or concentric bodies such as cannonball concretions, ooids, and accretionary lapilli share radius-selection logics while nucleation environments and growth regimes diverge; honeycomb (tafoni) textures produced by salt cycling or freeze–thaw can be indistinguishable at a glance; ring-like planforms tie together impact craters, volcanic ring dikes, and collapse dolines.

Terminology also drifts across communities and can obscure connections or suggest false contrasts. The same morphology may be labelled differently (for example, solution pipe versus soil pipe; chimney versus chemical garden), while a single term may span mechanisms (mudcrack versus polygonal terrain). To reduce ambiguity, we pair each morphology label with an explicit mechanism hypothesis, state the controlling parameter set using shared symbols and non-dimensional groups, and give the most common synonyms at first use. This keeps datasets comparable across geology, soft matter, and fluid physics while acknowledging that convergent forms need not imply identical drivers.

Overall, viewing these patterns through the lens of nonlinear dynamical systems yields constraints on the environmental and geodynamical conditions present during their formation. Such constraints aid both the reconstruction of Earth's geological history and the discrimination of abiotic from biologically influenced

mesoscale pattern formation. We hope this review helps advance that aim.

Acknowledgements

This review paper originated at the workshop "Geochemobrionics: Self-Organization in Geological Systems" organized by Sean McMahon at the University of Edinburgh in 2022. The workshop was funded by the European COST (Cooperation in Science and Technology) programme, action number CA17120, Chemobrionics. JHEC and CISD acknowledge support from the Spanish Ministerio de Ciencia, Innovación y Universidades through grant PID2024-160443NB-I00. EK acknowledges funding from the European Union´s Horizon 2020 research and innovation programme under the Marie Sklowdoska-Curie grant agreement No 101031812 ´NanoBioS´.

References

[1] P. J. Ortoleva, Geochemical Self-Organization, Oxford University Press, New York, 1994.

[2] B. Jamtveit, P. Meakin, Growth, Dissolution and Pattern Formation in Geosystems, Springer, Dordrecht, 1999.

[3] B. Jamtveit, Ø. Hammer, Sculpting of rocks by reactive fluids, Geochemical Perspectives 1 (2012) 341–481. doi:10.7185/geochempersp.1.3.

[4] A. Voigtländer, M. Houssais, K. A. Bacik, I. C. Bourg, J. C. Burton, K. E. Daniels, S. S. Datta, E. Del Gado, N. S. Deshpande, O. Devauchelle, et al., Soft matter physics of the ground beneath our feet, Soft Matter 20 (2024) 5859–5888. doi:10.1039/D4SM00391H.

[5] J. H. E. Cartwright, C. S. Cockell, J. G. Cosmidis, S. Holler, F. J. Huertas, S. F. Jordan, P. Knoll, E. Kotopoulou, C. C. Loron, S. McMahon, A. Neubeck, C. Pimentel, C. I. Sainz-Díaz, P. Szymczak, Self-assembled versus biological pattern formation in geology, preprint (2025). doi:10.48550/arXiv.2601.00323.

[6] P.-G. De Gennes, Soft matter, Science 256 (1992) 495–497. doi:10.1126/science.256.5056.495.

[7] D. J. Jerolmack, K. E. Daniels, Viewing Earth's surface as a soft-matter landscape, Nature Reviews Physics (2019). doi:10.1038/s42254-019-0111-x.

[8] D. J. Nash, S. J. McLaren, Geochemical Sediments and Landscapes, RGS-IBG Book Series, Blackwell Publishing Ltd, Oxford, UK, 2007. doi:10.1002/9780470712917.

[9] D. A. Budd, E. A. Hajek, S. J. Purkis (Eds.), Autogenic dynamics and self-organization in sedimentary systems, SEPM Society for Sedimentary Geology, 2016. doi:10.2110/sepmsp.106.

[10] R. Evans, D. Frenkel, M. Dijkstra, From simple liquids to colloids and soft matter, Physics Today 72 (2019) 38–39. doi:10.1063/PT.3.4135.

[11] J. H. Oehler, Hydrothermal crystallization of silica gel, Geological Society of America Bulletin 87 (1976) 1143–1152. doi:10.1130/0016-7606(1976)87<1143:HCOSG>2.0.CO;2.

[12] C. B. Howard, A. Rabinovitch, A new model of agate geode formation based on a combination of morphological features and silica sol–gel experiments, European Journal of Mineralogy 30 (2018) 97–106. doi:10.1127/ejm/2017/0029-2685.

[13] J. Langer, Dendrites, viscous fingers, and the theory of pattern formation, Science 243 (1989) 1150–1156. doi:10.1126/science.243.4895.1150.

[14] R. Mallet, On the origin and mechanism of production of the prismatic (or columnar) structure of basalt, Phil. Mag. 50 (1875) 122–135 and 201–226. doi:10.1080/14786447508641268.

[15] A. Spry, The origin of columnar jointing, particularly in basalt flows, J. Geol. Soc. Aust. 8 (1962) 191–216. doi:10.1080/14400956208527873.

[16] M. P. Ryan, C. G. Sammis, The glass transition in basalt, J. Geophys. Res. 86 (1981) 9519–9535. doi:10.1029/JB086iB10p09519.

[17] L. Goehring, S. Morris, Scaling of columnar joints in basalt, J. Geophys. Res. 113 (2008) B10203. doi:10.1029/2007JB005018.

[18] T. Monecke, T. J. Reynolds, T. Taksavasu, E. R. Tharalson, L. R. Zeeck, M. Guzman, G. Gissler, R. Sherlock, Natural growth of gold dendrites within silica gels, Geology 51 (2023) 189—-192. doi:10.1130/G48927.1.

[19] J. Kirkpatrick, C. Rowe, J. White, E. Brodsky, Silica gel formation during fault slip: Evidence from the rock record, Geology 41 (2013) 1015–1018. doi:10.1130/G34483.1.

[20] K. Borhara, C. M. Onasch, Evidence for silica gel and its role in faulting in the Tuscarora Sandstone, Journal of Structural Geology 139 (2020) 104140. doi:10.1016/j.jsg.2020.104140.

[21] J. Davidovits, Geopolymers: man-made rock geosynthesis and the resulting development of very early high strength cement, Journal of Materials education 16 (1994) 91–91.

[22] D. Kim, H.-T. Lai, G. V. Chilingar, T. F. Yen, Geopolymer formation and its unique properties, Environmental geology 51 (2006) 103–111. doi:10.1007/s00254-006-0308-z.

[23] C. Jaupart, S. Vergniolle, The generation and collapse of a foam layer at the roof of a basaltic magma chamber, Journal of Fluid Mechanics 203 (1989) 347–380. doi:/10.1017/S0022112089001497.

[24] R. Pal, Rheological behavior of bubble-bearing magmas, Earth and Planetary Science Letters 207 (2003) 165–179. doi:10.1016/S0012-821X(02)01104-4.

[25] J. Vasseur, F. B. Wadsworth, D. B. Dingwell, Permeability of polydisperse magma foam, Geology 48 (2020) 536–540. doi:10.1130/G47094.1.
[26] F. K. Morris, Amygdules and pseudo-amygdules, Bulletin of the Geological Society of America 41 (1930) 383–404. doi:10.1130/GSAB-41-383.
[27] S. Yariv, H. Cross, Geochemistry of colloid systems: For earth scientists, Springer Science & Business Media, 1979.
[28] M. Neelamma, S. R. Holla, M. Selvakumar, P. A. Chandran, S. De, Bentonite clay liquid crystals for high-performance supercapacitors, Journal of Electronic Materials 51 (2022) 2192–2202. doi:10.1007/s11664-022-09469-y.
[29] J. B. Jones, J. V. Sanders, E. R. Segnit, Structure of opal, Nature 204 (1964) 990–991. doi:10.1038/204990a0.
[30] J. A. Saunders, Colloids and nanoparticles: Implications for hydrothermal precious metal ore formation, SEG Discovery (2022) 15–21. doi:10.5382/SEGnews.2022-130.fea-01.
[31] H. Zöcher, Über freiwillige Strukturbildung in Solen, Z. anorg. Chem 147 (1925) 91–110.
[32] P. Davidson, J.-C. P. Gabriel, Mineral liquid crystals, Current opinion in colloid & interface science 9 (2005) 377–383. doi:10.1016/j.cocis.2004.12.001.
[33] J.-C. P. Gabriel, C. Sanchez, P. Davidson, Observation of nematic liquid-crystal textures in aqueous gels of smectite clays, The Journal of physical chemistry 100 (1996) 11139–11143. doi:10.1021/jp961088z.
[34] L. J. Michot, I. Bihannic, S. Maddi, S. S. Funari, C. Baravian, P. Levitz, P. Davidson, Liquid-crystalline aqueous clay suspensions, Proceedings of the National Academy of Sciences 103 (2006) 16101–16104. doi:10.1073/pnas.0605201103.
[35] E. Mattievich, J. Chadwick, J. D. Cashion, J. F. Boas, M. J. Clark, R. D. Mackie, Macroscopic ferronematic liquid crystals determine the structure of Kimberley Zebra Rock, in: 27th ann. cond. matt. phys. meet. conf. handbook, 2003.
[36] D. S. Kelley, J. A. Karson, G. L. Fruh-Green, D. R. Yoerger, T. M. Shank, D. A. Butterfield, J. M. Hayes, M. O. Schrenk, E. J. Olson, G. Proskurowski, M. Jakuba, A. Bradley, B. Larson, K. Ludwig, D. Glickson, K. Buckman, A. S. Bradley, W. J. Brazelton, M. J. E. Kevin Roe, A. Delacour, S. M. Bernasconi, M. D. Lilley, J. A. Baross, R. E. Summons, S. P. Sylva, A serpentinite-hosted ecosystem: the Lost City hydrothermal field, Science 307 (2005) 1428–1434. doi:10.1126/science.1102556.
[37] Y. K. Kharaka, F. A. P. Berry, Simultaneous flow of water and solutes through geological membranes—I. experimental investigation, Geochimica et Cosmochimica Acta 37 (1973) 2577–2603. doi:10.1016/0016-7037(73)90267-6.
[38] S. J. Fritz, Ideality of clay membranes in osmotic processes: a review, Clays and clay minerals 34 (1986) 214–223. doi:10.1346/CCMN.1986.0340212.
[39] C. E. Neuzil, Osmotic generation of 'anomalous' fluid pressures in geological environments, Nature 403 (2000) 182–184. doi:10.1038/35003174.
[40] M. J. Russell, R. M. Daniel, A. J. Hall, J. A. Sherringham, A hydrothermally precipitated catalytic iron sulphide membrane as a first step toward life, Journal of Molecular Evolution 39 (1994) 231–243. doi:10.1007/BF00160147.
[41] L. M. Barge, S. S. S. Cardoso, J. H. E. Cartwright, G. J. T. Cooper, L. Cronin, A. De Wit, I. J. Doloboff, B. Escribano, R. E. Goldstein, F. Haudin, D. E. H. Jones, A. L. Mackay, J. Maselko, J. J. Pagano, J. Pantaleone, M. J. Russell, C. I. Sainz-Díaz, O. Steinbock, D. A. Stone, Y. Tanimoto, N. L. Thomas, From chemical gardens to chemobrionics, Chemical Reviews 115 (2015) 8652–8703. doi:10.1021/acs.chemrev.5b00014.
[42] M. J. Zieg, B. D. Marsh, The Sudbury Igneous Complex: Viscous emulsion differentiation of a superheated impact melt sheet, Geological Society of America Bulletin 117 (2005) 1427–1450. doi:10.1130/B25579.1.
[43] B. Gogoi, A. Saikia, The genesis of emulsion texture owing to magma mixing in the Ghansura Felsic Dome of the Chotanagpur Granite Gneiss Complex of eastern India, The Canadian Mineralogist 57 (2019) 311–338. doi:10.3749/canmin.1800064.
[44] E. H. Cunningham-Craig, The origin of oil-shale, Proceedings of the Royal Society of Edinburgh 36 (1916) 44–86. doi:10.1017/S0370164600018125.
[45] M. R. Cicconi, D. R. Neuville, Natural glasses, Springer handbook of glass (2019) 771–812. doi:10.1007/978-3-319-93728-1_22.
[46] K. Heide, G. Heide, Vitreous state in nature—origin and properties, Geochemistry 71 (2011) 305–335. doi:10.1016/j.chemer.2011.10.001.
[47] C. Ma, J. Gresh, G. R. Rossman, G. C. Ulmer, E. P. Vicenzi, Micro-analytical study of the optical properties of rainbow and sheen obsidians, The Canadian Mineralogist 39 (2001) 57–71. doi:10.2113/gscanmin.39.1.57.
[48] M. A. Pasek, K. Block, V. Pasek, Fulgurite morphology: a classification scheme and clues to formation, Contributions to Mineralogy and Petrology 164 (2012) 477–492. doi:10.1007/s00410-012-0753-5.
[49] P. G. H. Boswell, The trend of research on the rheotropy of geological materials, Science Progress (1933-) 39 (1951) 608–622.
[50] M. A. Biot, Theory of folding of stratified viscoelastic media and its implications in tectonics and orogenesis, Geological Society of America Bulletin 72 (1961) 1595–1620. doi:10.1130/0016-7606(1961)72[1595:TOFOSV]2.0.CO;2.
[51] G. H. Matthes, Quicksand, Scientific American 188 (1953) 97–104.
[52] A. Khaldoun, E. Eiser, G. H. Wegdam, D. Bonn, Liquefaction of quicksand under stress, Nature 437 (2005) 635–635. doi:10.1038/437635a.
[53] D. Kadau, H. J. Herrmann, J. S. Andrade, A. D. Araújo, L. J. C. Bezerra, L. P. Maia, Living quicksand, Granular Matter 11 (2009) 67–71. doi:10.1007/s10035-008-0117-z.
[54] R. W. Griffiths, The dynamics of lava flows, Annual review of fluid mechanics 32 (2000) 477–518. doi:10.1146/annurev.fluid.32.1.477.
[55] E. Shalev, V. Lyakhovsky, Viscoelastic damage modeling of sinkhole formation, Journal of Structural Geology 42 (2012) 163–170. doi:10.1016/j.jsg.2012.05.010.
[56] A. M. Rubin, Dikes vs. diapirs in viscoelastic rock, Earth and Planetary Science Letters 117 (1993) 653–670. doi:10.

1016/0012-821X(93)90109-M.
[57] M. Veveakis, T. Poulet, A note on the instability and pattern formation of shrinkage cracks in viscoplastic soils, Geomechanics for Energy and the Environment 25 (2021) 100198. doi:10.1016/j.gete.2020.100198.
[58] P. Burnley, The importance of stress percolation patterns in rocks and other polycrystalline materials, Nature Communications 4 (2013) 2117. doi:10.1038/ncomms3117.
[59] B. Andreotti, Y. Forterre, O. Pouliquen, Granular media: between fluid and solid, Cambridge University Press, 2013.
[60] N. Gravish, D. I. Goldman, Entangled Granular Media, John Wiley & Sons, Ltd, 2016, pp. 341–354. doi:10.1002/9781119220510.ch17.
[61] H. Zheng, W. Niu, W. Mao, L. Li, F. Wang, Y. Huang, Mechanics of granular material and the application in engineering geology, Journal of Engineering Geology 29 (2021) 12–24. doi:10.13544/j.cnki.jeg.2021-0017.
[62] A. M. Turing, The chemical basis of morphogenesis, Phil. Trans. R. Soc. Lond. B 237 (1952) 37–72. doi:10.1098/rstb.1952.0012.
[63] J. D. Murray, Mathematical Biology: I. An Introduction, Springer, 1989.
[64] P. Ball, Forging patterns and making waves from biology to geology: a commentary on Turing (1952)'the chemical basis of morphogenesis', Philosophical Transactions of the Royal Society B: Biological Sciences 370 (2015) 20140218. doi:10.1098/rstb.2014.0218.
[65] E. F. McBride, M. D. Picard, Origin of honeycombs and related weathering forms in Oligocene Macigno Sandstone, Tuscan coast near Livorno, Italy, Earth Surface Processes and Landforms 29 (2004) 713–735. doi:10.1002/esp.1065.
[66] Ø. Hammer, D. Dysthe, B. Lelu, H. Lund, P. Meakin, B. Jamtveit, Calcite precipitation instability under laminar, open-channel flow, Geochimica et Cosmochimica Acta 72 (2008) 5009–5021. doi:10.1016/j.gca.2008.07.028.
[67] E. Meron, Pattern formation in excitable media, Physics reports 218 (1992) 1–66. doi:10.1016/0370-1573(92)90098-K.
[68] A. M. Zhabotinsky, A history of chemical oscillations and waves, Chaos: An Interdisciplinary Journal of Nonlinear Science 1 (1991) 379–386. doi:10.1063/1.165848.
[69] J. H. E. Cartwright, A. G. Checa, B. Escribano, C. Ignacio Sainz-Diaz, Crystal growth as an excitable medium, Philosophical Transactions of the Royal Society A: Mathematical, Physical and Engineering Sciences 370 (2012) 2866–2876. doi:10.1098/rsta.2011.0600.
[70] R. Burridge, L. Knopoff, Model and theoretical seismicity, Bulletin of the seismological society of america 57 (1967) 341–371. doi:10.1785/BSSA0570030341.
[71] J. H. E. Cartwright, E. Hernández-García, O. Piro, Burridge-Knopoff models as elastic excitable media, Physical Review Letters 79 (1997) 527. doi:10.1103/PhysRevLett.79.527.
[72] D. H. Rothman, Characteristic disruptions of an excitable carbon cycle, Proceedings of the National Academy of Sciences 116 (2019) 14813–14822. doi:10.1073/pnas.1905164116.
[73] J. D. Pelletier, How do spiral troughs form on Mars?, Geology 32 (2004) 365–367. doi:10.1130/G20228.2.
[74] K. Jabłczyński, Über Liesegang-Ringe, Kolloid-Zeitschrift 40 (1926) 22–28.
[75] R. Matalon, A. Packter, The Liesegang phenomenon. I. sol protection and diffusion, Journal of colloid science 10 (1955) 46–62. doi:10.1016/0095-8522(55)90076-3.
[76] F. F. Runge, Der Bildungstrieb der Stoffe : veranschaulicht in selbstständig gewachsenen Bildern (Fortsetzung der Musterbilder), Selbstverlag, Oranienburg, 1855.
[77] W. M. Ord, On the Influence of Colloids upon Crystalline Form and Cohesion, E. Stanford, London, 1879.
[78] R. E. Liesegang, Uber einige eigenschaften von gallerten, Naturwissensch Wochenschr 11 (1896) 353–362.
[79] H. K. Henisch, Periodic precipitation, Elsevier, 2014.
[80] I. L'Heureux, A. D. Fowler, Branching and oscillatory patterns in plagioclase and Mississippi-valley type sphalerite deposits, in: Growth, Dissolution and Pattern Formation in Geosystems, Springer, 1999, pp. 85–108. doi:10.1007/978-94-015-9179-9_4.
[81] H. Nabika, M. Itatani, I. Lagzi, Pattern formation in precipitation reactions: The Liesegang phenomenon, Langmuir 36 (2019) 481–497. doi:10.1021/acs.langmuir.9b03018.
[82] W. Ostwald, Besprechung der arbeit von liesegangs „a-linien", Z. Phys. Chem. 22 (1897) 289–330.
[83] S. Prager, Periodic precipitation, J. Chem. Phys. 25 (1956) 279–283. doi:10.1063/1.1742871.
[84] I. M. Lifshitz, V. V. Slyozov, The kinetics of precipitation from supersaturated solid solutions, Journal of physics and chemistry of solids 19 (1961) 35–50. doi:10.1016/0022-3697(61)90054-3.
[85] A. E. Boudreau, Crystal aging and the formation of fine-scale igneous layering, Mineralogy and Petrology 54 (1995) 55–69. doi:10.1007/BF01162758.
[86] H.-J. Krug, H. Brandtstädter, Morphological characteristics of Liesegang rings and their simulations, The Journal of Physical Chemistry A 103 (1999) 7811–7820. doi:10.1021/jp9910921.
[87] M. Dayeh, M. Ammar, M. Al-Ghoul, Transition from rings to spots in a precipitation reaction–diffusion system, RSC Advances 4 (2014) 60034–60038. doi:10.1039/C4RA11223G.
[88] P. Papp, B. Bohner, A. Tóth, D. Horváth, Fine tuning of pattern selection in the cadmium-hydroxide-system, The Journal of Chemical Physics 152 (2020) 094906. doi:10.1063/1.5144292.
[89] J. H. E. Cartwright, J. M. García-Ruiz, A. I. Villacampa, Pattern formation in crystal growth: Liesegang rings, Computer physics communications 121 (1999) 411–413. doi:10.1016/S0010-4655(99)00370-7.
[90] R. J. Reeder, R. O. Fagioli, W. J. Meyers, Oscillatory zoning of Mn in solution-grown calcite crystals, Earth-Science Reviews 29 (1990) 39–46. doi:10.1016/0012-8252(0)90026-R.
[91] M. Prieto, A. Fernández-González, A. Putnis, L. Fernández-Díaz, Nucleation, growth, and zoning phenomena in crystallizing (Ba,Sr)CO3, Ba(SO4,CrO4), (Ba,Sr)SO4, and (Cd,Ca)CO3 solid solutions from aqueous solutions, Geochimica et Cosmochimica Acta 61 (1997) 3383–3397. doi:10.1016/S0016-7037(97)00160-9.

[92] F. T. Ling, H. A. Hunter, J. P. Fitts, C. A. Peters, A. S. Acerbo, X. Huang, H. Yan, E. Nazaretski, Y. S. Chu, Nanospectroscopy captures nanoscale compositional zonation in barite solid solutions, Scientific Reports 8 (2018) 13041. doi:10.1038/s41598-018-31335-3.
[93] C. Ginibre, G. Wörner, A. Kronz, Crystal zoning as an archive for magma evolution, Elements 3 (2007) 261–266. doi:10.2113/gselements.3.4.261.
[94] M. Shore, A. D. Fowler, Oscillatory zoning in minerals; a common phenomenon, The Canadian Mineralogist 34 (1996) 1111–1126.
[95] D. J. Wollkind, J. I. D. Alexander, Kelvin–helmholtz instability in a layered newtonian fluid model of the geological phenomenon of rock folding, SIAM Journal on Applied Mathematics 42 (1982) 1276–1295. doi:10.1137/0142089.
[96] R. C. Fletcher, Folding of a single viscous layer: exact infinitesimal-amplitude solution, Tectonophysics 39 (1977) 593–606. doi:10.1016/0040-1951(77)90155-X.
[97] A. V. Getling, Rayleigh-Bénard convection: structures and dynamics, volume 11, World Scientific, 1998.
[98] E. Bodenschatz, W. Pesch, G. Ahlers, Recent developments in Rayleigh-Bénard convection, Annual review of fluid mechanics 32 (2000) 709–778. doi:10.1146/annurev.fluid.32.1.709.
[99] F. H. Busse, Fundamentals of thermal convection, in: W. R. Peltier (Ed.), Mantle Convection: Plate Tectonics and Global Dynamics, volume 4 of *Fluid Mechanics of Earth and Planets*, Gordon and Breach Science Publishers, New York, 1989, pp. 23–95.
[100] D. L. Anderson, Plate tectonics as a far-from-equilibrium self-organized system, Plate Boundary Zones 30 (2002) 411–425. doi:10.1029/GD030p0411.
[101] L. R. Wager, G. M. Brown, Layered Igneous Rocks, Oliver and Boyd, Edinburgh, 1968.
[102] R. G. Cawthorn, Layered igneous rocks: 25 years after Wager and Brown, South African Journal of Geology 97 (1994) 313–331. doi:10.10520/AJA10120750_509.
[103] P. Thy, C. Tegner, C. E. Lesher, Petrology of the Skaergaard Layered Series, GEUS Bulletin 51 (2023) e8327. doi:10.34194/geusb.v51.8327.
[104] M. A. Kessler, B. T. Werner, Self-organization of sorted patterned ground, Science 299 (2003) 380–383. doi:10.1126/science.1077300.
[105] B. Hallet, Stone circles: form and soil kinematics, Philosophical Transactions of the Royal Society A: Mathematical, Physical and Engineering Sciences 371 (2013) 20120357. doi:10.1098/rsta.2012.0357.
[106] M. M. Gibbons, D. Muldoon, I. Khalil, Demonstrating the kelvin-helmholtz instability using a low-cost experimental apparatus and computational fluid dynamics simulations, Fluids 8 (2023) 318. doi:10.3390/fluids8120318.
[107] H.-J. Kull, Theory of the Rayleigh-Taylor instability, Physics reports 206 (1991) 197–325. doi:10.1016/0370-1573(91)90153-D.
[108] J. A. Whitehead Jr, D. S. Luther, Dynamics of laboratory diapir and plume models, Journal of Geophysical Research 80 (1975) 705–717. doi:10.1029/JB080i005p00705.
[109] F. Trusheim, Über halokinese und ihre bedeutung für die strukturelle entwicklung norddeutschlands, Zeitschrift der deutschen geologischen Gesellschaft (1957) 111–151.
[110] M. R. Hudec, M. P. A. Jackson, Terra infirma: Understanding salt tectonics, Earth-Science Reviews 82 (2007) 1–28. doi:10.1016/j.earscirev.2007.01.001.
[111] I. Davison, G. I. Alsop, N. G. Evans, M. Safaricz, Overburden deformation patterns and mechanisms of salt diapir penetration in the Central Graben, North Sea, Marine and Petroleum Geology 17 (2000) 601–618. doi:10.1016/S0264-8172(00)00011-8.
[112] I. P. D. De Silva, H. J. S. Fernando, F. Eaton, D. Hebert, Evolution of Kelvin-Helmholtz billows in nature and laboratory, Earth and Planetary Science Letters 143 (1996) 217–231. doi:10.1016/0012-821X(96)00129-X.
[113] E. Heifetz, A. Agnon, S. Marco, Soft sediment deformation by Kelvin Helmholtz Instability: A case from Dead Sea earthquakes, Earth and Planetary Science Letters 236 (2005) 497–504. doi:10.1016/j.epsl.2005.04.019.
[114] A. J. Ryan, P. R. Christensen, Coils and polygonal crust in the Athabasca Valles region, Mars, as evidence for a volcanic history, Science 336 (2012) 449–452. doi:10.1126/science.1219437.
[115] K. Thomas, S. Herminghaus, H. Porada, L. Goehring, Formation of Kinneyia via shear-induced instabilities in microbial mats, Philosophical Transactions of the Royal Society A: Mathematical, Physical and Engineering Sciences 371 (2013) 20120362. doi:10.1098/rsta.2012.0362.
[116] S. Herminghaus, K. R. Thomas, S. Aliaskarisohi, H. Porada, L. Goehring, Kinneyia: a flow-induced anisotropic fossil pattern from ancient microbial mats, Frontiers in Materials 3 (2016) 30. doi:10.3389/fmats.2016.00030.
[117] S. Fabbri, J. Li, R. P. Howlin, A. Rmaile, B. Gottenbos, M. De Jager, E. M. Starke, M. Aspiras, M. T. Ward, N. G. Cogan, P. Stoodley, Fluid-driven interfacial instabilities and turbulence in bacterial biofilms, Environmental microbiology 19 (2017) 4417–4431. doi:10.1111/1462-2920.13883.
[118] M. F. Schatz, G. P. Neitzel, Experiments on thermocapillary instabilities, Annual Review of Fluid Mechanics 33 (2001) 93–127. doi:10.1146/annurev.fluid.33.1.93.
[119] R. V. Craster, O. K. Matar, Dynamics and stability of thin liquid films, Reviews of modern physics 81 (2009) 1131–1198. doi:10.1103/RevModPhys.81.1131.
[120] M. A. Baron, G. Fiquet, G. Morard, F. Miozzi, I. Esteve, B. Doisneau, A. S. Pakhomova, Y. Ricard, F. Guyot, Melting of basaltic lithologies in the Earth's lower mantle, Physics of the Earth and Planetary Interiors 333 (2022) 106938. doi:10.1016/j.pepi.2022.106938.
[121] D. Rouwet, M. Iorio, The sedimentation of Suminagashi-like floating clay patterns at El Chichón crater lake (Chiapas, Mexico), Geological Society, London, Special Publications 437 (2017) 153–161. doi:10.1144/SP437.9.
[122] F. Rehman, O. Singh, Role of rayleigh numbers on characteristics of double diffusive salt fingers, Heat and Mass Transfer

54 (2018) 3483–3492. doi:10.1007/s00231-018-2385-4.
[123] A. Toramaru, M. Matsumoto, Numerical experiment of cyclic layering in a solidified binary eutectic melt, Journal of Geophysical Research: Solid Earth 117 (2012). doi:doi.org/10.1029/2011JB008204.
[124] H. E. Huppert, J. S. Turner, Double-diffusive convection, J. Fluid Mech. 106 (1981) 299–329. doi:10.1017/S0022112081001614.
[125] R. W. Schmitt, The ocean's salt fingers, Sci. Am. 272 (1995) 70–75.
[126] T. Radko, Double-diffusive convection, Cambridge University Press, 2013.
[127] H. E. Huppert, R. S. J. Sparks, Double-diffusive convection due to crystallization in magmas, Annual Review of Earth and Planetary Sciences, Vol. 12, p. 11 12 (1984) 11. doi:10.1146/annurev.ea.12.050184.000303.
[128] J. S. Turner, H. E. Huppert, R. S. J. Sparks, Komatiites ii: Experimental and theoretical investigations of post-emplacement cooling and crystallization, Journal of Petrology 27 (1986) 397–437. doi:10.1093/petrology/27.2.397.
[129] U. Hansen, D. A. Yuen, Nonlinear physics of double-diffusive convection in geological systems, Earth-Science Reviews 29 (1990) 385–399. doi:10.1016/0012-8252(90)90050-6.
[130] J. L. Bischoff, R. J. Rosenbauer, Salinity variations in submarine hydrothermal systems by layered double-diffusive convection, The Journal of Geology 97 (1989) 613–623. doi:10.1086/629338.
[131] B. Charlier, O. Namur, R. Latypov, C. Tegner (Eds.), Layered intrusions, Springer, 2015.
[132] R. C. Kerr, J. S. Turner, Layered convection and crystal layers in multicomponent systems, Nature 298 (1982) 731–733. doi:10.1038/298731a0.
[133] H. R. Naslund, A. R. McBirney, Mechanisms of formation of igneous layering, Developments in petrology 15 (1996) 1–43. doi:10.1016/S0167-2894(96)80003-0.
[134] M. A. Rogerson, S. S. S. Cardoso, Patterns of bubble desorption during the solidification of a multicomponent melt, Journal of Fluid Mechanics 419 (2000) 263–282. doi:10.1017/S0022112000001208.
[135] D. A. Nield, A. Bejan, Convection in porous media, Springer, 2017.
[136] P. T. Imhoff, T. Green, Experimental investigation of double-diffusive groundwater fingers, Journal of Fluid Mechanics 188 (1988) 363–382. doi:10.1017/S002211208800076X.
[137] D. M. Anderson, P. Guba, Convective phenomena in mushy layers, Annual Review of Fluid Mechanics 52 (2020) 93–119. doi:10.1146/annurev-fluid-010719-060332.
[138] N. Shahidzadeh, M. F. L. Schut, J. Desarnaud, M. Prat, D. Bonn, Salt stains from evaporating droplets, Scientific Reports 5 (2015). doi:10.1038/srep10335.
[139] M. J. Qazi, H. Salim, C. A. W. Doorman, E. Jambon-Puillet, N. Shahidzadeh, Salt creeping as a self-amplifying crystallization process, Science Advances 5 (2019) eaax1853. doi:10.1126/sciadv.aax1853.
[140] R. Wijnhorst, F. Van der Sloot, L. Pel, N. Shahidzadeh, Effect of evaporative surface area on salt efflorescence and subflorescence formation in a given porous material, Physical Review Applied 21 (2024) 064055. doi:10.1103/PhysRevApplied.21.064055.
[141] J. Desarnaud, H. Derluyn, L. Molari, S. de Miranda, V. Cnudde, N. Shahidzadeh, Drying of salt contaminated porous media: Effect of primary and secondary nucleation, Journal of Applied Physics 118 (2015). doi:10.1063/1.4930292.
[142] P. G. Saffman, G. Taylor, The penetration of a fluid into a porous medium or hele-shaw cell containing a more viscous liquid, Proc. R. Soc. London A. 245 (1958) 312–329. doi:10.1098/rspa.1958.0085.
[143] G. Løvoll, Y. Méheust, R. Toussaint, J. Schmittbuhl, K. J. Måløy, Growth activity during fingering in a porous Hele-Shaw cell, Phys. Rev. E 70 (2004) 026301. doi:10.1103/PhysRevE.70.026301.
[144] S. Żukowski, S. Magni, F. Osselin, F. Dutka, M. Cooper, A. J. Ladd, P. Szymczak, Invariant forms of dissolution fingers, Phys. Rev. Lett. 134 (2025) 094101. doi:10.1103/PhysRevLett.134.094101.
[145] D. R. McDuff, C. E. Shuchart, S. K. Jackson, D. Postl, J. S. Brown, Understanding wormholes in carbonates: Unprecedented experimental scale and 3-D visualization, J. Petrol. Technol. 62 (2010) 78–81. doi:10.2118/134379-MS.
[146] S. Hill, Channeling in packed columns, Chemical Engineering Science 1 (1952) 247–253. doi:10.1016/0009-2509(52)87017-4.
[147] R. L. Chuoke, P. Van Meurs, C. van der Poel, The instability of slow, immiscible, viscous liquid-liquid displacements in permeable media, Transactions of the AIME 216 (1959) 188–194. doi:10.2118/1141-G.
[148] P. Ortoleva, J. Chadam, E. Merino, A. Sen, Geochemical self-organization II: The reactive-infiltration instability, Am. J. Sci. 287 (1987) 1008–1040. doi:10.2475/ajs.287.10.1008.
[149] E. J. Hinch, B. S. Bhatt, Stability of an acid front moving through porous rock, J. Fluid Mech. 212 (1990) 279–288. doi:10.1017/S0022112090001963.
[150] P. Szymczak, A. J. C. Ladd, Reactive infiltration instabilities in rocks. Fracture dissolution, J. Fluid Mech. 702 (2012) 239–264. doi:10.1017/jfm.2012.174.
[151] P. Szymczak, A. J. C. Ladd, Reactive infiltration instabilities in rocks. Part 2. Dissolution of a porous matrix, J. Fluid Mech. 738 (2014) 591–630. doi:10.1017/jfm.2013.586.
[152] C. G. Groves, A. D. Howard, Early development of karst systems. I. Preferential flow path enlargement under laminar flow, Water Resources Research 30 (1994) 2837–2846. doi:10.1029/94WR01303.
[153] R. B. Hanna, H. Rajaram, Influence of aperture variability on dissolutional growth of fissures in karst formations, Water Resour. Res. 34 (1998) 2843–2853. doi:10.1029/98WR01528.
[154] P. Szymczak, A. J. C. Ladd, The initial stages of cave formation: Beyond the one-dimensional paradigm, Earth Planet. Sci. Lett. 301 (2011) 424–432. doi:10.1016/j.epsl.2010.10.026.
[155] M. Lipar, P. Szymczak, S. Q. White, J. A. Webb, Solution pipes and focused vertical water flow: Geomorphology and modelling, Earth-Science Reviews 218 (2021) 103635. doi:10.1016/j.earscirev.2021.103635.
[156] M. L. Hoefner, H. S. Fogler, Pore evolution and channel formation during flow and reaction in porous media, AIChE

Journal 34 (1988) 45–54. doi:10.1002/aic.690340107.
[157] C. N. Fredd, H. S. Fogler, Influence of transport and reaction on wormhole formation in porous media, AIChE Journal 44 (1998) 1933–1949. doi:10.1002/aic.690440902.
[158] M. J. Economides, K. G. Nolte, Reservoir Stimulation, Wiley, Chichester, UK, 2000.
[159] A. N. Charalambous, Water well acidization revisited: includes oil and geothermal well perspectives, Quarterly Journal of Engineering Geology and Hydrogeology 54 (2021) qjegh2020–071. doi:10.1144/qjegh2020-071.
[160] E. Sutra, M. Spada, P. Burgherr, Chemicals usage in stimulation processes for shale gas and deep geothermal systems: a comprehensive review and comparison, Renewable and Sustainable Energy Reviews 77 (2017) 1–11. doi:10.1016/j.rser.2017.03.108.
[161] R. Toussaint, E. Aharonov, D. Koehn, J.-P. Gratier, M. Ebner, P. Baud, A. Rolland, F. Renard, Stylolites: A review, Journal of Structural Geology 114 (2018) 163–195. doi:10.1016/j.jsg.2018.05.003.
[162] T. Witten, L. M. Sander, Diffusion-limited aggregation, a kinetic critical phenomenon, Physical Review Letters 47 (1981) 1400. doi:10.1103/PhysRevLett.47.1400.
[163] S. S. S. Cardoso, J. T. H. Andres, Geochemistry of silicate-rich rocks can curtail spreading of carbon dioxide in subsurface aquifers, Nature communications 5 (2014) 5743. doi:10.1038/ncomms6743.
[164] P. K. Kang, P. De Anna, J. P. Nunes, B. Bijeljic, M. J. Blunt, R. Juanes, Pore-scale intermittent velocity structure underpinning anomalous transport through 3-D porous media, Geophysical Research Letters 41 (2014) 6184–6190. doi:10.1002/2014GL061475.
[165] D. Perugini, G. Poli, R. Mazzuoli, Chaotic advection, fractals and diffusion during mixing of magmas: evidence from lava flows, Journal of Volcanology and Geothermal Research 124 (2003) 255–279. doi:10.1016/S0377-0273(03)00098-2.
[166] H. Aref, Stirring by chaotic advection, Journal of Fluid Mechanics 143 (1984) 1–21. doi:10.1017/S0022112084001233.
[167] J. H. E. Cartwright, M. Feingold, O. Piro, An introduction to chaotic advection, Mixing: Chaos and turbulence (1999) 307–342. doi:10.1007/978-1-4615-4697-9_13.
[168] H. Aref, J. R. Blake, M. Budišić, S. S. S. Cardoso, J. H. E. Cartwright, H. J. H. Clercx, K. El Omari, U. Feudel, R. Golestanian, E. Gouillart, G. F. van Heijst, T. S. Krasnopolskaya, Y. L. Guer, R. S. MacKay, V. V. Meleshko, G. Metcalfe, I. Mezić, A. P. S. de Moura, O. Piro, M. F. M. Speetjens, R. Sturman, J.-L. Thiffeault, I. Tuval, Frontiers of chaotic advection, Reviews of Modern Physics 89 (2017) 025007. doi:10.1103/RevModPhys.89.025007.
[169] G. Metcalfe, D. Lester, A. Ord, P. Kulkarni, M. Trefry, B. E. Hobbs, K. Regenauer-Lieb, J. Morris, A partially open porous media flow with chaotic advection: towards a model of coupled fields, Philosophical Transactions of the Royal Society A: Mathematical, Physical and Engineering Sciences 368 (2010) 217–230. doi:10.1098/rsta.2009.0198.
[170] D. R. Lester, M. Dentz, T. Le Borgne, Chaotic mixing in three-dimensional porous media, Journal of Fluid Mechanics 803 (2016) 144–174. doi:10.1017/jfm.2016.486.
[171] D. Lester, M. Trefry, G. Metcalfe, Chaotic advection at the pore scale: Mechanisms, upscaling and implications for macroscopic transport, Advances in water resources 97 (2016) 175–192. doi:10.1016/j.advwatres.2016.09.007.
[172] D. R. Lester, A. Ord, B. E. Hobbs, The mechanics of hydrothermal systems: II. fluid mixing and chemical reactions, Ore geology reviews 49 (2012) 45–71. doi:10.1016/j.oregeorev.2012.08.002.
[173] M. G. Trefry, D. R. Lester, G. Metcalfe, J. Wu, Temporal fluctuations and poroelasticity can generate chaotic advection in natural groundwater systems, Water Resources Research 55 (2019) 3347–3374. doi:10.1029/2018WR023864.
[174] S. Schoofs, F. J. Spera, U. Hansen, Chaotic thermohaline convection in low-porosity hydrothermal systems, Earth and Planetary Science Letters 174 (1999) 213–229. doi:10.1016/S0012-821X(99)00264-2.
[175] S. Oberst, R. K. Niven, D. R. Lester, A. Ord, B. Hobbs, N. Hoffmann, Detection of unstable periodic orbits in mineralising geological systems, Chaos: An Interdisciplinary Journal of Nonlinear Science 28 (2018). doi:10.1063/1.5024134.
[176] D. A. Yuen, A. V. Malevsky, Strongly chaotic Newtonian and non-Newtonian mantle convection, in: Chaotic processes in the geological sciences, Springer, 1992, pp. 71–88. doi:10.1007/978-1-4684-0643-6_4.
[177] D. Perugini, M. Petrelli, G. Poli, A virtual voyage through 3D structures generated by chaotic mixing of magmas and numerical simulations: a new approach for understanding spatial and temporal complexity of magma dynamics, Visual Geosciences 13 (2008) 1–24. doi:10.1007/s10069-006-0004-x.
[178] C. P. De Campos, Chaotic flow patterns from a deep plutonic environment: a case study on natural magma mixing, Pure and applied geophysics 172 (2015) 1815–1833. doi:10.1007/s00024-014-0940-6.
[179] M. Petrelli, K. El Omari, Y. Le Guer, D. Perugini, Effects of chaotic advection on the timescales of cooling and crystallization of magma bodies at mid crustal levels, Geochemistry, Geophysics, Geosystems 17 (2016) 425–441. doi:10.1002/2015GC006109.
[180] S. S. S. Cardoso, J. H. E. Cartwright, Dynamics of osmosis in a porous medium, Royal Society Open Science 1 (2014) 140352. doi:10.1098/rsos.140352.
[181] S. S. S. Cardoso, J. H. E. Cartwright, Increased methane emissions from deep osmotic and buoyant convection beneath submarine seeps as climate warms, Nature communications 7 (2016) 13266. doi:10.1038/ncomms13266.
[182] L. A. M. Rocha, C. Gutiérrez-Ariza, C. Pimentel, I. Sánchez-Almazo, C. I. Sainz-Díaz, S. S. S. Cardoso, J. H. E. Cartwright, Formation and structures of horizontal submarine fluid conduit and venting systems associated with marine seeps, Geochemistry, Geophysics, Geosystems 22 (2021) e2021GC009724. doi:10.1029/2021GC009724.
[183] A. M. O. Morgado, L. A. M. Rocha, J. H. E. Cartwright, S. S. S. Cardoso, Osmosis drives explosions and methane release in Siberian permafrost, Geophysical Research Letters 51 (2024) e2024GL108987. doi:10.1029/2024GL108987.
[184] J. R. Glauber, Furni novi philosophici, sive Descriptio artis distillatoriæ novæ; nec non spirituum, olcorum, florum, aliorumque medicamentorum illus beneficio, facilimâ quâdam & perculiari viá è vegetabilibus, animalibus & mineralibus conficiendorum & quidem magno cum lucro; agens quoque de illorum usu tàm chymico quàm medico, edita & publicata in gratiam veritatis studiosorum, prostant apud J. Janssonium, Amsterodami, 1646.

[185] C. Pimentel, M. Zheng, J. H. E. Cartwright, C. I. SainzDíaz, Chemobrionics database: Categorisation of chemical gardens according to the nature of the anion, cation and experimental procedure, ChemSystemsChem 5 (2023) e202300002. doi:10.1002/syst.202300002.
[186] S. S. S. Cardoso, J. H. E. Cartwright, On the differing growth mechanisms of black-smoker and Lost City-type hydrothermal vents, Proceedings of the Royal Society A: Mathematical, Physical and Engineering Sciences 473 (2017) 20170387. doi:10.1098/rspa.2017.0387.
[187] C. I. Sainz-Díaz, E. Escamilla-Roa, J. H. E. Cartwright, Growth of self-assembling tubular structures of magnesium oxy/hydroxide and silicate related with seafloor hydrothermal systems driven by serpentinization, Geochemistry, Geophysics, Geosystems 19 (2018) 2813–2822. doi:10.1029/2018GC007594.
[188] J. H. E. Cartwright, M. J. Russell, The origin of life: the submarine alkaline vent theory at 30, Interface Focus 9 (2019). doi:10.1098/rsfs.2019.0104.
[189] J. H. E. Cartwright, B. Escribano, D. L. Gonzalez, C. I. Sainz-Diaz, I. Tuval, Brinicles as a case of inverse chemical gardens, Langmuir 29 (2013) 7655–7660. doi:10.1021/la4009703.
[190] S. Testón-Martínez, L. M. Barge, J. Eichler, C. I. Sainz-Díaz, J. H. E. Cartwright, Experimental modelling of the growth of tubular ice brinicles from brine flows under sea ice, The Cryosphere 18 (2024) 2195–2205. doi:10.5194/tc-18-2195-2024.
[191] S. D. Vance, L. M. Barge, S. S. S. Cardoso, J. H. E. Cartwright, Self-assembling ice membranes on Europa: brinicle properties, field examples, and possible energetic systems in icy ocean worlds, Astrobiology 19 (2019) 685–695. doi:10.1089/ast.2018.1826.
[192] M. J. Russell, A. J. Hall, The emergence of life from iron monosulphide bubbles at a submarine hydrothermal redox and ph front, Journal of the Geological Society 154 (1997) 377–402. doi:10.1144/gsjgs.154.3.0377.
[193] S. S. S. Cardoso, J. H. E. Cartwright, J. Čejková, L. Cronin, A. De Wit, S. Giannerini, D. Horváth, A. Rodrigues, M. J. Russell, C. I. Sainz-Díaz, A. Tóth, Chemobrionics: From self-assembled material architectures to the origin of life, Artificial Life 26 (2020) 315–326. doi:10.1162/artl_a_00323.
[194] Y. Ding, J. H. E. Cartwright, S. S. S. Cardoso, Intrinsic concentration cycles and high ion fluxes in self-assembled precipitate membranes, Interface Focus 9 (2019) 20190064. doi:10.1098/rsfs.2019.0064.
[195] Y. Ding, S. S. S. Cardoso, J. H. E. Cartwright, Dynamics of the osmotic lysis of mineral protocells and its avoidance at the origins of life, Geobiology 22 (2024) e12611. doi:10.1111/gbi.12611.
[196] J. H. E. Cartwright, A. L. Mackay, Beyond crystals: the dialectic of materials and information, Philosophical Transactions of the Royal Society A: Mathematical, Physical and Engineering Sciences 370 (2012) 2807–2822. doi:10.1098/rsta.2012.0106.
[197] J. H. E. Cartwright, S. Giannerini, D. L. González, DNA as information: at the crossroads between biology, mathematics, physics and chemistry, Philosophical Transactions of the Royal Society A: Mathematical, Physical and Engineering Sciences 374 (2016) 20150071. doi:10.1098/rsta.2015.0071.
[198] J. H. E. Cartwright, J. Čejková, E. Fimmel, S. Giannerini, D. L. Gonzalez, G. Goracci, C. Grácio, J. Houwing-Duistermaat, D. Matić, N. Mišić, et al., Information, coding, and biological function: The dynamics of life, Artificial Life 30 (2024) 16–27. doi:10.1162/artl_a_00432.
[199] T. A. Witten, L. M. Sander, Diffusion-limited aggregation, Physical review B 27 (1983) 5686. doi:10.1103/PhysRevB.27.5686.
[200] P. Meakin, Diffusion-controlled flocculation: The effects of attractive and repulsive interactions, Journal of Chemical Physics 79 (1983) 2426–2429. doi:10.1063/1.446051.
[201] P. Garik, Anisotropic growth of diffusion-limited aggregates, Physical Review A 32 (1985) 1275–1278. doi:10.1103/PhysRevA.32.1275.
[202] J. Erlebacher, P. C. Searson, K. Sieradzki, Computer simulation of dense-branching patterns, Physical Review Letters 71 (1993) 3311–3314. doi:10.1103/PhysRevLett.71.3311.
[203] P. Meakin, Fractals, Scaling and Growth Far from Equilibrium, Cambridge University Press, Cambridge, UK, 1998.
[204] T. C. Halsey, Diffusion-limited aggregation: A model for pattern formation, Physics Today 53 (2000) 36–41. doi:10.1063/1.1333284.
[205] M. Mineev-Weinstein, P. B. Wiegmann, A. Zabrodin, Integrable structure of interface dynamics, Physical Review Letters 84 (2000) 5106–5109. doi:10.1103/PhysRevLett.84.5106.
[206] M. Mineev-Weinstein, M. Putinar, R. Teodorescu, Random matrices in 2D, laplacian growth and operator theory, Journal of Physics A: Mathematical and Theoretical 41 (2008) 263001. doi:10.1088/1751-8113/41/26/263001.
[207] A. Khan, Z. Abas, H. S. Kim, I.-K. Oh, Piezoelectric thin films: an integrated review of transducers and energy harvesting, Smart Materials and Structures 25 (2016) 053002. doi:10.1088/0964-1726/25/5/053002.
[208] M. Pishvar, R. L. Harne, Foundations for soft, smart matter by active mechanical metamaterials, Advanced science 7 (2020) 2001384. doi:10.1002/advs.202001384.
[209] C. R. Voisey, N. J. Hunter, A. G. Tomkins, J. Brugger, W. Liu, Y. Liu, V. Luzin, Gold nugget formation from earthquake-induced piezoelectricity in quartz, Nature Geoscience (2024) 1–6. doi:10.1038/s41561-024-01514-1.
[210] Z. Zhang, Z. Wang, S. He, C. Wang, M. Jin, Y. Yin, Redox reaction induced Ostwald ripening for size- and shape-focusing of palladium nanocrystals, Chemical Science 6 (2015) 5197–5203. doi:10.1039/C5SC01787D.
[211] C. Wagner, Theorie der Alterung von Niederschlägen durch Umlösen (Ostwald-Reifung), Zeitschrift für Elektrochemie, Berichte der Bunsengesellschaft für physikalische Chemie 65 (1961) 581–591. doi:10.1002/bbpc.19610650704.
[212] I. M. Lifshitz, V. V. Slyozov, The kinetics of precipitation from supersaturated solid solutions, Journal of Physics and Chemistry of Solids 19 (1961) 35–50. doi:10.1016/0022-3697(61)90054-3.
[213] T. van Westen, R. D. Groot, Effect of temperature cycling on Ostwald ripening, Crystal Growth & Design 18 (2018) 4952–4962. doi:10.1021/acs.cgd.8b00267.

[214] M. Caccin, Z. Li, J. R. Kermode, A. De Vita, A framework for machine-learning-augmented multiscale atomistic simulations on parallel supercomputers, International Journal of Quantum Chemistry 115 (2015) 1129–1139. doi:10.1002/qua.24952.
[215] D. D. Eberl, J. Środoń, M. Kralik, B. E. Taylor, Z. E. Peterman, Ostwald ripening of clays and metamorphic minerals, Science 248 (1990) 474–477. doi:10.1126/science.248.4954.474.
[216] J. W. Morse, W. H. Casey, Ostwald processes and mineral paragenesis in sediments, American Journal of Science 288 (1988) 537–560. doi:10.2475/ajs.288.6.537.
[217] H. Cabane, D. Laporte, A. Provost, An experimental study of Ostwald ripening of olivine and plagioclase in silicate melts: implications for the growth and size of crystals in magmas, Contributions to Mineralogy and Petrology 150 (2005) 37–53. doi:10.1007/s00410-005-0002-2.
[218] E. Hastie, M. Schindler, D. Kontak, B. Lafrance, Transport and coarsening of gold nanoparticles in an orogenic deposit by dissolution–reprecipitation and Ostwald ripening, Communications Earth & Environment 2 (2021) 57. doi:10.1038/s43247-021-00126-6.
[219] J. H. E. Cartwright, O. Piro, I. Tuval, Ostwald ripening, chiral crystallization, and the common-ancestor effect, Physical review letters 98 (2007) 165501. doi:10.1103/PhysRevLett.98.165501.
[220] T. L. Anderson, Fracture mechanics: fundamentals and applications, 4th ed., CRC press, 2017.
[221] K. B. Broberg, Cracks and fracture, Elsevier, 1999.
[222] D. Meyer, M. Brückner-Foit, Crack interaction modelling, Fatigue & Fracture of Engineering Materials & Structures 23 (2000) 315–323. doi:10.1046/j.1460-2695.2000.00283.x.
[223] Y. Sun, M. G. Edwards, B. Chen, C. Li, A state-of-the-art review of crack branching, Engineering Fracture Mechanics 257 (2021) 108036. doi:10.1016/j.engfracmech.2021.108036.
[224] V. Hakim, A. Karma, Crack path prediction in anisotropic brittle materials, Physical review letters 95 (2005) 235501. doi:10.1103/PhysRevLett.95.235501.
[225] R. Shcherbakov, D. L. Turcotte, Damage and self-similarity in fracture, Theoretical and applied fracture mechanics 39 (2003) 245–258. doi:10.1016/S0167-8442(03)00005-3.
[226] S. Tarasovs, A. Ghassemi, Self-similarity and scaling of thermal shock fractures, Physical Review E 90 (2014) 012403. doi:10.1103/PhysRevE.90.012403.
[227] Z. P. Bažant, Scaling laws in mechanics of failure, Journal of Engineering Mechanics 119 (1993) 1828–1844. doi:10.1061/(ASCE)0733-9399(1993)119:9(1828).
[228] S. E. Laubach, R. Lander, L. J. Criscenti, L. M. Anovitz, J. Urai, R. M. Pollyea, J. N. Hooker, W. Narr, M. A. Evans, S. N. Kerisit, J. E. Olson, T. Dewers, D. Fisher, R. Bodnar, B. Evans, P. Dove, L. M. Bonnell, M. P. Marder, L. Pyrak-Nolte, The role of chemistry in fracture pattern development and opportunities to advance interpretations of geological materials, Reviews of Geophysics 57 (2019) 1065–1111. doi:10.1029/2019RG000671.
[229] B. Jamtveit, C. V. Putnis, A. Malthe-Sørenssen, Reaction induced fracturing during replacement processes, Contributions to Mineralogy and Petrology 157 (2009) 127–133. doi:10.1007/s00410-008-0324-y.
[230] E. Walger, G. Mattheß, V. Seckendorff, F. Liebau, The formation of agate structures: models for silica transport, agate layer accretion, and for flow patterns and flow regimes in infiltration channels, Neues Jahrbuch für Mineralogie-Abhandlungen (2009) 113–152. doi:10.1127/0077-7757/2009/0141.
[231] B. Jackson, Structures and micro-structures in Scottish agates, in: Symposium on Agate and Cryptocrystalline Quartz, Golden, Colorado, 2003, pp. 89–94.
[232] T. Moxon, G. Palyanova, Agate genesis: A continuing enigma, Minerals 10 (2020) 953. doi:10.3390/min10110953.
[233] J. Götze, R. Möckel, Y. Pan, Mineralogy, geochemistry and genesis of agate—a review, Minerals 10 (2020) 1037. doi:10.3390/min10111037.
[234] P. Heaney, A. Davis, Observation and origin of self-organized textures in agates, Science 269 (1995) 1562–1565. doi:10.1126/science.269.5230.1562.
[235] S. Cady, H.-R. Wenk, M. Sintubin, Microfibrous quartz varieties: characterization by quantitative X-ray texture analysis and transmission electron microscopy, Contributions to Mineralogy and Petrology 130 (1998) 320–335. doi:10.1007/s004100050368.
[236] C. Frondel, Systematic compositional zoning in the quartz fibers of agates, American Mineralogist 70 (1985) 975–979.
[237] M. W. French, R. H. Worden, D. R. Lee, Electron backscatter diffraction investigation of length-fast chalcedony in agate: implications for agate genesis and growth mechanisms, Geofluids 13 (2013) 32–44. doi:10.1111/gfl.12006.
[238] F. T. Jones, Iris agate, American Mineralogist: Journal of Earth and Planetary Materials 37 (1952) 578–587.
[239] C. Frondel, Characters of quartz fibers, American Mineralogist 63 (1978) 17–27.
[240] M. Landmesser, Das problem der Achatgenese, Mitt. Pollichia 72 (1984) 5–137.
[241] R. Liesegang, Die entstehung der achate, Zentralblatt für Mineralogie 11 (1910) 593–597.
[242] T. Hsu, A. Lucas, Fordite from the Corvette assembly plant, Gems & Gemology 52 (2016) 87–88.
[243] N. Nova, N. Maigret, M. Roszkowska, The Bestiary of the Anthropocene, Onomatopée, 2021.
[244] O. C. Farrington, B. Laufer, Agate: physical properties and origin, archaeology and folklore, Field Museum of Natural History, 1927.
[245] O. Schalm, K. Proost, K. De Vis, S. Cagno, K. Janssens, F. Mees, P. Jacobs, J. Caen, Manganese staining of archaeological glass: the characterization of Mn-rich inclusions in leached layers and a hypothesis of its formation, Archaeometry 53 (2011) 103–122. doi:10.1111/j.1475-4754.2010.00534.x.
[246] W. Haidinger, Über die metamorphose der gebirgsarten, Ber. über die Mittheilungen von Freunden der Naturwissenschaften in Wien 4 (1848) 103–134.
[247] J. Noeggerath, Sendschreiben an den k.k. wirklichen Bergrath und Prof., Herrn W. Haidinger in Wien, über die Achat

Mandeln in den Melaphyren, Verh. naturhist. Vereins preuss. Rheinlande u. Westphalens (1849) 243–260.
[248] J. Kenngott, Über die Achatmandeln in den Melaphyren, namentlich über die von Theiss in Tirol, Naturwiss. Abh. gesammelt und durch Subscription herausgeg. von W. Haidinger 4 (1851) 71–104.
[249] E. Reusch, Über den Agat, Ann. Phys. Chem. 123 (1864) 94–114.
[250] C. Harris, Oxygen-isotope zonation of agates from Karoo volcanics of the Skeleton Coast, Namibia, American Mineralogist 74 (1989) 476–481.
[251] R. E. Liesegang, Die Achate, Springer, 1914.
[252] R. K. Pabian, A. Zarins, Banded Agates, Origins and Inclusions, University of Nebraska-Lincoln, 1994.
[253] Y. Wang, E. Merino, Self-organizational origin of agates: Banding, fiber twisting, composition, and dynamic crystallization model, Geochimica et Cosmochimica Acta 54 (1990) 1627–1638. doi:10.1016/0016-7037(90)90396-3.
[254] R. Nacken, Über die nachbildung von chalcedon-mandeln, Natur Folk 78 (1948) 2–8.
[255] J. White, J. Corwin, Synthesis and origin of chalcedony, American Mineralogist: Journal of Earth and Planetary Materials 46 (1961) 112–119.
[256] A. E. Fallick, J. Jocelyn, T. Donnelly, M. Guy, C. Behan, Origin of agates in volcanic rocks from Scotland, Nature 313 (1985) 672–674. doi:10.1038/313672a0.
[257] S. Emmanuel, B. Berkowitz, Effects of pore-size controlled solubility on reactive transport in heterogeneous rock, Geophysical Research Letters 34 (2007) L06404. doi:10.1029/2006GL028962.
[258] F. Theeuwes, Elementary osmotic pump, Journal of pharmaceutical sciences 64 (1975) 1987–1991. doi:10.1002/jps.2600641218.
[259] J. G. Goodchild, On the genesis of some Scottish minerals, Proc. Royal Phys. Soc. Edinburgh 14 (1899) 181–220.
[260] K. Schlossmacher, Die Entstehung der Achate, Teil II, Z. deutsch. Ges. Edelsteinkde. 33 (1960) 11–16.
[261] Z. Hou, D. Woś, C. Tschegg, A. Rogowitz, A. H. N. Rice, L. Nasdala, F. Fusseis, P. Szymczak, B. Grasemann, Three-dimensional mineral dendrites reveal a nonclassical crystallization pathway, Geology 51 (2023) 626–630. doi:10.1130/G51127.1.
[262] Pliny the Elder, Naturalis Historia, 77.
[263] J. J. Scheuchzer, Dissertatio epistolica acarnanis de dendritis aliisque lapidibus, qui in superficie sua plantarum, foliorum, florum figuras exprimunt, Miscellanea Curiosa Sive Ephemeridum Medico-Physicarum Germanicarum Academiae Caesareo-Leopoldinae Naturae Curiosorum Decuriae III. Annus Quintus Et Sextus, Anni M. DC. XCVII & XCVIII. Continens Celeberrimorum Virorum Tum Medicorum tum aliorum Eruditorum in Germania & extra eam Observationes Medico-Physico-Anatomico-Botanico-Mathematicas Cum Appendice & Privilegio Sac. Caes. Majestatis. (1700) 57–80.
[264] G. F. Mylius, Memorabilium SaxoniæSubterraneæ, F. Groschuff, 1709.
[265] E. Mendes da Costa, A Natural History of Fossils, L. Davis and C. Reymers, 1757.
[266] L. Van Straaten, Dendrites, Journal of the Geological Society 135 (1978) 137–151. doi:10.1144/gsjgs.135.1.0137.
[267] J. M. García-Ruiz, F. Otálora, A. Sanchez-Navas, F. J. Higes-Rolando, The formation of manganese dendrites as the mineral record of flow structures, Fractals and dynamic systems in geoscience (1994) 307–318. doi:10.1007/978-3-662-07304-9_23.
[268] R. Trivedi, W. Kurz, Dendritic growth, International Materials Reviews 39 (1994) 49–74. doi:10.1179/imr.1994.39.2.49.
[269] A. D. Fowler, H. E. Stanley, G. Daccord, Disequilibrium silicate mineral textures: Fractal and non-fractal features, Nature 341 (1989) 134–138. doi:10.1038/341134a0.
[270] B. Welsch, F. Faure, V. Famin, A. Baronnet, P. Bachèlery, Dendritic crystallization: A single process for all the textures of olivine in basalts?, Journal of Petrology 54 (2013) 539–574. doi:10.1093/petrology/egs077.
[271] P. Barbey, F. Faure, J. L. Paquette, K. Pistre, C. Delangle, J. P. Gremilliet, Skeletal quartz and dendritic biotite: Witnesses of primary disequilibrium growth textures in an alkali-feldspar granite, Lithos 348–349 (2019). doi:10.1016/j.lithos.2019.105202.
[272] B. Chopard, H. Herrmann, T. Vicsek, Structure and growth mechanism of mineral dendrites, Nature 353 (1991) 409–412. doi:10.1038/353409a0.
[273] D. Li, J. Yang, W. Tang, X. Wu, L. Wei, Y. Chen, Controlled synthesis of hierarchical MnO2 microspheres with hollow interiors for the removal of benzene, RSC Advances 4 (2014) 26796–26803. doi:10.1039/C4RA01146E.
[274] M. Huang, F. Li, F. Dong, Y. X. Zhang, L. L. Zhang, MnO2-based nanostructures for high-performance supercapacitors, Journal of Materials Chemistry A 3 (2015) 21380–21423. doi:10.1039/C5TA05523G.
[275] H. Cöelfen, M. Antonietti, Mesocrystals and Nonclassical Crystallization, Wiley, 2008.
[276] J. J. De Yoreo, P. U. Gilbert, N. A. Sommerdijk, R. L. Penn, S. Whitelam, D. Joester, H. Zhang, J. D. Rimer, A. Navrotsky, J. F. Banfield, A. F. Wallace, F. M. Michel, F. C. Meldrum, H. Cölfen, P. M. Dove, Crystallization by particle attachment in synthetic, biogenic, and geologic environments, Science 349 (2015) aaa6760. doi:10.1126/science.aaa6760.
[277] J. Mathiesen, I. Procaccia, H. L. Swinney, M. Thrasher, The universality class of diffusion-limited aggregation and viscous fingering, Europhysics Letters 76 (2006) 257. doi:10.1209/epl/i2006-10246-x.
[278] R. M. Potter, G. R. Rossman, Mineralogy of manganese dendrites and coatings, American mineralogist 64 (1979) 1219–1226.
[279] P. A. Schoenly, J. A. Saunders, Natural gold dendrites from hydrothermal Au-Ag deposits: characteristics and computer simulations, Fractals 1 (1993) 585–593. doi:10.1142/S0218348X93000617.
[280] J. A. Saunders, M. Burke, Formation and aggregation of gold (electrum) nanoparticles in epithermal ores, Minerals 7 (2017) 163. doi:10.3390/min7090163.
[281] J. A. Saunders, Silica and gold textures in bonanza ores of the Sleeper Deposit, Humboldt County, Nevada; evidence for colloids and implications for epithermal ore-forming processes, Economic Geology 89 (1994) 628–638. doi:10.2113/gsecongeo.89.3.628.

[282] J. A. Saunders, M. Burke, M. E. Brueseke, Scanning-electron-microscope imaging of gold (electrum) nanoparticles in middle Miocene bonanza epithermal ores from northern Nevada, USA, Mineralium Deposita 55 (2020) 389–398. doi:10.1007/s00126-019-00935-y.
[283] P. Keller, Gemstones and Their Origin, Springer, 1990.
[284] D. Papineau, Chemically oscillating reactions in the formation of botryoidal malachite, Am. Mineral. 105 (2020) 447–454. doi:10.2138/am-2020-7029.
[285] V. S. Balitsky, T. M. Bublikova, S. L. Sorolzjna, L. V. Balitskaya, A. S. Shteinberg, Man-made jewelry malachite, Gems & Gemology 23 (1987) 152–157. doi:10.5741/GEMS.23.3.152.
[286] T. Petrov, E. Protopopov, A. Shuyskiy, Decorative grown malachite. nature and technology, Russ. J. Earth Sci. 13 (2013) ES2001. doi:10.2205/2013ES000529.
[287] D. Craw, K. Lilly, Gold nugget morphology and geochemical environments of nugget formation, southern New Zealand, Ore Geology Reviews 79 (2016) 301–315. doi:10.1016/j.oregeorev.2016.06.001.
[288] C. R. M. Butt, R. M. Hough, M. Verrall, Gold nuggets: the inside story, Ore and Energy Resource Geology 4 (2020) 100009. doi:10.1016/j.oreoa.2020.100009.
[289] N. J. Curtis, J. R. Gascooke, M. R. Johnston, A. Pring, A Review of the Classification of Opal with Reference to Recent New Localities, Minerals 9 (2019) 299. doi:10.3390/min9050299.
[290] E. Gaillou, E. Fritsch, B. Aguilar-Reyes, B. Rondeau, J. Post, A. Barreau, M. Ostroumov, Common gem opal: An investigation of micro- to nano-structure, American Mineralogist 93 (2008) 1865–1873. doi:10.2138/am.2008.2518.
[291] N. J. Curtis, J. R. Gascooke, A. Pring, Silicon-Oxygen Region Infrared and Raman Analysis of Opals: The Effect of Sample Preparation and Measurement Type, Minerals 11 (2021) 173. doi:10.3390/min11020173.
[292] R. K. Iler, Formation of precious opal, Nature 207 (1965) 472–473. doi:10.1038/207472a0.
[293] D. J. Norris, E. G. Arlinghaus, L. Meng, R. Heiny, L. E. Scriven, Opaline photonic crystals: How does self-assembly work?, Advanced Materials 16 (2004) 1393–1399. doi:10.1002/adma.200400455.
[294] A. Stewart, L. T. Chadderton, B. R. Senior, Self-assembly in the growth of precious opal, Journal of Crystal Growth 312 (2010) 391–396. doi:10.1016/j.jcrysgro.2009.09.042.
[295] W. Stöber, A. Fink, E. Bohn, Controlled growth of monodisperse silica spheres in the micron size range, Journal of Colloid and Interface Science 26 (1968) 62–69. doi:10.1016/0021-9797(68)90272-5.
[296] G. H. Bogush, M. A. Tracy, C. F. Zukoski, Preparation of monodisperse silica particles: Control of size and mass fraction, Journal of Non-Crystalline Solids 104 (1988) 95–106. doi:10.1016/0022-3093(88)90187-1.
[297] M. Liesegang, R. Milke, Australian sedimentary opal-A and its associated minerals: Implications for natural silica sphere formation, American Mineralogist 99 (2014) 1488–1499. doi:10.2138/am.2014.4791.
[298] W. Gao, M. Rigout, H. Owens, Facile control of silica nanoparticles using a novel solvent varying method for the fabrication of artificial opal photonic crystals, Journal of Nanoparticle Research 18 (2016) 387. doi:10.1007/s11051-016-3691-8.
[299] Z. M. Migaszewski, A. Gałuszka, T. Durakiewicz, E. Starnawska, Middle Oxfordian–Lower Kimmeridgian chert nodules in the Holy Cross Mountains, south-central Poland, Sedimentary Geology 187 (2006) 11–28. doi:10.1016/j.sedgeo.2005.12.003.
[300] J. Sowerby, British Mineralogy, London: R. Taylor, 1804.
[301] S. P. Woodward, On the nature and origin of banded flints, Geological Magazine 1 (1864) 145–149. doi:10.1017/S0016756800163526.
[302] Z. M. Migaszewski, A. Gałuszka, A. Migaszewski, Geochemistry and petrology of striped chert as a provenance tool for artefacts from the Krzemionki Neolithic mining area (Poland), Archaeometry 64 (2022) 1093–1109. doi:10.1111/arcm.12778.
[303] L. P. Knauth, Petrogenesis of chert, in: P. J. Heaney, C. T. Prewitt, G. V. Gibbs (Eds.), Silica, De Gruyter, Berlin, Boston, 1994, pp. 233–258. doi:10.1515/9781501509698-012.
[304] McBride, A. Abdel-Wahab, A. R. M. El-Younsy, Origin of spheroidal chert nodules, Drunka Formation (lower Eocene), Egypt, Sedimentology 46 (1999) 733–755. doi:10.1046/j.1365-3091.1999.00253.x.
[305] J. H. Oehler, J. W. Schopf, Artificial microfossils: experimental studies of permineralization of blue-green algae in silica, Science 174 (1971) 1229–1231. doi:10.1126/science.174.4015.1229.
[306] A. J. Coward, A. C. Slim, J. Brugger, S. Wilson, T. Williams, B. Pillans, A. Maksimenko, Mineralogy and geochemistry of pattern formation in zebra rock from the East Kimberley, Australia, Chemical Geology 622 (2023) 121336. doi:10.1016/j.chemgeo.2023.121336.
[307] C. O. G. Larcombe, Some rocks from four miles east of Argyle Station, Ord River, King district, Kimberley division, Annual Progress Report of the Geological Survey of Western Australia (1927) 139–140.
[308] H. Kawahara, H. Yoshida, K. Yamamoto, N. Katsuta, S. Nishimoto, A. Umemura, R. Kuma, Hydrothermal formation of Fe-oxide bands in zebra rocks from northern Western Australia, Chemical Geology 590 (2022) 120699. doi:10.1016/j.chemgeo.2021.120699.
[309] G. Retallack, Zebra rock and other Ediacaran paleosols from Western Australia, Australian Journal of Earth Sciences 68 (2021) 532–556. doi:10.1080/08120099.2020.1820574.
[310] C. O. G. Larcombe, Rock specimens from Ord River and Oakover River respectively, Annual Progress Report of the Geological Survey of Western Australia (1925) 122.
[311] D. W. Trainer, Jr., "Zebra" rock, American Mineralogist 16 (1931) 221–225.
[312] A. J. Coward, How the zebra rock got its stripes: the formation of hematite banding in Western Australian siltstones, Ph.D. thesis, Monash University, 2022. doi:10.26180/21721031.
[313] F. C. Loughnan, F. I. Roberts, Composition and origin of the 'zebra rock' from the East Kimberley region of Western Australia, Australian Journal of Earth Sciences 37 (1990) 201–205. doi:10.1080/08120099008727920.

[314] C. Liu, V. M. Calo, K. Regenauer-Lieb, M. Hu, Coefficients of reaction-diffusion processes derived from patterns in rocks, Journal of Geophysical Research: Solid Earth 128 (2023) e2022JB026253. doi:10.1029/2022JB026253.
[315] M. W. Wallace, A. v. S. Hood, Zebra textures in carbonate rocks: Fractures produced by the force of crystallization during mineral replacement, Sedimentary Geology 368 (2018) 58–67. doi:10.1016/j.sedgeo.2018.03.009.
[316] S. Lugli, J. Torres-Ruiz, G. Garuti, F. Olmedo, Petrography and geochemistry of the Eugui magnesite deposit (Western Pyrenees, Spain): Evidence for the development of a peculiar zebra banding by dolomite replacement, Economic Geology 95 (2000) 1775–1791. doi:10.2113/gsecongeo.95.8.1775.
[317] L. Fontbote, H. Gorzawski, Genesis of the mississippi valley-type Zn-Pb deposit of San Vicente, central Peru; geologic and isotopic (Sr, O, C, S, Pb) evidence, Economic Geology 85 (1990) 1402–1437. doi:10.2113/gsecongeo.85.7.1402.
[318] D. W. Morrow, Zebra and boxwork fabrics in hydrothermal dolomites of northern Canada: Indicators for dilational fracturing, dissolution or in situ replacement?, Sedimentology 61 (2014) 915–951. doi:10.1111/sed.12094.
[319] L. Fontboté, Self-organization fabrics in carbonate-hosted ore deposits: the example of diagenetic crystallization rhythmites (DCRs), in: Current research in geology applied to ore deposits. Proceedings of the Second Biennial SGA Meeting, Granada, Spain, 1993, pp. 11–14.
[320] E. Merino, A. Canals, R. C. Fletcher, Genesis of self-organized zebra textures in burial dolomites: Displacive veins, induced stress, and dolomitization, Geologica Acta 4 (2006) 383–394. doi:10.1344/105.000000352.
[321] C. F. Park, Dolomite and jasperoid in the Metaline District, northeastern Washington, Economic Geology 33 (1938) 709–729. doi:10.2113/gsecongeo.33.7.709.
[322] R. Swennen, V. Vandeginste, R. Ellam, Genesis of zebra dolomites (Cathedral Formation: CanadianCordillera Fold and Thrust Belt, British Columbia), Journal of Geochemical Exploration 78-79 (2003) 571–577. doi:10.1016/S0375-6742(03)00065-7.
[323] U. Kelka, M. Veveakis, D. Koehn, N. Beaudoin, Zebra rocks: compaction waves create ore deposits, Scientific Reports 7 (2017) 14260. doi:10.1038/s41598-017-14541-3.
[324] H. J. Krug, H. Brandstädter, K. H. Jacob, Morphological instabilities in pattern formation by precipitation and crystallization processes, Geologische Rundschau 85 (1996) 19–28. doi:10.1007/BF00192056.
[325] D. C. Arne, L. W. Curtis, S. A. Kissin, Internal zonation in a carbonate-hosted Zn-Pb-Ag deposit, Nanisivik, Baffin Island, Canada, Economic Geology 86 (1991) 699–717. doi:10.2113/gsecongeo.86.4.699.
[326] A. S.-H. Chen, S. W. Morris, Experiments on the morphology of icicles, Phys. Rev. E 83 (2011) 026307. doi:10.1103/PhysRevE.83.026307.
[327] A. S.-H. Chen, S. W. Morris, On the origin and evolution of icicle ripples, New Journal of Physics 15 (2013) 103012. doi:10.1088/1367-2630/15/10/103012.
[328] A. S.-H. Chen, Experiments on the growth and form of icicles, Ph.D. thesis, University of Toronto, 2018.
[329] J. Ladan, S. W. Morris, Pattern of inclusions inside rippled icicles, Phys. Rev. E 106 (2022) 054211. doi:10.1103/PhysRevE.106.054211.
[330] J. Ladan, S. W. Morris, Experiments on the dynamic wetting of growing icicles, New Journal of Physics 23 (2021) 123017. doi:10.1088/1367-2630/ac3cf4.
[331] J. Ladan, Experiments on the formation of rippled icicles, Ph.D. thesis, University of Toronto, 2023.
[332] A. S.-H. Chen, J. Ladan, S. W. Morris, The icicle atlas: an online open access archive of icicle data, 2006. URL: https://borealisdata.ca/dataverse/Icicle$_$Atlas.
[333] A. S.-H. Chen, J. Ladan, S. W. Morris, Icicle atlas run m7q10, 2006. URL: https://doi.org/doi:10.5683/SP/WG4KKE.
[334] A. S.-H. Chen, J. Ladan, S. W. Morris, Icicle atlas run m7q12, 2006. URL: https://doi.org/doi:10.5683/SP/NJNOBS.
[335] A. S.-H. Chen, J. Ladan, S. W. Morris, Icicle atlas run 120906, 2006. URL: https://doi.org/10.5683/SP/HION8G.
[336] L. Makkonen, A Model of Icicle Growth, Journal of Glaciology 34 (1988) 64–70. doi:10.3189/S0022143000009072.
[337] M. B. Short, J. C. Baygents, J. W. Beck, D. A. Stone, R. S. Toomey, R. E. Goldstein, Stalactite growth as a free-boundary problem: A geometric law and its Platonic ideal, Physical Review Letters 94 (2005) 018501. doi:10.1103/PhysRevLett.94.018501.
[338] M. B. Short, J. C. Baygents, R. E. Goldstein, Stalactite growth as a free-boundary problem, Physics of Fluids 17 (2005) 083101. doi:10.1063/1.2006027.
[339] C. Camporeale, L. Ridolfi, Hydrodynamic-driven stability analysis of morphological patterns on stalactites and implications for cave paleoflow reconstructions, Phys. Rev. Lett. 108 (2012) 238501. doi:10.1103/PhysRevLett.108.238501.
[340] P. Meakin, B. Jamtveit, Geological pattern formation by growth and dissolution in aqueous systems, Proceedings of the Royal Society A: Mathematical, Physical and Engineering Sciences 466 (2010) 659–694. doi:10.1098/rspa.2009.0189.
[341] J. L. Macalady, D. S. Jones, E. H. Lyon, Extremely acidic, pendulous cave wall biofilms from the frasassi cave system, Italy, Environmental Microbiology 9 (2007) 1402–1414. doi:10.1111/j.1462-2920.2007.01256.x.
[342] D. R. Cullimore, L. A. Johnston, Microbiology of concretions, sediments and mechanisms influencing the preservation of submerged archaeological artifacts, International Journal of Historical Archaeology 12 (2008) 120–132. doi:10.1007/s10761-008-0045-y.
[343] M. Demmenie, L. Reus, P. Kolpakov, S. Woutersen, D. Bonn, N. Shahidzadeh, Growth and form of rippled icicles, Phys. Rev. Appl. 19 (2023) 024005. doi:10.1103/PhysRevApplied.19.024005.
[344] M. B. Short, J. C. Baygents, R. E. Goldstein, A free-boundary theory for the shape of the ideal dripping icicle, Physics of Fluids 18 (2006) 083101. doi:10.1063/1.2335152.
[345] N. Ogawa, Y. Furukawa, Surface instability of icicles, Physical Review E 66 (2002) 041202. doi:10.1103/PhysRevE.66.041202.
[346] K. Ueno, M. Farzaneh, S. Yamaguchi, H. Tsuji, Numerical and experimental verification of a theoretical model of ripple formation in ice growth under supercooled water film flow, Fluid Dynamics Research 42 (2010) 025508. doi:10.1088/

0169-5983/42/2/025508.
[347] M. Demmenie, B. Gorin, P. Kolpakov, S. Smith, H. Kellay, D. Bonn, Partial wetting of water on ice, Phys. Rev. Fluids 10 (2025) 054002. doi:10.1103/PhysRevFluids.10.054002.
[348] M. G. Worster, On icicle ripples, Journal of Engineering Mathematics 145 (2024) 15–45. doi:10.1007/s10665-024-10336-4.
[349] A. Huerre, C. Josserand, T. Séon, Freezing and capillarity, Annual Review of Fluid Mechanics (2024). doi:10.1146/annurev-fluid-121021-111652.
[350] H. W. Franke, The theory behind stalagmite shapes, Studies in Speleology 1 (1965) 89–95.
[351] D. Romanov, G. Kaufmann, W. Dreybrodt, Modeling stalagmite growth by first principles of chemistry and physics of calcite precipitation, Geochimica et Cosmochimica Acta 72 (2008) 423–437. doi:10.1016/j.gca.2007.09.038.
[352] P. Szymczak, A. J. Ladd, M. Lipar, D. Pekarovič, Shapes of ideal stalagmites, Proceedings of the National Academy of Sciences 122 (2025) e2513263122. doi:10.1073/pnas.2513263122.
[353] C. Lyell, On the tubular cavities filled with gravel and sand called "sand-pipes," in the chalk near Norwich, Phil. Mag. 15 (1839) 257–266. doi:10.1080/14786443908649874.
[354] M. P. Cooper, R. P. Sharma, S. Magni, T. P. Blach, A. P. Radlinski, K. Drabik, A. Tengattini, P. Szymczak, 4d tomography reveals a complex relationship between wormhole advancement and permeability variation in dissolving rocks, Advances in Water Resources 175 (2023) 104407. doi:10.1016/j.advwatres.2023.104407.
[355] J. Trimmer, On the pipes or sand-galls in the chalk and chalk-rubble of Norfolk, Quarterly Journal of the Geological Society 1 (1845) 300–317. doi:10.1144/GSL.JGS.1845.001.01.71.
[356] J. Prestwich, On the origin of the sand-and gravel-pipes in the chalk of the London Tertiary District, Quarterly Journal of the Geological Society 11 (1855) 64–84. doi:10.1144/GSL.JGS.1855.011.01-02.18.
[357] J. H. Bretz, Bermuda: A partially drowned, late mature, Pleistocene karst, Geological Society of America Bulletin 71 (1960) 1729–1754. doi:10.1130/0016-7606(1960)71[1729:BAPDLM]2.0.CO;2.
[358] N. Boutakoff, The geology and geomorphology of the Portland area, Geological Survey of Victoria Memoir 22 (1963) 1–172.
[359] S. R. Herwitz, Stemflow influences on the formation of solution pipes in Bermuda eolianite, Geomorphology 6 (1993) 253–271. doi:10.1016/0169-555X(93)90050-C.
[360] K. G. Grimes, Solution pipes or petried forests? drifting sands and drifting opinions!, Vic. Nat. 121 (2004) 14–22.
[361] J. Lundberg, B. E. Taggart, Dissolution pipes in northern Puerto Rico: An exhumed paleokarst, Carbonates Evaporites 10 (1995) 171–183. doi:10.1007/BF03175402.
[362] J. De Waele, S.-E. Lauritzen, M. Parise, On the formation of dissolution pipes in Quaternary coastal calcareous arenites in Mediterranean settings, Earth Surf. Processes Landforms 36 (2011) 143–157. doi:10.1002/esp.2022.
[363] M. Lipar, J. A. Webb, S. Q. White, K. G. Grimes, The genesis of solution pipes: Evidence from the middle–late Pleistocene Bridgewater formation calcarenite, southeastern Australia, Geomorphology 246 (2015) 90–103. doi:10.1016/j.geomorph.2015.06.013.
[364] I. Morawiecka, P. Walsh, A study of solution pipes preserved in the Miocene limestones (Staszow, Poland), Acta Carsologica 20 (1997) 337–350. doi:10.1016/S0031-0182(01)00317-0.
[365] P. Walsh, I. Morawiecka-Zacharz, A dissolution pipe palaeokarst of mid-Pleistocene age preserved in Miocene limestones near Staszow, Poland, Palaeogeography, Palaeoclimatology, Palaeoecology 174 (2001) 327–350. doi:10.1016/S0031-0182(01)00317-0.
[366] R. Dobrowolski, P. Mroczek, Clay cortex in epikarst forms as an indicator of age and morphogenesis—case studies from Lublin–Volhynia chalkland (East Poland, West Ukraine), Geomorphology 247 (2015) 66–75. doi:10.1016/j.geomorph.2014.12.018.
[367] S. E. Lauritzen, R. O. Skoglund, Glacier ice-contact speleogenesis in marble stripe karst, in: Proceedings of the 16th International Congress of Speleology, July 21–28, Brno, volume 3, Academic Press San Diego, 2013, pp. 363–396.
[368] S. Doerr, R. Shakesby, R. Walsh, Soil water repellency: its causes, characteristics and hydro-geomorphological significance, Earth Sci. Rev. 51 (2000) 33–65. doi:10.1016/S0012-8252(00)00011-8.
[369] D. A. Devitt, S. D. Smith, Root channel macropores enhance downward movement of water in a Mojave Desert ecosystem, J. Arid Environ. 50 (2002) 99–108. doi:10.1006/jare.2001.0853.
[370] F. Coetzee, Solution pipes in coastal aeolianites of Zululand and Mozambique, Trans. Geol. Soc. S. Afr. 78 (1975) 323–333.
[371] K. G. Grimes, Solution pipes and pinnacles in syngenetic karst, in: Karst Rock Features. Karren Sculpturing, Karst Research Institute, 2009, pp. 513–526.
[372] A. R. Mitchell, T. R. Ellsworth, B. D. Meek, Effect of root systems on preferential flow in swelling soil, Commun. Soil Sci. Plan. 26 (1995) 2655–2666. doi:10.1080/00103629509369475.
[373] M. S. Johnson, J. Lehmann, Double-funneling of trees: Stemflow and root-induced preferential flow, Ecoscience 13 (2006) 324–333. doi:10.2980/i1195-6860-13-3-324.1.
[374] V. K. Upadhyay, P. Szymczak, A. J. C. Ladd, Initial conditions or emergence: What determines dissolution patterns in rough fractures?, J. Geophys. Res. Solid Earth 120 (2015) 6102–6121. doi:10.1002/2015JB012233.
[375] K. Petrus, P. Szymczak, Influence of layering on the formation and growth of solution pipes, Front. Phys. 3 (2016) 92. doi:10.3389/fphy.2015.00092.
[376] W. Cheung, H. Rajaram, Dissolution finger growth in variable aperture fractures: Role of the tip-region flow field, Geophys. Res. Lett. 29 (2002) 2075. doi:10.1029/2002GL015196.
[377] P. Maheshwari, V. Balakotaiah, Comparison of carbonate HCI acidizing experiments with 3D simulations, SPE Prod. Oper. 28 (2013) 402–413. doi:10.2118/164517-PA.

[378] N. Kalia, V. Balakotaiah, Effect of medium heterogeneities on reactive dissolution of carbonates, Chem. Eng. Sci. 64 (2009) 376–390. doi:10.1016/j.ces.2008.10.026.
[379] P. Maheshwari, R. R. Ratnakar, N. Kalia, V. Balakotaiah, 3-d simulation and analysis of reactive dissolution and wormhole formation in carbonate rocks, Chem. Eng. Sci. 90 (2013) 258–274. doi:10.1016/j.ces.2012.12.032.
[380] R. L. Detwiler, R. J. Glass, W. L. Bourcier, Experimental observations of fracture dissolution: The role of Péclet number in evolving aperture variability, Geophys. Res. Lett. 30 (2003) 1648. doi:10.1029/2003GL017396.
[381] P. Gouze, C. Noiriel, C. Bruderer, D. Loggia, X-ray tomography characterization of fracture surfaces during dissolution, Geophys. Res. Lett. 30 (2003) 1267. doi:10.1029/2002GL016755.
[382] V. Starchenko, C. J. Marra, A. J. C. Ladd, Three-dimensional simulations of fracture dissolution, J. Geophys. Res. Solid 121 (2016) 6421–6444. doi:10.1002/2016JB013321.
[383] F. Osselin, A. Budek, O. Cybulski, P. Kondratiuk, P. Garstecki, P. Szymczak, Microfluidic observation of the onset of reactive infiltration instability in an analog fracture, Geophys. Res. Lett. 43 (2016) 6907–6915. doi:10.1002/2016GL069261.
[384] W. Dreybrodt, The role of dissolution kinetics in the development of karst aquifers in limestone: A model simulation of karst evolution, J. Geol. 98 (1990) 639–655. doi:10.1086/629431.
[385] I. Sharp, P. Gillespie, D. Morsalnezhad, C. Taberner, R. Karpuz, J. Vergés, A. Horbury, N. Pickard, J. Garland, D. Hunt, Stratigraphic architecture and fracture-controlled dolomitization of the Cretaceous Khami and Bangestan groups: an outcrop case study, Zagros Mountains, Iran, Geological Society, London, Special Publications 329 (2010) 343–396. doi:10.1144/SP329.14.
[386] W. B. White, Role of solution kinetics in the development of karst aquifers, Mem. Int. Assoc. Hydrogeol. 12 (1977) 503–517.
[387] A. Ginés, M. Knez, T. Slabe, W. Dreybrodt, Karst Rock Features. Karren Sculpturing: Karren Sculpturing, volume 9, Založba ZRC, 2009.
[388] J. R. Glew, D. C. Ford, A simulation study of the development of rillenkarren, Earth Surface Processes 5 (1980) 25–36. doi:10.1002/esp.3760050104.
[389] A. Guérin, J. Derr, S. Courrech du Pont, M. Berhanu, Streamwise dissolution patterns created by a flowing water film, Physical Review Letters 125 (2020) 194502. doi:0.1103/PhysRevLett.125.194502.
[390] D. Nahon, Y. Tardy, The ferruginous laterites, in: Handbook of exploration geochemistry, volume 4, Elsevier, 1992, pp. 41–55. doi:10.1016/B978-0-444-89095-5.50010-9.
[391] G. J. J. Aleva, Laterites: concepts, geology, morphology and chemistry, ISRIC: Wageningen, 1994.
[392] D. S. Korzhinskii, The theory of metasomatic zoning, Miner. Deposita 231 (1968) 222–231. doi:10.1007/BF00207435.
[393] A. Putnis, Mineral replacement reactions, Rev. Mineral. Geochem. 70 (2009) 87–124. doi:10.2138/rmg.2009.70.3.
[394] P. Kondratiuk, H. Tredak, V. Upadhyay, A. J. C. Ladd, P. Szymczak, Instabilities and finger formation in replacement fronts driven by an oversaturated solution, J. Geophys. Res. Solid 122 (2017) 5972—-5991. doi:10.1002/2017JB014169.
[395] A. Koeshidayatullah, H. Corlett, J. Stacey, P. K. Swart, A. Boyce, C. Hollis, Origin and evolution of fault-controlled hydrothermal dolomitization fronts: A new insight, Earth and Planetary Science Letters 541 (2020) 116291. doi:10.1016/j.epsl.2020.116291.
[396] S. Centrella, N. E. Beaudoin, H. Derluyn, G. Motte, G. Hoareau, P. Lanari, F. Piccoli, C. Pecheyran, J. P. Callot, Micro-scale chemical and physical patterns in an interface of hydrothermal dolomitization reveals the governing transport mechanisms in nature: Case of the Layens anticline, Pyrenees, France, Sedimentology 68 (2021) 834–854. doi:10.1111/sed.12808.
[397] E. Merino, À. Canals i Sabaté, Self-accelerating dolomite-for-calcite replacement: Self-organized dynamics of burial dolomitization and associated mineralization, American Journal of Science 311 (2011) 573–607. doi:10.2475/07.2011.01.
[398] J. N. Dewynne, A. C. Fowler, P. S. Hagan, Multiple reaction fronts in the oxidation/reduction of iron-rich uranium ores, Siam J. Appl. Math. 53 (1993) 971–989. doi:10.1137/0153048.
[399] E. Merino, A. Banerjee, Terra rossa genesis, implications for karst, and eolian dust: A geodynamic thread, J. Geol. 116 (2008) 62–75. doi:10.1086/524675.
[400] U. S. Lundström, N. van Breemen, D. C. Bain, The podzolization process. a review, Geoderma 94 (2000) 91–107. doi:10.1016/S0016-7061(99)00036-1.
[401] R. J. Schaetzl, C. Kasmerchak, P. Samonil, C. Baish, M. Hadden, D. Rothstein, Acidification and weathering associated with deep tongues in sandy Spodosols, Michigan, USA, Geoderma Regional 23 (2020) e00332. doi:10.1016/j.geodrs.2020.e00332.
[402] J. O. Skjemstad, R. W. Fitzpatrick, B. A. Zarcinas, C. H. Thompson, Genesis of podzols on coastal dunes in southern Queensland. II. geochemistry and forms of elements as deduced from various soil extraction procedures, Australian Journal of Soil Research 30 (1992) 615–644. doi:10.1071/SR9920615.
[403] R. R. Bourgault, D. S. Ross, S. W. Bailey, Chemical and morphological distinctions between vertical and lateral podzolization at Hubbard Brook, Soil Science Society of America Journal 79 (2015) 428–439. doi:10.2136/sssaj2014.05.0190.
[404] M. Sommer, D. Halm, C. Geisinger, I. Andruschkewitsch, M. Zarei, K. Stahr, Lateral podzolization in a sandstone catchment, Geoderma 103 (2001) 231–247. doi:10.1016/S0016-7061(01)00018-0.
[405] C. H. Thompson, Genesis of podzols on coastal dunes in southern Queensland. I. field relationships and profile morphology, Australian Journal of Soil Research 30 (1992) 593–613. doi:10.1071/SR9920593.
[406] M. Jankowski, The evidence of lateral podzolization in sandy soils of Northern Poland, Catena 112 (2014) 139–147. doi:10.1016/j.catena.2013.03.013.
[407] T. K. Lowenstein, L. A. Hardie, Criteria for the recognition of salt-pan evaporites, Sedimentology 32 (1985) 627–644. doi:10.1111/j.1365-3091.1985.tb00478.x.

[408] P. R. Briere, Playa, playa lake, sabkha: Proposed definitions for old terms, J. Arid Environ. 45 (2000) 1–7. doi:10.1006/jare.2000.0633.
[409] J. C. Dixon, Aridic Soils, Patterned Ground, and Desert Pavements, Springer Netherlands, Dordrecht, 2009, pp. 101–122. doi:10.1007/978-1-4020-5719-9_5.
[410] S. Tyler, S. Kranz, M. Parlange, J. Albertson, G. Katul, G. Cochran, B. Lyles, G. Holder, Estimation of groundwater evaporation and salt flux from Owens Lake, California, USA, J. Hydrol. 200 (1997) 110–135. doi:10.1016/S0022-1694(97)00007-3.
[411] D. Groeneveld, J. Huntington, D. Barz, Floating brine crusts, reduction of evaporation and possible replacement of fresh water to control dust from Owens Lake bed, California, J. Hydrol. 392 (2010) 211–218. doi:10.1016/j.jhydrol.2010.08.010.
[412] A. Bertenthal, Scaling the baseline: Technicalities and environmental regulation in Owens Valley, California, Law & Policy 43 (2021) 30–50. doi:10.1111/lapo.12162.
[413] J. M. Nield, R. G. Bryant, G. F. Wiggs, J. King, D. S. Thomas, F. D. Eckardt, R. Washington, The dynamism of salt crust patterns on playas, Geology 43 (2015) 31–34. doi:10.1130/G36175.1.
[414] J. Lasser, J. M. Nield, L. Goehring, Surface and subsurface characterisation of salt pans expressing polygonal patterns, Earth Syst. Sci. Data 12 (2020) 2881–2898. doi:10.5194/essd-12-2881-2020.
[415] J. Lasser, J. M. Nield, M. Ernst, V. Karius, G. F. S. Wiggs, M. R. Threadgold, C. Beaume, L. Goehring, Salt Polygons and Porous Media Convection, Phys. Rev. X 13 (2023) 011025. doi:10.1103/PhysRevX.13.011025.
[416] J. M. Prospero, Environmental characterization of global sources of atmospheric soil dust identified with the NIMBUS 7 Total Ozone Mapping Spectrometer (TOMS) absorbing aerosol product, Rev. Geophys. 40 (2002) 2. doi:10.1029/2000rg000095.
[417] M. Klose, T. E. G. abnd Vicken Etyemezian, G. Nikolich, Z. G. Zadeh, N. P. Webb, R. S. V. Pelt, Dust emission from crusted surfaces: Insights from field measurements and modelling, Aeolian Res. 40 (2019) 1–14. doi:10.1016/j.aeolia.2019.05.001.
[418] J. F. Kok, T. Storelvmo, V. A. Karydis, A. A. Adebiyi, N. M. Mahowald, A. T. Evan, C. He, D. M. Leung, Mineral dust aerosol impacts on global climate and climate change, Nature Reviews Earth and Environment 4 (2023) 71–86. doi:10.1038/s43017-022-00379-5.
[419] W. A. Wurtsbaugh, C. Miller, S. E. Null, R. J. DeRose, P. Wilcock, M. Hahnenberger, F. Howe, J. Moore, Decline of the world's saline lakes, Nature Geosci. 10 (2017) 816. doi:10.1038/ngeo3052.
[420] D. Krinsley, A geomorphological and paleoclimatological study of the playas of Iran. Part 1, volume CP 70-800, U.S. Geol. Survey, 1970. URL: http://hdl.handle.net/2346/63229.
[421] F. W. Christiansen, Polygonal fracture and fold systems in the salt crust, Great Salt Lake Desert, Utah, Science 139 (1963) 607–609. doi:10.1126/science.139.3555.607.
[422] J. Lasser, M. Ernst, L. Goehring, Stability and dynamics of convection in dry salt lakes, J. Fluid Mech. 917 (2021) A14. doi:10.1017/jfm.2021.225.
[423] R. J. Flatt, F. Caruso, A. M. A. Sanchez, G. W. Scherer, Chemo-mechanics of salt damage in stone, Nat. Commun. 5 (2014) 4823. doi:10.1038/ncomms5823.
[424] D. Hewitt, Vigorous convection in porous media, Proc. R. Soc. A 476 (2020) 20200111. doi:10.1098/rspa.2020.0111.
[425] D. A. Nield, A. Bejan, Convection in Porous Media, 7th ed., Springer Cham, 2017.
[426] R. A. Wooding, S. W. Tyler, I. White, Convection in groundwater below an evaporating Salt Lake: 1. Onset of instability, Water Resour. Res. 33 (1997) 1199–1217. doi:10.1029/96WR03533.
[427] R. A. Wooding, Rayleigh instability of a thermal boundary layer in flow through a porous medium, J. Fluid Mech. 9 (1960) 183–192. doi:10.1017/S0022112060001031.
[428] R. A. Wooding, S. W. Tyler, I. White, P. A. Anderson, Convection in groundwater below an evaporating Salt Lake: 2. Evolution of fingers or plumes, Water Resour. Res. 33 (1997) 1219–1228. doi:10.1029/96WR03534.
[429] G. M. Homsy, A. E. Sherwood, Convective instabilities in porous media with through flow, AIChE J. 22 (1976) 168–174. doi:10.1002/aic.690220121.
[430] C. Bringedal, T. Schollenberger, G. J. M. Pieters, C. J. van Duijn, R. Helmig, Evaporation-Driven Density Instabilities in Saturated Porous Media, Transp. Porous Med. 143 (2022) 297–341. doi:10.1007/s11242-022-01772-w.
[431] C. Bringedal, S. Kiemle, C. J. van Duijn, R. Helmig, Impact of Saturation on Evaporation-Driven Density Instabilities in Porous Media: Mathematical and Numerical Analysis, Transport in Porous Media 152 (2025). doi:10.1007/s11242-025-02207-y.
[432] R. L. Van Dam, C. T. Simmons, D. W. Hyndman, W. W. Wood, Natural free convection in porous media: First field documentation in groundwater, Geophysical Research Letters 36 (2009) L11403. doi:10.1029/2008GL036906.
[433] J. D. Stevens, J. M. S. Jr., C. T. Simmons, T. Fenstemaker, Evidence of free convection in groundwater: Field-based measurements beneath wind-tidal flats, J. Hydrol. 375 (2009) 394–409. doi:10.1016/j.jhydrol.2009.06.035.
[434] X. Liu, C. Zhang, Y. Liu, C. Li, C. Shen, P. Xin, L. Li, D. A. Lockington, Processes controlling formation of salt efflorescence in coastal salt flats, Water Resources Research 59 (2023) e2022WR034279. doi:10.1029/2022WR034279.
[435] I. Haque, R. A. Mitra, A. Jyoti, T. Dutta, Three-dimensional modeling of polygonal ridges in salt playas, Langmuir 40 (2024) 17311–17319. doi:10.1021/acs.langmuir.4c01160.
[436] E. Kotopoulou, A. Delgado Huertas, J. M. Garcia-Ruiz, J. M. Dominguez-Vera, J. M. Lopez-Garcia, I. Guerra-Tschuschke, F. Rull, A polyextreme hydrothermal system controlled by iron: the case of Dallol at the Afar Triangle, ACS Earth Space Chemistry 3 (2019) 90–99. doi:10.1021/acsearthspacechem.8b00141.
[437] M. G. Pitman, A. Läuchli, Global impact of salinity and agricultural ecosystems, in: Salinity: environment — plants — molecules, Springer, 2002, p. 20. doi:10.1007/0-306-48155-3_1.

[438] R. U. Cooke, I. J. Smalley, Salt weathering in deserts, Nature 220 (1968) 1226–1227. doi:10.1038/2201226a0.
[439] N. Shahidzadeh-Bonn, J. Desarnaud, F. Bertrand, X. Chateau, D. Bonn, Damage in porous media due to salt crystallization, Physical Review E 81 (2010) 066110. doi:10.1103/PhysRevE.81.066110.
[440] E. R. Washburn, The creeping of solutions, The Journal of Physical Chemistry 31 (1927) 1246–1248. doi:10.1021/j150278a009.
[441] B.-J. Huang, J.-C. Huang, Creeping-film phenomenon of potassium chloride solution, Nature 261 (1976) 36–38. doi:10.1038/261036a0.
[442] R. Hird, M. D. Bolton, Migration of sodium chloride in dry porous materials, Proceedings of the Royal Society A: Mathematical, Physical and Engineering Sciences 472 (2016) 20150710. doi:10.1098/rspa.2015.0710.
[443] M. J. Qazi, D. Bonn, N. Shahidzadeh, Drying of salt solutions from porous media: Effect of surfactants, Transport in Porous Media 128 (2019) 881–894. doi:10.1007/s11242-018-1164-5.
[444] S. Veran-Tissoires, M. Marcoux, M. Prat, Discrete salt crystallization at the surface of a porous medium, Physical review letters 108 (2012) 054502. doi:10.1103/PhysRevLett.108.054502.
[445] R. Wijnhorst, M. Prat, N. Shahidzadeh, Self-similarity in creeping salt crystallization, ArXiv preprint (2025). doi:10.48550/arXiv.2508.18779.
[446] M. Brocx, V. Semeniuk, The geoheritage significance of crystals, Geology Today 26 (2010) 216–225. doi:10.1111/j.1365-2451.2010.00773.x.
[447] K. Heinrichs, Diagnosis of weathering damage on rock-cut monuments in Petra, Jordan, Environmental Geology 56 (2008) 643–675. doi:10.1007/s00254-008-1358-1.
[448] B. Fitzner, K. Heinrichs, D. La Bouchardiere, Weathering damage on Pharaonic sandstone monuments in Luxor-Egypt, Building and Environment 38 (2003) 1089–1103. doi:10.1016/S0360-1323(03)00086-6.
[449] H. W. Wellman, A. T. Wilson, Salt weathering, a neglected geological erosive agent in coastal and arid environments, Nature 205 (1965) 1097–1098. doi:10.1038/2051097a0.
[450] E. Doehne, Salt weathering: a selective review, Geological society, London, special publications 205 (2002) 51–64. doi:10.1144/GSL.SP.2002.205.01.05.
[451] G. E. Mustoe, The origin of honeycomb weathering, Geological Society of America Bulletin 93 (1982) 108–115. doi:10.1130/0016-7606(1982)93<108:TOOHW>2.0.CO;2.
[452] C. Rodriguez-Navarro, E. Doehne, E. Sebastian, Origins of honeycomb weathering: The role of salts and wind, Geological Society of America Bulletin 111 (1999) 1250–1255. doi:10.1130/0016-7606(1999)111<1250:OOHWTR>2.3.CO;2.
[453] M. A. Chan, A. Örmö, T. C. Perry, W. T. Potter, D. E. Bowen, E. F. McDonald, Models of iron oxide concretion formation: Field, numerical, and laboratory comparisons, Geofluids 7 (2007) 356–368. doi:10.1111/j.1468-8123.2007.00187.x.
[454] K. M. Groom, C. D. Allen, L. Mol, T. R. Paradise, K. Hall, Defining tafoni: Re-examining terminological ambiguity for cavernous rock decay phenomena, Progress in Physical Geography 39 (2015) 775–793. doi:10.1177/0309133315605037.
[455] H. P. Huinink, L. Pel, K. Kopinga, Simulating the growth of tafoni, Earth Surface Processes and Landforms: The Journal of the British Geomorphological Research Group 29 (2004) 1225–1233. doi:10.1002/esp.1087DigitalObjectIdentifier(DOI).
[456] R. Weinberger, Initiation and growth of cracks during desiccation of stratified muddy sediments, Journal of structural geology 21 (1999) 379–386. doi:10.1016/S0191-8141(99)00029-2.
[457] P. S. Plummer, V. A. Gostin, Shrinkage cracks; desiccation or synaeresis?, Journal of Sedimentary Research 51 (1981) 1147–1156. doi:10.1306/212F7E4B-2B24-11D7-8648000102C1865D.
[458] E. Bonnet, O. Bour, N. E. Odling, P. Davy, I. Main, P. Cowie, B. Berkowitz, Scaling of fracture systems in geological media, Reviews of geophysics 39 (2001) 347–383. doi:10.1029/1999RG000074.
[459] Z.-y. Zhao, Y.-r. Guo, W. Yan, L. Hong, Q. Zhang, Growth patterns and dynamics of mud cracks at different diagenetic stages and its geological significance, International Journal of Sediment Research 29 (2014) 82–98. doi:10.1016/S1001-6279(14)60024-X.
[460] A. H. Lachenbruch, Mechanics of thermal contraction cracks and ice-wedge polygons in permafrost, volume 70, Geological Society of America, 1962.
[461] J. Cartwright, D. James, A. Bolton, The genesis of polygonal fault systems: a review, Geological Society, London, Special Publications 216 (2003) 223–243. doi:10.1144/GSL.SP.2003.216.01.15.
[462] D. M. Hansen, J. W. Shimeld, M. A. Williamson, H. Lykke-Andersen, Development of a major polygonal fault system in Upper Cretaceous chalk and cenozoic mudrocks of the Sable Subbasin, Canadian Atlantic margin, Marine and Petroleum Geology 21 (2004) 1205–1219. doi:10.1016/j.marpetgeo.2004.07.004.
[463] B. R. Pratt, Syneresis cracks: subaqueous shrinkage in argillaceous sediments caused by earthquake-induced dewatering, Sedimentary Geology 117 (1998) 1–10. doi:10.1016/S0037-0738(98)00023-2.
[464] S. McMahon, A. v. S. Hood, D. McIlroy, The origin and occurrence of subaqueous sedimentary cracks, Geological Society, London, Special Publications 448 (2017) 285–309. doi:10.1144/SP448.15.
[465] C. G. S. C. Kendall, J. K. Warren, A review of the origin and setting of tepees and their associated fabrics, Sedimentology 34 (1987) 1007–1027. doi:10.1111/j.1365-3091.1987.tb00590.x.
[466] B. R. Pratt, Tepees in peritidal carbonates: origin via earthquake-induced deformation, with example from the Middle Cambrian of western Canada, Sedimentary Geology 153 (2002) 57–64. doi:10.1016/S0037-0738(02)00318-4.
[467] J. Han, H. Zhu, Y. Lu, S. Yang, M. Yang, E. Shi, Y. Qi, Microstructural analysis of organic-rich shales: Insights from an electron microscopic study by application of FIBSEM and TEM, Nanomaterials 12 (2022) 4135. doi:10.3390/nano12234135.
[468] M. Kobchenko, H. Panahi, F. Renard, D. K. Dysthe, A. Malthe-Sørenssen, A. Mazzini, J. Scheibert, B. Jamtveit, P. Meakin, 4D imaging of fracturing in organic-rich shales during heating, Journal of Geophysical Research: Solid Earth

116 (2011) B12201. doi:10.1029/2011JB008565.
[469] R. S. Bassler, The formation of geodes with remarks on the silicification of fossils, volume 35, US Government Printing Office, 1908.
[470] J. Rakovan, Word to the wise: Geode (and friends), Rocks & Minerals 92 (2017) 85–91. doi:10.1080/00357529.2017.1241695.
[471] Á. Fernández-Cortés, J. M. Calaforra, J. García-Guinea, The Pulpí gigantic geode (Almería, Spain): geology, metal pollution, microclimatology, and conservation, Environmental Geology 50 (2006) 707–716. doi:10.1007/s00254-006-0243-z.
[472] R. Raiswell, Q. Fisher, Mudrock-hosted carbonate concretions: a review of growth mechanisms and their influence on chemical and isotopic composition, Journal of the Geological Society 157 (2000) 239–251. doi:10.1144/jgs.157.1.239.
[473] A. Seilacher, Concretion morphologies reflecting diagenetic and epigenetic pathways, Sedimentary Geology 143 (2001) 41–57. doi:10.1016/S0037-0738(01)00092-6.
[474] J. D. Marshall, D. Pirrie, Carbonate concretions—explained, Geology today 29 (2013) 53–62. doi:10.1111/gto.12002.
[475] R. Raiswell, Q. J. Fisher, Mudrock-hosted carbonate concretions: a review of growth mechanisms and their influence on chemical and isotopic composition, Journal of the Geological Society 157 (2000) 239–251. doi:10.1144/jgs.157.1.239.
[476] A. Seilacher, Concretion morphologies reflecting diagenetic and epigenetic pathways, Sedimentary Geology 143 (2001) 41–57. doi:10.1016/S0037-0738(01)00092-6.
[477] T. R. Astin, Septarian crack formation in carbonate concretions from shales and mudstones, Clay Minerals 21 (1986) 617–631. doi:10.1180/claymin.1986.021.4.12.
[478] M. W. Hounslow, Significance of localized pore pressures to the genesis of septarian concretions, Sedimentology 44 (1997) 1133–1147. doi:10.1046/j.1365-3091.1997.d01-64.x.
[479] B. R. Pratt, Septarian concretions: internal cracking caused by synsedimentary earthquakes, Sedimentology 48 (2001) 189–213. doi:10.1046/j.1365-3091.2001.00366.x.
[480] J. P. Hendry, M. J. Pearson, N. H. Trewin, A. E. Fallick, Jurassic septarian concretions from NW Scotland record interdependent bacterial, physical and chemical processes of marine mudrock diagenesis, Sedimentology 53 (2006) 537–565. doi:10.1111/j.1365-3091.2006.00779.x.
[481] I. C. Scotchman, The geochemistry of concretions from the Kimmeridge Clay Formation of southern and eastern England, Sedimentology 38 (1991) 79–106. doi:10.1111/j.1365-3091.1991.tb01856.x.
[482] T. R. Astin, I. C. Scotchman, The diagenetic history of some septarian concretions from the Kimmeridge Clay, England, Sedimentology 35 (1988) 349–368. doi:10.1111/j.1365-3091.1988.tb00952.x.
[483] J. D. Hudson, M. L. Coleman, B. Barreiro, N. T. J. Hollingworth, Septarian concretions from the Oxford Clay (Jurassic, England, UK): involvement of original marine and multiple external pore fluids, Sedimentology 48 (2001) 507–531. doi:10.1046/j.1365-3091.2001.00374.x.
[484] M. De Craen, R. Swennen, E. Keppens, Petrography and geochemistry of septarian carbonate concretions from the Boom Clay Formation (Oligocene, Belgium), Geologie en Mijnbouw 77 (1998) 63–76. doi:10.1023/A:1003468328212.
[485] J. D. Green, D. Pirrie, Early diagenetic septarian concretions from the Oxfordian (Jurassic) Corallian Group, Osmington Mills, Dorset, UK, Geoscience in South-West England 10 (2001) 142–148.
[486] J. M. Molina, M. Reolid, Barite septarian concretions in the Albian (Cretaceous) of the Subbetic (Southern Spain), Journal of Iberian Geology 50 (2024) 431–448. doi:10.1007/s41513-024-00256-8.
[487] R. B. Paxton, P. F. Dennis, A. D. Marca, J. P. Hendry, J. D. Hudson, J. E. Andrews, Taking the heat out of British Jurassic septarian concretions, The Depositional Record 7 (2021) 333–343. doi:10.1002/dep2.139.
[488] S. Boggs Jr, Petrology of sedimentary rocks, Cambridge university press, 2009.
[489] S. L. Potter-McIntyre, M. A. Chan, E. U. Petersen, M. D. Dyar, E. C. Sklute, Characterization of Navajo Sandstone Concretions: Mars comparison and criteria for distinguishing diagenetic origins, Earth and Planetary Science Letters 301 (2011) 444–456. doi:10.1016/j.epsl.2010.11.027.
[490] N. Katsuta, S. Sirono, A. Umemura, H. Kawahara, Y. Masuki, C. Yoshimizu, I. Tayasu, T. Murakami, H. Yoshida, Rhythmic iron-oxide bands of Navajo Sandstone Concretions and Kimberley Banded Claystone: Formation process and buffering reaction rate by diagenetic alteration, Sedimentology 71 (2024) e13135. doi:10.1111/sed.13135.
[491] H. K. Henisch, Periodic Precipitation, Pergamon Press, Oxford, 1991.
[492] H. Nabika, M. Itatani, I. Lagzi, Pattern formation in precipitation reactions: The Liesegang phenomenon, Langmuir 36 (2020) 481–497. doi:10.1021/acs.langmuir.9b03018.
[493] R. Joesten, Evolution of mineral assemblage zoning in diffusion metasomatism, Geochimica et Cosmochimica Acta 41 (1977) 649–670. doi:10.1016/0016-7037(77)90303-9.
[494] J. R. Ashworth, J. J. Birdi, Diffusion modelling of coronas around olivine in an open system, Geochimica et Cosmochimica Acta 54 (1990) 2389–2401. doi:10.1016/0016-7037(90)90227-C.
[495] W. C. Park, E. H. Schot, Stylolites; their nature and origin, Journal of Sedimentary Research 38 (1968) 175–191. doi:10.1306/74D71910-2B21-11D7-8648000102C1865D.
[496] P. B. Stockdale, Stylolites: Their Nature and Origin, Master's thesis, Indiana University, Bloomington, IN, 1922. Published as Indiana University Studies, vol. 9, no. 55, pp. 1-97.
[497] B. M. Shaub, The origin of stylolites, Journal of Sedimentary Research 9 (1939) 47–61. doi:10.1306/D426903F-2B26-11D7-8648000102C1865D.
[498] D. Koehn, M. P. Rood, N. Beaudoin, P. Chung, P. D. Bons, E. Gomez-Rivas, A new stylolite classification scheme to estimate compaction and local permeability variations, Sedimentary Geology 346 (2016) 60–71. doi:10.1016/j.sedgeo.2016.10.007.
[499] M. J. Heap, P. Baud, T. Reuschlé, P. G. Meredith, Stylolites in limestones: Barriers to fluid flow?, Geology 42 (2014) 51–54. doi:10.1130/G34900.1.

[500] P.-O. Bruna, A. P. C. Lavenu, C. Matonti, G. Bertotti, Are stylolites fluid-flow efficient features?, Journal of Structural Geology 125 (2019) 270–277. doi:10.1016/j.jsg.2018.05.018.
[501] P. K. Weyl, Pressure solution and the force of crystallization: a phenomenological theory, J. Geophys. Res. 64 (1959) 2001–2025. doi:10.1029/JZ064i011p02001.
[502] M. T. Heald, Significance of stylolites in permeable sandstones, J. Sediment. Res. 29 (1959) 251–253. doi:10.1306/74D708F3-2B21-11D7-8648000102C1865D.
[503] R. Asaro, W. Tiller, Interface morphology development during stress corrosion cracking: Part I. Via surface diffusion, Metall. Trans. 3 (1972) 1789–1796. doi:10.1007/BF02642562.
[504] M. Grinfel'd, Instability of the separation boundary between a nonhydrostatically stressed elastic body and a melt, in: Soviet Physics Doklady, volume 31, 1986, p. 831.
[505] K. Kassner, C. Misbah, J. Müller, J. Kappey, P. Kohlert, Phase-field modeling of stress-induced instabilities, Phys. Rev. E 63 (2001) 036117. doi:10.1103/PhysRevE.63.036117.
[506] R. C. Fletcher, D. D. Pollard, Anticrack model for pressure solution surfaces, Geology 9 (1981) 419–424. doi:10.1130/0091-7613(1981)9<419:AMFPSS>2.0.CO;2.
[507] E. Aharonov, R. Katsman, Interaction between pressure solution and clays in stylolite development: Insights from modeling, Am. J. Sci. 309 (2009) 607–632. doi:10.2475/07.2009.04.
[508] J. Schmittbuhl, F. Renard, J.-P. Gratier, R. Toussaint, Roughness of stylolites: implications of 3D high resolution topography measurements, Phys. Rev. Lett. 93 (2004) 238501. doi:10.1103/PhysRevLett.93.238501.
[509] E. Bonnetier, C. Misbah, F. Renard, R. Toussaint, J.-P. Gratier, Does roughening of rock-fluid-rock interfaces emerge from a stress-induced instability?, Eur. Phys. J. B. 67 (2009) 121–131. doi:10.1140/epjb/e2009-00002-2.
[510] A. Rolland, R. Toussaint, P. Baud, J. Schmittbuhl, N. Conil, D. Koehn, F. Renard, J.-P. Gratier, Modeling the growth of stylolites in sedimentary rocks, Journal of Geophysical Research: Solid Earth 117 (2012). doi:10.1029/2011JB009065.
[511] L. L. Ben-Itzhak, E. Aharonov, R. Toussaint, A. Sagy, Upper bound on stylolite roughness as indicator for amount of dissolution, Earth Planet. Sci. Lett. 337 (2012) 186–196. doi:10.1016/j.epsl.2012.05.026.
[512] M. Ebner, R. Toussaint, J. Schmittbuhl, D. Koehn, P. Bons, Anisotropic scaling of tectonic stylolites: A fossilized signature of the stress field?, J.Geophys. Res. Solid Earth 115 (2010). doi:10.1029/2009JB006649.
[513] D. Koehn, M. Ebner, F. Renard, R. Toussaint, C. Passchier, Modelling of stylolite geometries and stress scaling, Earth Planet. Sci. Lett. 341 (2012) 104–113. doi:10.1016/j.epsl.2012.04.046.
[514] J.-P. Gratier, L. Muquet, R. Hassani, F. Renard, Experimental microstylolites in quartz and modeled application to natural stylolitic structures, J. Struct. Geol. 27 (2005) 89–100. doi:10.1016/j.jsg.2004.05.007.
[515] S. Z. Shah, M. Sayab, D. Aerden, M. A. Khan, Foliation intersection axes preserved in garnet porphyroblasts from the Swat area, NW Himalaya: A record of successive crustal shortening directions between the Indian plate and Kohistan–Ladakh Island Arc, Tectonophysics 509 (2011) 14–32. doi:10.1016/j.tecto.2011.05.010.
[516] C. Fay, T. H. Bell, Porphyroblast rotation versus nonrotation: Conflict resolution!, Geology 36 (2008) 307—310. doi:10.1130/G24499A.1.
[517] P. D. Bons, M. W. Jessell, A. Griera, C. Fay, Porphyroblast rotation versus nonrotation: Conflict resolution!: COMMENT, Geology 37 (2009) e182—e188. doi:10.1130/G25131C.1.
[518] P. O. Brunn, Slow motion of a sphere in a second-order fluid, Rheol. Acta 15 (1976) 163–171. doi:10.1007/BF01526063.
[519] F. Gauthier, H. L. Goldsmith, S. G. Mason, Particle motions in non-Newtonian media I. Couette flow, Rheol. Acta 10 (1971) 344–364. doi:10.1007/BF01993709.
[520] G. D'Avino, M. A. Hulsen, F. Snijkers, J. Vermant, Rotation of a sphere in a viscoelastic liquid subjected to shear flow. Part I: Simulation results, J. Rheol. 52 (2008) 1331–1346. doi:10.1122/1.2998219.
[521] F. Snijkers, G. D'Avino, P. L. Maffettone, F. Greco, Rotation of a sphere in a viscoelastic liquid subjected to shear flow. Part II. Experimental results, J. Rheol. 53 (2009) 459–480. doi:10.1122/1.3073052.
[522] J. Michele, R. Pätzold, R. Donis, Alignment and aggregation effects in suspensions of spheres in non-Newtonian media, Rheol. Acta 16 (1977) 317–321. doi:10.1007/BF01523742.
[523] D. Won, C. Kim, Alignment and aggregation of spherical particles in viscoelastic fluid under shear flow, J. Non-Newtonian Fluid Mech. 117 (2004) 141–146. doi:10.1016/j.jnnfm.2004.01.005.
[524] R. Scirocco, J. Vermant, J. Mewis, Effect of the viscoelasticity of the suspending fluid on structure formation in suspensions, J. Non-Newtonian Fluid Mech. 117 (2004) 183–192. doi:10.1016/j.jnnfm.2004.01.010.
[525] W. R. Hwang, M. A. Hulsen, Structure formation of non-colloidal particles in viscoelastic fluids subjected to simple shear flow, Macromol. Materials Eng. 296 (2011) 321–330. doi:10.1002/mame.201000303.
[526] T. H. Bell, M. D. Bruce, Progressive deformation partitioning and deformation history: Evidence from millipede structures, Journal of Structural Geology 29 (2007) 18–35. doi:10.1016/j.jsg.2006.08.005.
[527] S. Katsev, I. L'Heureux, A. D. Fowler, Mechanism and duration of banding in Mississippi Valley-type sphalerite, Geophysical Research Letters 28 (2001) 4643–4646. doi:10.1029/2001GL013080.
[528] C. Zhu, S. Liao, W. Wang, Y. Zhang, T. Yang, H. Fan, H. Wen, Variations in Zn and S isotope chemistry of sedimentary sphalerite, Wusihe Zn-Pb deposit, Sichuan Province, China, Ore Geology Reviews 95 (2018) 639–648. doi:10.1016/j.oregeorev.2018.03.018.
[529] L. M. Cathles, A. T. Smith, Thermal constraints on the formation of Mississippi Valley-type lead-zinc deposits and their implications for episodic basin dewatering and deposit genesis, Economic Geology 78 (1983) 983–1002. doi:10.2113/gsecongeo.78.5.983.
[530] B. Yardley, C. Rochelle, A. Barnicoat, G. Lloyd, Oscillatory zoning in metamorphic minerals: an indicator of infiltration metasomatism, Mineralogical Magazine 55 (1991) 357–365. doi:10.1180/minmag.1991.055.380.06.
[531] I. S. Oen, P. Kager, C. Kieft, Oscillatory zoning of a discontinuous solid-solution series: sphalerite-stannite, American

Mineralogist 65 (1980) 1220–1232.
[532] I. L'Heureux, Origin of banded patterns in natural sphalerite, Physical Review E 62 (2000) 3234–3245. doi:10.1103/PhysRevE.62.3234.
[533] S. Katsev, I. L'Heureux, Two-dimensional model of banding pattern formation in minerals by means of coarsening waves: Mississippi Valley-type sphalerite, Physics Letters A 292 (2001) 66–74. doi:10.1016/S0375-9601(01)00767-8.
[534] R. D. Benedetto, G. P. Bernardini, P. Costagliola, D. Plant, D. J. Vaughan, Compositional zoning in sphalerite crystals, American Mineralogist 90 (2005) 1384–1392. doi:10.2138/am.2005.1754.
[535] R. Feeney, S. Schmidt, P. Strickholm, J. Chadam, P. Ortoleva, Periodic precipitation and coarsening waves: Applications of the competitive particle growth model, The Journal of Chemical Physics 78 (1983) 1293–1311. doi:10.1063/1.444867.
[536] H. Kucha, E. Schroll, J. Raith, S. Hałas, Microbial sphalerite formation in carbonate-hosted Zn-Pb ores, Bleiberg, Austria: Micro- to nanotextural and sulfur isotope evidence, Economic Geology 105 (2010) 1005–1023. doi:10.2113/econgeo.105.5.1005.
[537] C. Breitkreuz, Spherulites and lithophysae—200 years of investigation on high-temperature crystallization domains in silica-rich volcanic rocks, Bulletin of Volcanology 75 (2013) 1–16. doi:10.1007/s00445-013-0705-6.
[538] R. D. Roots, Thunder eggs, Rocks & Minerals 27 (1952) 234–236. doi:10.1080/00357529.1952.11768071.
[539] D. E. Kile, Occurrence and genesis of thunder eggs containing plume and moss agate: from the Del Norte Area, Saguache County, Colorado, Rocks & Minerals 77 (2002) 252–268. doi:10.1080/00357529.2002.9925643.
[540] W. H. Bryan, The later history of expanded spherulites, Journal of the Geological Society of Australia 10 (1963) 141–149. doi:10.1080/00167616308728536.
[541] J. Philpotts, J. R. Evans, Rare earth minerals in "thunder eggs" from Zarembo Island, Southeast Alaska, US Geological Survey Bulletin 2041 (1991) 98.
[542] J. J. J. J. Sederholm, On orbicular granites, spotted and nodular granites, etc., and on the Rapakivi texture, number 83 in Bulletin de la Commission Géologique de Finlande, Government Press, 1928.
[543] D. J. Leveson, Orbicular rocks: a review, Geological Society of America Bulletin 77 (1966) 409–426. doi:10.1130/0016-7606(1966)77[409:ORAR]2.0.CO;2.
[544] R. Vernon, Possible role of superheated magma in the formation of orbicular granitoids, Geology 13 (1985) 843–845. doi:10.1130/0091-7613(1985)13<843:PROSMI>2.0.CO;2.
[545] S. I. Lahti, P. Raivio, I. Laitakari, Orbicular rocks in Finland, Geological Survey of Finland, 2005.
[546] C. Argentino, S. Conti, C. Fioroni, D. Fontana, Evidences for paleo-gas hydrate occurrence: What we can infer for the Miocene of the Northern Apennines (Italy), Geosciences 9 (2019) 134. doi:10.3390/geosciences9030134.
[547] J. P. Kennett, B. N. Fackler-Adams, Relationship of clathrate instability to sediment deformation in the upper Neogene of California, Geology 28 (2000) 215–218. doi:10.1130/0091-7613(2000)28<215:ROCITS>2.0.CO;2.
[548] J. P. Smith, R. B. Coffin, Methane flux and authigenic carbonate in shallow sediments overlying methane hydrate bearing strata in Alaminos Canyon, Gulf of Mexico, Energies 7 (2014) 6118–6141. doi:10.3390/en7096118.
[549] E. Suess, Marine cold seeps and their manifestations: geological control, biogeochemical criteria and environmental conditions, International Journal of Earth Sciences 103 (2014) 1889–1916. doi:10.1007/s00531-014-1010-0.
[550] G. Aloisi, C. Pierre, J.-M. Rouchy, J.-P. Foucher, J. Woodside, the MEDINAUT Scientific Party, Methane-related authigenic carbonates of eastern Mediterranean Sea mud volcanoes and their possible relation to gas hydrate destabilisation, Earth and Planetary Science Letters 184 (2000) 321–338. doi:10.1016/S0012-821X(00)00322-8.
[551] J. Greinert, G. Bohrmann, E. Suess, Gas hydrate-associated carbonates and methane-venting at Hydrate Ridge: classification, distribution and origin of authigenic lithologies, Geophysical Monograph-American Geophysical Union 124 (2001) 99–114. doi:10.1029/GM124p0099.
[552] C. Pimentel, C. Gutiérrez-Ariza, A. G. Checa, C. I. Sainz-Díaz, J. H. E. Cartwright, Mineralogical description and hypothesis on the formation of menilites from Galera, Granada (Spain), Physics and Chemistry of Minerals 51 (2024) 7. doi:10.1007/s00269-023-01267-0.
[553] M. A. Molina Grande, J. Molina García, Ídolos naturales de piedra en el bronce del Sureste Peninsular, Murgetana 59 (1980) 5–36.
[554] S. Foley, T. Molyneux, An account of the Giants CausWay in the North of Ireland, Phil. Trans. R. Soc. Lond. 18 (1694) 170–182. doi:10.1098/rstl.1694.0036.
[555] M. P. Ryan, C. G. Sammis, Cyclic fracture mechanisms in cooling basalt, Geol. Soc. Am. Bull. 89 (1978) 129–1308. doi:10.1130/0016-7606(1978)89<1295:CFMICB>2.0.CO;2.
[556] P. E. Long, B. J. Wood, Structures, textures and cooling histories of Columbia River basalt flows, Geol. Soc. Am. Bull. 97 (1986) 1144–1155. doi:10.1130/0016-7606(1986)97<1144:STACHO>2.0.CO;2.
[557] A. Aydin, J. M. DeGraff, Evolution of polygonal fracture patterns in lava flows, Science 239 (1988) 471–476. doi:10.1126/science.239.4839.471.
[558] J. C. Phillips, M. C. S. Humphreys, K. A. Daniels, R. J. Brown, F. Witham, The formation of columnar joints produced by cooling in basalt at Staffa, Scotland, Bull. Volcanol. 75 (2013) 715. doi:10.1007/s00445-013-0715-4.
[559] J. M. DeGraff, A. Aydin, Surface morphology of columnar joints and its significance to mechanics and direction of joint growth, Geol. Soc. Am. 99 (1987) 605–617. doi:10.1130/0016-7606(1987)99<605:SMOCJA>2.0.CO;2.
[560] M. Milazzo, L. Keszthelyi, W. Jaeger, M. Rosiek, S. Mattson, C. Verba, R. Beyer, P. Geissler, A. McEwen, the HiRISE Team, Discovery of columnar jointing on Mars, Geology 37 (2009) 171–174. doi:10.1130/G25187A.1.
[561] M. Milazzo, D. K. Weiss, B. Jackson, J. Barne, Columnar jointing on Mars: Earth analog studies , 43rd Lunar Planet. Sci. Conf. (2012) 2726.
[562] Z. Xiao, Z. Zeng, Z. Li, D. M. Blair, L. Xiao, Cooling fractures in impact melt deposits on the Moon and Mercury: Implications for cooling solely by thermal radiation, J. Geophys. Res. Planets 119 (2014) 1496–1515. doi:10.1002/

2013JE004560.
[563] A. Basilevsky, A. Abdrakhimov, J. Head, C. Pieters, Y. Wu, L. Xiao, Geologic characteristics of the Luna 17/Lunokhod 1 and Chang'E-3/Yutu landing sites, Northwest Mare Imbrium of the Moon, Planetary Space Sci. 117 (2015) 385–400. doi:10.1016/j.pss.2015.08.006.
[564] N. S. Summer, A. Ayalon, Dike intrusion into unconsolidated sandstone and the development of quartzite contact zones, J. Struct. Geol. 17 (1995) 997–1010. doi:10.1016/0191-8141(95)00009-3.
[565] R. Weinberger, A. Burg, Reappraising columnar joints in different rock types and settings, J. Struct. Geol. 125 (2019) 185–194. doi:10.1016/j.jsg.2018.04.015.
[566] J. W. French, The fracture of homogeneous media, Trans. Geol. Soc. Glasgow 17 (1925) 50–68. doi:10.1144/transglas.17.1.50.
[567] D. L. Peck, T. Minakami, The formation of columnar joints in the upper part of Kilauean lava lakes, Hawaii, Geol. Soc. Am. Bull. 79 (1968) 1151–1168. doi:10.1130/0016-7606(1968)79[1151:TFOCJI]2.0.CO;2.
[568] J. Lore, A. Aydin, K. Goodson, A deterministic methodology for prediction of fracture distribution in basaltic multiflows, J. Geophys. Res. 106 (2001) 6447–6459. doi:10.1029/2000JB900407.
[569] J. Gottsmann, A. J. L. Harris, D. B. Dingwell, Thermal history of hawaiian pahoehoe lava crusts at the glass transition: implications for flow rheology and emplacement, Earth Planetary Sci. Lett. 228 (2004) 343–353. doi:10.1016/j.epsl.2004.09.038.
[570] A. Lamur, Y. Lavallée, F. E. Iddon, A. J. Hornby, J. E. Kendrick, F. W. von Aulock, F. B. Wadsworth, Disclosing the temperature of columnar jointing in lavas, Nat. Commun. 9 (2018) 1432. doi:10.1038/s41467-018-03842-4.
[571] P. Budkewitsch, P.-Y. Robin, Modelling the evolution of columnar joints, J. Volcanol. Geotherm. Res. 59 (1994) 219–239. doi:10.1016/0377-0273(94)90092-2.
[572] D. Pollard, A. Aydin, Progress in understanding jointing over the past century, Geol. Soc. Am. Bull. 100 (1988) 1181–1204. doi:10.1130/0016-7606(1988)100<1181:PIUJOT>2.3.CO;2.
[573] S. Bohn, L. Pauchard, Y. Couder, Hierarchical crack pattern as formed by successive domain divisions. I. temporal and geometrical hierarchy, Phys. Rev. E 71 (2005) 046214. doi:10.1103/PhysRevE.71.046214.
[574] L. Goehring, Evolving fracture patterns: columnar joints, mud cracks and polygonal terrain, Phil. Trans. R. Soc. A 371 (2013) 20120353–20120353. doi:10.1098/rsta.2012.0353.
[575] L. Goehring, S. W. Morris, Cracking mud, freezing dirt and breaking rocks, Phys. Today 67 (2014) 39–44. doi:10.1063/PT.3.2584.
[576] S. A. Kattenhorn, C. J. Schaefer, Thermal–mechanical modeling of cooling history and fracture development in inflationary basalt lava flows, J. Volcanol. Geotherm. Res. 170 (2008) 181–197. doi:10.1016/j.jvolgeores.2007.10.002.
[577] H. C. Hardee, Solidification in Kilauea Iki lava lake, J. Volcanol. Geotherm. Res. 7 (1980) 211–223. doi:10.1016/0377-0273(80)90030-X.
[578] S. I. Tomkeieff, The basalt lavas of the Giant's Causeway district of Northern Ireland, Bull. Volcanol. 6 (1940) 89–146. doi:10.1007/BF02994875.
[579] A. E. S. Forbes, S. Blake, H. Tuffen, Entablature: fracture types and mechanisms, Bull. Volcanol. 76 (2014). doi:10.1007/s00445-014-0820-z.
[580] A. Hamada, A. Toramaru, Analogue experiments on morphological transition from colonnade to entablature of columnar joints, J. Volcanol. Geotherm. Res. 402 (2020) 106979. doi:10.1016/j.jvolgeores.2020.106979.
[581] K. A. Grossenbacher, S. M. McDuffie, Conductive cooling of lava: columnar joint diameter and stria width as functions of cooling rate and thermal gradient, J. Volcanol. Geotherm. Res. 69 (1995) 95–103. doi:10.1016/0377-0273(95)00032-1.
[582] L. Goehring, L. Mahadevan, S. W. Morris, Nonequilibrium scale selection mechanism for columnar jointing, Proc. Nat. Acad. Sci. 106 (2009) 387–392. doi:10.1073/pnas.0805132106.
[583] J. M. DeGraff, A. Aydin, Effect of thermal regime on growth increment and spacing of contraction joints in basaltic lava, J. Geophys. Res. 98 (1993) 6411–6430. doi:10.1029/92JB01709.
[584] R. T. Helz, Major-element compositional data and thermal data for drill core from Kilauea Iki lava lake, plus analyses of glasses from scoria of the 1959 summit eruption of Kilauea Volcano, Hawaii, USGS Numbered Series (2020) 2020–1012.
[585] T. Bai, D. D. Pollard, H. Gao, Explanation for fracture spacing in layered materials, Nature 403 (2000) 753–756. doi:10.1038/35001550.
[586] H. M. Yin, Fracture saturation and critical thickness in layered materials, Int. J. Solids Struct. 47 (2010) 1007–1015. doi:10.1016/j.ijsolstr.2009.12.016.
[587] A. Groisman, E. Kaplan, An experimental study of cracking induced by desiccation, Europhys. Lett. 25 (1994) 415–420. doi:10.1209/0295-5075/25/6/004.
[588] D. Hull, B. D. Caddock, Simulation of prismatic cracking of cooling basalt lava flows by the drying of sol-gels, J. Mat. Sci. 34 (1999) 5707–5720. doi:10.1023/A:1004793731308.
[589] K. A. Shorlin, J. R. de Bruyn, M. Graham, S. W. Morris, Development and geometry of isotropic and directional shrinkage crack patterns, Phys. Rev. E. 61 (2000) 6950. doi:10.1103/PhysRevE.61.6950.
[590] G. Müller, Experimental simulation of basalt columns, J. Volcanology and Geothermal Res. 86 (1998) 93–96. doi:10.1016/S0377-0273(98)00045-6.
[591] T. H. Huxley, Physiography: An Introduction to the Study of Nature, MacMillan and Co., London, 1881.
[592] A. Toramaru, T. Matsumoto, Columnar joint morphology and cooling rate: A starch–water mixture experiment, J. Geophys. Res. 109 (2004) B02205. doi:10.1029/2003JB002686.
[593] L. Goehring, S. W. Morris, Order and disorder in columnar joints, Europhys. Lett. 69 (2005) 739–745. doi:10.1209/epl/i2004-10408-x.
[594] T. Mizuguchi, A. Nishimoto, S. Kitsunezaki, Y. Yamazaki, I. Aoki, Directional crack propagation of granular water

systems, Phys. Rev. E 71 (2005) 056122. doi:10.1103/PhysRevE.71.056122.
[595] A. Nishimoto, T. Mizuguchi, S. Kitsunezaki, Numerical study of drying process and columnar fracture process in granule-water mixtures, Phys. Rev. E 76 (2007) 016102. doi:10.1103/PhysRevE.76.016102.
[596] G. Müller, T. Dahm, Fracture morphology of tensile cracks and rupture velocity, J. Geophys. Res. 105 (2000) 723–738. doi:10.1029/1999JB900314.
[597] H. Sakaguchi, K. Yamada, M. Shimokawa, Observation and a simple model of plumose pattern on fracture surfaces of drying pastes, Europhys. Lett. 138 (2022) 16002. doi:10.1209/0295-5075/ac61b0.
[598] L. Goehring, Z. Lin, S. W. Morris, Experimental investigation of the scaling of columnar joints, Phys. Rev. E 74 (2006) 036115. doi:10.1103/PhysRevE.74.036115.
[599] H.-A. Crostack, J. Nellesen, G. Fischer, M. Hofmann, H.-G. Rademacher, W. Tillmann, Analysis of crack patterns in drying corn starch by in-situ radiography and X-ray computer tomography, Exp. Mech. 532 (2012) 912–932. doi:10.1007/s11340-011-9581-1.
[600] P. Bacchin, D. Brutin, A. Davaille, E. D. Giuseppe, X. D. Chen, I. Gergianakis, F. Giorgiutti-Dauphiné, L. Goehring, Y. Hallez, R. Heyd, R. Jeantet, C. L. Floch-Fouéré, M. Meireles, E. Mittelstaedt, C. Nicloux, L. Pauchard, M.-L. Saboungi, Drying colloidal systems: Laboratory models for a wide range of applications, Eur. Phys. J. E 41 (2018) 94. doi:10.1140/epje/i2018-11712-x.
[601] L. Goehring, A. Nakahara, T. Dutta, S. Kitsunezaki, S. Tarafdar, Desiccation cracks and their patterns: Formation and Modelling in Science and Nature, Wiley-VCH, Singapore, 2015.
[602] G. Domokos, D. J. Jerolmack, F. Kun, J. Török, Plato's cube and the natural geometry of fragmentation, Proc. Nat. Acad. Sci. 117 (2020) 18178–18185. doi:10.1073/pnas.2001037117.
[603] A. Roy, R. A. I. Haque, A. J. Mitra, S. Tarafdar, T. Dutta, Combinatorial topology and geometry of fracture networks, Phys. Rev. E 105 (2022) 034801. doi:10.1103/PhysRevE.105.034801.
[604] G. Domokos, K. Regös, A discrete time evolution model for fracture networks, Cent. Eur. J. Oper. Res. 32 (2024) 83–94. doi:10.1007/s10100-022-00838-w.
[605] J. G. Moore, Mini-columns and ghost columns in Columbia River lava, Journal of Volcanology and Geothermal Research 374 (2019) 242–251. doi:10.1016/j.jvolgeores.2019.01.015.
[606] Y. Akiba, A. Takashima, A. Inoue, H. Ishidaira, H. Shima, Geometric attributes of polygonal crack patterns in columnar joints, Earth Space Sci. 8 (2021) e2020EA001457. doi:10.1029/2020EA001457.
[607] J. Vasseur, F. B. Wadsworth, The permeability of columnar jointed lava, J. Geophys. Res.: Solid Earth 124 (2019) 11305–11315. doi:10.1029/2019JB018118.
[608] Z. Chao, G. Ma, X. Hu, G. Luo, Research on anisotropic permeability and porosity of columnar jointed rock masses during cyclic loading and unloading based on physical model experiments, Bull. Eng. Geol. Env. 79 (2020) 5433—-5454. doi:10.1007/s10064-020-01892-x.
[609] Z. Niu, Z. Zhu, X. Que, Y. He, X. Xie, Hydromechanical behaviour of columnar jointed rock masses under true triaxial conditions: An experimental and theoretical investigation, Geoenergy Sci. Eng. 224 (2023) 211623. doi:10.1016/j.geoen.2023.211623.
[610] X. Que, Z. Zhu, Y. He, Z. Niu, H. Huang, Strength and deformation characteristics of irregular columnar jointed rock mass: A combined experimental and theoretical study, J. Rock Mech. Geotech. Eng. 15 (2023) 429–441. doi:10.1016/j.jrmge.2022.03.007.
[611] R. S. Jayne, H. Wu, R. M. Pollyea, Geologic CO_2 sequestration and permeability uncertainty in a highly heterogeneous reservoir, Int. J. Greenhouse Gas Control 83 (2019) 128–139. doi:0.1016/j.ijggc.2019.02.001.
[612] H. Wu, R. S. Jayne, R. J. Bodnar, R. M. Pollyea, Simulation of CO_2 mineral trapping and permeability alteration in fractured basalt: Implications for geologic carbon sequestration in mafic reservoirs, Int. J. Greenhouse Gas Control 109 (2021) 103383. doi:10.1016/j.ijggc.2021.103383.
[613] M. K. Tivey, Generation of seafloor hydrothermal vent fluids and associated mineral deposits, Oceanography 20 (2007) 50–65. doi:10.5670/oceanog.2007.80.
[614] R. Hékinian, J. Francheteau, R. D. Ballard, Morphology and evolution of hydrothermal deposits at the axis of the East Pacific Rise, Ocean. Acta. 8 (1985) 147–155.
[615] J. Karson, Growth at Lost City, 2005. URL: https://web.archive.org/web/20250507092543/https://oceanexplorer.noaa.gov/explorations/05lostcity/logs/july25/july25.html.
[616] C. Gutiérrez-Ariza, L. M. Barge, Y. Ding, S. S. S. Cardoso, S. E. McGlynn, R. Nakamura, D. Giovanelli, R. Price, H. E. Lee, F. J. Huertas, C. I. Sainz-Díaz, J. H. E. Cartwright, Magnesium silicate chimneys at the Strytan hydrothermal field, Iceland, as analogues for prebiotic chemistry at alkaline submarine hydrothermal vents on the early Earth, Progress in Earth and Planetary Science 11 (2024) 11. doi:10.1186/s40645-023-00603-w.
[617] J. Turner, Laboratory models of growing flanges, and a comparison with other growth mechanisms of "black smoker" chimneys, Earth and Planetary Science Letters 134 (1995) 491–499. doi:10.1016/0016-7037(95)00118-2.
[618] J. H. E. Cartwright, B. Escribano, C. I. Sainz-Díaz, Chemical-garden formation, morphology, and composition. I. effect of the nature of the cations, Langmuir 27 (2011) 3286–3293. doi:10.1021/la104192y.
[619] J. H. E. Cartwright, J. M. García-Ruiz, M. L. Novella, F. Otálora, Formation of chemical gardens, Journal of colloid and interface science 256 (2002) 351–359. doi:0.1006/jcis.2002.8620.
[620] W. Martin, M. J. Russell, On the origin of biochemistry at an alkaline hydrothermal vent, Philosophical transactions of the Royal Society of London. Series B, Biological sciences 362 (2007) 1887–1925. doi:10.1098/rstb.2006.1881.
[621] S. G. Sander, A. Koschinsky, Metal flux from hydrothermal vents increased by organic complexation, Nature Geoscience 2011 4:3 4 (2011) 145–150. doi:10.1038/ngeo1088.
[622] V. Sojo, B. Herschy, A. Whicher, E. Camprubí, N. Lane, The origin of life in alkaline hydrothermal vents, Astrobiology

16 (2016) 181–197. doi:10.1089/ast.2015.1406.
[623] R. Stanulla, C. Stanulla, E. Bogason, T. Pohl, B. Merkel, Structural, geochemical, and mineralogical investigation of active hydrothermal fluid discharges at Strýtan hydrothermal chimney, Akureyri Bay, Eyjafjörður region, Iceland, Geothermal Energy 5 (2017) 1–11. doi:10.1186/s40517-017-0065-0.
[624] C. Monnin, V. Chavagnac, C. Boulart, B. Ménez, M. Gérard, E. Gérard, C. Pisapia, M. Quemeneur, G. Erauso, A. Postec, L. Guentas-Dombrowski, C. Payri, B. Pelletier, Fluid chemistry of the low temperature hyperalkaline hydrothermal system of Prony Bay (New Caledonia), Biogeosciences 11 (2014) 5687–5706. doi:10.5194/bg-11-5687-2014.
[625] E. De Boever, D. Birgel, V. Thiel, P. Muchez, J. Peckmann, L. Dimitrov, R. Swennen, The formation of giant tubular concretions triggered by anaerobic oxidation of methane as revealed by archaeal molecular fossils (Lower Eocene, Varna, Bulgaria), Palaeogeography, Palaeoclimatology, Palaeoecology 280 (2009) 23–36. doi:10.1016/j.palaeo.2009.05.010.
[626] A. Judd, M. Hovland, Seabed fluid flow: the impact on geology, biology and the marine environment, Cambridge University Press, 2009.
[627] A. J. Kopf, Significance of mud volcanism, Reviews of geophysics 40 (2002) 2–1. doi:10.1029/2000RG000093.
[628] M. Hovland, On the self-sealing nature of marine seeps, Continental Shelf Research 22 (2002) 2387–2394. doi:10.1016/S0278-4343(02)00063-8.
[629] K. M. Brown, The nature and hydrogeologic significance of mud diapirs and diatremes for accretionary systems, Journal of Geophysical Research: Solid Earth 95 (1990) 8969–8982. doi:10.1029/JB095iB06p08969.
[630] B. M. Teichert, G. Bohrmann, E. Suess, Chemoherms on Hydrate Ridge—Unique microbially-mediated carbonate build-ups growing into the water column, Palaeogeography, Palaeoclimatology, Palaeoecology 227 (2005) 67–85. doi:10.1016/j.palaeo.2005.04.029.
[631] S. Conti, D. Fontana, Miocene chemoherms of the northern Apennines, Italy, Geology 27 (1999) 927–930. doi:/10.1130/0091-7613(1999)027<0927:MCOTNA>2.3.CO;2.
[632] L. D. Hermann, Maslographia Oder Beschreibung Des Schlesischen Massel Im Oelß-Bernstädtischen Fürstenthum mit seinen Schauwürdigkeiten: Theils Unterschiedlicher so wohl Heydnischer, als Christlicher Antiquitæten, Monumenten und Epitaphien, Theils Auf dem so genan [n] ten Töppelberge gefundener Sonderbahren Reliquien, von Urnis oder Todten-Gefässen, Fibulis, Stylis, Nadeln oder Grieffeln, Messern, Müntzen, Donnerkeilen [et] c. Theils In, und als auch umb Massel In Regno Animali, Vegetabili, und Minerali befindlicher Naturalien, versteinter Muscheln, oder Muschel-Steinen, auch anderen figurirten Stein-Wesens, geschliffenen, und polirten Steinen, wunderbahren Brunnen, Erd-Baum-und Feld-Gewächsen, Nebst Dazu gehörigen Kupffer-Stücken, Brachvogel, 1711.
[633] Alfonso X, J. Fernandez Montana, Lapidario del Rey D. Alfonso X: códice original, 1881.
[634] M. A. Pasek, V. D. Pasek, The forensics of fulgurite formation, Mineralogy and Petrology 112 (2018) 185–198. doi:10.1007/s00710-017-0527-x.
[635] R. Grapes, Pyrometamorphism, 2nd ed., Springer-Verlag Berlin Heidelberg, 2010.
[636] J. J. Petty, The origin and occurrence of fulgurites in the Atlantic Coastal Plain, American Journal of Science s5-31 (1936) 188–201. doi:10.2475/ajs.s5-31.183.188.
[637] M. P. Gailliot, Petrified lightning, Rocks & Minerals 55 (1980) 13–17. doi:10.1080/00357529.1980.11764615.
[638] E. A. Carter, M. D. Hargreaves, T. P. Kee, M. A. Pasek, H. G. M. Edwards, A Raman spectroscopic study of a fulgurite, Philosophical Transactions: Mathematical, Physical and Engineering Sciences 368 (2010) 3087–3097. doi:10.1098/rsta.2010.0022.
[639] J. Garcia-Guinea, M. Furio, M. Fernandez-Hernan, M. A. Bustillo, E. Crespo-Feo, V. Correcher, L. Sanchez-Munoz, E. Matesanz, The quartzofeldspathic fulgurite of Bustaviejo (Madrid): Cathodoluminescence and Raman emission, AIP Conference Proceedings 1163 (2009) 128–134. doi:10.1063/1.3222878.
[640] P. Martín-Ramos, F. P. Gil, F. J. Martín-Gil, J. Martín-Gil, Characterization of exogenic fulgurites from an archaeological site in Tiedra, Valladolid, Spain, Geological Magazine 156 (2019) 1455–1462. doi:10.1017/S0016756819000438.
[641] B. L. Hess, S. Piazolo, J. Harvey, Lightning strikes as a major facilitator of prebiotic phosphorus reduction on early Earth, Nature Communications 12 (2021) 1535. doi:10.1038/s41467-021-21849-2.
[642] L. Niemeyer, L. Pietronero, H. J. Wiesmann, Fractal dimension of dielectric breakdown, Physical Review Letters 52 (1984) 1033–1036. doi:10.1103/PhysRevLett.52.1033.
[643] C. W. Passchier, J. S. Myers, A. Kröner, Field geology of high-grade gneiss terrains, Springer Science & Business Media, 2012.
[644] A. Seilacher, Fault-graded beds interpreted as seismites, Sedimentology 13 (1969) 155–159. doi:10.1111/j.1365-3091.1969.tb01125.x.
[645] P. Alfaro, L. Gibert, M. Moretti, F. J. García-Tortosa, C. S. de Galdeano, J. Galindo-Zaldivar, A. C. Lopez-Garrido, The significance of giant seismites in the Plio-Pleistocene Baza palaeo-lake (S Spain), Terra Nova 22 (2010) 172–179. doi:10.1111/j.1365-3121.2010.00930.x.
[646] P. Alfaro, M. Moretti, J. M. Soria, Soft-sediment deformation structures induced by earthquakes (seismites) in Pliocene lacustrine deposits (Guadix-Baza Basin, Central Betic Cordillera), Eclogae Geologicae Helvetiae 90 (1997) 531–540.
[647] C. Montenat, P. Barrier, P. Ott d'Estevou, C. Hibsch, Seismites: An attempt at critical analysis and classification, Sedimentary Geology 196 (2007) 5–30. doi:10.1016/j.sedgeo.2006.08.004.
[648] M. Moretti, A. Ronchi, Liquefaction features interpreted as seismites in the Pleistocene fluvio-lacustrine deposits of the Neuquén Basin (Northern Patagonia), Sedimentary Geology 235 (2011) 200–209. doi:10.1016/j.sedgeo.2010.09.014.
[649] G. Shanmugam, The seismite problem, Journal of Palaeogeography 5 (2016) 318–362. doi:10.1016/j.jop.2016.06.002.
[650] H. E. Jewell, F. R. Ettensohn, An ancient seismite response to Taconian far-field forces, Journal of Geodynamics 37 (2004) 487–511. doi:10.1016/j.jog.2004.02.017.
[651] G. H. Bachmann, M. A. Aref, A seismite in Triassic gypsum deposits (Grabfeld Formation, Ladinian), southwestern

Germany, Sedimentary Geology 180 (2005) 75–89. doi:10.1016/j.sedgeo.2005.04.006.
[652] E. Kagan, M. Stein, S. Marco, Integrated paleoseismic chronology of the Last Glacial Lake Lisan: From lake margin seismites to deep-lake mass transport deposits, Journal of Geophysical Research: Solid Earth 123 (2018) 2806–2824. doi:10.1002/2017JB014117.
[653] M. Rodriguez-Pascua, J. Calvo, G. De Vicente, D. Gómez-Gras, Soft-sediment deformation structures interpreted as seismites in lacustrine sediments of the Prebetic Zone, SE Spain, and their potential use as indicators of earthquake magnitudes during the Late Miocene, Sedimentary Geology 135 (2000) 117–135. doi:10.1016/S0037-0738(00)00067-1.
[654] I. Leslie, R. Heinse, Characterizing soil–pipe networks with pseudo-three-dimensional resistivity tomography on forested hillslopes with restrictive horizons, Vadose Zone Journal 12 (2013) vzj2012–0200. doi:10.2136/vzj2012.0200.
[655] K. Grimes, A. Spate, Laterite karst, Ackma Journal 73 (2008) 49–52.
[656] C. Harloff, Zonal structure in plagioclases: Leidsche Geol, 1927.
[657] J. Phemister, Zoning in plagioclase felspar, Mineralogical magazine and journal of the Mineralogical Society 23 (1934) 541–555. doi:10.1180/minmag.1934.023.145.02.
[658] E. S. Hills, Reverse and oscillatory zoning in plagioclase felspars, Geological Magazine 73 (1936) 49–56. doi:10.1017/S0016756800087914.
[659] G. W. Fisher, Nonequilibrium thermodynamics as a model for diffusion-controlled metamorphic processes, American Journal of Science 273 (1973) 897–924. doi:10.2475/ajs.273.10.897.
[660] D. G. Fraser, Thermodynamics in Geology: Proceedings of the NATO Advanced Study Institute Held in Oxford, England, September 17–27, 1976, volume 30, Springer Science & Business Media, 1977.
[661] P. Ortoleva, From nonlinear waves to spiral and speckle patterns: Nonequilibrium phenomena in geological and biological systems, Physica D: Nonlinear Phenomena 12 (1984) 305–320. doi:10.1016/0167-2789(84)90535-9.
[662] P. Ortoleva, E. Merino, C. Moore, J. Chadam, Geochemical self-organization I; reaction-transport feedbacks and modeling approach, American Journal of science 287 (1987) 979–1007. doi:10.2475/ajs.287.10.979.
[663] M. M. Hanczyc, S. S. Mansy, J. W. Szostak, Mineral surface directed membrane assembly, Origins of Life and Evolution of Biospheres 37 (2007) 67–82. doi:10.1007/s11084-006-9018-5.
[664] S. E. McGlynn, I. Kanik, M. J. Russell, Peptide and RNA contributions to iron–sulphur chemical gardens as life's first inorganic compartments, catalysts, capacitors and condensers, Philosophical Transactions of the Royal Society A: Mathematical, Physical and Engineering Sciences 370 (2012) 3007–3022. doi:/10.1098/rsta.2011.0211.
[665] E. Kotopoulou, Mineral self-organization in extreme geochemical environments: implications for prebiotic chemistry and life detection, Ph.D. thesis, Universidad de Granada, 2020.
[666] J. M. García-Ruiz, M. A. Van Zuilen, W. Bach, Mineral self-organization on a lifeless planet, Physics of Life Reviews 34 (2020) 62–82. doi:10.1016/j.plrev.2020.01.001.
[667] E. Kotopoulou, M. Lopez-Haro, J. J. Calvino Gamez, J. M. García-Ruiz, Nanoscale anatomy of iron-silica self-organized membranes: implications for prebiotic chemistry, Angewandte Chemie International Edition 60 (2021) 1396–1402. doi:10.1002/anie.202012059.
[668] J. M. Garcia-Ruiz, S. T. Hyde, A. Carnerup, A. Christy, M. Van Kranendonk, N. Welham, Self-assembled silica-carbonate structures and detection of ancient microfossils, Science 302 (2003) 1194–1197. doi:10.1126/science.1090163.